Probing Electron-Electron Interactions with a Quantum Antidot

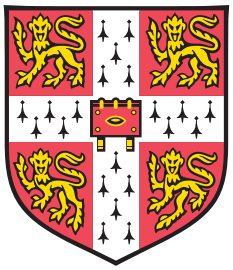

Lee Christopher Bassett

King's College

University of Cambridge

A thesis submitted for the degree of

Doctor of Philosophy

September 2009

To my parents, who taught me to ask questions,
and to Dani, who is the only answer I need.

Summary

In the integer quantum Hall (IQH) regime, an antidot provides a finite, controllable 'edge' of quantum Hall fluid which is an ideal laboratory for investigating the collective dynamics of large numbers of interacting electrons. Transport measurements of single antidots probe the excitation spectra of the antidot edge, and gate-defined antidot devices offer the flexibility to vary both the dimensions of the antidot and the couplings to the extended IQH edge modes which serve as leads. We can also use the spin-selectivity of the IQH edge modes to perform spin-resolved transport measurements, from which we can infer the antidot spin-structure. This thesis describes a combination of such transport experiments and related computational models designed to investigate the effects of electron-electron interactions in quantum antidots, with general implications for the physics of spin and charge in IQH systems.

We focus on the regime of relatively low magnetic fields ($B \lesssim 1\,\mathrm{T}$) and antidot filling factor $\nu_{\mathrm{AD}} = 2$, in which the standard antidot transport experiments are well-described by a single-particle (SP) model of antidot orbital states in the lowest Landau level (LLL). We find that the *orbital-excitation* energies observed in standard transport experiments are well-described by SP physics but that the *spin-excitation* energy implied by spin-resolved measurements are much smaller than that predicted by the SP model. By treating the $\nu_{\mathrm{AD}} = 2$ antidot as a 'dot of holes' in the LLL and developing a computational model for spin-resolved sequential transport, we show that this observed spin-charge separation is consistent with the edge-excitations predicted for a 'maximum density droplet' (MDD) of interacting holes in the LLL.

Our work provides a powerful example of the practical applications of IQH edge modes for selective transport in mesoscopic quantum electronics, which we have used to perform the first spin-resolved measurements of $\nu_{\mathrm{AD}} = 2$ transmission resonances. Our discovery of spin-charge separation in the low-field antidot excitation spectrum paints a picture of the antidot as a finite droplet of interacting IQH fluid in the LLL, with all of the rich physics of exchange, collective modes, spin textures, etc., which this entails. Our results are therefore relevant not only for the physics of antidots, but more broadly for the understanding of interacting electronic systems of many particles in the IQH regime.

Acknowledgements

As it is with just about everything I do, this thesis ended up taking far longer to complete than I expected. I think it was my invaluable colleague Jon Griffiths who first taught me Hofstadter's rule: that everything you try to do takes roughly 150% of the time you might expect, even when you account for Hofstadter's rule. Still, this Ph.D., thesis writing included, has been an incredibly enjoyable experience. Everyone should have the opportunity to be paid to live in a fairy-tale town and play with expensive toys every day. But unfortunately not everyone is so lucky, and so I am keenly aware of the many people and organisations who have helped me to live the life to which I have become accustomed, and which I shall dearly miss in the coming years.

First, I acknowledge the unflinching support, valuable advice, and almost unfathomable optimism of my supervisor Dr. Chris Ford. He always seemed to know that together we would make something of what sometimes seemed to me to be an abyss of utter confusion, and although it took longer than we hoped (thanks, Hofstadter), he was right. He is a fount of knowledge and experience on everything from dilution refrigerators to rubber bungs, and I already realise that I am leaving without having taken advantage of it nearly enough.

These types of experiments are necessarily the result of many people's contributions, and several colleagues and collaborators have been particularly helpful. On the experimental side, Jon Griffiths, Jon Prance, Abi Graham, Antonio Corcoles, Francois Sfigakis, and Masaya Kataoka have all generously offered their help and hard-earned advice in the lab, and Ken Cooper, David Anderson, and Jon Griffiths have provided essential help with device processing and electron-beam fabrication. Masaya in particular was a valuable resource for his deep knowledge of antidot experiments, and taught by example with his skeptical and plodding style which nearly always *worked*. On the theoretical side, Crispin Barnes provided many useful bits of insight, and provided the code for the Green's function calculations I used for some of the modeling in this thesis. Nigel Cooper of the Theory of Condensed Matter group contributed many of the initial ideas regarding the importance of exchange interactions for making sense of our spin-resolved measurements, and gave a great deal of his time to several useful discussions. Adam Thorn was nearly always 'willing' to be distracted to help with computer problems, and

has also kindly offered to take care of the printing/binding/submitting of this thesis in exchange for beer.

I am grateful to the funding bodies which supported my study in Cambridge, notably the Marshall Aid Commemoration Commission, the National Science Foundation, and King's College, Cambridge. I also offer sincere thanks to my two examiners, Dr. Andrew Ferguson and Prof. Steve Simon, for their patience as this ran behind schedule.

Many of my friends and family members offered their encouragement and support over the years, and pretended not to mind that we lived an ocean apart for five years. My parents in particular have always been supportive and understanding, and were even willing to sacrifice their dining room table for three weeks as I raced to the finish line which seemed to keep moving father away.

Finally, I owe a deepest debt of gratitude to my amazing wife Danielle, mainly for just putting up with me. She put up with the late nights I spent at the lab, and the months of my experiments where we lived like ships literally passing in the night, as I would come to bed around the time she woke up to head to the river. She was even known to occasionally provide her company in the cryostat lab in the wee hours, even during Christmas when there was no heat. She put up with me being late for dinner every time my 'five minute job' ended up taking two hours. And she put up with this thesis taking a month longer to write than it was supposed to and then even a bit longer (thanks again, Hofstadter), giving up her vacation for the summer, and seems to be putting up with me keeping her awake by typing these last sentences in the corner of our hotel room. Dani has also acted as primary proofreader for my work, and has even pretended to enjoy it. Since I expect that very few people will set eyes on this document who are not physicists (Mom, Dad, have you made it this far?), and that most will be students, I'll offer a piece of unsolicited advice: if you have a chance to marry another physicist, take it, because nobody else will ever understand.

Contents

List of Figures

Preface

It is a great irony that we must work so hard to study interaction effects in solid-state electronic devices. In a typical two-dimensional electron system (2DES) with carrier density around $n_e = 2 \times 10^{11}$ cm^{-2}, the Coulomb energy between neighbouring electrons is $e^2 n_e^{1/2}/4\pi\epsilon\epsilon_0 \approx 5$ meV, which is almost always the largest relevant energy scale in a mesoscopic device. Especially given the small effective mass of electrons in GaAs, $m^* = 0.067 m_e$, the forces associated with such Coulomb interactions are immense; if an electron were given this energy in free space, it would no longer be gravitationally bound to the solar system! In retrospect, it might therefore seem quite surprising that early experiments with mesoscopic devices failed to show evidence of interacting electrons, seeming instead to reflect the 'ballistic' dynamics of free particles [e.g., 1–3]. The explanation for this behaviour rests in the theory of the Fermi liquid which describes the two-dimensional electron gas, in which the quasiparticle excitations are essentially equivalent to free electrons. Each electron becomes 'dressed' by interactions with other particles, and the collective excitations of the system have well-defined charges, masses, momenta, etc., exactly as if the system contained only a single electron [4]. Of course this does not mean that Coulomb effects are completely absent, but rather that their experimental signatures are often more subtle than might be expected. It is also worth noting that in some cases the description of the 2DES as a normal Fermi liquid breaks down, and the quasiparticle excitations are entirely different; the 'composite fermions' which serve as quasiparticles in the fractional quantum Hall regime are prime examples.

In this thesis we are interested in the effects of interactions in the integer quantum Hall (IQH) regime, where the quasiparticles are indeed 'electron-like.' We investigate these interactions by studying electron transport through single quantum antidots, which embody the physics of a finite edge of IQH fluid. Fundamentally, an antidot is simply an 'island' in the potential landscape of a 2DES on which electrons are absent, the exact opposite of a quantum dot, which is a small valley or 'puddle' of electrons. Even so, magnetic confinement leads to a quantised energy spectrum of zero-dimensional antidot

states which is in many ways analogous to the spectrum of similarly-sized quantum dots. Theoretically, it is in fact possible to treat an antidot as a 'dot of holes' in the 2DES, allowing for comparisons between antidot experiments and the literature on interactions in quantum Hall systems and in large quantum dots. Since a full description of the dynamics of many interacting particles remains a hard theoretical problem, experimental investigations of these effects are of fundamental interest.

Many of the important consequences of the Coulomb interaction are manifest through its interplay with electron spin. In particular, the *exchange interaction* results from the combination of Coulomb repulsion and Pauli exclusion, and it can lead to very complicated spin dynamics even for a system of just two electrons. The development of few-electron quantum dots over the past few years has opened promising avenues for research into coherent single-spin dynamics and the controlled manipulation of electron spins for quantum-information purposes (see [5] for a recent review), most of which relies on the physics of exchange. For systems of many particles, spin-charge interactions may lead to exotic effects such as spin-density waves or Skyrmions, particularly at the edge of the IQH fluid where nearby empty states make it possible for particles to rearrange [e.g., 6–8]. Interest in such 'collective modes' has spawned a vast literature of theoretical studies, but it has been difficult to find clear experimental examples of such idealised constructions in the real world. Some progress has been made with large quantum dots [9–11], but it is difficult to infer spin structure from transport experiments alone, and large quantum dots are often complicated by the tendency of electrons to rearrange between the 'edge' and the 'core' as experimental parameters are varied. This rearrangement is absent for antidots, since the antidot 'core' is always depleted, so we can be sure that the features we observe are due to the behaviour of the edge alone.

In our experiments we also take advantage of the unique properties of transport in the IQH regime, in which the 'leads' are extended edge modes whose topology we can control with appropriate gate designs. Electrons propagate coherently through these edge modes over mesoscopic distances, and the ability to control the topology of edge mode networks using surface gates has led to the recent realisation of electronic analogues to standard optical experiments, such as Fabry-Perot [12] and Mach-Zehnder [13] interferometers. While IQH edge modes share many properties with their optical counterparts, the addition of charge and spin interactions makes such electronic experiments extremely interesting, and has produced unexpected behaviour [14, 15]. In this work we use the spin-selectivity of these edge modes to perform spin-resolved measurements of the antidot transport, from which we can infer details about the spin-structure of the antidot edge.

Evidence for electron-electron interactions in antidots is certainly not new. While standard transport experiments at low magnetic fields ($B \lesssim 1$ T) appear to be well-described by a non-interacting model of single-particle (SP) antidot orbital states [16], this model is known to fail at higher B [17–20]. We expect that at some point the structure of the antidot edge changes fundamentally, as the characteristic orbital length scale $\ell_{\mathrm{B}} = \sqrt{\hbar/eB}$ shrinks and Coulomb interactions begin to dominate over the SP energy scales, but the nature of the evolution between these two regimes has not been well-understood up to this point. The high-B antidot edge probably takes the form of alternating compressible and incompressible 'stripes' for successive Landau levels, similar to the self-consistent model of IQH edge modes predicted to minimise the total energy along the extended edge [21]. The recent review by Sim, Kataoka, and Ford [22] provides a useful discussion of previous antidot studies, treating particularly those effects at higher fields which seem to require a self-consistent model.

In this work we look more closely at the low-B regime in which the SP model seems to be valid. We choose this regime for two main reasons. First, in order to develop a unified picture of antidot physics which connects the SP model at low fields with the self-consistent description at higher B, we seek evidence of 'inconsistencies' with SP physics at low B which reveal the subtle influence of interactions. In this sense our work follows directly from the experiments of Chris Michael [23], who studied antidot transport in the 'crossover' regime ($B \approx 1$–2 T) and noticed several intriguing effects. We consider a few of his findings in detail, and incorporate them into the general picture of low-B antidot physics developed in this work. Second, the simplicity of the SP antidot model has suggested several potential applications for antidots, such as a quantum Hall 'pump' [24], or a 'spin filter' [25]. We consider the spin-filtering proposal in detail with our spin-resolved measurements, and although we find that interactions destroy the filtering ability of the antidots we study, we do still believe that it is probably possible to design devices in which the spin-selectivity is preserved for the purposes of this application. We hope that other members of the scientific community, upon learning of our work, will recognise the flexibility of antidot devices both for applications such as this and for the experimental study of the fundamental physics of interactions in the quantum Hall regime.

The experiments described in this thesis were carried out in the Semiconductor Physics Group at the University of Cambridge. Except where noted otherwise, all aspects of the experiments, including device design, fabrication, testing, measurements, and analysis were performed by myself, although I have gained invaluable help and advice from many other members of the Semiconductor Physics group. Most notably, all

of this work was conceived and executed in close collaboration with my supervisor, Dr. Chris Ford. The theoretical modeling presented herein is also predominantly my own, but I have benefited greatly from the generous guidance of two experts in the theory of mesoscopic electronic devices: Dr. Crispin Barnes of the Semiconductor Physics group and Dr. Nigel Cooper of the Theory of Condensed Matter group here at Cambridge.

Structure of this thesis

Immediately following this preface begins the first of two theoretical chapters designed to provide the background and theoretical framework which is necessary for an understanding of the results presented in the remainder of the work. Much of the information in these two chapters is widely understood and is available elsewhere, but I have tried to unify the notation as much as possible and to justify the major results used in the modeling and analysis of later chapters. Moreover, I have tried to address in detail many of the issues which I found confusing at first (or second or third) encounter, and to present some of the derivations which I undertook because I could not find them printed elsewhere. I hope that these chapters will be useful for future students interested in mesoscopic electronic devices, and in quantum dots and antidots in particular.

Chapter 1 deals with the physics of single antidots. I present the SP model in terms of the stationary solutions of Schrödinger's equation for a circularly-symmetric antidot in a magnetic field, and discuss it in the context of the integer quantum Hall effect for lowest Landau level (LLL) states in particular. I try to develop an intuition for the interpretation of experimental results in terms of these SP states by considering several 'observable' properties of these eigenstates and their classical analogues in terms of 'skipping orbit' trajectories around the antidot. Finally, the Hartree-Fock mean-field theory for an antidot is developed in terms of a system of interacting 'holes' in the LLL, which takes the form of a maximum density droplet (MDD) at low fields.

Chapter 2 deals more generally with the theory of transport in mesoscopic electronic systems. I present the Landauer-Büttiker formalism for the analysis of linear-response transport coefficients in the IQH regime, which I use throughout this work to analyse edge-mode networks. I then make the connection between the Landauer-Büttiker formula and a more general theory of linear-response ballistic transport, formulated in terms of time-independent Green's functions. Such Green's function calculations are used to study the effects of realistic device geometries in Chapter 3. Finally, I present the theory of sequential transport through quantum dots, which is the basis for the model developed in Chapter 5 to describe transport through antidot states in the presence of

interactions.

A discussion of the results of new measurements and modeling begins in Chapter 3. In this first study, I consider orbital excitation spectra in the low-B regime obtained through non-linear transport measurements by Chris Michael [23], in which the orbital excitation energy ΔE_{SP} seems to decrease faster with B than the SP model predicts. Using a simple model supported by transport calculations based on the non-interacting Green's function of a realistic device, I show that this behaviour may be attributed to the inherent asymmetry of a real device rather than to interactions.

Chapter 4 is the heart of this work, in which I discuss the results of spin-resolved measurements of antidot transport. Using a set of quantum point contacts as injectors and detectors, the AD scattering coefficients for individual edge modes are directly measured in the low-B regime, with some surprising implications for AD spin physics. While the measured excitation spectra fit the SP picture in agreement with the results of Chapter 3, the spin-dependent transport clearly does not; whereas transport through individual Zeeman-split SP states should be spin-polarised, experiments show that both spins are transmitted through every resonance. These measurements also uncover spin-orbit mediated anticrossings between AD states and the presence of 'molecular' states resulting from an impurity in one of the channels, further demonstrating the power of the selective injection/detection technique to investigate details of quantum transport.

I propose an explanation for these findings in Chapter 5. The results are interpreted as signatures of exchange interactions which lower the spin excitation energy while preserving orbital SP energy scales. By treating the antidot theoretically as an MDD of holes in the LLL, I am able to reproduce many aspects of the measurements within a computational model of spin-resolved sequential transport. I discuss the features of this model and its limitations, and the implications of the experiments for a general theoretical understanding of low-lying excitations of the IQH edge.

Finally, I present in Chapter 6 the results of several additional measurements on the same device with the addition of an *in situ* rotating sample holder. By changing the orientation of the device relative to the magnetic field, I am able to vary the Zeeman energy (which depends on the total field) independently of the orbital energy scales (which depend only on the perpendicular component of the field). These data show clear evidence of crossing orbital states, although a relatively high electron temperature unfortunately means that the spin-selective technique used in Chapter 4 would not add much useful information. I also present evidence of coherently-coupled 'antidot molecules' which form as a result of unintentional impurities close to our antidot.

The thesis concludes with a brief discussion of its central results and their implica-

tions, and with suggestions for how these findings could be extended or considered in more detail in the future.

Declaration of Originality

This dissertation is the result of my own work and includes nothing which is the outcome of work done in collaboration except where specifically indicated in the text. It contains less than 60,000 words.

Chapter 1

Theoretical Background

In many cases, the physics of quantum antidots is analogous to that of comparably sized quantum dots at high magnetic fields, and so much of the vast literature concerning transport experiments on lithographically-defined quantum dots is directly relevant to the study of antidots. At first consideration this correspondence is surprising, since fundamentally an antidot device is an open system of an effectively infinite number of electrons, while a quantum dot is a zero-dimensional object with a finite number of particles. But as we will see, the effect of a magnetic field perpendicular to a two-dimensional electron system (2DES) is to establish zero-dimensional electronic states which encircle an antidot. Analogous to the semi-classical picture of 'skipping' cyclotron orbits, these are the stationary solutions to the time-independent Schrödinger equation. Furthermore, because transport measurements probe only those states near the surface of the electronic Fermi sea, our experiments explore the properties of just a few of these zero-dimensional states at any given situation and we can generally ignore the continuum of electrons stretching away from the antidot. In this chapter we consider the theoretical description of such zero-dimensional antidot states, a framework which is necessary for the interpretation of the experiments and models presented in this thesis.

The chapter is divided into three sections. In the first we solve the single-particle (SP) Schrödinger equation for the non-interacting eigenstates of a parabolic antidot potential, i.e. the inverse of a parabolic quantum dot. At the relatively low magnetic fields ($B \lesssim 1$ T) studied in this work, the SP wave functions are well-separated in both space and energy, and so a non-interacting model is often sufficient to describe the features observed in standard transport measurements. So in the second section, we further investigate the properties of these SP states, hopefully to aid the reader's intuition about their physics. Finally, in the third section we consider the treatment of electron-electron interactions

through Hartree-Fock theory, which we will eventually use in Chapter 5 to explain many of the features we observe which appear to be inconsistent with the non-interacting SP model.

1.1 Single-particle eigenstates

We begin with a consideration of the non-interacting SP eigenstates for electrons in two dimensions subject to a perpendicular magnetic field, since these form a useful starting point for discussion in many aspects of this thesis. The Hamiltonian for an electron (charge $-e$) in the presence of a time-independent magnetic field $\mathbf{B}$ and electric potential $\varphi(\mathbf{x})$ is

$$\hat{H} = \frac{1}{2m^*}(\hat{\mathbf{p}} + e\mathbf{A})^2 - e\varphi(\mathbf{x}), \tag{1.1}$$

where $\mathbf{p} = -i\hbar\nabla$ is the canonical momentum, $\mathbf{A}$ is the magnetic vector potential ($\mathbf{B} = \nabla \wedge \mathbf{A}$), and $m^* = 0.067m_e$ is the effective electron mass in GaAs. In most cases we are interested in problems with cylindrical symmetry, so it makes sense to choose the symmetric gauge,

$$\mathbf{A} = \frac{1}{2}\mathbf{B} \wedge \mathbf{x}. \tag{1.2}$$

In a semiconductor heterostructure like the GaAs/AlGaAs structures used in this work, the confinement along the growth (z) direction is strong enough that, at the low temperatures used for measurements, only a single energy level is populated. Dynamics in this dimension are then completely decoupled from those in the plane of the 2DES, and the problem becomes purely two-dimensional. We therefore seek solutions to the Schrödinger equation

$$\hat{H}\psi = E\psi \tag{1.3}$$

in the remaining (x, y) coordinates. To describe a circularly-symmetric antidot potential $\varphi(r)$, we shift to polar coordinates (r, ϕ) in which $\mathbf{A} = \frac{1}{2}B_z r\hat{\phi}$ to write Eq. (1.3) in the form

$$\left[\frac{\hat{p}^2}{2m^*} + \left(\frac{\omega_C}{2}\right)\hat{L}_z + \frac{1}{2}m^*\left(\frac{\omega_C}{2}\right)^2 r^2 - e\varphi(r)\right]\psi = E\psi, \tag{1.4}$$

where $\omega_C = eB_z/m^*$ is the cyclotron frequency,

$$\hat{p}^2 = -\hbar^2\left(\frac{1}{r}\frac{\partial}{\partial r}\left(r\frac{\partial}{\partial r}\right) + \frac{1}{r^2}\frac{\partial^2}{\partial\phi^2}\right), \tag{1.5}$$

and

$$\hat{L}_z = \hat{r} \wedge \hat{p} = -i\hbar \frac{\partial}{\partial \phi} \tag{1.6}$$

is the canonical angular momentum operator. Since the circular symmetry implies that the eigenvalue of $\hat{L}_z$ is conserved, we separate $\psi(r, \phi)$ by coordinates as

$$\psi(r, \phi) = f(r) e^{im\phi}, \tag{1.7}$$

where $m = 0, \pm 1, \pm 2, \ldots$ is the azimuthal quantum number ($\hat{L}_z \psi = m\hbar\psi$).

1.1.1 SP states in a parabolic antidot potential

The particular case of a parabolic electric potential is frequently encountered in the quantum dot literature, since it simply adds to the quadratic effective potential from the magnetic field, and Eq. (1.4) has a well-known analytic solution [26]. Since we are often interested only in AD states near the Fermi level, where we may locally approximate the potential by a suitable inverted parabola, these wave functions form a useful basis for calculations, and so we explore some of their properties below.

With a parabolic antidot potential with curvature determined by the parameter ω_0,

$$-e\varphi(r) = -\frac{1}{2} m^* \omega_0^2 r^2, \tag{1.8}$$

and the definition of Eq. (1.7), the radial part of the Schrödinger Eq. (1.4) becomes

$$\left[-\frac{\hbar^2}{2m^*} \left(\frac{1}{r} \frac{\partial}{\partial r} \left(r \frac{\partial}{\partial r} \right) - \frac{m^2}{r^2} \right) + \frac{m\hbar\omega_\mathrm{C}}{2} + \frac{1}{2} m^* \left(\frac{b\omega_\mathrm{C}}{2} \right)^2 r^2 \right] f(r) = E f(r), \tag{1.9}$$

where

$$b = \sqrt{1 - \left(\frac{2\omega_0}{\omega_\mathrm{C}} \right)^2}. \tag{1.10}$$

Note that while we focus on the case of an antidot potential, the analogous results for a quantum dot may be obtained by reversing the sign under the square root in Eq. (1.10) (or through the identification $\omega_0 \to i\omega_0$), as well as those of a free particle, for which $b = 1$.

We proceed to solve Eq. (1.9) in terms of the dimensionless coordinate

$$\xi = \frac{b m^* \omega_\mathrm{C} r^2}{2\hbar} = \frac{1}{2} \left(\frac{r}{\ell} \right)^2, \tag{1.11}$$

where $\ell = \sqrt{\hbar/(eB_z b)}$ is the natural length scale of the system. This leads to the ODE

$$\xi f'' + f' + \left(-\frac{\xi}{4} + \beta - \frac{m^2}{4\xi}\right) f = 0, \tag{1.12}$$

where

$$\beta = \frac{E}{\hbar b \omega_{\mathrm{C}}} - \frac{m}{2b}. \tag{1.13}$$

This equation may be solved in a variety of ways, for example through a power series expansion or by using raising and lowering operators [27]. The method we present here rests on the recognition that Eq. (1.12) is very similar to the Laguerre ODE, given by

$$xy'' + (\nu + 1 - x)y' + \lambda y = 0, \tag{1.14}$$

for real constants ν and λ. By making the substitution $f(\xi) = e^{a\xi}\xi^d g(\xi)$, we recast Eq. (1.12) as

$$\xi g'' + (2d + 1 + 2a\xi)g' + \left(\xi a^2 - \frac{\xi}{4} + 2ad + a + \beta + \frac{d^2}{\xi} - \frac{m^2}{4\xi^2}\right) g = 0. \tag{1.15}$$

Thus, by setting $a = -1/2$ and $d = |m|/2$, we obtain the Laguerre equation

$$\xi g'' + (|m| + 1 - \xi)g' + \left(\beta - \frac{|m|}{2} - \frac{1}{2}\right) g = 0, \tag{1.16}$$

in which we identify

$$\begin{cases} \nu = |m| \\ \lambda = \beta - \frac{|m|}{2} - \frac{1}{2}. \end{cases} \tag{1.17}$$

Solutions to Eq. (1.14) may be written in terms of the associated Laguerre functions $L_\lambda^\nu(x)$, where $\lambda = n$ must be a non-negative integer in order to satisfy the boundary condition that $\lim_{\xi\to\infty} f(\xi) = 0$.[1] This condition determines the energy eigenvalues

$$E_{n,m} = b\hbar\omega_{\mathrm{C}}\left(n + \frac{|m|}{2} + \frac{1}{2}\right) + \frac{m}{2}\hbar\omega_{\mathrm{C}}, \tag{1.18}$$

with the corresponding radial wave functions

$$f_{n,m}(\xi) = C_{n,m} e^{-\xi/2}\xi^{|m|/2} L_n^{|m|}(\xi), \tag{1.19}$$

[1] With this condition, the $L_n^{|m|}(x)$ are polynomials with a finite number of terms.

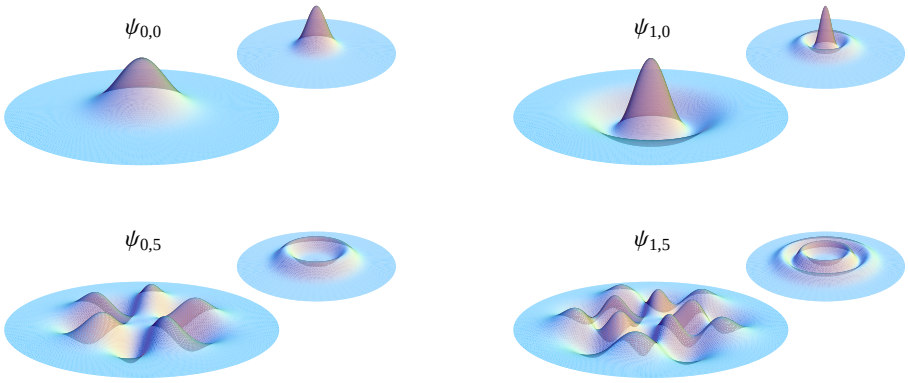

Figure 1.1: Eigenstates $\psi_{n,m}(r,\phi)$ for electrons subject to a parabolic potential and a perpendicular magnetic field B. Each figure shows $\Re\{\psi_{n,m}\}$ as well as $|\psi_{n,m}|^2$ as an inset.

where the normalisation constants

$$C_{n,m} = \frac{1}{\ell}\sqrt{\frac{n!}{2\pi(n+|m|)!}} \tag{1.20}$$

are easily computed with the help of the orthogonality relation for the Laguerre polynomials:

$$\int_0^\infty e^{-x}x^k L_n^k(x)L_m^k(x)dx = \frac{(n+k)!}{n!}\delta_{nm}. \tag{1.21}$$

A few examples of these wave functions are shown in Fig. 1.1.

1.1.2 Landau levels and the quantum Hall effect

In the context of quantum dots, it makes sense to consider the evolution of states between the low-B ($\omega_C \ll \omega_0$) and high-B ($\omega_C \gg \omega_0$) regimes, known as the Darwin-Fock spectrum [28, 29]. For an antidot, however, the low-B case is not especially interesting, since for $\omega_C < 2\omega_0$ the electrons are no longer confined, and so experiments are always performed in the presence of a large magnetic field. Under these circumstances, the states begin to converge to a set of Landau levels (LLs), which are the free electron

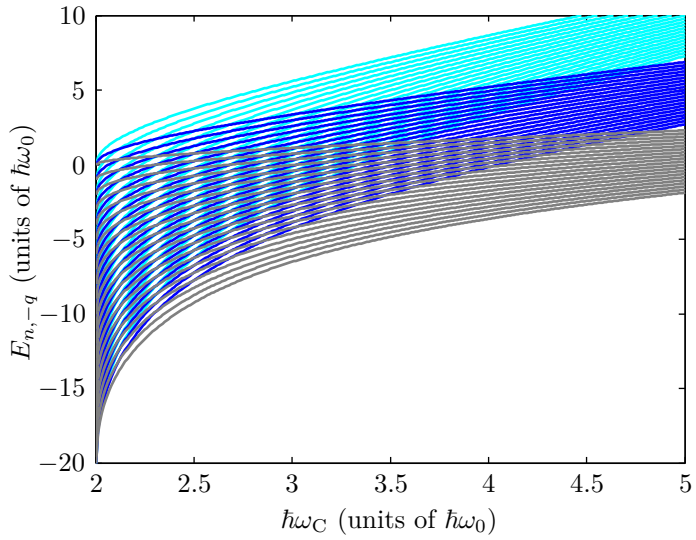

Figure 1.2: Antidot eigenenergies $E_{n,-q}$ of states in the three lowest LLs, with $n = 0, 1, 2$ and $q = 0$–20, as a function of magnetic energy $\hbar\omega_C$. Note that no stationary states are defined for $\omega_C < 2\omega_0$. In a real device, saddle points in the constrictions define a maximum q for each LL, such that only states from lower LLs exist below the Fermi energy.

eigenstates obtained in the high-B limit ($b \to 1$),

$$E^{\text{free}}_{n,m} = \hbar\omega_C \left(n + \frac{|m| + m}{2} + \frac{1}{2} \right) \tag{1.22a}$$

$$= \hbar\omega_C \left(n_{LL} + \frac{1}{2} \right), \tag{1.22b}$$

where $n_{LL} = 0, 1, 2, \ldots$ is the LL quantum number, defined as

$$n_{LL} = \begin{cases} n & \text{if } m \leq 0, \\ n + |m| & \text{if } m > 0. \end{cases} \tag{1.23}$$

The B-dependence of some of the eigenenergies in Eq. (1.18) is shown in Fig. 1.2.

In a 2DES at low temperature, the occupied states are those below the Fermi energy, E_F, which is fixed by the two-dimensional electron density of the sample, n_e. At a fixed field, n_e also determines the *filling factor*,

$$\nu = \frac{n_e h}{e B_\perp}, \tag{1.24}$$

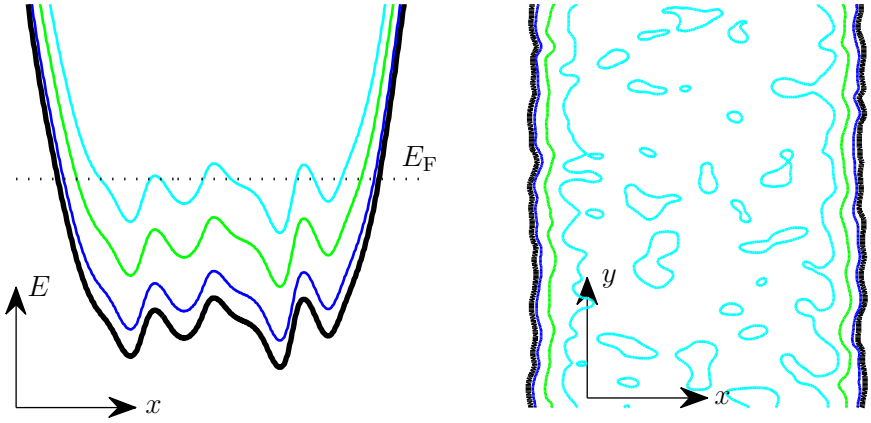

Figure 1.3: Landau level energies as a function of position across a real device containing random disorder. The states in the bulk of the device are localised around dots and antidots in the disorder potential, such that only electrons at the edges of the sample propagate macroscopic distances.

as the number of electrons per magnetic flux quantum h/e, or equivalently the number of filled (spin non-degenerate) LLs.[1] Through the application of voltages to surface gates patterned above the 2DES, n_e (and hence ν) may be varied throughout a device. If this electric potential variation is small on the length scale of free-electron wave functions (the magnetic length, $\ell_B = \sqrt{\hbar/(eB_\perp)}$), then it may be treated as a small perturbation which adds a position-dependent offset to the LL energy $(n_{LL} + \frac{1}{2})\hbar\omega_C$.

The above picture of two-dimensional electron states leads to a simple description of the quantum Hall effect [30, 31] in terms of LLs, as depicted in Fig. 1.3. Most of the electron states in the bulk 2D regions are localised by the background disorder potential (naturally-occurring dots and antidots) and so cannot contribute to equilibrium transport. Near the edges of the sample, however, the filled LLs follow the potential up through E_F, creating a set of extended *edge states* capable of carrying current across the device. In contrast to the closed edge of a quantum dot or antidot (with circumference smaller than the phase coherence length), these edge states have a continuous spectrum, and so serve as metallic leads with a density of states given by the Fermi distribution. In order to probe antidot states via transport measurements, these edge states must

[1] To see this relationship, consider the free electron wave function given by Eq. (1.19). The envelope $e^{-\xi/2}\xi^{|m|/2}$ has a maximum at $\xi = |m|$, and so the number of electrons within a radius $\xi = |m|$ is $\approx |m|$ (this can be shown to be strictly true for infinite systems). Hence, each LL has density $n_e^{LL} = 1/(2\pi\ell_B^2) = eB_\perp/h$.

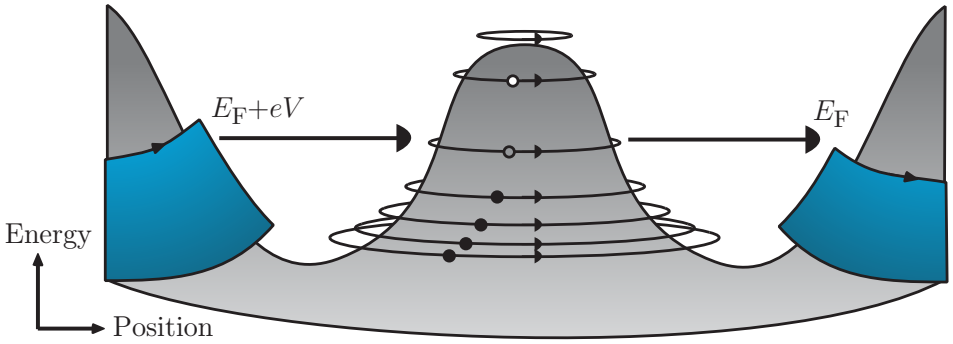

Figure 1.4: Cross-sectional view of an antidot at the centre of a split-gate, where tunnelling occurs between the edge states acting as metallic leads and the quantised antidot states.

be brought within tunnelling distance (of order ℓ_B) of the antidot states, as shown in Fig. 1.4. This is accomplished by fabricating an antidot in the centre of a split-gate, creating two constrictions in which the filling factor ν_C may be independently varied. The minimum ν_C defines the highest LL with states fully encircling the antidot, which we denote as ν_{AD}. This may be chosen anywhere from zero to the bulk value ν_B, but in this work we are usually interested in the case when only one spin-degenerate LL is occupied, such that $\nu_{AD} = 2$. We investigate the properties of these SP states in further detail below.

1.1.3 The single-particle picture of a $\nu_{AD} = 2$ antidot

When the constrictions on either side of an antidot are set to $\nu_C = 2$, the only occupied antidot states are those in the lowest Landau level (LLL). These states are given by $n = 0$, $m \leq 0$, and so with $q = -m$ as a non-negative integer (such that the canonical angular momentum $L_z = -q\hbar$), they have energies

$$E_q^{\mathrm{LLL}} = \frac{1}{2}b\hbar\omega_C - \frac{q}{2}(1-b)\hbar\omega_C \qquad (q = 0, 1, 2, \ldots), \tag{1.25}$$

and corresponding wave functions ($L_0^k(x) = 1$)

$$\psi_q^{\mathrm{LLL}} = \frac{1}{\ell}\sqrt{\frac{1}{2\pi 2^q q!}}\left(\frac{r}{\ell}\right)^q e^{-r^2/4\ell^2} e^{-iq\phi}. \tag{1.26}$$

From Eq. (1.25) we see that the orbital energies are evenly spaced, as expected for a system with harmonic confinement, and we identify

$$\Delta E_{\mathrm{SP}} = (1-b)\frac{\hbar\omega_{\mathrm{C}}}{2} \tag{1.27}$$

as the single-particle energy scale. As we will see in Chapter 2, ΔE_{SP} may be measured through transport spectroscopy, and so by rearranging Eq. (1.27) we obtain

$$b = 1 - \frac{2\Delta E_{\mathrm{SP}}}{\hbar\omega_{\mathrm{C}}}, \tag{1.28}$$

as a useful relation for the effective harmonic parameter b in a given experiment.

Up to this point we have considered only the orbital part of the electron wave function, but of course spin plays an important role as well. In the simplest case it enters the Hamiltonian only through the Zeeman term:

$$\hat{H}_{\mathrm{Z}} = g\mu_{\mathrm{B}}B\hat{s}_z, \tag{1.29}$$

where μ_{B} is the Bohr magneton, g is the effective electron g-factor,[1] and $\hat{s}_z$ is the spin operator: $\hat{s}_z\psi_\sigma = \sigma\psi_\sigma$, where $\sigma = \pm\frac{1}{2}$ is the electron spin. In the absence of any additional interactions which couple the spin and orbital parts of the wave function (e.g., hyperfine interactions with lattice nuclei or spin-orbit coupling), this simply adds a spin-dependent constant to the energy eigenvalues:

$$\hat{H}_{\mathrm{Z}}\psi_\sigma = -\sigma E_{\mathrm{Z}}\psi_\sigma, \tag{1.30}$$

where $E_{\mathrm{Z}} = |g|\mu_{\mathrm{B}}B$ is the Zeeman energy. Note that it is the *total* magnetic field B which enters the expression for E_{Z}, in contrast to the orbital part which responds only to the perpendicular component $B_\perp$ through the vector potential $\mathbf{A}$. This suggests a potentially useful experimental handle to vary E_{Z} independently from the orbital wave functions, by changing both the total field B and the angle at which it is applied relative to the plane of the 2DES. This technique is explored in the experiments presented in

[1] Some confusion seems to exist in the literature about the sign of the Zeeman term. The magnetic moment of the electron is $\boldsymbol{\mu} = -g\mu_{\mathrm{B}}\boldsymbol{\sigma}$ (the sign accounts for the negative electrostatic charge) and the Zeeman energy is $-\boldsymbol{\mu}\cdot\mathbf{B}$, which leads to Eq. (1.29). The effective g-factor in GaAs is negative due to the strong effect of spin-orbit coupling ($g = -0.44$ in bulk GaAs), and so the lower energy state has $s_z = +\frac{1}{2}$. Normally the labeling of spin states is not important as long as one sticks with a consistent definition, although the sign does matter in the context of hyperfine and spin-orbit coupling between levels, as discussed in §4.3.1. We refer to the lower (higher) energy state as spin-↑ (spin-↓) throughout this thesis.

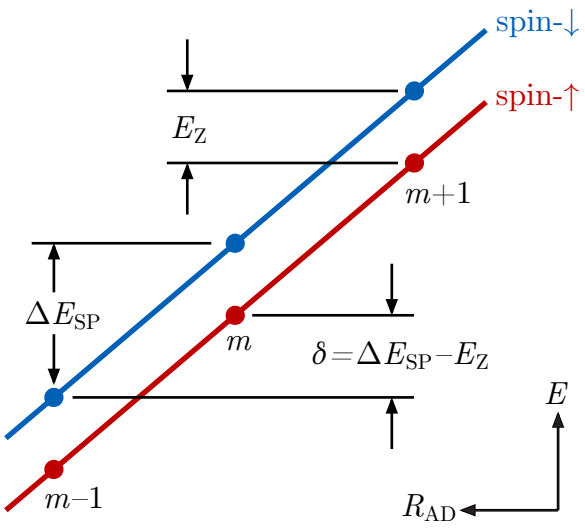

Figure 1.5: Single-particle energy spectrum of a $\nu_{AD} = 2$ antidot. When $\Delta E_{SP} > E_Z$, as shown here, the smallest excitations are E_Z and $\delta = \Delta E_{SP} - E_Z$ when the highest-occupied state is spin-↑ and spin-↓, respectively.

Chapter 6 of this thesis.

Therefore, the primary effect of the electron spin is to split each LL into two spin-polarised bands separated by E_Z, where $E_Z \ll \hbar\omega_C$ unless $\mathbf{B}$ is applied nearly in the plane of the 2DES. The SP spectrum in the LLL thus consists of two 'ladders' of orbital states with spacing ΔE_{SP}, separated from each other by E_Z, as shown in Fig. 1.5. In this model, particle and hole excitations are governed by these two energy scales alone, with the possible values

$$E_{ex} = \pm s E_Z + j \Delta E_{SP}, \tag{1.31}$$

where $s = 0$ or 1 for spin-conserving or spin-flip transitions, respectively, the upper (lower) sign is for an initial spin-↑ (spin-↓) electron, and j is any integer. In particular, when $\Delta E_{SP} > E_Z$ as shown in Fig. 1.5, the smallest particle excitation energies for spin-↑ and spin-↓ electrons are E_Z and $\Delta E_{SP} - E_Z$, respectively. These are also the SP contribution to the ground-state transition energies measured in equilibrium transport.

1.2 Properties of antidot eigenstates

In this section we explore some of the observable physical properties of the SP eigenstates defined above. To begin, we consider the physical meaning of the principal quantum numbers (n, m), since it is helpful to have a more intuitive understanding of their role in relation to n_{LL} in light of the rather strange identification in Eq. (1.23).

The radial quantum number n counts the number of nodes in the radial wavefunction and so measures the degree of excitation. A change of n therefore corresponds to changing LLs. On the other hand, the primary role of the azimuthal quantum number m is to determine the distance of the wave function peak from the origin, as can be seen in fig. 1.1 on page 5. Using standard integrals[1] it is straightforward to show that

$$\langle r^2 \rangle = 2\ell^2(2n + |m| + 1), \tag{1.32}$$

independent of the sign of m. Still, the sign of m is of critical importance. The transformation $m \to -m$ corresponds to taking the complex conjugate of ψ; this leaves the radial part of the wavefunction unchanged, and yet these two wave functions belong to different LLs, with vastly differing energies when $\hbar\omega_{\mathrm{C}}$ is large.

To visualise this, consider that, from a classical perspective, an 'orbit' of radius R can be achieved in two ways, in terms of a guiding centre X and cyclotron radius a, as depicted in Fig. 1.6:

- $X \sim 0$, $a \sim R$ (Fig. 1.6a):

  Classically, the kinetic energy of a particle with cyclotron radius a is given by $K = \frac{1}{2}m^*\omega_{\mathrm{C}}^2 a^2$, so these states will have energy $\propto R^2$, and therefore $n_{\mathrm{LL}} \propto |m|$. This description fits states with $m > 0$, and although they are valid solutions to the Schrödinger equation for states at radius R, they have energies $\gg E_{\mathrm{F}}$ for typical experimental parameters, and so will never be populated.

- $X \sim R$, $a \ll R$ (Fig. 1.6b):

  In this case, the energy of the state is small and determined by the background potential at radius R rather than the cyclotron energy. These states, which we identify with the $m < 0$ case, are analogous to classical 'skipping orbits' of electrons in lower LLs circling the antidot. It is these states which we probe in transport experiments.

[1] In particular, $\int_0^\infty e^{-x}x^{k+1}[L_n^k(x)]^2dx = \frac{(n+k)!}{n!}(2n+k+1)$.

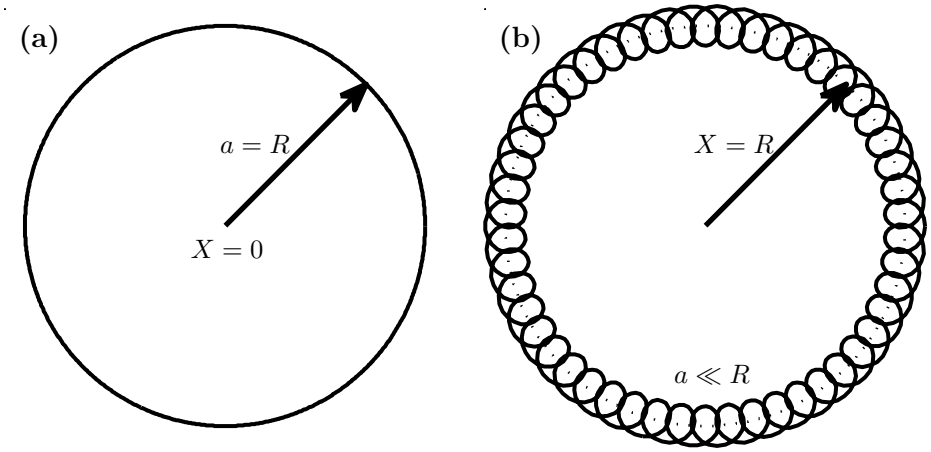

Figure 1.6: Examples of electron orbits at radius R, in terms of the guiding centre X and the cyclotron radius a. Case (a) corresponds to states $\psi_{n,m}$ in higher LLs, with $m > 0$, while case (b) corresponds to lower LL states with $m < 0$.

The remainder of this section discusses the physical properties of these $m < 0$ states in greater detail, drawing parallels to the classical picture of electron motion where applicable.

1.2.1 Angular momentum

As described above, the LLL states are labelled by their canonical angular momentum, $L_z = -q\hbar$, where $q = 0, 1, 2, \ldots$ measures the distance from the origin. The quantity L_z is not the 'real' angular momentum, however, since it is not gauge invariant. To see this, we imagine piercing the centre of the antidot with a single flux quanta of infinitesimal area. This is equivalent to the gauge transformation

$$\psi(r, \phi) \rightarrow e^{-i\phi}\psi(r, \phi) \tag{1.33a}$$

$$A_\phi(r, \phi) \rightarrow A_\phi(r, \phi) + \frac{\hbar}{er}, \tag{1.33b}$$

which leaves the magnetic field (for $r \neq 0$) and all other observables unchanged. The canonical angular momentum, however, clearly transforms as $L_z \rightarrow L_z - \hbar$ under this transformation, and so cannot be an observable quantity. The observable, or *kinetic* angular momentum is given by

$$\mathbf{l} = \mathbf{r} \wedge m^*\mathbf{v}, \tag{1.34}$$

where $m^*\mathbf{v} = \mathbf{p} + e\mathbf{A}$ is the similarly gauge-invariant kinetic momentum (as opposed to the canonical momentum $\mathbf{p}$). With $\mathbf{L} = \mathbf{r} \wedge \mathbf{p}$, we therefore have

$$\mathbf{l} = \mathbf{L} + e(\mathbf{r} \wedge \mathbf{A}), \tag{1.35}$$

for which the z-component is

$$\begin{aligned} l_z &= L_z + erA_\phi & (1.36)\\ &= L_z + \frac{eB}{2}r^2, & (1.37) \end{aligned}$$

and so we can write the quantum operator for kinetic angular momentum in the form

$$\hat{l}_z = \hat{L}_z + \frac{eB}{2}\langle r^2 \rangle. \tag{1.38}$$

From Eq. (1.36) it is clear that the kinetic angular momentum is invariant under the gauge transformation of Eqs. (1.33), since the change in the magnetic vector potential cancels the change in L_z. Furthermore, using Eq. (1.32) we can evaluate

$$\begin{aligned} \hat{l}_z\psi_{n,-q} &= \left[-q\hbar + \frac{\hbar}{b}(2n + |q| + 1)\right]\psi_{n,-q} & (1.39)\\ &= \frac{\hbar}{b}\left[1 + 2n_{\mathrm{LL}} + q(1-b)\right]\psi_{n,-q}. & (1.40) \end{aligned}$$

So, within a LL, each successive state moving away from the AD centre has increased angular momentum by an amount $\hbar(1-b)/b$, as we would expect for classical orbits of increasing radius (and constant angular frequency, as we show below).

1.2.2 Current density

Continuing our investigation of the classical analogues to antidot SP states, we can find further insight into the 'dynamics' of these states[1] by considering the circulation of charge around the ring, which is described by the probability current density:

$$\mathbf{J} = \frac{\hbar}{2m^* i}\left[\psi^*(\mathbf{D}\psi) - (\mathbf{D}\psi)^*\psi\right], \tag{1.41}$$

where

$$\mathbf{D} = \nabla + \frac{ie}{\hbar}\mathbf{A} \tag{1.42}$$

[1] Of course these are stationary solutions to the time-independent Schrödinger equation and so are not dynamical in any quantum sense.

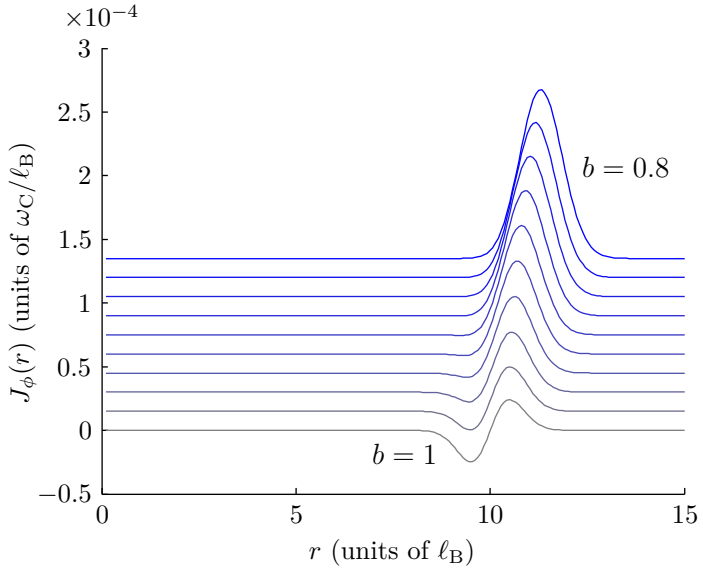

Figure 1.7: Current density, Eq. (1.43), of the LLL state $\psi_{0,-50}$ with b chosen in uniform steps from $b = 1$ (the free electron state) to 0.8. The curves are vertically offset for clarity.

is the gauge covariant derivative.[1] In polar coordinates we have $\nabla = (\frac{\partial}{\partial r}\hat{\mathbf{r}}, \frac{\partial}{r\partial\phi}\hat{\phi})$, and so $J_r = 0$ for SP states (since complex conjugation does not affect the radial wave function), such that

$$\mathbf{J}_{n,m}(r) = \frac{\omega_\mathrm{C}}{2}\left(r + \frac{2m\ell_\mathrm{B}^2}{r}\right)[f_{n,m}(r)]^2\hat{\phi}, \tag{1.43}$$

where $\ell_\mathrm{B} = \sqrt{\hbar/eB} = b\ell$ is the magnetic length.

This quantity is manifestly gauge invariant due to its definition in terms of the covariant derivative, and so represents the physical charge circulation of an electron in the state $\psi_{n,m}$. For our antidot states with $q = -m > 0$, note that J_ϕ changes sign from negative to positive as r increases through the critical radius $r_\mathrm{c} = \sqrt{2q}\ell_\mathrm{B}$. As the electric field from the antidot potential increases, either through a larger curvature parameter ω_0 or by considering states with larger q (and hence larger radius), the difference between the centre of the wave function at $\sqrt{2q}\ell$ and r_c becomes larger, and so a larger fraction of the state has $J_\phi > 0$, as shown in Fig. 1.7.

[1] This is defined such that the quantity $(\mathbf{D}\psi)$ transforms as $(\mathbf{D}\psi) \to e^{if(x)}(\mathbf{D}\psi)$ under the gauge transformation

$$\begin{cases}\psi \to e^{if(x)}\psi \\ \mathbf{A} \to \mathbf{A} - \frac{\hbar}{e}\nabla f.\end{cases}$$

Using the normalisation of Laguerre polynomials, Eq. (1.21), and the additional integral relation

$$\int_0^\infty e^{-x}x^{k-1}[L_n^k(x)]^2dx = \frac{(n+k)!}{kn!} \qquad (k \geq 1), \tag{1.44}$$

we evaluate the effective 'orbital frequency' for SP states (with $m \neq 0$) to be

$$\begin{aligned} f_{\text{orbit}} &= \int_0^\infty J_\phi(r)dr \\ &= \frac{\omega_{\text{C}}}{2}\int_0^\infty \left(r + \frac{2m\ell_{\text{B}}^2}{r}\right)[f_{n,m}(r)]^2dr \\ &= \frac{\omega_{\text{C}}}{4\pi}(1 + b\,\text{sign}(m)), \end{aligned} \tag{1.45}$$

which is in fact independent of the values of (n, m). In particular, we note that for free electrons ($b \to 1$), the integrated current density equals zero, so there is no net orbital velocity for these states.[1] Thus, one may interpret the free-electron state $\psi_{n,-q}$ as a superposition of $\psi_{n,0}$ cyclotron states distributed about a ring of radius $r_{\text{c}} = \sqrt{2|q|}\ell_{\text{B}}$. With this interpretation it is clear that the free-electron wave functions within a LL are indeed all the same up to a spatial translation, a point which is obvious for the wave functions obtained in other gauges but less so in the symmetric gauge.

In the presence of the antidot potential, the same interpretation of the LLL states in terms of translated cyclotron ground states clearly holds, but now the electric field generated by the potential causes the electrons to gain a net orbital velocity. Classically, this is described by $\mathbf{E} \wedge \mathbf{B}$ drift, in which the orbital velocity is

$$\mathbf{v}_{\text{drift}} = \frac{\mathbf{E} \wedge \mathbf{B}}{|B|^2} = \frac{|E|}{|B|}\hat{\phi}. \tag{1.46}$$

With the electric field given by

$$\mathbf{E}(r) = -\nabla\varphi(r) = -\frac{m\omega_0^2 r}{e}\hat{\mathbf{r}}, \tag{1.47}$$

this corresponds to an orbital frequency

$$f_{E\wedge B} = \frac{\langle v_{\text{drift}}\rangle}{2\pi\langle r\rangle} = \frac{\omega_0^2}{2\pi\omega_{\text{C}}}. \tag{1.48}$$

[1] Note, however, that the angular momentum, given by Eq. (1.40), is non-zero: $l_z = (1 + 2n_{\text{LL}})\hbar$.

In the high-B limit ($\omega_{\rm C} \gg \omega_0$) of Eq. (1.45), we indeed have

$$f_{\rm orbit} = \frac{\omega_{\rm C}}{4\pi}\left(1 - \sqrt{1 - \frac{4\omega_0^2}{\omega_{\rm C}^2}}\right) \simeq \frac{\omega_0^2}{2\pi\omega_{\rm C}}, \tag{1.49}$$

in agreement with this estimate.

1.2.3 The Aharonov-Bohm effect and its relation to antidots

The Aharonov-Bohm (AB) effect [32, 33] is probably the most well-known example of a *geometrical phase* (or Berry phase, after Michael Berry who generalised the concept [34]), and concerns the observable effects of electromagnetic potentials. In classical electrodynamics, Maxwell's equations are formulated in terms of the fields $(\mathbf{E}, \mathbf{B})$ and the potentials $(\varphi, \mathbf{A})$ are not physically observable, since they may be changed by any gauge transformation, leaving the fields invariant. But it is the potentials which directly enter the quantum-mechanical Hamiltonian, as in Eq. (1.1), and this can lead to physical consequences for a particle subject to nonzero potentials, even in a region where $\mathbf{E}$ and $\mathbf{B}$ are zero.

In general, observable quantities may depend on the path dependent quantity $e^{i\gamma}$, where

$$\gamma = \frac{q}{\hbar}\int_P^Q (\varphi dt - \mathbf{A}\cdot d\mathbf{x}) \tag{1.50}$$

is the geometrical phase acquired by a particle of charge q moving between spacetime points P and Q [35]. In particular, if a particle may travel from P to Q along two different paths, the phase difference $\Delta\gamma$ between the resulting wave functions is given by

$$\Delta\gamma = \frac{q}{\hbar}\oint (\varphi dt - \mathbf{A}\cdot d\mathbf{x}), \tag{1.51}$$

with the integral evaluated around the spacetime loop created by the two paths, since topologically path $\mathcal{P}_1$ equals path $\mathcal{P}_2$ plus the loop $(\mathcal{P}_1 - \mathcal{P}_2)$. This relative phase is observable when the two paths form part of an interference experiment, and such studies have confirmed Eq. (1.51) for both electric [36] and magnetic [37] potentials.

The 'magnetic' part in particular is recognised as an important property of electronic devices in two-dimensions, since it is straightforward to construct electron interferometers such as Aharonov-Bohm rings [38], in which electrons may take either of two paths in traversing a loop in the presence of a magnetic field. Since the electric potential in this case is constant (or at least equal for the two paths) there is no contribution from the first term of Eq. (1.51), and the remaining loop integral in two spatial dimensions

may be rewritten using Stokes' theorem as

$$\Delta\gamma = \frac{e}{\hbar}\iint_{\mathcal{S}} \mathbf{B}\cdot d\mathbf{S} = 2\pi\frac{\Phi}{\phi_0}, \tag{1.52}$$

where Φ is the magnetic flux through the surface $\mathcal{S}$ enclosed by the loop and $\phi_0 = h/e$ is the quantum unit of magnetic flux.

In the literature on quantum antidots, this result is often used to justify the statement that orbital radii (and hence energies via the background antidot potential) are quantised by the condition

$$\pi\langle r^2\rangle B_\perp = m\phi_0 \tag{1.53}$$

for integer m. Indeed, from Eq. (1.32) we see that the free-electron eigenstates $\psi^{\text{free}}_{n,m}$ satisfy

$$\pi\langle r^2\rangle = \frac{h}{eB_\perp}(2n + |m| + 1), \tag{1.54}$$

in agreement with this argument. But while convenient, this explanation is misleading for several reasons. First, from Eq. (1.32) we see that the quantity $\pi\langle r^2\rangle$ for parabolic antidot states differs from the free-electron case by a non-negligible factor b^{-1}. A similar result holds for any antidot potential: the SP states are pushed outwards relative to the free-electron states by the repulsive electric field. Furthermore, it is straightforward to show that, even for the free electron states,[1] the spacing Δr of the wave function maxima for successive states $(|m|, |m|+1)$ satisfies $\Delta r \ll \ell_{\text{B}}$ for large $|m|$. Since the states have width $\approx \ell_{\text{B}}$, it is clear that the electrons are not in any sense 'prohibited' from existing at a radius which does not satisfy the flux-quantisation condition.

The confusion on this point seems to lie with the interpretation of Eq. (1.52). The AB phase represents the phase difference between two wave packets which follow *different* paths through spacetime. While this has a natural interpretation for a particle traversing an AB ring (at low B such that both paths are allowed) or other interferometer, it is difficult to identify two paths which may interfere for a particle in a chiral antidot state, or in any stationary state for that matter. An electron cannot, for example, interfere with itself simply by circling the antidot — it encloses no area in spacetime and so there can be no interference term. It is therefore preferable to think of the SP eigenstates simply as the natural solutions to Schrödinger's equation in the presence of magnetic confinement rather than a consequence of the AB effect.

Understandably, an argument based on flux quantisation via the AB effect is usually used to describe the periodicity of so-called Aharonov-Bohm oscillations which are

[1] From Eq. (1.54) we have $\Delta r \simeq \ell_{\text{B}}^2/r$ for $|m| \gg 1$.

observed as a function of magnetic field. AB oscillations constituted the first experimental observations of single quantum antidots [39], and the details of their periodicity and line-shapes continue to yield important insight into the underlying physics in these systems. It is well-established experimentally that an antidot with filling factor $\nu_{\mathrm{AD}} = f$ shows periodic conductance resonances in B, with f resonances occurring per base period ΔB,[1] for f up to at least six [40]. The AB argument is straightforward: if the flux-quantisation condition of Eq. (1.53) holds, then it is easy to show that a state with area A enclosing m flux quanta will be replaced by the adjacent $(m+1)$ state when the field has changed by

$$\Delta B_{\perp} = \frac{h}{eA}. \tag{1.55}$$

Since the area is fixed by the Fermi energy and the antidot potential, we therefore expect periodic resonances for each of the f spin-polarised LLs as the SP states pass through E_{F} with period ΔB, and hence f resonances per cycle.

In many experiments, Eq. (1.55) is a valid approximation, although the reasoning used to obtain it should concern the SP states rather than the AB effect. In particular, if the antidot potential varies on a scale much larger than ℓ_{B}, then it is a good approximation to use the free particle wave functions $\psi^{\mathrm{free}}_{n,m}$ and treat the electric potential as a small perturbation which simply modifies the SP energies:

$$E_{nm\sigma} \simeq \hbar\omega_{\mathrm{C}} \left(n_{\mathrm{LL}} + \frac{1}{2} \right) - \sigma E_{\mathrm{Z}} + \langle \varphi(r) \rangle. \tag{1.56}$$

For the parabolic potential we have been considering in this chapter, this corresponds to the limit $\omega_0 \ll \omega_{\mathrm{C}}$ ($b \approx 1$), and in many experiments this is indeed the case.[2] If so, then we know from Eq. (1.54) that the flux-quantisation does approximately hold, and so the AB period will in fact be given by Eq. (1.55). For stronger antidot potentials and/or weaker magnetic fields, however, this perturbative approximation is not valid, and the AB period will be modified. For the parabolic antidot, for example, it is in general given by

$$\Delta B_{\perp} = \frac{h}{ebA}, \tag{1.57}$$

which may be significantly larger than that predicted by Eq. (1.55).

Thus far we have been considering a purely non-interacting model, but as we will see in the next section, Coulomb interactions affect antidot physics in readily observable ways. Coulomb blockade, in particular, plays a fundamental role in the description of

[1] Note that this does *not* mean that the resonances necessarily have period $\Delta B/f$.

[2] For example, with a typical value of $\Delta E_{\mathrm{SP}} \approx 100$ μeV at $B = 1$ T, we have $b \approx 0.9$ from Eq. (1.28).

sequential transport of electrons through an antidot. In the context of AB oscillations, it is therefore important to consider the effects of changing magnetic fields on the charge of the system. If the electrons around the antidot do not rearrange as the field changes (for instance, if the ground state can be written as a 'maximum density droplet' of holes occupying a fixed set of SP orbitals — see §1.3.3), then the excess charge[1] accumulated at the perimeter of the antidot may be approximated as

$$\delta q = (2\pi r \delta r) e n_e, \tag{1.58}$$

where n_e is the electron density, given by

$$n_e = \frac{eB}{h} \nu_{\mathrm{AD}}. \tag{1.59}$$

For the SP orbitals we have from Eq. (1.32) that

$$\delta r = -\frac{r}{2B} \delta B, \tag{1.60}$$

and so

$$\delta q = -e\nu_{\mathrm{AD}} \frac{r^2}{2\ell_{\mathrm{B}}^2} \frac{\delta B}{B}. \tag{1.61}$$

The charging condition $\Delta q = \pm e$ therefore implies a resonance period

$$\Delta B = \frac{1}{\nu_{\mathrm{AD}}} \frac{h}{e\pi r^2}, \tag{1.62}$$

in agreement with our estimate based on the non-interacting energy levels. Such periodic charging as a function of B has been directly measured experimentally, using the conductance of a quantum point contact as a capacitively-coupled charge sensor [41], and in many cases the energy associated with charging dominates over the SP energy scale.

1.3 Theoretical treatment of electron interactions

The preceding sections of this chapter concern a non-interacting description of antidot electronic states. In some cases the physics of the SP model, with the important ad-

[1] Note that although the physical 'antidot charge' (i.e. number of holes) remains fixed, the 'excess charge' of Eq. (1.58) is unbalanced by the system since the chemical potential, rather than the number of electrons, is fixed in the 2DES. We can therefore think of δq as effectively a 'gate charge' induced by the magnetic field.

dition of a charging energy to reflect Coulomb blockade, is sufficient to describe the major features of antidot transport measurements. Especially at relatively low fields ($B \lesssim 1$ T), the SP model provides a good description of both equilibrium conductance experiments (such as the AB oscillations discussed in the previous section) and the excitation spectra obtained from non-equilibrium transport measurements. By including the variability of the tunnel couplings between the SP states and the current-carrying edge states, even very complicated conductance traces may be reproduced accurately within a non-interacting picture [16]. At larger fields, additional structure begins to appear, such as 'double-frequency' AB oscillations [17–19, 42] and Kondo resonances [43], which cannot be described within the SP framework. A recent review covering these effects and relevant theoretical descriptions is given in Ref. [22].

The experiments discussed in this thesis are almost all in the low-B regime, and indeed Chapters 3 and 6 present examples of effects which can mostly be described within a non-interacting model. Still, when one looks more deeply, for example through the spin-resolved transport measurements described in Fig. 4, inconsistencies with the SP model emerge which may only be explained through the introduction of additional physics. In this section we consider a microscopic picture of electron-electron interactions based on Hartree-Fock theory, in which we transform the electronic system into a 'maximum density droplet' of holes in the LLL. This model forms an appropriate description of the physics at low to intermediate B, and similar methods have been used recently to describe the ground-state transitions responsible for the Kondo effect [44, 45]. An alternate phenomenological description in terms of capacitive charging interactions has successfully explained observations at high-B [20], as outlined in the review [22] cited above.

1.3.1 Hartree-Fock theory

The full Hamiltonian for a system of N interacting electrons, within the standard Born-Oppenheimer approximation in which the electronic degrees of freedom are decoupled from those of the lattice [4], can be written in the form

$$\hat{H} = \sum_{i}^{N} \hat{h}_i + \frac{e^2}{4\pi\epsilon\epsilon_0} \sum_{i>j}^{N} \frac{1}{|\mathbf{x}_i - \mathbf{x}_j|}, \tag{1.63}$$

where $\hat{h}_i$ is the SP Hamiltonian acting on the i^{th} electron, which in our case is given by

$$\hat{h}_i = \frac{1}{2m^*}(-i\hbar\nabla_i + e\mathbf{A})^2 - e\varphi(\mathbf{x}_i) - g\mu_{\text{B}} B \hat{s}_{zi}. \tag{1.64}$$

No analytic solutions are known for a general Hamiltonian of this form with more than one electron, and much of solid-state physics concerns various methods for approximating the effect of the interaction term in Eq. (1.63).

The Hartree-Fock (HF) method is one of several 'mean field' approaches to this problem, in which each electron in a system is influenced by an effective potential due to the charge density of all the other electrons. In particular, we assume that each electron in the system is described by its own SP wave function, such that the multielectron wave function may be written as a Slater determinant of orthonormal SP spin orbitals ψ_i:

$$\Psi = \frac{1}{\sqrt{N!}} \begin{vmatrix} \psi_1(\xi_1) & \psi_1(\xi_2) & \cdots & \psi_1(\xi_N) \\ \psi_2(\xi_1) & \psi_2(\xi_2) & \cdots & \psi_2(\xi_N) \\ \vdots & \vdots & \ddots & \vdots \\ \psi_N(\xi_1) & \psi_N(\xi_2) & \cdots & \psi_N(\xi_N) \end{vmatrix}, \tag{1.65}$$

where ξ_i represents both the position and spin projection of the i^{th} particle.[1] By construction, this wave function satisfies the antisymmetry requirement for fermions, that is

$$\Psi(\xi_1, \xi_2, \ldots, \xi_i, \ldots, \xi_j, \ldots, \xi_N) = -\Psi(\xi_1, \xi_2, \ldots, \xi_j, \ldots, \xi_i, \ldots, \xi_N), \tag{1.66}$$

since the interchange of particles i and j corresponds to the interchange of two columns of the determinant, and hence a change of sign. Thus the Pauli exclusion principle is satisfied: the wave function Ψ vanishes when $\xi_i = \xi_j$ for any $i \neq j$.[2]

General expressions for matrix elements between determinantal wave functions like Eq. (1.65) are well known, given for example in the book by Bethe and Jackiw [46]. In the expectation value for the energy of Ψ, many of the terms vanish due to the orthogonality of the ψ_i, leaving

$$\langle \Psi | \hat{H} | \Psi \rangle = \sum_i \langle i | \hat{h} | i \rangle + \sum_{i<j} \Big(\langle ij | V_{\text{C}} | ij \rangle - \langle ij | V_{\text{C}} | ji \rangle \Big), \tag{1.67}$$

in terms of the SP energies

$$\langle i | \hat{h} | i \rangle = \int d\mathbf{x}\, \psi_i(\mathbf{x}) \hat{h}_i \psi_i(\mathbf{x}) = \varepsilon_i^{\text{SP}}, \tag{1.68}$$

[1] It is assumed that the orbital and spin parts of the wave function are separable, i.e. that $\psi_i(\xi) = \psi_{n_i,m_i}(\mathbf{x})\chi_i(s)$, where $\chi = \binom{1}{0}$ or $\binom{0}{1}$ in terms of the argument $s = 1, 2$ in spin space. Matrix elements between spin orbitals therefore imply integration of spatial coordinates and summation over spin projections.

[2] For similar reasons, clearly $\Psi = 0$ identically if any $\psi_i = \psi_j$ for $i \neq j$, enforcing the condition that the SP spin orbitals chosen must be distinct.

and two-particle matrix elements of the Coulomb operator

$$\langle ij|V_{\rm C}|kl\rangle = \frac{e^2}{4\pi\epsilon\epsilon_0}\delta_{\sigma_i\sigma_k}\delta_{\sigma_j\sigma_l}\iint d\mathbf{x}d\mathbf{x}'\,\psi_i^*(\mathbf{x})\psi_j^*(\mathbf{x}')\frac{1}{|\mathbf{x}-\mathbf{x}'|}\psi_k(\mathbf{x})\psi_l(\mathbf{x}'), \tag{1.69}$$

where we have completed the spin summations using the identity

$$\sum_s \chi_i^\dagger(s)\chi_j(s) = \delta_{\sigma_i\sigma_j}. \tag{1.70}$$

The total energy of the state Ψ may therefore be written in the form[1]

$$E = \sum_i \varepsilon_i^{\rm SP} + \frac{1}{2}\sum_{ij}(J_{ij} - \delta_{\sigma_i\sigma_j}K_{ij}), \tag{1.71}$$

where

$$J_{ij} = \frac{e^2}{4\pi\epsilon\epsilon_0}\iint d\mathbf{x}d\mathbf{x}'\,|\psi_i(\mathbf{x})|^2\frac{1}{|\mathbf{x}-\mathbf{x}'|}|\psi_j(\mathbf{x}')|^2, \tag{1.72}$$

$$K_{ij} = \frac{e^2}{4\pi\epsilon\epsilon_0}\iint d\mathbf{x}d\mathbf{x}'\,\psi_i^*(\mathbf{x})\psi_j^*(\mathbf{x}')\frac{1}{|\mathbf{x}-\mathbf{x}'|}\psi_j(\mathbf{x})\psi_i(\mathbf{x}') \tag{1.73}$$

are the so-called 'direct' and 'exchange' Coulomb matrix elements, respectively.

The part of Eq. (1.71) due to the direct term J is exactly the Coulomb 'overlap' energy we expect between particles occupying a charge distribution given by $-e\sum_i|\psi_i|^2$, and if we had used a simple product wavefunction of these orbitals instead of the Slater determinant, it would be the only contribution from the Coulomb interaction. The nonlocal exchange term K therefore reflects the effects of the wave function antisymmetry introduced through the Slater determinant. Due to the Pauli exclusion principle, Eq. (1.66), electrons of the same spin 'avoid each other' more in the antisymmetric Ψ than they would in a simple product wave function. This means that the direct Coulomb interaction actually overestimates the configuration energy, and the exchange term may be thought of as a correction accounting for the indistinguishability and antisymmetry of fermions. Slightly more rigorously, it can be shown [46] that the effective Coulomb interaction of an electron with N other electrons of the same spin (therefore including both the direct and exchange terms) is equivalent to the potential from a charge distribution containing total charge $-e(N-1)$, i.e. from one less than the total number of other electrons. Thus it is as if each electron carries with it a hole (often called a Fermi

[1] We have used the facts that J and K are symmetric in i,j and that $J_{ii} = K_{ii}$ in rewriting the sum in Eq. (1.71).

hole) which affects its interaction with other electrons of the same spin.

By the variational principle, the energy E thus obtained for our choice of wave function Ψ represents an upper bound on the ground-state energy of the system. The best approximation of a single Slater determinant like Eq. (1.65) to the true ground state of the system can therefore be found from the variational condition $\delta\langle\hat{H}\rangle = 0$ under arbitrary variations $\delta\psi_i$. Using the method of Lagrange multipliers to enforce the condition that the ψ_i are normalised,[1] this may be written

$$\frac{\delta}{\delta\psi_i}\left[\langle\Psi|\hat{H}|\Psi\rangle + \sum_i \varepsilon_i\left(\int|\psi_i(\mathbf{x})|^2 d\mathbf{x} - 1\right)\right] = 0. \tag{1.74}$$

This procedure leads to the Hartree-Fock equations

$$\begin{aligned}\varepsilon_i\psi_i(\mathbf{x}) = \hat{h}\psi_i(\mathbf{x}) + \sum_j \int d\mathbf{x}' \frac{|\psi_j(\mathbf{x}')|^2}{|\mathbf{x}-\mathbf{x}'|}\psi_i(\mathbf{x}) \\ - \sum_i \delta_{\sigma_i\sigma_j}\int d\mathbf{x}' \frac{\psi_j^*(\mathbf{x}')\psi_i(\mathbf{x}')}{|\mathbf{x}-\mathbf{x}'|}\psi_j(\mathbf{x}),\end{aligned} \tag{1.75}$$

which resemble a set of SP Schrödinger equations. Indeed, by taking the inner product of Eq. (1.75) with $\psi_i^*(\mathbf{x})$, we see that the eigenvalue ε_i represents the part of the total energy E involving the i^{th} electron:

$$\varepsilon_i = \varepsilon_i^{\text{SP}} + \sum_j (J_{ij} - \delta_{\sigma_i\sigma_j}K_{ij}). \tag{1.76}$$

Notice, however, that the 'operators' in the last two terms of Eq. (1.75) involve the solutions ψ_i. The HF equations must therefore be solved self-consistently, which is normally accomplished by writing the orbitals ψ_i as an expansion over a set of basis orbitals ϕ_k,

$$\psi_i = \sum_k c_{ik}\phi_k, \tag{1.77}$$

and then solving the resulting linear algebra problem (the Roothaan-Hall equations [47, 48]) for the coefficients c_{ik} through an iterative procedure.

[1] It can be shown that the ψ_i remain orthogonal as a result of this calculation [46].

1.3.2 The particle-hole transformation

In Chapter 4 we will use the Hartree-Fock method to treat electron-electron interactions in an antidot at filling factor $\nu_{\mathrm{AD}} = 2$. Neglecting mixing with higher LLs,[1] the natural basis states to use are the LLL wave functions $\psi_{m\sigma}$ given by Eq. (1.26)[2]

$$\psi_{m\sigma} = \frac{1}{\ell}\sqrt{\frac{1}{2\pi 2^m m!}}\left(\frac{r}{\ell}\right)^m e^{-r^2/4\ell^2} e^{-im\phi}\chi_\sigma, \tag{1.78}$$

As we have seen, these wave functions are exact solutions of the SP Schrödinger equation for a parabolic antidot potential, in which case $\ell = \ell_{\mathrm{B}}/\sqrt{b}$ and the SP energies are

$$\varepsilon^{\mathrm{SP}}_{m\sigma} = \frac{1}{2}b\hbar\omega_{\mathrm{C}} - \frac{m}{2}(1-b)\hbar\omega_{\mathrm{C}} - \sigma E_{\mathrm{Z}}. \tag{1.79}$$

In the case of a non-parabolic but slowly-varying (on the scale of ℓ_{B}) potential, the $\psi_{m\sigma}$ are suitable approximations to the true wave functions, with $\ell \approx \ell_{\mathrm{B}}$ and SP energies given to first order in the antidot perturbation by Eq. (1.56). The Coulomb matrix elements in Eqs. (1.72) and (1.73) between these LLL states may be evaluated numerically [52] or analytically [53].

We therefore have an intuitive picture of an isolated $\nu_{\mathrm{AD}} = 2$ antidot in terms of a set of electronic occupation vectors $(\mathbf{n}^{\mathrm{e}}_\uparrow, \mathbf{n}^{\mathrm{e}}_\uparrow)$, with components $n^{\mathrm{e}}_{m\sigma} = 0$ or 1 for each orbital m. Since the orbitals extend infinitely into the bulk, in practice we must choose a cutoff orbital which is far enough away from the antidot states we are considering not to influence the calculations. Alternatively, we may describe the same configuration in terms of an infinite, spin-split LL containing finite integer numbers $(N^{\mathrm{h}}_\uparrow, N^{\mathrm{h}}_\downarrow)$ of 'holes' in the spin-↑ and spin-↓ parts, respectively. The equivalent hole-occupation vectors are therefore $\mathbf{n}^{\mathrm{h}}_\sigma = \mathbf{1} - \mathbf{n}^{\mathrm{e}}_\sigma$, and as we show below, a description in terms of interactions be-

[1] Such mixing is not necessarily negligible. With the addition of the Coulomb term to the Hamiltonian, the LL index n is no longer a good quantum number, so the true eigenstates will be mixtures of orbitals with definite z-projections of angular momentum, $L_z = M\hbar$, i.e. $\Psi_{M\sigma} = \sum_{n,m} c_{nm\sigma}\psi_{nm\sigma}$. The strength of this mixing depends on the dimensionless ratio $\kappa = E_{\mathrm{C}}/\hbar\omega_{\mathrm{C}} \sim 1/\sqrt{B}$ between the Coulomb energy scale $E_{\mathrm{C}} = e^2/4\pi\epsilon\epsilon_0\ell$ and the LL spacing $\hbar\omega_{\mathrm{C}}$. For experimentally accessible magnetic fields in GaAs, κ is $O(1)$ (for example, $\kappa \approx 2.5$ for $B = 1$ T), suggesting that LL mixing should not be weak in these systems. However, several studies concerned with the effects of LL mixing with regards to fractional quantum Hall states [e.g., 49, 50] have concluded that LL mixing has only a small ($\lesssim 5\%$) effect on measurable properties such as transport gaps. More generally, Bishara and Nayak [51] have recently shown that the *renormalised* effective interactions due to LL mixing in the first and second LLs are indeed smaller than naïvely expected, of order $\lesssim 0.1\kappa$. We therefore believe that neglecting this mixing forms a reasonable, if not perfect, approximation. Although it is beyond the scope of this work, it would certainly be of interest to theoretically investigate the implications of this assumption in the future.

[2] Note we have made the identification $m = q > 0$ from Eq. (1.26).

tween holes is essentially equivalent to the corresponding electron picture, but it removes the need to worry about the convergence of sums over an infinite number of particles in calculations. At this point it is also important to note that, in general, the states of this 'fermionic basis' (characterised by the occupation numbers of fermion orbitals) are not eigenstates of the interacting Hamiltonian. They form a natural basis for calculations, however, and can be related to the true eigenstates by a standard procedure, which we discuss further in the next section.

First we consider the electron description at $\nu_{\mathrm{AD}} = 2$. Consider the case of an infinite, fully-filled LL ($n^{\mathrm{e}}_{m\sigma} = 1 \,\forall\, m, \sigma$). According to Eq. (1.76), the energy of the i^{th} electron in a Slater-determinant wave function composed of these SP states is

$$E_{m_i\sigma_i} = \varepsilon^{\mathrm{SP}}_{m_i\sigma_i} + U_{\mathrm{Sheet}}(m_i), \tag{1.80}$$

where

$$U_{\mathrm{Sheet}}(m) = \sum_n (2J_{m,n} - K_{m,n}) \tag{1.81}$$

is the Coulomb energy required to add an electron to orbital m (of either spin) in an otherwise filled LL. The sum over $J_{m,n}$ in Eq. (1.81) does not converge to a finite value, reflecting the infinite self-energy of a 2-dimensional sheet of charge.[1] We can make the calculations finite by adding a uniform positive background charge to the system which supplies the potential $V_{\mathrm{BG}}(m)$ for an electron in orbital m such that

$$\Delta U_{\mathrm{S}}(m) = U_{\mathrm{Sheet}}(m) - eV_{\mathrm{BG}}(m) \tag{1.82}$$

is finite. Specifically, since the Hartree product wave function of a fully-filled LL has uniform probability distribution,[2] we can choose the background potential to precisely cancel the contribution from the direct term, such that

$$\Delta U_{\mathrm{S}}(m) = -\sum_n K_{m,n}. \tag{1.83}$$

This is a convergent sum, but it is still over infinitely many orbital states, and so in using the electron description we must always be careful that we take the sum far enough to reach convergence for a given m. To avoid this ambiguity, it is preferable to transform the infinite electron system into the one containing a finite number of holes discussed

[1] The matrix element $J_{m,m+q} \sim 1/\sqrt{q}$ for $q \gg 1$.

[2] This is easier to see in another gauge (e.g. the Landau gauge in which the wave functions are 'stripes' in one Cartesian coordinate with arbitrary translations in the other), but since the probability density must be gauge invariant we know the result holds in the symmetric gauge as well.

above.

The transformation proceeds as follows. If for the moment we leave out the neutralising background charge, we see from Eq. (1.80) that by removing (adding) the 1st electron (hole) from (to) the state (m_1, σ_1), the total configuration energy changes by $\Delta E_1 = -E_{m_1\sigma_1}$. If we then remove a second electron, the resulting change in energy is

$$\begin{aligned} \Delta E_2 &= -\varepsilon^{\mathrm{SP}}_{m_2\sigma_2} - \sum_{i>1} \left(J_{m_2,m_i} - \delta_{\sigma_2,\sigma_i} K_{m_2,m_i}\right) && (1.84) \\ &= -\varepsilon^{\mathrm{SP}}_{m_2\sigma_2} - U_{\mathrm{Sheet}}(m_2) + J_{m_2,m_1} - \delta_{\sigma_2,\sigma_1} K_{m_2,m_1}. && (1.85) \end{aligned}$$

Following this pattern, the state with N_h holes has energy (relative to the fully-filled state)

$$U(N_\mathrm{h}) = -\sum_i^{N_\mathrm{h}} \varepsilon^{\mathrm{SP}}_{m_i\sigma_i} - \sum_i^{N_\mathrm{h}} U_{\mathrm{Sheet}}(m_i) + \sum_{i>j}^{N_\mathrm{h}} \left(J_{m_i,m_j} - \delta_{\sigma_i,\sigma_j} K_{m_i,m_j}\right). \tag{1.86}$$

Now, choosing the background potential as in Eq. (1.83) to cancel the infinite part of U_{Sheet}, we can write the configuration of the N-hole state as (rewriting the sum in Eq. (1.86) using the symmetry of J and K)

$$U(N_\mathrm{h}) = -\sum_i^{N_\mathrm{h}} \tilde{\varepsilon}_{m_i\sigma_i} + \frac{1}{2}\sum_{i,j}^{N_\mathrm{h}} (J_{m_i,m_j} - \delta_{\sigma_i,\sigma_j} K_{m_i,m_j}), \tag{1.87}$$

where

$$\tilde{\varepsilon}_{m_i\sigma_i} = \varepsilon^{\mathrm{SP}}_{m_i\sigma_i} - \sum_n K_{m_i,n}. \tag{1.88}$$

In practice it is usually a good approximation to treat the exchange corrections to $\varepsilon^{\mathrm{SP}}_{m\sigma}$ as constant for all m (in which case they can be absorbed into the definition of the background charge), since the variation of Eq. (1.83) for different m is generally orders of magnitude smaller than the variation in $\varepsilon^{\mathrm{SP}}_{m\sigma}$. In terms of the hole orbital-occupation vectors $\mathbf{n}^\mathrm{h}_\sigma$, the total HF configuration energy of a state in the fermionic basis may be written in the form convenient for calculations,

$$\begin{aligned} U(\mathbf{n}^\mathrm{h}_\uparrow, \mathbf{n}^\mathrm{h}_\downarrow) = &-\tilde{\varepsilon}\cdot(\mathbf{n}^\mathrm{h}_\uparrow + \mathbf{n}^\mathrm{h}_\downarrow) \\ &+ \frac{1}{2}\left[(\mathbf{n}^\mathrm{h}_\uparrow + \mathbf{n}^\mathrm{h}_\downarrow)^\mathrm{T}\mathrm{J}(\mathbf{n}^\mathrm{h}_\uparrow + \mathbf{n}^\mathrm{h}_\downarrow) - (\mathbf{n}^\mathrm{h}_\uparrow)^\mathrm{T}\mathrm{K}(\mathbf{n}^\mathrm{h}_\uparrow) - (\mathbf{n}^\mathrm{h}_\downarrow)^\mathrm{T}\mathrm{K}(\mathbf{n}^\mathrm{h}_\downarrow)\right]. \end{aligned} \tag{1.89}$$

Aside from the sign of the SP energies, reflecting the confining property of the antidot po-

tential for holes, and the aforementioned exchange correction, this is entirely equivalent to the interaction energy of a finite system of electrons.

1.3.3 Maximum density droplets

As alluded to above, the fermionic basis states discussed thus far are in general not eigenstates of the interacting Hamiltonian, Eq. (1.63). This is because the SP angular momentum operators $\hat{L}_{zi}$, acting on the i^{th} electron only, do not commute with the electron-electron interaction term. The total system is still rotationally symmetric, however, and so the total angular momentum projection $M = \sum_{m\sigma} m n^{\text{h}}_{m\sigma}$ is a good quantum number of the multiparticle state. Similarly, although the individual spin operators $\hat{s}_{zi}$ do commute with the Hamiltonian, our choice of a Slater-determinant wave function couples the individual spins to the spatial symmetry (and hence the energy) of the state. Hence we must consider instead the total spin projection $S_z = \frac{1}{2}\sum_m (n^{\text{e}}_{m\uparrow} - n^{e}_{m\downarrow})$.[1] The eigenenergies of the system may therefore be obtained by diagonalising the matrix Hamiltonian constructed from the subspace of fermionic basis states with a given (M, S_z), using the rules for addition of angular momentum. This process leads to a 'bosonic' basis [52], in which the neutral excitations are described by a spectrum of 'edge waves' similar to the one-dimensional Tomonaga-Luttinger liquid model [54, 55].

In the particular case of a 'maximum density droplet' (MDD), however, the fermionic basis states we have been considering are actually exact eigenstates of the interacting Hamiltonian (within the approximation that mixing from higher LLs can be neglected — see footnote 1 on page 24). A hole MDD is defined by the total number of holes, N_{h}, and its spin, S_z, such that (recall that $m = 0, 1, 2, \ldots$)

$$n^{\text{h}}_{m\sigma} = \begin{cases} 1 & \text{for } m \leq N^{\text{h}}_{\sigma} - 1, \\ 0 & \text{otherwise,} \end{cases} \tag{1.90}$$

where $N^{\text{h}}_{\uparrow/\downarrow} = \frac{1}{2}(N^{\text{h}} \mp 2S_z)$. The total angular momentum of this state, $M = N^{\text{h}}_{\uparrow} + N^{\text{h}}_{\downarrow} - 2$, is the minimum value allowed by the Pauli exclusion principle, and this is the *only* such configuration with spin S_z and total angular momentum M, so it is therefore an eigenstate of both L_z and the Hamiltonian. If this configuration is stable (i.e. any states with higher M have greater energy), then it must be the ground state of the system for

[1] Note that in our convention S_z is defined in terms of electron numbers, such that $S_z = \frac{1}{2}(N^{\text{h}}_{\downarrow} - N^{\text{h}}_{\uparrow})$. Total angular momentum, however, is defined in terms of hole occupation $M = \sum_{m\sigma} m n^{\text{h}}_{m\sigma}$ such that it will be finite (the sign is not important since we are considering excitations from the MDD state, which depend on $|\Delta M|$).

given S_z. The stability of the MDD is controlled by the interplay between the repulsive Coulomb interaction and the attractive (for holes) antidot potential. Since hole states at higher m occur at larger radii, larger antidot confinement favours the MDD as the ground state, but of course holes farther away from the antidot experience a reduced Coulomb potential from the remaining holes, favouring a different configuration. For a given set of parameters, we can test the stability of the MDD by considering the energy associated with each particle in the system,

$$\varepsilon^{\mathrm{HF}}_{m_i\sigma_i} = -\tilde{\varepsilon}_{m_i\sigma_i} + \sum_{j}^{N_{\mathrm{h}}} (J_{m_i,m_j} - \delta_{\sigma_i,\sigma_j} K_{m_i,m_j}). \tag{1.91}$$

If all of these satisfy the condition

$$\varepsilon^{\mathrm{HF}}_{m_i\sigma_i} \leq \varepsilon^{\mathrm{HF}}_{(N^{\mathrm{h}}_{\sigma}-1)\sigma}, \tag{1.92}$$

then the MDD will be the stable ground state for the spin S_z. Examples of both stable and unstable ground states are shown in Fig. 1.8.

In calculations, we control the strength of the confining potential through the SP energy spectrum, and add an additional parameter η_{C} multiplying the Coulomb term in the Hamiltonian, which we can then use as a 'knob' to control the strength of electron-electron interactions. In comparing directly with experiments, we find it is often necessary to set $\eta_{\mathrm{C}} \approx 0.1$. This is certainly unsatisfying, and reflects the notorious difficulties involved with quantitative comparisons between theoretical predictions of energy gaps and real experimental data [e.g., 56]. Several factors likely contribute to the 'softening' of the Coulomb interactions in real devices, including LL mixing, screening by nearby gates and compressible regions of the 2DES, and the finite thickness of the electron wave functions in the growth direction, all of which are ignored in our calculations. We believe that it is not unreasonable to believe that a combination of these factors might reduce the Coulomb interaction between electrons by an order of magnitude from its bare value.

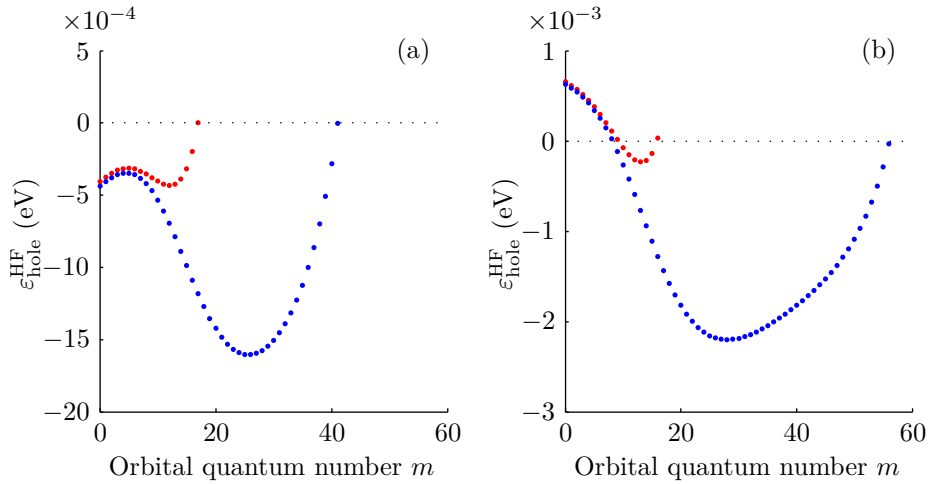

Figure 1.8: Self-energy of holes in an MDD confined by a parabolic antidot potential computed according to Eq. (1.91), showing both stable (a) and unstable (b) configurations. The MDD is stable if all of the spin-↑ (red) and spin-↓ (blue) holes have lower self-energy than the outermost states, which is shown by a dotted line. The spin S_z used in each plot is the ground-state spin for an MDD with N_h holes. As seen above, typically the antidot becomes highly spin polarised before the MDD configuration becomes unstable. Calculation parameters are chosen to match the device used in Chapter 4: $R_\mathrm{AD} = 400\,\mathrm{nm}$, $B_\perp = 0.6\,\mathrm{T}$, $E_\mathrm{Z} = 30\,\mu\mathrm{eV}$, with $\Delta E_\mathrm{SP} = 350\,\mu\mathrm{eV}$ in (a) and 300 μeV in (b). The Coulomb interaction is at its full value ($\eta_\mathrm{C} = 1$).

Chapter 2

Transport Theory

From an experimental point of view, we have frustratingly little access to the physics of microscopic quantum systems at the bottom of a dilution refrigerator. Without the addition of complicated additional equipment such as optical or scanning probes, we are limited to transport experiments, through which we can measure two things: electrical currents and voltages. It is therefore the physicist's task to make connections between the device physics we would like to understand and a measurable current or voltage. To accomplish this task, we have a wide variety of experimental 'knobs' to vary, in the form of device parameters, electric and magnetic fields, and temperature. In this chapter we briefly review the theory of transport in two-dimensional quantum electronic systems, which we shall need to interpret our experimental results in terms of the antidot physics presented in Chapter 1.

2.1 The Landauer-Büttiker formalism

It is often convenient to treat transport in mesoscopic electronic devices through a scattering framework, in which currents injected to and from the active region are resolved into a set of known eigenfunctions, or 'modes', in the leads which connect the system to the outside world. If these lead modes form a complete basis, then the transport properties of the device may be described in terms of an S-matrix, composed of scattering amplitudes which give the 'connections' between each mode in every lead of the system. In many cases the form of these lead modes is obvious, such as when a coherent device is probed through a set of quantum point contacts (QPCs) which are naturally modelled as one-dimensional quantum wires. We have already seen in Chapter 1 how a perpendicular magnetic field splits the density of states of a 2DES into a set of LLs,

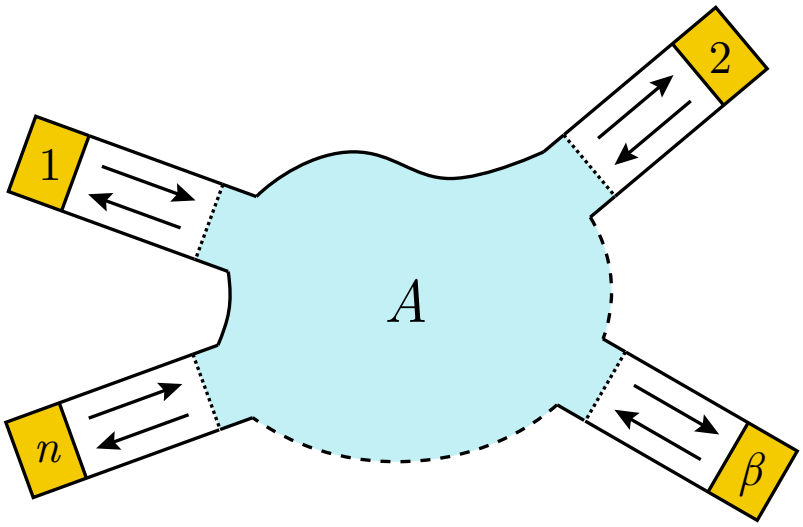

Figure 2.1: A general multi-terminal device, in which a set of n ideal leads connect to an arbitrary elastic scattering centre, or 'active region,' A, which is described by a unitary S-matrix. We consider the case where all of the leads and the bulk have the same filling factor N, although this simplification is not strictly necessary.

which form localised states throughout the bulk of a device and chiral edge states along the sample edges. These edge modes provide a set of one-dimensional eigenfunctions for the scattering states, and, as pointed out by Büttiker [31, 57], their chirality often leads to enormous simplifications of the S-matrix, such that the transport properties of even very complicated devices may be evaluated straightforwardly with only a little algebra.

The work of Büttiker resulted from efforts to explain the experimental observations of the quantum Hall effect [30], in which four-terminal electrical measurements can provide exactly quantised resistance/conductance values even in macroscopic samples which are clearly not phase-coherent throughout. He extended the earlier work by Landauer [58, 59] (reformulated around the same time as Büttiker's own work in Ref. [60]) to consider a multi-terminal geometry, in which a set of perfect leads connect to an arbitrary elastic scattering centre,[1] as shown in Fig. 2.1. Here we consider the case where the active

[1] Additional features of real devices may be incorporated as well. For example, non-ideal ohmic contacts which produce non-equilibrium populations of edge modes may be modelled as ideal contacts separated from the lead by appropriate elastic scattering centres, and inelastic scattering between modes along the same edge can be included by adding additional 'ideal voltage probes' to the system, which act as inelastic scatters and fully equilibrate the populations within an edge.

region and all of the leads are characterised by the same filling factor N, although it is straightforward to treat situations (such as the selective-injection device studied in Chapters 4, 5 and 6) in which the number of modes in each lead is different.

The eigenfunctions of the leads are the solutions to the Schrödinger equation for two-dimensional electrons in the presence of a perpendicular magnetic field B, with the SP Hamiltonian given by Eq. (1.1). In contrast to our approach to zero-dimensional antidot states in Chapter 1, the one-dimensional states are best described in the Landau gauge $\mathbf{A} = (-By, 0, 0)$, where we choose Cartesian coordinates with x along the direction of the lead,[1] such that

$$\hat{H} = \frac{1}{2m^*}\left[(\hat{p}_x - eBy)^2 + \hat{p}_y^2\right] - e\varphi(y), \tag{2.1}$$

where $\varphi(y)$ is the confining potential of the lead. The solutions in this gauge are propagating waves $\psi_n = e^{ikx}\phi_n(y)$, where $\phi_n(y)$ solves the one-dimensional eigenvalue equation

$$\left[-\frac{\hbar}{2m^*}\frac{\partial^2}{\partial y^2} + \frac{1}{2}m^*\omega_{\mathrm{C}}^2(y - y_0)^2 - e\varphi(y)\right]\phi_{n,k}(y) = E_{n,k}\phi_{n,k}(y), \tag{2.2}$$

with the k-dependent parameter y_0 given by

$$y_0 = \frac{\hbar k}{eB} = \ell_{\mathrm{B}}^2 k. \tag{2.3}$$

In a region with a uniform potential, $\varphi \equiv 0$, Eq. (2.2) has harmonic oscillator solutions with

$$E_{n,k} = \hbar\omega_{\mathrm{C}}\left(n + \frac{1}{2}\right), \tag{2.4}$$

where n is the LL index as expected, and $\phi_{n,k}$ is localised near $y = y_0$ with a length scale given by ℓ_{B}. Exactly as we found in Chapter 1, if the potential $\varphi(y)$ varies slowly on the scale of ℓ_{B}, then the true solutions will be similar to the free-electron wave functions, with eigenenergies $E_{n,k}$ given as a function of y_0:

$$E_{n,k} = E(n, B, y_0(k)). \tag{2.5}$$

The total number N of occupied modes is then determined by the Fermi energy, E_{F}, through the maximum value of the LL index n for which $E_{n,k} < E_{\mathrm{F}}$ at the centre of the lead. These states are analogous to the semiclassical 'skipping orbits' we considered for the antidot SP states in §1.2, except that the spectrum within each LL n is continuous,

[1] It is in general possible to choose a consistent gauge for the system as a whole such that $\mathbf{A}$ is given in the Landau gauge asymptotically for each lead, as described in Appendix E of Ref. [61].

labelled by the wavevector k, rather than discrete. As for the antidot states, they have a group velocity along the edge as a result of the confining potential, given by[1]

$$v_{n,k} = \frac{1}{\hbar}\frac{dE_{n,k}}{dk} = \frac{1}{\hbar}\left(\frac{dE_{n,k}}{dy_0}\right)\left(\frac{dy_0}{dk}\right) = \frac{1}{eB}\frac{dE_{n,k}}{dy_0}. \tag{2.6}$$

The current carried by mode n within an energy window $\Delta\mu$ (at zero temperature) is then given in terms of the group velocity and the density of states dn/dE,

$$I_n = ev_{n,k}\left(\frac{dn}{dE}\right)\Delta\mu, \tag{2.7}$$

and since $dn/dk = 1/2\pi$ in one dimension,[2] we have

$$\frac{dn}{dE} = \left(\frac{dn}{dk}\right)\left(\frac{dk}{dE}\right) = \frac{1}{2\pi\hbar v}, \tag{2.8}$$

such that

$$I_n = \frac{e}{h}\Delta\mu. \tag{2.9}$$

Each mode in the lead therefore carries a current proportional to its chemical potential.

This result allows us to directly connect the experimentally measured currents and voltages (related to the chemical potential through $\mu = -eV$) to a simple scattering problem. Büttiker's central result is an expression for the current in lead α as a function of the chemical potentials in each lead:

$$I_\alpha = \frac{e}{h}\left[(N - R_\alpha)\mu_\alpha - \sum_{\beta\neq\alpha} T_{\alpha\beta}\,\mu_\beta\right], \tag{2.10}$$

where $T_{\alpha\beta}$ are the transmission coefficients for current to pass from lead β to lead α, and $R_\alpha = T_{\alpha\alpha}$ is the reflection coefficient for current to return to lead α after entering the device. As we will see in more detail in the next section, these coefficients represent the summed scattering probabilities of all the modes in the system, given by

$$T_{\alpha\beta} = \sum_{n,m}^{N} |t_{\alpha\beta,nm}|^2\,, \tag{2.11}$$

where $t_{\alpha\beta,nm}$ is the scattering probability amplitude (an element of the S-matrix) for a

[1] Semiclassically, for a perturbative confining potential such that $E_{n,k} \simeq -e\varphi(y_0) + \hbar\omega_C(n + \frac{1}{2})$, Eq. (2.6) gives the expected result for $\mathbf{E}\wedge\mathbf{B}$ drift: $v_{n,k} \simeq |\nabla\varphi|/|B|$.

[2] For a system of length L, each state occupies a length $2\pi/L$ in k-space, such that the total number of states is $N = k(L/2\pi)$, and hence $dn/dk = 1/2\pi$.

transition from mode m in lead β to mode n in lead α, evaluated at the Fermi energy.

In an experiment, the leads are part of a larger electronic circuit, and are typically used in one of two ways. Either we fix the voltage (and hence μ) in order to source or measure a current, or we fix the current by attaching the lead to a known current source. Voltage probes are a special case of the latter method, for which $I = 0$, and hence Eq. (2.10) gives

$$V_\alpha = \frac{\sum_{\beta\neq\alpha} T_{\alpha\beta} V_\beta}{N - R_\alpha}. \tag{2.12}$$

Alternatively, current-measuring probes are typically set to ground potential ($\mu = 0$), and therefore measure a current given by

$$I_\alpha = \frac{e^2}{h} \sum_{\beta\neq\alpha} T_{\alpha\beta} V_\beta, \tag{2.13}$$

which is independent of the probe's reflection coefficient.

As mentioned previously, the key simplification of the quantum Hall regime results from the *chirality* of the edge modes. Unless the edge modes originating from different contacts are brought within direct tunnelling distance in the active region of the device, there is a very low probability that an electron can leave a given edge, even though it experiences many scattering events between the various modes on that edge. If all the edges in Fig. 2.1 remain separated, all of the current in the N modes leaving a contact will enter the next one, such that, for clockwise-circulating edge modes, $T_{\alpha+1,\alpha} = N$, and all other $T_{\alpha\beta} = 0$ (including the R_α). Combined with Eq. (2.10), this scenario leads directly to the observed four-terminal resistances which define the quantum Hall effect [31]. For an arbitrary device in the QH regime, it is usually straightforward to identify the transmission coefficients in a similar manner, and then to work out the desired currents and voltages algebraically from Eq. (2.10) using the known currents and voltages of the experimental circuit.

Consider as an example a typical antidot device as sketched in Fig. 2.2. We split the ν_B total modes of the upper (lower) edge into the N (N') which flow through the upper (lower) constriction and the M (M') which are reflected. We consider the case in which the constrictions are tuned symmetrically, i.e. $N = N' = \nu_\mathrm{AD}$ (the primed and unprimed notation allows us to distinguish between the modes at the antidot which originated from contacts 4 and 2, respectively). In a standard four-terminal measurement, we apply a voltage V_0 to lead 1 to drive a current through the device, measure the current flowing out of lead 3 (setting $V_3 = 0$), and measure the voltage difference $V_{24} = V_2 - V_4$ between the contacts in leads 2 and 4. We first consider the voltage probes 2 and 4, described

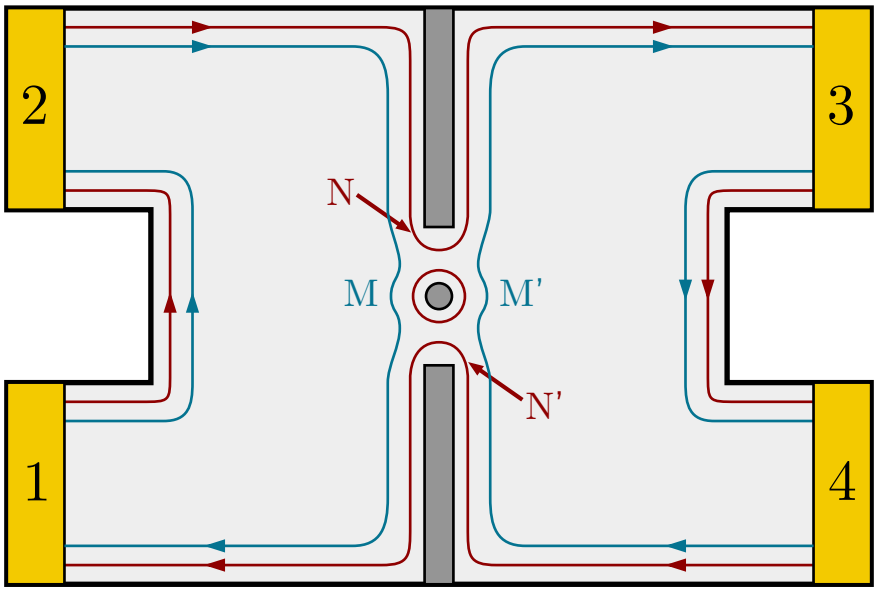

Figure 2.2: Schematic diagram showing the edge-mode network for a four-terminal measurement of a single antidot.

by Eq. (2.12). Considering the topology of the edge modes, we immediately see that

$$T_{2\alpha} = \begin{cases} \nu_{\mathrm{B}} & \text{for } \alpha = 1 \\ 0 & \text{otherwise,} \end{cases} \tag{2.14}$$

and similarly $T_{43} = \nu_{\mathrm{B}}$ with all other $T_{4\alpha} = 0$. Thus Eq. (2.12) implies that $V_2 = V_0$ and $V_4 = 0$, such that the measured voltage $V_{24} = V_0$. Then, to compute the four-terminal conductance of the device,

$$G_{13,24} = \frac{I_3}{V_{24}} \qquad \text{(with current source at 1),} \tag{2.15}$$

we need only work out the current in probe 3, which is given by Eq. (2.13) with only one nonvanishing term,

$$I_3 = \frac{e^2}{h} T_{32} V_0. \tag{2.16}$$

The conductance is therefore given by[1]

$$G_{13,24} = \frac{e^2}{h} \sum_{n,m}^{\nu_B} |t_{32,nm}|^2 \,, \tag{2.17}$$

in terms of the individual scattering probabilities between the modes originating from contact 2 and those which eventually enter contact 3.

We can express this result in a slightly more transparent form by defining a set of antidot scattering probabilities $p_{m'n} = p_{nm'}$ for transitions between modes $n \in (N, M)$ and $m' \in (N', M')$. Recognising that, in the absence of scattering through the antidot, $T_{32} = N = \nu_{AD}$, and using the fact that $T_{32} + T_{12} = T_{14} + T_{34} = \nu_B$, we obtain

$$G_{13,24} = \frac{e^2}{h} \left(\nu_{AD} + \sum_{n \in M, m' \in M'} p_{nm'} - \sum_{n \in N, m' \in N'} p_{nm'} \right) . \tag{2.18}$$

With this formulation, we have a natural interpretation of the first term as the base conductance of the constrictions, and the second and third as 'forward-scattering' between states (M, M') and 'back-scattering' between states (N, N') which result in increased and decreased conductance, respectively.[2] In the specific case of $\nu_{AD} = 2$, if we assume spin-conservation and that only the modes of the second LL ($\nu = 3, 4$) contribute to forward-scattering, then the antidot conductance is given by

$$G_{13,24} = \frac{e^2}{h} \left(2 + p_{33'} + p_{44'} - p_{11'} - p_{22'} \right) . \tag{2.19}$$

Thus, the Landauer-Büttiker formalism reduces the problem of modeling electrical transport through an antidot to the evaluation of the individual antidot scattering probabilities, which reflect the antidot physics in which we are interested. Several approaches exist for this purpose, a few of which we will discuss in the remainder of this chapter. Natural extensions of the procedure described in this example allow the deconstruction of more complicated devices and measurement setups, such as those we consider in Chapter 4 of this work.

[1] N.B., although the scattering probabilities for any *particular* scattering event depend on the phase information included in the scattering amplitudes $t_{\alpha\beta,nm}$, the measured quantities I and V are time-averaged, and so depend only on the probabilities $|t_{\alpha\beta,nm}|^2$ because the relative phases of the input states are uncorrelated.

[2] Note that several potential scattering events, such as transitions between modes in states (N, M) or (N', M'), do not appear in Eq. (2.18), since they do not change the current which flows through the device. They do still occur, of course, and are measurable with the selective injection/detection technique presented in Chapter 4.

2.2 Green's functions and linear-response theory

We have seen in the previous section how the linear-response conductance of the device may be written in terms of the scattering probabilities between the eigenfunctions of the leads through the Landauer-Büttiker formula, Eq. (2.10). Around the same time as Büttiker's own work, Baranger and Stone [61] developed a more general theory of electrical linear-response for mesoscopic devices, through which the individual scattering amplitudes $t_{\alpha\beta,nm}$ are expressed in terms of the time-independent Green's function for the device, evaluated at the Fermi energy. As we shall discuss below, efficient algorithms exist for the calculation of such Green's functions for arbitrary potentials, and so this provides a flexible method for modelling ballistic transport in coherent electronic devices, which we will use in Chapter 3 to investigate the effects on the antidot SP spectrum of the asymmetry introduced by the QPC in which the antidot is embedded.

2.2.1 Definitions

Green's functions, or propagators, provide a powerful and versatile approach to scattering problems. They supply a framework within which to include arbitrary potentials and many types of more complicated interactions. Here we consider only a time-independent, non-interacting theory in the linear-response regime, since this will be useful to us in Chapter 3, but applications of the general technique are in principle much broader.[1] For example, Green's functions including interactions through local spin-density functional theory have been used recently [62] to investigate the formation of compressible regions around antidots. We do not attempt a systematic review of the properties of Green's functions here, and simply quote many of the results that we shall need, generally following the treatment of Baranger and Stone [61]. Many introductory quantum mechanics textbooks [e.g., 63] treat time-independent scattering theory through a Green's function approach, and for more detail on Green's functions in particular, the book by Economou [64] is quite a good reference.

Fundamentally, a time-independent Green's function is defined as the solution to the differential equation

$$[z - \mathcal{L}(\mathbf{x})]G(\mathbf{x}, \mathbf{x}'; z) = \delta(\mathbf{x} - \mathbf{x}'), \tag{2.20}$$

where $z = \lambda \pm i\eta$ is a complex variable, and $\mathcal{L}$ is a linear Hermitian operator with

[1] See, for example, the recent review by Sim et al. on the topic of interactions in antidots [22] for a somewhat more general formulation of the antidot scattering problem.

eigenvalues λ_n and eigenfunctions $\phi_n(\mathbf{x})$,

$$\mathcal{L}(\mathbf{x})\phi_n(\mathbf{x}) = \lambda_n\phi_n(\mathbf{x}), \tag{2.21}$$

which are orthonormal and complete, i.e.,

$$\int \phi_n^*(\mathbf{x})\phi_m(\mathbf{x})d\mathbf{x} = \delta_{n,m} \qquad \text{and} \qquad \sum_n \phi_n(\mathbf{x})\phi_n(\mathbf{x}') = \delta(\mathbf{x}-\mathbf{x}'). \tag{2.22}$$

From Eq. (2.20) it is clear that, if $u(\mathbf{x})$ solves the inhomogeneous equation

$$\big[z - \mathcal{L}(\mathbf{x})\big]u(\mathbf{x}) = f(\mathbf{x}), \tag{2.23}$$

then $u(\mathbf{x})$ is given by[1]

$$u(\mathbf{x}) = \int G(\mathbf{x},\mathbf{x}';z)f(\mathbf{x}')\,d\mathbf{x}', \tag{2.24}$$

since acting on the above equation with $\big[z - \mathcal{L}(\mathbf{x})\big]$ returns Eq. (2.23) through the definition of G in Eq. (2.20). So we can think of $G(\mathbf{x},\mathbf{x}';z)$ as the inverse of the differential operator $\big[z - \mathcal{L}(\mathbf{x})\big]$, in the sense given by Eq. (2.24).

We consider the same general scattering problem as in the previous section, depicted in Fig. 2.1, in which a set of ideal metallic leads connect to the active region A, where the potential is given by $U(\mathbf{x}) = -e\varphi(\mathbf{x})$. The Green's function we need is that defined by the full Hamiltonian for the active region,

$$\mathcal{L} = \hat{H}(\mathbf{x}) = \hat{H}_0 + U(\mathbf{x}), \tag{2.25}$$

composed of both the potential $U(\mathbf{x})$ and the free-particle part,

$$\hat{H}_0 = \frac{1}{2m^*}(\hat{\mathbf{p}} + e\mathbf{A})^2. \tag{2.26}$$

The eigenfunctions ψ_a of this Hamiltonian are the wave functions of the complete problem, i.e., the solutions to Schrödinger's equation

$$\hat{H}\psi_a(\mathbf{x}) = \varepsilon_a\psi_a(\mathbf{x}), \tag{2.27}$$

where a represents a complete set of quantum numbers.[2] If we rewrite the Schrödinger

[1] Note that a slightly different definition must be used if $z = \lambda_n$ where λ_n is one of the eigenvalues of $\mathcal{L}$. See, for example, (2.54) later in this section.

[2] For simplicity we ignore spin as in the previous section. In the absence of any spin-mixing, spin is easily included by adding a spin-dependent constant to the potential $U(\mathbf{x})$ corresponding to the Zeeman

equation using Eq. (2.24), we obtain

$$\psi_a(\mathbf{x}) = \int G(\mathbf{x}, \mathbf{x}'; z)(z - \varepsilon_a)\psi_a(\mathbf{x}')d\mathbf{x}', \tag{2.28}$$

and then using the orthonormality of the eigenfunctions, Eq. (2.22), we find that we can express the Green's function in terms of the wave functions,

$$G(\mathbf{x}, \mathbf{x}'; z) = \sum_a \frac{\psi_a(\mathbf{x})\psi_a^*(\mathbf{x}')}{z - \varepsilon_a}. \tag{2.29}$$

From this definition it is obvious that $G(\mathbf{x}, \mathbf{x}'; z)$ is not analytic if z is equal to any of the eigenvalues ε_a (which may have a continuous spectrum), and so we define instead the limits

$$G^{\pm}(\mathbf{x}, \mathbf{x}'; E) = \lim_{\eta \to 0^+} G(\mathbf{x}, \mathbf{x}'; E \pm i\eta), \tag{2.30}$$

where E and η are real, which are known as the retarded $(+)$ and advanced $(-)$ Green's functions, respectively.

Besides the link between the Green's function of a device and the transport properties we discuss below, $G^{\pm}(\mathbf{x}, \mathbf{x}'; E)$ is also directly related to the density of states and in particular the *local density of states*, given by

$$\rho(\mathbf{x}; E) = \sum_a \delta(E - E_a)\psi_a^*(\mathbf{x})\psi_a(\mathbf{x}). \tag{2.31}$$

By expressing $G^{\pm}$ through Eq. (2.29) and applying the identity[1]

$$\lim_{y \to 0^+} \frac{1}{x \pm iy} = \mathrm{P}\frac{1}{x} \mp i\pi\delta(x), \tag{2.32}$$

we obtain

$$G^{\pm}(\mathbf{x}, \mathbf{x}; E) = \mathrm{P}\sum_a \frac{\psi_a(\mathbf{x})\psi_a^*(\mathbf{x})}{E - E_a} \mp i\pi \sum_a \delta(E - E_a)\psi_a(\mathbf{x})\psi_a^*(\mathbf{x}), \tag{2.33}$$

from which we identify the local density of states,

$$\rho(\mathbf{x}; E) = \mp\frac{1}{\pi}\Im[G^{\pm}(\mathbf{x}, \mathbf{x}; E)]. \tag{2.34}$$

energy.

[1] P denotes the principal value, understood to mean that an integral $\int \mathrm{P}(\frac{1}{x})dx$ will exclude the singularity at $x = 0$.

We can also obtain the full density of states $N(E) = \sum_a \delta(E - E_a)$ by integrating over space,

$$N(E) = \int \rho(\mathbf{x}; E)\, d\mathbf{x} = \mp\frac{1}{\pi}\Im\big[\operatorname{Tr} G^{\pm}(E)\big]. \tag{2.35}$$

When modelling transport in mesoscopic structures, the local density of states is very useful as a visualisation tool, allowing one to 'see' the scattering states at a given energy, which helps to identify the source of features in the conductance.

2.2.2 Connection to scattering theory

To establish the scattering framework more concretely, we want to expand the wave functions ψ_a in terms of the eigenfunctions in the leads. Following Baranger and Stone [61], we choose the Landau gauge to describe the lead eigenstates, and a set of local coordinates (x_β, y_β) for lead β, such that

$$\xi_a^{\pm}(\mathbf{x}_\beta) = \frac{1}{\sqrt{\theta_a}} e^{\pm i k_a x} \phi^{\pm}_{n_a,k_a}(y_\beta), \tag{2.36}$$

where $\phi_{n,k}(y_\beta)$ are the transverse wave functions determined by the lead confining potential, as in Eq. (2.2). We have explicitly separated the outgoing (+) and incoming (−) states, and the normalisation factor θ_a is the outgoing 'particle flux' through the lead, related to the current by $I_a = -e\theta_a$. This somewhat unusual normalisation ensures that the S-matrix linking these states will be unitary. The current is computed in terms of the probability current-density operator given by Eq. (1.41) on page 13. To simplify notation, we write the matrix elements of the probability current-density operator as

$$[\hat{\mathbf{J}}(\mathbf{x})]_{ab} = \frac{\hbar}{2m^* i}\big[\psi_a^*(\mathbf{x}) \overleftrightarrow{\mathbf{D}} \psi_b(\mathbf{x})\big], \tag{2.37}$$

in terms of the double-sided derivative operator defined by

$$f \overleftrightarrow{\mathbf{D}} g = f(\mathbf{x})\mathbf{D}g(\mathbf{x}) - g(\mathbf{x})\mathbf{D}^* f(\mathbf{x}), \tag{2.38}$$

where $\mathbf{D}$ is the gauge covariant derivative defined in Eq. (1.42) on page 13. Then the normalisation θ_a is computed by integrating the current passing through the cross-section $\mathcal{C}_\beta$ of lead β, i.e.,

$$\theta_a = \frac{\hbar}{2m^* i}\int_{\mathcal{C}_\beta} dy_\beta \big[e^{+ik_a x}\phi^+_{n_a,k_a}\big]^* (\overleftrightarrow{\mathbf{D}} \cdot \hat{\mathbf{x}}_\beta) e^{+ik_a x}\phi^+_{n_a,k_a}, \tag{2.39}$$

where $\hat{\mathbf{x}}_\beta$ is the unit normal vector perpendicular to $\mathcal{C}_\beta$.

Current conservation provides a set of identities for lead eigenstates at the same energy which are similar to standard orthogonality relations:[1]

$$\int_{\mathcal{C}_\beta} dy_\beta\, \xi_a^{\pm *}(\mathbf{x}_\beta)(\overleftrightarrow{\mathbf{D}}\cdot\hat{\mathbf{x}}_\beta)\xi_b^{\pm}(\mathbf{x}_\beta) = \pm\frac{2m^* i}{\hbar}\delta_{ab}, \quad \varepsilon_a = \varepsilon_b, \tag{2.40a}$$

$$\int_{\mathcal{C}_\beta} dy_\beta\, \xi_a^{+ *}(\mathbf{x}_\beta)(\overleftrightarrow{\mathbf{D}}\cdot\hat{\mathbf{x}}_\beta)\xi_b^{-}(\mathbf{x}_\beta) = 0, \tag{2.40b}$$

$$\int_{\mathcal{C}_\beta} dy_\beta\, \xi_a^{- *}(\mathbf{x}_\beta)(\overleftrightarrow{\mathbf{D}}\cdot\hat{\mathbf{x}}_\beta)\xi_b^{+}(\mathbf{x}_\beta) = 0. \tag{2.40c}$$

Now, we can expand a scattering wave $\psi_{\beta,a}(\mathbf{x})$, which originates in state a of lead β, in terms of these lead eigenstates, such that asymptotically in each lead,

$$\psi_{\beta,a}(\mathbf{x}) \to \begin{cases} \xi_a^-(\mathbf{x}_\beta) + \sum_c^\varepsilon t_{\beta\beta,ca}\xi_c^+(\mathbf{x}_\beta), & \mathbf{x} \text{ in lead } \beta, \\ \sum_c^\varepsilon t_{\gamma\beta,ca}\xi_c^+(\mathbf{x}_\gamma), & \mathbf{x} \text{ in lead } \gamma, \end{cases} \tag{2.41}$$

where the energy-restricted sum $\sum_c^\varepsilon$ is defined as

$$\sum_c^\varepsilon \equiv \int dc\, \delta(\varepsilon - \varepsilon_c). \tag{2.42}$$

The energy-dependent $t_{\alpha\beta,ab}$ are the elements of the S-matrix, which gives the asymptotic components of an output state

$$\psi^{\text{out}}(\mathbf{x}) = \sum_\beta \sum_a^\varepsilon c_{\beta,a}^{\text{out}}\xi_a^+(\mathbf{x}_\beta) \tag{2.43}$$

resulting from an arbitrary input state

$$\psi^{\text{in}}(\mathbf{x}) = \sum_\beta \sum_a^\varepsilon c_{\beta,a}^{\text{in}}\xi_a^-(\mathbf{x}_\beta) \tag{2.44}$$

through the matrix equation

$$c_{\beta,a}^{\text{out}} = \sum_\gamma \sum_c^\varepsilon t_{\beta\gamma,ac}c_{\gamma,c}^{\text{in}}. \tag{2.45}$$

[1] The states $\phi_{n,k}^\pm(y)$ are not orthogonal at fixed energy $\varepsilon_{n,k} = E$ due to the dependence of Eq. (2.2) on k (which defines the minimum of the effective magnetic potential through y_0), so it is not possible to resolve the scattering state into lead eigenstates by simply projecting onto the set $\phi_{n,k}^\pm(y)$, as one could do at $B = 0$. Instead, we compute matrix elements with the current-density operator and use the 'orthogonality' relations of Eqs. (2.40).

Current conservation means that the total current carried by the scattering wave $\psi_{\beta,a}(\mathbf{x})$ in Eq. (2.41), integrated across all leads, should be zero. Using the current-operator identities of Eqs. (2.40), we easily obtain the identity

$$\sum_{\gamma}\sum_{c}^{\varepsilon} t^{*}_{\alpha\gamma,ac}t_{\gamma\beta,cb} = \delta_{\alpha\beta}\delta_{ab}, \tag{2.46}$$

which is an expression of the unitarity of the S-matrix. From this immediately follows the relationship stated in Eq. (2.11) on page 33, recast for energy-dependent scattering amplitudes as

$$T_{\alpha\beta}(\varepsilon) = \sum_{a,b}^{\varepsilon} |t_{\alpha\beta,ab}|^2, \tag{2.47}$$

making explicit the connection to the Landauer-Büttiker formalism.

Finally, to determine the conductance properties of a given device, we compute the scattering amplitudes using the lead eigenfunctions and the Green's function for the active region, which naturally provides the 'connections' between states at different points in space at a given energy. Using the properties of $G^{\pm}(\mathbf{x},\mathbf{x}';\varepsilon)$, Baranger and Stone [61] arrive at the expression

$$\psi_{\beta,a}(\mathbf{x}) = -\frac{\hbar^2}{2m^*}\int_{\mathcal{C}_\beta} dy'_\beta\, G^{+}(\mathbf{x},\mathbf{x}'_\beta;\varepsilon)(\overleftrightarrow{\mathbf{D}}'\cdot\hat{\mathbf{x}}_\beta)\xi^{-}_a(\mathbf{x}'_\beta), \qquad \mathbf{x}\text{ in }A. \tag{2.48}$$

By taking the projection with $\xi^{+*}_b(\mathbf{x}_\alpha)$ through the current-density operator, we extract the S-matrix elements to reach the desired result

$$t_{\alpha\beta,ab} = -\frac{i\hbar^3}{4m^{*2}}\int_{\mathcal{C}_\alpha} dy_\alpha \int_{\mathcal{C}_\beta} dy'_\beta\, G^{+}(\mathbf{x}_\alpha,\mathbf{x}'_\beta;\varepsilon)(\overleftrightarrow{\mathbf{D}}^{*}\cdot\hat{\mathbf{x}}_\alpha)(\overleftrightarrow{\mathbf{D}}'\cdot\hat{\mathbf{x}}_\beta)\xi^{+*}_b(\mathbf{x}_\alpha)\xi^{-}_a(\mathbf{x}'_\beta). \tag{2.49}$$

This formalism also provides a natural way to incorporate the effects of finite temperature. The nonzero contributions to the current still come from the scattering amplitudes near the Fermi level, but we must average over the range of energies which are 'partially occupied' according to the Fermi distribution

$$f(\varepsilon) = \frac{1}{1+\exp(\frac{\varepsilon-E_{\mathrm{F}}}{kT})}. \tag{2.50}$$

This leads to an expression for the current flowing out of lead α,

$$I_\alpha = -\frac{e^2}{h}\left[N_\alpha V_\alpha - \sum_\beta V_\beta \int d\varepsilon\,[-f'(\varepsilon)]T_{\alpha\beta}(\varepsilon)\right], \tag{2.51}$$

where the sum runs over all leads (including α), and N_α is the number of modes in lead α. This expression is equivalent to the Landauer-Büttiker formula, Eq. (2.10), in the limit of zero temperature, or in the case of energy-independent transmission coefficients.

2.2.3 Calculating time-independent Green's functions

Given the connection presented in the previous section between Green's functions and the currents and voltages measured in transport experiments, we have a powerful framework with which to model ballistic transport in mesoscopic devices. All that remains is the calculation of the Green's function $G^+(\mathbf{x}, \mathbf{x}'; \varepsilon)$ in Eq. (2.49). In some sense, the calculation of the full Green's function for the Hamiltonian $\hat{H}_0 + U(\mathbf{x})$ (with appropriate boundary conditions in the leads) is equivalent to solving the time-independent Schrödinger equation,[1] but methods exist for the Green's function calculation which are far more efficient than diagonalising the full Hamiltonian. These mainly rely a slightly indirect method, starting with the known Green's function for a simplified Hamiltonian (in this case, the free-particle Hamiltonian $\hat{H}_0$), and then building up the full Green's function through an iterative process.

This procedure takes advantage of the easily quantifiable change to $G(\mathbf{x}, \mathbf{x}'; z)$ which results from the addition of a small perturbation to the Hamiltonian. Consider the free-particle Green's function defined by

$$[z - \hat{H}_0(\mathbf{x})]G_0(\mathbf{x}, \mathbf{x}'; z) = \delta(\mathbf{x} - \mathbf{x}'), \tag{2.52}$$

which is given by Eq. (2.29) in terms of the known free-particle wave functions $\phi_n(\mathbf{x})$ (LL eigenstates). Now suppose we add a perturbing potential $\tilde{U}(\mathbf{x})$, and write Schrödinger's equation for the new eigenstates $\psi_n(\mathbf{x})$ in the form

$$[\varepsilon_n - \hat{H}_0(\mathbf{x})]\psi_n(\mathbf{x}) = \tilde{U}(\mathbf{x})\psi_n(\mathbf{x}). \tag{2.53}$$

Comparing this to Eqs. (2.23) and (2.24), we obtain the Lippmann-Schwinger equation,

$$\psi_n(\mathbf{x}) = \phi_n(\mathbf{x}) + \int G_0^{\pm}(\mathbf{x}, \mathbf{x}'; \varepsilon_n)\tilde{U}(\mathbf{x}')\psi_n(\mathbf{x}')\, d\mathbf{x}', \tag{2.54}$$

in which it is necessary to use the retarded/advanced Green's functions which are defined at $z = \varepsilon_n$, and to include the term $\phi_n(\mathbf{x})$ to satisfy Eq. (2.53) as $\tilde{U}(\mathbf{x}) \to 0$. The Green's

[1] Essentially this is because the poles of $G(\mathbf{x}, \mathbf{x}'; z)$ coincide with the eigenvalues of $\hat{H}$, as seen in Eq. (2.29), and so knowledge of the poles of G gives us the energy spectrum of $\hat{H}$.

function for the perturbed Hamiltonian is then defined by

$$[z - \hat{H}_0(\mathbf{x}) - \tilde{U}(\mathbf{x})]G(\mathbf{x}, \mathbf{x}'; z) = \delta(\mathbf{x} - \mathbf{x}'), \tag{2.55}$$

from which we obtain the related integral expression, similar to Eq. (2.54),

$$\psi_n(\mathbf{x}) = \phi_n(\mathbf{x}) + \int G^{\pm}(\mathbf{x}, \mathbf{x}'; \varepsilon_n)\tilde{U}(\mathbf{x}')\phi_n(\mathbf{x}')\, d\mathbf{x}'. \tag{2.56}$$

By inserting Eq. (2.56) into the Lippmann-Schwinger equation, and comparing the result again with Eq. (2.56), we obtain the Dyson equation relating $G^{\pm}$ to $G_0^{\pm}$,

$$G^{\pm}(\mathbf{x}, \mathbf{x}'; \varepsilon) = G_0^{\pm}(\mathbf{x}, \mathbf{x}'; \varepsilon) + \int d\mathbf{x}''\, G_0^{\pm}(\mathbf{x}, \mathbf{x}''; \varepsilon)\tilde{U}(\mathbf{x}'')G^{\pm}(\mathbf{x}'', \mathbf{x}'; \varepsilon), \tag{2.57}$$

or, in abstract matrix form,

$$G = G_0 + G_0\tilde{U}G. \tag{2.58}$$

The solution for G from the Dyson equation is obviously still implicit, but in practice we can choose the 'perturbation' $\tilde{U}$ such that the calculation remains computationally efficient at every step, and thereby iteratively build up the full potential $U(\mathbf{x})$.

In calculations, we divide the active region of the device into a lattice, for which $\hat{H}$ is the well-known tight-binding Hamiltonian, in matrix form.[1] We must choose the lattice spacing to be less than the smallest length scale of the problem, which for mesoscopic devices is usually the magnetic length, $\ell_{\mathrm{B}} = 26\,\mathrm{nm}\cdot\mathrm{T}^{-1}$. Therefore, in modelling micron-scale devices at fields $\approx 1\,\mathrm{T}$, we can easily have lattice dimensions of order ≈ 1000. If the computational region A is rectangular, with lattice dimension $N \times M$, then the Hamiltonian matrix will be of size $NM \times NM$, and thus solving the eigenvalue problem for the Hamiltonian directly is often computationally prohibitive. Instead, we use the Dyson equation to build up the full Green's function iteratively, dealing with only a small portion of the system at each step, such that the matrices involved remain manageable. The particular computation we use in Chapter 3 is based on the work of MacKinnon [65] and implemented in a program written by C. H. W. Barnes. Essentially, the $N \times M$ rectangular computational domain is divided in to N 'slices' each containing M lattice points. Tight-binding versions of the Dyson equation lead to a relationship between the Green's function of a system with $n+1$ slices and that of the system with n slices. Starting with the free-particle G_0 determined by the boundary conditions at the first slice,

[1] Baranger and Stone provide the lattice form of the continuum results quoted in §2.2.2 in Appendix B of their paper [61].

we can add successive slices to the system in this way, dealing only with the Green's functions of individual slices, which are size $M \times M$. Clearly, this method is particularly well-suited to anisotropic systems with $M \ll N$, such as quantum wires, but the method is suitable for any system with dimensions such that the inversion of $M \times M$ matrices is computationally feasible.

We have used Green's functions calculated through this method to investigate several important effects of non-interacting particles which are ignored in the idealised model presented in Chapter 1. For example, the effects of tunnel-coupling between the quasi-zero-dimensional antidot states and the extended edge-modes in the two-dimensional regions are naturally incorporated in the Green's function of the full region, and we can easily investigate the dependence of these couplings on the potential gradients, antidot dimensions, and applied magnetic field. In Chapter 3 we use the Green's function technique to explore the effects of the split gates; these gates bring the edge modes within tunneling distance of the antidot but also break the circular symmetry of the system, which we show has measurable effects on the single-particle energy levels.

For the investigation of non-interacting effects like these, the approach presented here is relatively easy-to-use and extremely flexible. In order to incorporate additional physics due to interactions, however, a great deal of additional theoretical machinery is necessary. Methods do exist to compute Green's functions self-consistently which include spin and charge interactions, but these are beyond the scope of this work. For example, in a recent study antidot Green's functions were computed using spin density functional theory [62], in order to investigate the formation of 'compressible regions' at the antidot edge, which have been predicted to exist at high magnetic fields [18, 20]. In many experimental regimes, however, antidot transport is well-described by the model of sequential tunneling commonly used to represent transmission through a quantum dot. The quantum-Hall energy gaps provide natural tunnel barriers between the zero-dimensional antidot states and the 'leads,' which in this case are nearby edge-modes. This description separates the relatively well-understood quantum Hall physics of the leads from the properties of the antidot states, and so we can include the effects of spin and charge interactions on the antidot energy spectrum and tunneling selection-rules in a straightforward manner. By treating the antidot as an isolated zero-dimensional system with capacitive couplings to the gates and leads, we can also move beyond the linear-response regime to explore the effects of finite drain-source bias. We discuss this 'dot model' of antidot transport in the following section.

2.3 Sequential transport

In the theory of sequential transport, we consider a zero-dimensional island which is weakly connected to a set of metallic leads by tunneling barriers. In this section we refer to the island as a dot, although the description of an antidot is entirely equivalent as long as the couplings are weak. Transitions between different occupation states of the dot are modeled as a Markov chain, in which a 'master equation' describes the stochastic evolution of the system. The solution of the master equation provides the equilibrium occupation probability for each state, from which the transport current may be computed. For a given set of dot states, we must therefore compute the transition rates which make up the master equation. These are described by a tunneling Hamiltonian including energy conservation, dot selection rules, and the (possibly energy- and/or spin-dependent) lead-dot tunnel couplings. In many cases, it is sufficient to consider only the lowest-order terms in the perturbation theory for tunneling, in which the rates are given by Fermi's golden rule for the transition rate between individual eigenstates and the continuum in the leads. This theory was developed from earlier descriptions of small metallic islands [e.g., 66] to include the quantised levels in a quantum dot [67–69] and has now become an essential tool in the study of quantum dots. Here we generally follow the review of Kouwenhoven, Schön, and Sohn [70], with a few minor alterations to clarify intermediate steps and to express results in the form we use to model spin-resolved antidot transport in Chapter 5.

2.3.1 Coulomb blockade

We begin with a brief review of Coulomb blockade and the interpretation of non-linear conductance measurements of quantum dots in the constant-interaction model. The electrostatics of the system may be represented by an equivalent capacitor network,[1] as shown for example in Fig. 2.3. From the capacitor network we can relate the charge Q on the dot with its potential ϕ through the equation

$$Q = C_{\mathrm{S}}(\phi - V_{\mathrm{S}}) + C_{\mathrm{D}}(\phi - V_{\mathrm{D}}) + C_{\mathrm{G}}(\phi - V_{\mathrm{G}}) + C_{\mathrm{R}}\phi, \tag{2.59}$$

such that

$$\phi = \frac{Q}{C} + \phi_{\mathrm{ext}}, \tag{2.60}$$

[1] Tunnel couplings between the dot and the leads may more realistically be modeled as a capacitor and resistor connected in parallel, to account for the finite current which flows through these connections.

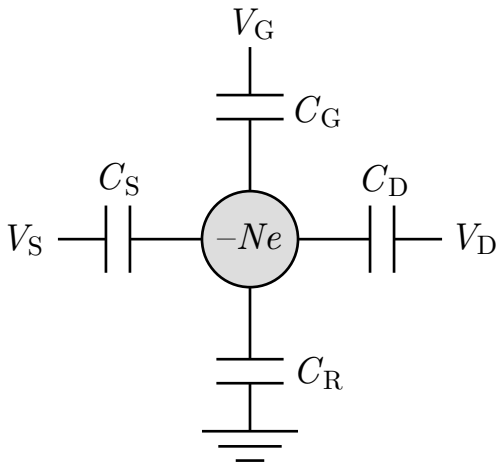

Figure 2.3: Equivalent capacitor network for transport through a quantum dot. The charge on the dot is quantised by the electron charge, with $Q = -Ne$, and the potential ϕ is determined by the capacitive couplings (C_S, C_D, C_G) to the source, drain and gate voltages (V_S, V_D, V_G), respectively. We model any remaining coupling to other elements of the device which have fixed voltages as an additional capacitance C_R to ground potential.

where $C = C_S + C_D + C_G + C_R$ is the total capacitance and

$$\phi_{ext} = \frac{C_S V_S + C_D V_D + C_G V_G}{C} \tag{2.61}$$

is the potential due to the external voltages. The dot charge Q is quantised by the electron charge, and when the dot contains N electrons, its energy is

$$U(N) = \int_0^{-Ne} \phi \, dQ = \frac{(Ne)^2}{2C} - Ne\phi_{ext}. \tag{2.62}$$

On the other hand, ϕ_{ext} may be varied continuously through the external voltages, with a corresponding effective charge

$$Q_{ext} = C\phi_{ext} = +en_G. \tag{2.63}$$

Therefore, Eq. (2.62) may be rewritten as

$$U(N) = E_{\mathrm{C}}(N - n_{\mathrm{G}})^2 + n_{\mathrm{G}}^2 E_{\mathrm{C}}, \tag{2.64}$$

where $E_{\mathrm{C}} = \frac{e^2}{2C}$ is the charging energy.

In the constant-interaction model, we assume that the effect of the electron charge is entirely described through the electrostatic energy of Eq. (2.64), and we can simply add to this the single-particle eigenenergies ε_i of the dot. A general N-electron state is characterised by a set of occupation numbers $\{n_i\}$, where $n_i = 0$ or 1 due to Fermi exclusion and $\sum n_i = N$, such that

$$U(\{n_i\}) = E_{\mathrm{C}}(N - n_{\mathrm{G}})^2 + n_{\mathrm{G}}^2 E_{\mathrm{C}} + \sum_i n_i \varepsilon_i. \tag{2.65}$$

Often we are concerned only with transitions between ground states, in which only states $i = 1, 2, \ldots, N$ are filled, which have energy

$$U_0(N) = E_{\mathrm{C}}(N - n_{\mathrm{G}})^2 + n_{\mathrm{G}}^2 E_{\mathrm{C}} + \sum_{i=1}^{N} \varepsilon_i. \tag{2.66}$$

Tunneling between the dot and the leads conserves energy, so we need to compare the chemical potentials of the leads, e.g., $\mu_{\mathrm{D}} = -eV_{\mathrm{D}}$, with that of the dot. For transitions between ground states, the dot chemical potential is given by

$$\mu_{\mathrm{dot}}(N) = U(N+1) - U(N) = 2E_{\mathrm{C}}(N - n_{\mathrm{G}}) + E_{\mathrm{C}} + \varepsilon_{N+1}. \tag{2.67}$$

Transport requires an occupied state in the source and an unoccupied state in the drain (or vice versa) with $\mu_{\mathrm{S}} = \mu_{\mathrm{D}} = \mu_{\mathrm{dot}}$, and so at zero bias transport only occurs for $\mu_{\mathrm{dot}} \approx 0$ within a few kT. Outside this regime, transport is forbidden due to the 'Coulomb blockade' resulting from the quantisation of electronic charge. The dependence of n_{G} on the gate voltage V_{G} therefore leads to a set of conductance peaks as a function of V_{G}, as the chemical potentials of subsequent transitions align with those of the leads.

If we vary the source and/or drain potentials, current can flow through the dot when $\mu_{\mathrm{dot}}(N)$ lies in the transport window defined by μ_{S} and μ_{D}. In the plane of V_{G} and $V_{\mathrm{DS}} = V_{\mathrm{D}} - V_{\mathrm{S}}$, this produces a pattern of 'Coulomb diamonds' within which transport is blockaded, as shown in Fig. 2.4. By analysing the slopes and spacings of the various lines in such data, we can extract the values of the capacitances and, more importantly,

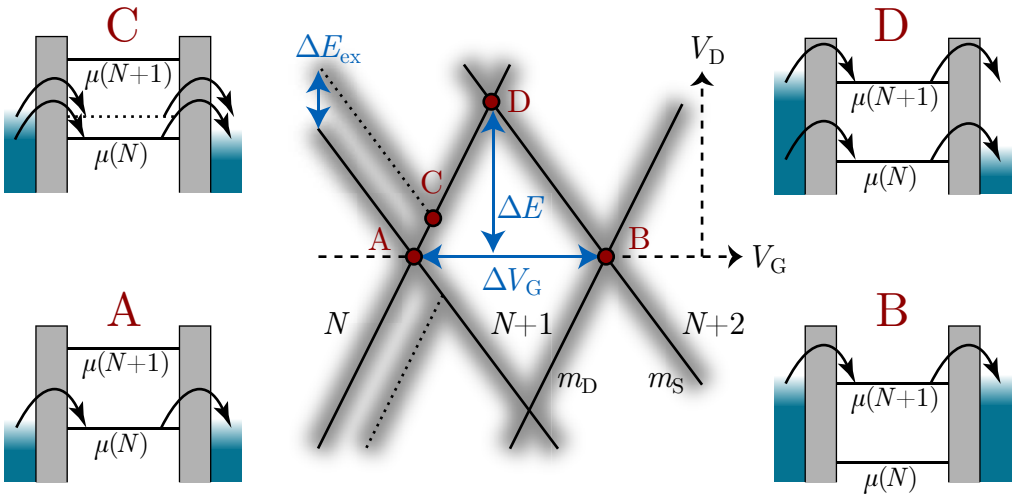

Figure 2.4: Schematic diagram of non-linear conductance through a quantum dot, as a function of V_G and V_{DS} (with bias applied to the drain contact). Transport occurs when the chemical potential for a dot transition sits in the 'window' between $\mu_S = 0$ and $\mu_D = -eV_D$. Peaks in conductance are observed when one of the dot chemical potentials passes either μ_S or μ_D, with a broadening proportional to the electron temperature in the leads. Inside the diamond, transport is forbidden due to Coulomb blockade, and the number of electrons remains fixed at $N+1$ as shown. The capacitances of the system and energy scales of the dot may be extracted from such plots as explained in the text, by measuring the slopes (m_S, m_D) of the source and drain lines, and the spacings of peaks in either gate voltage or bias, which is proportional to energy through $\Delta E = -e\Delta V_D$. The $N \leftrightarrow N+1$ excited state drawn as a dotted line and shown in the transport diagram labeled 'C' corresponds to electrons tunneling through the same orbital state as the ground-state $N+1 \leftrightarrow N+2$ transition, but without the charging energy E_C associated with adding the $N+2^{nd}$ electron to the dot. Identification of such lines allows us to separate the charging and single-particle contributions to the addition spectrum.

the 'lever-arm' scaling factor

$$\alpha_{\mathrm{G}} = \frac{\partial \phi_{\mathrm{ext}}}{\partial V_{\mathrm{G}}} = \frac{C_{\mathrm{D}}}{C}, \tag{2.68}$$

which allows us to convert adjustments of V_{D} into changes in μ_{dot}. This factor is determined by the dimensions of the Coulomb diamonds, as shown in Fig. 2.4, as the ratio of the spacing in V_{G} between subsequent peaks and the value of V_{DS} at which they intersect,

$$\alpha_{\mathrm{G}} = \frac{\Delta V_{\mathrm{G}}}{\Delta V_{\mathrm{DS}}}. \tag{2.69}$$

Assuming that bias is applied only to the drain contact,[1] such that $V_{\mathrm{S}} = 0$ always, the slopes of the 'source lines' ($\mu_{\mathrm{dot}} = \mu_{\mathrm{S}} = 0$) and 'drain lines' ($\mu_{\mathrm{dot}} = \mu_{\mathrm{D}} = -eV_{\mathrm{D}}$) are given by

$$m_{\mathrm{S}} = -\frac{\alpha_{\mathrm{G}}}{\alpha_{\mathrm{D}}} = -\frac{C_{\mathrm{G}}}{C_{\mathrm{D}}} \tag{2.70a}$$

$$m_{\mathrm{D}} = \frac{\alpha_{\mathrm{G}}}{1-\alpha_{\mathrm{D}}} = \frac{C_{\mathrm{G}}}{C-C_{\mathrm{D}}}, \tag{2.70b}$$

where $\alpha_{\mathrm{D}} = \partial \phi_{\mathrm{ext}} / \partial V_{\mathrm{D}}$ is the lever arm factor for changes in V_{D}.

The addition energy ΔE shown in Fig. 2.4 contains both electrostatic and quantum-mechanical contributions,

$$\begin{aligned} \Delta E &= \mu_{\mathrm{dot}}(N+1) - \mu_{\mathrm{dot}}(N) \\ &= 2E_{\mathrm{C}} + \varepsilon_{N+1} - \varepsilon_N. \end{aligned} \tag{2.71}$$

The quantum contribution $\Delta E_{\mathrm{ex}} = \varepsilon_{N+1} - \varepsilon_N$ is often observable as the first of several extra lines which appear outside the Coulomb blockade region, as shown in Fig. 2.4. By measuring such excitations we can isolate the charging energy E_{C} from Eq. (2.71) and then solve Eqs. (2.70) for the individual capacitances C, C_{G}, and C_{D}. If we swap the source and drain contacts for additional measurements, we can extract C_{S} and C_{R} through a similar analysis.

2.3.2 Master equation approach

In this section we consider a quantum-mechanical description of the dot in terms of a set of 'fermionic' states $|s\rangle = |\{n_{\ell,\sigma}\}\rangle$, labeled by occupation numbers $n_{\ell,\sigma} = 0, 1$ for the state with orbital and spin quantum numbers ℓ and σ, respectively. These are suitable

[1] We choose this convention since, in our experiments, we typically bias the input offset of the current preamplifier which acts as the drain for our device.

states when electron-electron interactions are ignored, and provide the most convenient basis for calculations, but they do not correctly reproduce the energies or degeneracies of an interacting system. We discuss this issue further and consider other choices for basis states in Chapter 5.

We split the system into three parts, such that the total Hamiltonian is $H = H_{\text{dot}} + H_{\text{res}} + H_{\text{tun}}$, representing the physics of the dot, the reservoirs, and the tunneling between them. The Hamiltonian for the dot is

$$H_{\text{dot}} = \sum_s E_s |s\rangle\langle s|, \tag{2.72}$$

where, within the constant interaction model,

$$E_s = \sum_{\ell\sigma} \varepsilon_{\ell\sigma} n_{\ell\sigma} + E_{\text{C}}(N - n_{\text{G}})^2, \tag{2.73}$$

as in Eq. (2.65).[1] Similarly, the Hamiltonians describing the reservoirs and tunneling to and from the dot are given in second-quantised form by

$$H_{\text{res}} = \sum_{r=\text{S,D}} \left[\sum_{k\sigma} \varepsilon_{k\sigma r} a^\dagger_{k\sigma r} a_{k\sigma r} + \mu_r \hat{n}_r \right], \tag{2.74a}$$

$$H_{\text{tun}} = \sum_{r=\text{S,D}} \left[\sum_{k\ell\sigma} T^r_{k\ell\sigma} a^\dagger_{k\sigma r} a_{\ell\sigma} + \text{h.c.} \right], \tag{2.74b}$$

where the leads (assumed to be non-interacting) are labeled by reservoir r, wave vector k, and spin σ. The operators $a_{k\sigma r}$ and $a_{\ell\sigma}$ annihilate particles in the lead states $|k\sigma\rangle$ of reservoir r and dot states $|\ell\sigma\rangle$, respectively, and $\hat{n}_r$ is the particle-number operator for lead r, with chemical potential $\mu_r = -eV_r$.

Assuming the couplings to the leads $T^r_{k\ell\sigma}$ are small relative to kT, such that thermal fluctuations dominate over quantum-mechanical fluctuations, we can use Fermi's golden rule to write the tunneling rates for the transition between dot states $s' \to s$ and reservoir states $\chi' \to \chi$ to first order as

$$W^p_{s'\chi'\to s\chi} \simeq \frac{2\pi}{\hbar} \left| \langle \chi s | H_{\text{tun}} | \chi' s' \rangle \right|^2 \delta(E_s - E_{s'} + E_\chi - E_{\chi'} + p\mu_r), \tag{2.75}$$

where $p = \pm 1$ denotes the change of electron number on the dot, and E_χ is the energy of the reservoir state χ. We are interested in the rates between individual dot states which

[1] We have dropped the N-independent term $n_{\text{G}}^2 E_{\text{C}}$ from Eq. (2.65) since it affects all states equally and hence does not appear in the chemical potential.

are obtained by summing out the contributions from all lead states,

$$\gamma^{p}_{s'\to s} = \sum_{\substack{\chi\chi' \\ N(\chi')=N(\chi)+p}} W^{p}_{s'\chi'\to s\chi}\rho^{\mathrm{eq}}_{\mathrm{res}}(\chi'), \tag{2.76}$$

where $\rho^{\mathrm{eq}}_{\mathrm{res}}$ is the equilibrium density of states in the reservoirs. This calculation is outlined in Appendix B, from which we obtain the result

$$\gamma^{+}_{r,s'\to s} = \sum_{\ell\ell'\sigma} \Gamma^{r}_{\ell\ell'\sigma}(E_s - E_{s'})\langle s|a^{\dagger}_{\ell\sigma}|s'\rangle\langle s'|a_{\ell'\sigma}|s\rangle f_r(E_s - E_{s'}), \tag{2.77a}$$

$$\gamma^{-}_{r,s'\to s} = \sum_{\ell\ell'\sigma} \Gamma^{r}_{\ell\ell'\sigma}(E_{s'} - E_s)\langle s|a_{\ell\sigma}|s'\rangle\langle s'|a^{\dagger}_{\ell'\sigma}|s\rangle\Big[1 - f_r(E_{s'} - E_s)\Big], \tag{2.77b}$$

where the spectral function is defined as

$$\Gamma^{r}_{\ell\ell'\sigma}(E) = \frac{2\pi}{\hbar}\sum_{k} T^{r}_{k\ell\sigma}T^{r*}_{k\ell'\sigma}\delta(E - \varepsilon_{k\sigma r}), \tag{2.78}$$

and

$$f_r(E) = \frac{1}{1 + e^{(E-\mu_r)/kT}} \tag{2.79}$$

are the Fermi functions which describe the occupation of states in the reservoirs.

With the total transition rate given by[1]

$$\gamma_{s's} = \sum_{r=\mathrm{S,D}} (\gamma^{+}_{r,s'\to s} + \gamma^{-}_{r,s'\to s}), \tag{2.80}$$

we proceed to construct the master equation to solve for the equilibrium occupation probabilities $P(s)$. In equilibrium, the total evolution 'out' of state s must equal the total evolution 'in,' i.e.,

$$0 = \sum_{s}\big[\gamma_{s's}P(s') - \gamma_{ss'}P(s)\big]. \tag{2.81}$$

By combining Eq. (2.81) with the normalisation condition $\sum_i^n P(s_i) = 1$, for n available

[1] Note that at least one of the terms in Eq. (2.80) will be zero due to selection rules (the matrix elements in Eqs. (2.77)).

states, we obtain the master equation in matrix form:

$$\begin{pmatrix} \sum_i \gamma_{s_i s_1} & -\gamma_{s_1 s_2} & \cdots & -\gamma_{s_1 s_n} \\ -\gamma_{s_2 s_1} & \sum_i \gamma_{s_i s_2} & \cdots & -\gamma_{s_2 s_n} \\ \vdots & \vdots & \ddots & \vdots \\ -\gamma_{s_n s_1} & -\gamma_{s_N s_2} & \cdots & \sum_i \gamma s_i s_n \\ 1 & 1 & \cdots & 1 \end{pmatrix} \begin{pmatrix} P(s_1) \\ P(s_2) \\ \vdots \\ P(s_n) \end{pmatrix} = \begin{pmatrix} 0 \\ 0 \\ \vdots \\ 0 \\ 1 \end{pmatrix}. \tag{2.82}$$

Once the master equation has been solved for the probabilities $P(s)$, we can compute the current flowing out of each lead from the expression

$$\begin{aligned} I_r &= e \sum_{ss'} [\gamma^+_{r,s'\to s} P(s') - \gamma^-_{r,s\to s'} P(s)] \\ &= e \sum_{ss'} [\gamma^+_{r,s'\to s} - \gamma^-_{r,s'\to s}] P(s'), \end{aligned} \tag{2.83}$$

where we have used Eq. (2.81) to simplify the second term. Using the relation

$$\sum_r [\gamma^+_{r,s'\to s} - \gamma^-_{r,s'\to s}] = \Big(N(s) - N(s')\Big)\gamma_{s's}, \tag{2.84}$$

it is straightforward to show that $\sum_r I_r = 0$, i.e. that the total current is conserved.

We can further simplify the expression for the current by noting that the rates satisfy the 'detailed balance' condition[1]

$$\frac{\gamma^-_{r,s\to s'}}{\gamma^+_{r,s'\to s}} = \frac{1 - f_r(\mu_{ss'})}{f_r(\mu_{ss'})} = e^{(\mu_{\rm dot} - \mu_r)/kT}, \tag{2.85}$$

where $\mu_{ss'} = E_s - E_{s'}$ is the chemical potential for the dot transition. In terms of the quantity

$$\gamma^\Sigma_{r,ss'} = \gamma^+_{r,s'\to s} + \gamma^-_{r,s\to s'}, \tag{2.86}$$

Eq. (2.85) gives

$$\gamma^+_{r,s'\to s} = \gamma^\Sigma_{r,ss'} f_r(\mu_{ss'}), \tag{2.87a}$$

$$\gamma^-_{r,s\to s'} = \gamma^\Sigma_{r,ss'} [1 - f_r(\mu_{ss'})], \tag{2.87b}$$

and by comparison with Eqs. (2.77) we see that $\gamma^\Sigma_{r,ss'}$ is independent of the reservoir chemical potentials μ_r. If the states $|s\rangle$ do in fact represent non-interacting configurations

[1] From this point we adopt the convention $N(s) = N(s') + 1$.

of single-particle orbital states, then the matrix elements in Eqs. (2.77) simplify through

$$\langle s|a^\dagger_{\ell\sigma}|s'\rangle\langle s'|a_{\ell'\sigma}|s\rangle = \delta_{\ell\ell'}\big|\langle s|a^\dagger_{\ell\sigma}|s'\rangle\big|^2, \tag{2.88}$$

and we obtain

$$\gamma^\Sigma_{r,ss'} = \sum_{\ell\sigma}\Gamma^r_{\ell\ell\sigma}(\mu_{ss'})\big|\langle s|a^\dagger_{\ell\sigma}|s'\rangle\big|^2. \tag{2.89}$$

In general the tunnel couplings $\Gamma^r_{\ell\sigma}(\mu_{ss'})$ may depend on the dot states $|\ell\sigma\rangle$ and on the transport chemical potential $\mu_{ss'}$. In Chapter 5 we consider in detail the case of spin-dependent tunnel barriers, but for now we drop the dependence on $|\ell\sigma\rangle$ to write Eq. (2.83) in the form

$$I_r = e\sum_{ss'}\Gamma_r(\mu_{ss'})M_{ss'}\Big[f_r(\mu_{ss'})P(s') - (1-f_r(\mu_{ss'}))P(s)\Big], \tag{2.90}$$

where

$$M_{ss'} = \sum_{\ell\sigma}\big|\langle s|a^\dagger_{\ell\sigma}|s'\rangle\big|^2 \tag{2.91}$$

represents the selection rules for transitions between states $s' \leftrightarrow s$. Using current conservation we can derive the relation

$$\sum_{ss'}M_{ss'}P(s) = \sum_{ss'r}\frac{\Gamma_r}{\Gamma}M_{ss'}\big[P(s')+P(s)\big]f_r(\mu_{ss'}), \tag{2.92}$$

where $\Gamma = \sum_r\Gamma_r$ and we have suppressed the dependence of the Γ's on $\mu_{ss'}$. We can use this relation to eliminate the term independent of f_r in Eq. (2.90) to obtain our final expression for the current out of lead r,

$$I_r = e\sum_{ss'r'}\frac{\Gamma_r\Gamma_{r'}}{\Gamma}M_{ss'}\big[P(s')+P(s)\big]\times\big[f_r(\mu_{ss'}) - f_{r'}(\mu_{ss'})\big]. \tag{2.93}$$

We use this expression to calculate the current transmitted through our antidot in the model described in Chapter 5, and compute the conductance at finite bias by

$$G(V_{\rm D}) = \frac{I(V_{\rm D}+\delta V_{\rm D}) - I(V_{\rm D}-\delta V_{\rm D})}{2\delta V_{\rm D}}, \tag{2.94}$$

which is typically a good approximation if $e\delta V_{\rm D} \lesssim kT$.

To make a connection to the linear-response theory discussed in the first two sections of this chapter, we can set $\mu_r = \mu - e\delta V_r$ and solve for the conductance coefficients defined

by

$$I_r = \sum_{r'} G_{rr'}(\delta V_r - \delta V_{r'}). \tag{2.95}$$

This was first considered by Beenakker [68] with the well-known result

$$G_{rr'} = -e^2 \sum_{ss'} \frac{\Gamma_r \Gamma_{r'}}{\Gamma} M_{ss'} \left[P(s) + P(s')\right] f'_\mu(\mu_{ss'}). \tag{2.96}$$

In the special case of sequential tunneling through a single level, we have only two states to consider (occupied and unoccupied), which satisfy $P(1) + P(2) = 1$, and so the conductance through the dot is given by

$$G_{\mathrm{SD}} = -2e^2 \left(\frac{\Gamma_{\mathrm{S}} \Gamma_{\mathrm{D}}}{\Gamma_{\mathrm{S}} + \Gamma_{\mathrm{D}}} \right) f'_\mu(\mu_{\mathrm{dot}}). \tag{2.97}$$

If the tunnel couplings are energy-independent, the line-shape of this resonance as a function of μ_{dot} will be determined by the derivative of the Fermi function,

$$-f'_\mu(\mu_{\mathrm{dot}}) = \frac{1}{4kT} \cosh^{-2}\left(\frac{\mu_{\mathrm{dot}} - \mu}{2kT} \right). \tag{2.98}$$

By comparing Eq. (2.97) with Eq. (2.51) on page 42, we can also identify the transmission coefficient of this single level within the Landauer-Büttiker formalism, given by

$$T(\varepsilon) = h\Gamma_{\mathrm{eff}} \delta(\varepsilon - \mu_{\mathrm{dot}}), \tag{2.99}$$

where

$$\Gamma_{\mathrm{eff}} = \frac{2\Gamma_{\mathrm{S}} \Gamma_{\mathrm{D}}}{\Gamma_{\mathrm{S}} + \Gamma_{\mathrm{D}}} \tag{2.100}$$

is the effective tunnel coupling.

Chapter 3

Geometrical Effects on Single-Particle Excitation Energies

The precise role of electron-electron interactions in antidot transport experiments has remained elusive. Although the Coulomb energy scale $(e^2/4\pi\epsilon\epsilon_0)n_e^{1/2}$ dominates all other relevant energies in a typical antidot device with electron density $n_e \approx 1\text{–}3 \times 10^{11}$ cm^{-2}, we find that many of the experimental observations, particularly at low magnetic fields ($B \lesssim 2$ T), may be fully understood through the non-interacting single-particle (SP) picture described in §1.1. This is presumably due to the nature of the Fermi liquid which constitutes the two-dimensional electron system (2DES), in which the quasiparticle excitations are essentially equivalent to free electrons. At higher fields this picture no longer seems to suffice, since observations of 'double-frequency' Aharonov-Bohm oscillations [17, 71] and Kondo-like effects [72] have no straightforward interpretation within the SP model.

Michael et al. [23, 73] performed antidot transport experiments at intermediate fields ($B \approx 1\text{–}2$ T) in an attempt to clarify the nature of the transition away from non-interacting physics. They noticed several interesting effects, but chief among them was an observed 'softening' of the single-particle orbital energy spacing ΔE_{SP} at higher magnetic fields. They suggested that this observation might indicate the breakdown of the SP model in favour of an interacting picture of alternating compressible and incompressible strips, in which the orbital excitation energy would be suppressed. This compressible-region (CR) model has been proposed to explain experimental observations at higher fields [18, 20], but the details of its emergence from the SP-like physics at

lower fields has not been well-understood. There have also been disagreements within the community concerning the implications of experiments in this regime [18, 74–76]. Despite the observed reduction in ΔE_{SP}, several other features of the experiments by Michael et al. seem to be inconsistent with the CR picture. For example, it is not clear that well-defined excitation energies should be observable at all in a CR picture, in which a 'band' of partially-occupied states is available for transport near the Fermi energy. In this chapter we reconsider the observations of Michael et al. within a non-interacting model, and we find an explanation for the suppression of ΔE_{SP} by taking into account a realistic geometry for the full antidot device, including the split-gate within which it is embedded.

This conclusion does not rule out the formation of CRs at high fields, or the importance of interactions with regards to some of the more subtle effects observed in the intermediate-B regime. In Chapters 4 and 5 of this thesis we discuss several of these observations in more detail, and we propose a model for $\nu_{\mathrm{AD}} = 2$ antidots in the low- to intermediate-B regime in terms of a 'maximum density droplet' of holes in the lowest Landau level (LLL), in which interactions influence many aspects of the antidot spin-structure through exchange effects, while preserving the SP-like excitations we observe in non-linear transport measurements. The results of this chapter therefore serve as an example of the flexibility of non-interacting physics and the importance of a full consideration of device geometry for precise comparisons with experimental measurements. Clearly, when one is looking for evidence of new physics based on the disparity between measurements and the predictions of an accepted model, it is important to carefully consider whether certain features are completely incompatible with the model at hand, or if they could be explained through minor alterations.

3.1 Background and motivation

The CR model of antidot transport is based on the self-consistent model of quantum Hall edge-modes due to Chklovskii, Shklovskii, and Glazman [21], as depicted in Fig. 3.1. In order to avoid the large Coulomb-energy cost associated with the abrupt change in electron density at the antidot edge which is predicted by the SP model, the spin-split LLL could rearrange as shown in the right-hand side of Fig. 3.1. The orbital states in each CR are partially occupied, such that they screen the antidot potential and allow n_e to vary smoothly between LLs (n_e changes by eB/h in each CR). This ability of CRs to screen electric charge results in experimentally observable effects. In a similar manner to a set of concentric cylinders acting as a capacitor, the outer CR, composed of the $\nu = 2$

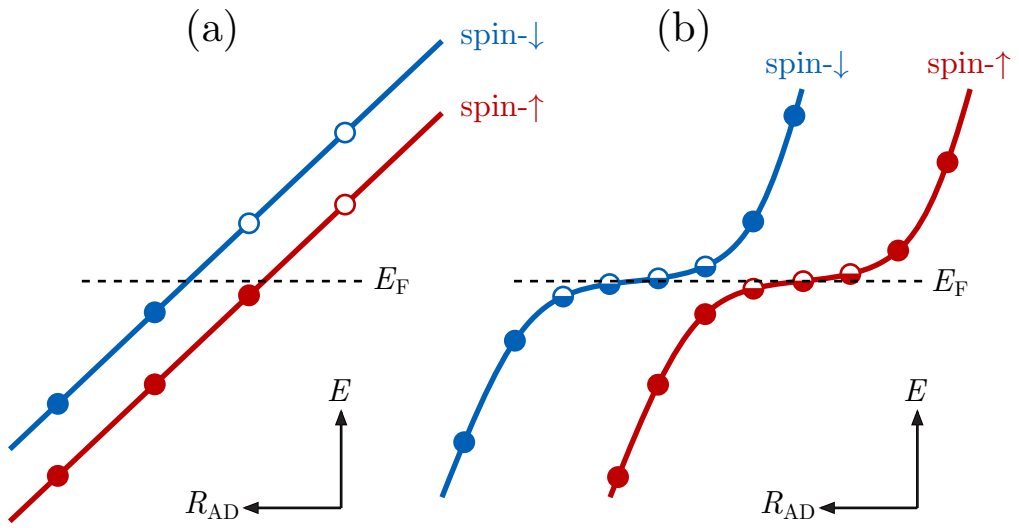

Figure 3.1: Schematic of antidot orbital energy-levels within the LLL for the SP model (a) and in a self-consistent model including compressible regions (b). The CRs consist of partially-occupied orbitals which screen the background antidot potential, separated by incompressible regions in which the self-consistent potential varies rapidly between LLs.

(spin-↓) electrons, is able to screen the charge which accumulates in the inner $\nu = 1$ (spin-↑) states. Transport through the antidot then occurs entirely through the spin-↓ CR with the resonance condition $\mu_\downarrow = 0$, determined the by gate- and field-dependent chemical potential

$$\mu_\downarrow(N_\uparrow, N_\downarrow) = E(N_\uparrow, N_\downarrow + 1) - E(N_\uparrow, N_\downarrow), \tag{3.1}$$

where $E(N_\uparrow, N_\downarrow)$ is the configuration energy of an antidot containing $N_\uparrow$ and $N_\downarrow$ particles in the spin-↑ and spin-↓ states, respectively. Such a system may be naturally modeled as a classical capacitor network, and it is straightforward to show that strong coupling between the two rings results in periodic transport resonances for the outer ring at twice the Aharonov-Bohm frequency, in agreement with experimental observations at high fields [20]. Kondo resonances in antidots may also be explained through the capacitive model, as a second-order transport process which occurs at $\mu^{\pm}_{SF} = 0$, where

$$\mu^{\pm}_{SF} = E(N_\uparrow \pm 1, N_\downarrow \mp 1) - E(N_\uparrow, N_\downarrow), \tag{3.2}$$

but this requires nearly equal antidot-lead couplings for both spin-↑ and spin-↓ tunneling, which seems unlikely given the spatial separation of CRs in the self-consistent model. The Kondo effect also emerges naturally from the microscopic model of antidot maximum density droplets [44, 45], and it is probably that regime in which it is most relevant. Experimentally, we find that Kondo resonances disappear as B increases, leaving behind pure double-frequency oscillations; this may reflect the breakdown of the maximum density droplet and the separation of spins into separate CRs.

As mentioned above, the proposal of a self-consistent antidot model including CRs has provoked some disagreement within the transport community. Karakurt et al. [74] made careful measurements of the temperature dependence of individual antidot resonances, and concluded that they were consistent with a model of thermally-broadened sequential transport through an individual quantum state. Noting that the temperature dependence of charging-dominated transport through a uniform continuum of states would be quite different (temperature independent, in fact), they concluded that CRs were absent in their device. Since then it has been pointed out [75] that the density of states for a CR is highly non-uniform, being strongly peaked near the Fermi energy, and thus that the temperature dependence of transport resonances would be similar to that of a single state. At present, exactly what measurement could constitute an irrefutable proof or disproof for the presence of CRs in antidots is still an open question. On the theoretical side, Ihnatsenka and Zozoulenko have performed density functional theory calculations, including spin, to investigate the self-consistent quantum structure of antidots [62]. They found that, for an antidot of radius 200 nm, a CR forms only for the outer (spin-↓) state at fields above ≈ 4 T. It is worth pointing out that an outer CR is all that is necessary within the capacitive model for double-frequency oscillations, as long as it may efficiently screen the spin-↑ charge which accumulates within it.

In their measurements of an antidot at intermediate fields, Michael et al. [73] were the first to obtain clear examples of antidot *excitation spectra* from non-linear transport measurements. Such excitations are routinely observed in quantum dot measurements as a function of source-drain bias, allowing for the identification of quantum numbers and comparisons with theoretical calculations [e.g., 77], but have been elusive in antidot measurements. On the whole, the observed antidot excitation spectra offer further support for the SP model, reflecting a pair of excitation energies which are readily identified with the Zeeman energy E_Z and the SP spacing between adjacent orbital levels, ΔE_{SP}. Charging effects are incorporated within the constant-interaction model [78], and the charging energy E_C may also be extracted from the non-linear transport measurements.

In the perturbative limit discussed in §1.2.3, where the antidot potential varies on

a length scale much larger than the magnetic length $\ell_{\mathrm{B}} = \sqrt{\hbar/eB}$, we can use the free-particle LLL eigenstates as approximate antidot wave functions. The radial positions of these states are governed by the flux-quantisation condition $\pi\langle r^2\rangle B = mh/e$, where m is an integer, and so we can approximate the energy-separation between adjacent states as

$$\Delta E_{\mathrm{SP}} \simeq \Delta r \left.\frac{dU}{dr}\right|_{R_{\mathrm{AD}}} \simeq \left(\frac{\hbar}{eBR_{\mathrm{AD}}}\right) \left.\frac{dU}{dr}\right|_{R_{\mathrm{AD}}}, \tag{3.3}$$

in terms of the antidot potential $U(r)$ and the change Δr required to add one flux quantum h/e to the loop. The antidot radius R_{AD} is determined by the antidot gate potential and the electron density, so we expect it to be roughly independent of B. Since the potential slope at R_{AD} is also independent of B, we therefore expect to observe $\Delta E_{\mathrm{SP}} \propto 1/B$. Michael et al. observed a significant suppression of ΔE_{SP} below the expected $1/B$ dependence at higher fields, and they suggested that this could imply a reorganisation of states into a CR. Here we propose an alternate explanation, namely that the presence of the potential due to the split-gate in which the antidot is embedded breaks the circular symmetry of the problem, and can lead to a significant reduction of ΔE_{SP} for states near the saddle point of each constriction. We were guided to this theory by a realisation that the observed suppression of ΔE_{SP} seemed to coincide more with the gate-dependent position of the high-B end of the $\nu_{\mathrm{AD}} = 2$ plateau, at which states begin to be reflected across the antidot constrictions, than with any fixed value of B.

The idea may be easily understood from a consideration of the antidot states shown in Fig. 3.2. Assuming that the states are well-approximated by 'loops' of width ℓ_{B}, with contours determined by the flux-quantisation condition, we observe that the 'bulging' of states near saddle point in each constriction accounts for a relatively large amount of additional enclosed area. This results in a reduced spatial separation around the remainder of the antidot, and assuming a roughly linear potential gradient in these regions, requires ΔE_{SP} to be much less than Eq. (3.3) predicts. We can generalise Eq. (3.3) to account for this asymmetry, by computing ΔE_{SP} from the contours obtained for a given antidot potential at the Fermi energy E_{F}:

$$\Delta E_{\mathrm{SP}} = -\frac{h}{eB}\left[\int_0^{2\pi}\left(\frac{dU}{dr}\right)^{-1}_{(\mathcal{C},\theta)} \mathcal{C}(\theta)d\theta\right]^{-1}, \tag{3.4}$$

where $\mathcal{C}(\theta)$ is the contour defined by $U_{\mathrm{eff}}(\mathcal{C},\theta) = E_{\mathrm{F}}$, using the effective potential

$$U_{\mathrm{eff}} = U(r,\theta) + E_{\mathrm{cyc}} + E_{\mathrm{Z}}, \tag{3.5}$$

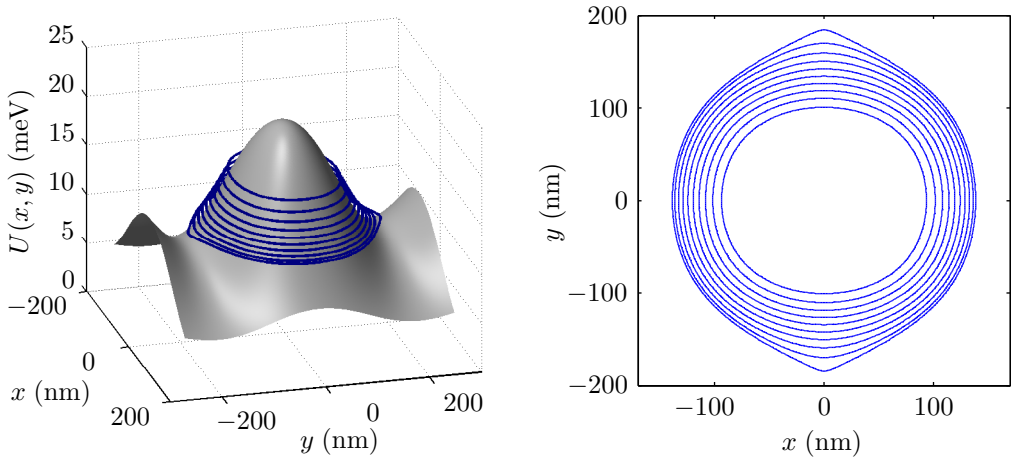

Figure 3.2: Left panel — Bare potential created by an antidot at the centre of a split gate (computed as in [79]), with contours computed according to Eq. (3.4) at $B = 0.8$ T. Right panel — top view of the contours, showing the 'bulging' effect for states close to the saddle point, which results in a reduced energy spacing.

where $E_{\mathrm{cyc}} = \hbar\omega_{\mathrm{C}}/2$ and $E_{\mathrm{Z}} = g\mu_{\mathrm{B}}B\sigma$ are the cyclotron and Zeeman energies for the LLL states in the constrictions (with spin $\sigma = \pm\frac{1}{2}$), as described in §1.1 of this thesis. In the following discussion, we find that this model is highly successful at describing the observed B-dependence of ΔE_{SP}, and we will justify the flux-quantisation assumption on which it is based by comparing its predictions with a calculation of the full non-interacting Green's function for a realistic 'antidot + split gate' geometry.

3.2 Results

The measurements of ΔE_{SP} versus B shown in panels (a) and (b) of Fig. 3.3 were obtained by Chris Michael, having been extracted from a series of non-linear transport measurements as described in Ref. [73]. The device consists of an AD gate 200 nm in diameter centred in a split gate of width 1 μm. Complete device details may be found in Ref. [73]. These two sets of measurements were taken at different settings of the antidot and split-gate voltages, to tune the $\nu_{\mathrm{AD}} = 2$ plateau to different values of B, and are representative of measurements taken throughout the range $B \approx 0.5$–2.5 T. It is clearly observed that ΔE_{SP} changes faster than expected with B (the dashed red lines represents best-fit functions $\propto 1/B$). Our model based on Eq. (3.4) (black curves in Fig. 3.3) performs much better. It is based on the bare potential produced by the lithographic arrangement of gates, computed as the solution to the Laplace equation at

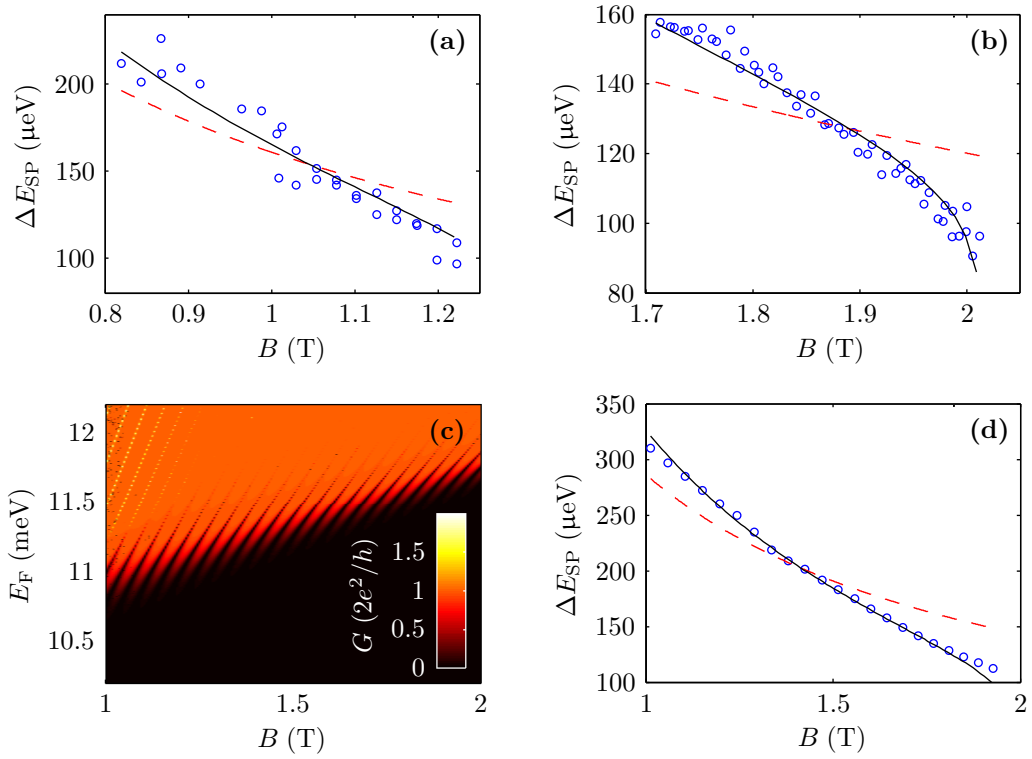

Figure 3.3: Top panels — Single-particle energy ΔE_{SP} (circles) extracted from DC-bias measurements in different ranges of magnetic field (with different gate voltages). A fit $\propto 1/B$ (dashed red curve) fails to match the data while our model (solid black curve) predicts the reduction of ΔE_{SP} at higher fields. Bottom panels — Conductance (c) in units of $2e^2/h$ as a function of B and E_{F}, calculated from the noninteracting Green's function for the antidot potential shown in Fig. 3.2, and the corresponding energy spacing (d), calculated from (c) at $E_{\mathrm{F}} = 11.7$ meV. As for the experimental data in (a) and (b), our model based on Eq. (3.4) (solid curve) accounts for the discrepancy of the calculated values of ΔE_{SP} from a $1/B$ dependence (dashed curve).

the position of the 2DES, as described in Ref. [79]. We allow for a constant screening factor to account for the ionised donor layer, but this is completely determined by the measured Aharonov-Bohm period and ΔE_{SP} at the low-B end of the plateau. We can also estimate E_{F} from the field at which the $\nu = 2$ state is depopulated in the channel (the midpoint of the transition between the $\nu_{\mathrm{AD}} = 1$ and $\nu_{\mathrm{AD}} = 2$ plateaux). The remaining parameters E_{cyc} and E_{Z} are determined solely by B, so the functions shown in Fig. 3.3 actually have no free parameters for fitting. This calculation includes no effects of tunneling in the constrictions, which results in an artificial drop to zero as the saddle point reaches E_{F} and closed orbits no longer exist.

For additional comparison with this essentially classical model, and to justify the flux-quantisation condition which leads to Eq. (3.4), we have calculated the full non-interacting Green's function for an AD + split-gate geometry using an iterative procedure [65]. The connection between the time-independent Green's function of an open geometry and the quantities measured in transport experiments is discussed in §2.2. The calculation does not include spin, but the orbital spacing ΔE_{SP} is an orbital effect, a consideration of spin is not really necessary. We note that, although the values of ΔE_{SP} may actually be slightly different for spin-↑ and spin-↓ states at the Fermi energy due to this geometric effect, the lowest-energy excitations of an antidot with total spin $S_z = \frac{1}{2}$ and $S_z = 0$ are E_{Z} and $\Delta E_{\mathrm{SP}} - E_{\mathrm{Z}}$ respectively, where ΔE_{SP} is the value for spin-↓ only, so it is a suitable approximation to consider spinless electrons in this calculation. Panel (c) of Fig. 3.3 shows the calculated antidot conductance as a function of E_{F} and B, from which we extract ΔE_{SP} as the vertical spacing between resonances along a horizontal line at constant E_{F}, as shown in Fig. 3.3d. The agreement between this calculation and our model is highly satisfactory, and since the calculation includes no effects of electron interactions, we can conclude that a self-consistent model (e.g., including CRs) is not necessary to explain these observations.

From the Green's function we can also compute the local density of states, derived in §2.2 as

$$\rho(\mathbf{x}; E) = \mp\frac{1}{\pi}\Im\left[G^{\pm}(\mathbf{x}, \mathbf{x}; E)\right]. \tag{3.6}$$

This is useful as a visualisation tool, showing the spatial structure of states near E_{F}. In Fig. 3.4, we plot the calculated local density of states at the locations of both a transmission and reflection resonance, in the left and right panels respectively. The departure from circular symmetry can be easily observed in these plots, particularly for the reflection resonance which is due to an antidot state very near to the saddle point.

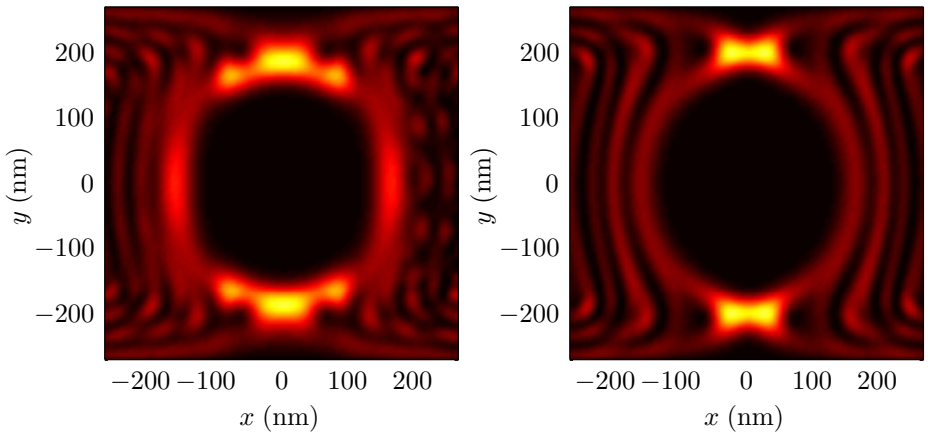

Figure 3.4: Local density of states calculated from the noninteracting Green's function for the AD shown in Fig. 3.2. Note that the transmission resonance (left panel) at low field (≈ 1 T) is more circularly symmetric than the reflection resonance (right panel) at higher field (≈ 1.5 T), which appears vertically elongated due to the 'bulging' of the SP states into the constrictions.

3.3 Conclusions

We therefore conclude that the observed suppression of ΔE_{SP} is a simple result of the potential profile in our experimental geometry, rather than a signature of a reorganisation of states into a CR. Although we know that interaction effects become essential for an understanding of AD resonances at high fields, this study demonstrates the ability of the SP model to explain relatively complicated features of the excitation spectrum of ADs in the low-field regime. An understanding of these effects is critical for the design of antidot-based applications which seek to utilise SP processes in a specific regime, or for the study of other aspects of transport which we do believe are signatures of electron-electron interactions, as discussed in Chapters 4 and 5.

Chapter 4

Spin-Resolved Transport: Signatures of Interactions

The spin structure of a quantum antidot is intimately connected to the details of the Coulomb interactions between electrons through the exchange effect which results from Pauli exclusion, as we have seen in Chapter 1. Furthermore, electron spin is generally conserved for quantum Hall (QH) transport experiments in GaAs; of the two relevant spin-mixing processes, spin-orbit coupling is relatively weak, and the hyperfine interaction requires a close degeneracy (in both energy and space) between electrons of opposite spins, which is usually absent in QH systems. The antidot SP spectrum described in Chapter 1, being composed of pure spin states, clearly imposes strict spin selection rules for tunnelling events between the antidot and the leads. Even after including interactions, the total spin projection S_z of the antidot remains a good quantum number, as long as the spin-mixing effects mentioned above are negligible, and so similar selection rules remain. We can therefore gain valuable information about the underlying structure of the antidot states by measuring the spin of the electrons involved in transport. Experimentally, this is made possible by the unique properties of QH systems in which the 'leads' of different spins actually correspond to spatially distinct QH edge modes, which we can physically separate in a device by means of quantum point contacts (QPCs). By isolating the current in each mode before and after they reach the antidot, we identify the spin of the relevant electrons. In this chapter, we describe how such measurements lead to a detailed picture of the energy spectrum at the $\nu_{\mathrm{AD}} = 2$ antidot edge, including spin. Our surprising result is that, while standard transport measurements seem broadly consistent with the non-interacting model, the observed spin-resolved transport is not. We interpret these results as the signatures of electron-electron interactions which

lead to a separation of scales for orbital and spin excitations of the many-body antidot ground state. The results are consistent with the ground state being a maximum-density-droplet (MDD) of 'holes' in the LLL, and so these measurements are of general interest as a method of experimentally probing the many-body physics of such systems.

4.1 Motivation and Previous Studies

To date, most studies of electron-electron interactions in single antidot structures have concerned the region of intermediate ($B \approx 1$–$3\,\mathrm{T}$) to high ($B \gtrsim 3\,\mathrm{T}$) magnetic field, because it is in this regime that the SP picture clearly breaks down, failing to describe even equilibrium conductance measurements. The AB reflection resonances between ν_{AD} =1–2 have received particular attention, since this is the 'simplest' regime in which to study interacting electrons of both spins.[1] At intermediate fields, extra resonances appear (in addition to the two resonances per period expected from the SP model) which have many of the features of Kondo resonances in quantum dots [43, 72]. Then, at even higher fields, these additional resonances disappear and the frequency of the oscillations doubles *exactly*, in the sense that no modulation remains at the base AB period observed at lower fields [17]. This frequency-doubling is naturally explained by a model in which Coulomb (plus exchange) interactions drive the spin-↑ and spin-↓ edges apart spatially, eventually leading to the formation of a set of concentric compressible regions similar to those believed to exist for bulk edge states [21]. The classical electrostatic interaction between the edges of opposite spin results in charging resonances at twice the AB frequency, as the outer state screens the charge accumulated in the inner ring [18]. Although there has been some disagreement about the observable properties of CRs and the fields at which they should form [74–76], it is generally accepted that a self-consistent description including electron-electron interactions is necessary to describe antidot physics at these high fields. The generalised charging model presented by Ref. [20] captures most of these features well, and is also sufficient to explain the pattern of Kondo resonances observed at intermediate fields. Aharonov-Bohm 'subperiods' have also been observed in large quantum dots, and have been explained through similar arguments based on charging-dominated transport [80]. A recent review of both experimental observations and relevant theoretical descriptions of antidots in this regime is given by Ref. [22].

In magnetic fields below 1 T, it has been generally assumed that Coulomb interac-

[1] The transmission resonances observed above the $\nu_{\mathrm{AD}} = 2$ plateau disappear at relatively low fields, since the inter-LL spacing cannot be controlled with gate voltages as can the intra-LL distance in the constrictions, and the inter-LL tunnel couplings drop off rapidly with the decreasing magnetic length.

tions play only a minor role, contributing a charging energy to the resonance condition as in the constant interaction model described in §2.3 but otherwise leaving the SP spectrum unaltered. Equilibrium conductance measurements as a function of both gate voltages and B are well-described by this model, with even complicated lineshapes and amplitude modulation explained through a consideration of the geometry and variation of the antidot-lead tunnel couplings, as in the edge-state model of Mace et al. [16] (hereafter, the Mace-Barnes model). Recently, Michael et al. performed a series of non-linear conductance measurements in this regime, obtaining the first unambiguous examples of antidot excitation spectra [23, 73]. Especially on the $\nu_{\mathrm{AD}} = 2$ plateau, the excitation spectrum thus observed qualitatively fits the SP model, reflecting a pair of energy scales which are straightforwardly identified with the bare orbital and Zeeman energies ΔE_{SP} and E_{Z}, respectively.

The major open question, then, is the nature of the evolution of the SP antidot states at low B to a more complicated self-consistent arrangement dominated by electron-electron interactions at higher fields. It is of course possible that interactions are important throughout the entire field range, but a model including them needs to preserve the observed structure of the SP model at low fields and explain the changes which occur as B increases. Suspiciously, beyond the basic picture of SP excitations in the observations of Michael [23] are several intriguing details which do not seem consistent with non-interacting physics. We considered one of these in Chapter 3 — the observed suppression of ΔE_{SP} with increasing B — and showed that a realistic consideration of the antidot geometry is sufficient to explain it within the SP model. Still, several other puzzles remain. The 'competition' between transmission and reflection resonances at the high-B edge of the $\nu_{\mathrm{AD}} = 2$ plateau is particularly intriguing, since associated peaks and dips occasionally appear at slightly different positions and with different widths, resulting in asymmetric lineshapes in the transition region. This behaviour is clearly inconsistent with the Mace-Barnes model, in which the transmission and reflection resonances result respectively from inter- and intra-LL tunnelling through the same antidot state.[1] The behaviour of the Zeeman splitting poses another puzzle. As a function of increasing B, the spacing of peaks/dips within each pair of resonances initially increases linearly as expected within the SP picture,[2] but then appears to saturate, fluctuating about a value close to half of the full AB period before locking at exactly that value in the double-frequency regime at high field, hinting at a crossover regime between non-

[1] Similar features were reported at the analogous position on the $\nu_{\mathrm{AD}} = 1$ plateau, which is particularly surprising since the antidot states (and transport electrons) should be fully spin-polarised.

[2] The slope of this increase, however, reflects a somewhat enhanced value for the Landé g-factor of $|g| \approx 0.6$–0.7 compared to the bulk GaAs value of $|g| = 0.44$ [73].

interacting and self-consistent behaviour.

Most of the open questions described above concern the rearrangement of spins in the $\nu_{\mathrm{AD}} = 2$ antidot as a function of B and the coupling of these states to the various bulk edge modes which convey the transport electrons. Information about the spin(s) involved in each resonance in this regime is therefore highly desirable, which we present in this Chapter through a set of spin-resolved transport experiments. Spin-resolved experiments have been performed before on antidots, as pioneered by Kataoka et al. [19], but they were limited to the high-B regime by the equilibration between edge modes which prevents selective injection/detection at lower fields. We circumvented this restriction through a careful selection of device parameters as described in the next section. Besides the desire for a more complete understanding of electron interactions in antidot systems, we were motivated to perform spin-selective measurements in the low-B regime by the proposal [25] to use a single antidot as a spin filter, or a system of two antidots in series as a 'spin switch,' in which a current of either spin polarisation can be turned on and off at will through minute adjustments of the antidot gate voltages. The proposal relies essentially on the Mace-Barnes picture of reflection resonances in SP antidots, which we have found is somewhat flawed, but the concept is still feasible with transmission resonances instead, requiring only an antidot operating in the SP regime with well-separated pure-spin states which serve as polarisers for the transmitted current. Such a tunable spin injector/detector could be useful as a component in larger devices which use QH edge channels for coherent electron transport.

4.2 Experimental methods

The zero-field transport mean free path of two-dimensional electrons at the Fermi energy in typical high-mobility GaAs-AlGaAs heterostructures is on the order of 10–100 μm, which is already larger than the active region of the mesoscopic devices we are considering. In the QH regime, the equilibration length for electrons traveling in edge modes is larger still, reaching ≈ 1 mm in fields of several Telsa [81, 82]. The suppression of scattering events is due to a small spatial overlap of the states — for scattering between LLs this is naturally explained by an increased spatial separation (through the LL spacing $\hbar\omega_{\mathrm{C}}$) and decreased width (the magnetic length ℓ_{B}) at higher B. The situation of spin-flip scattering within LLs is more complicated, since the Zeeman energy due to the bare g-factor is too small to separate opposite-spin states significantly,[1] but both spin-orbit and exchange effects lead to an enhanced effective g-factor for electrons at the sample

[1] In GaAs, $E_{\mathrm{Z}}/\hbar\omega_{\mathrm{C}} = gm_e^*/2m_e \approx 0.01$.

edge [82], which reduces wave function overlap sufficiently to suppress spin-flip scattering through the available mechanisms (spin-orbit and/or hyperfine coupling) mentioned in the introduction to this chapter.

Our measurements take advantage of this extraordinarily long equilibration length to selectively introduce and subsequently measure small non-equilibrium populations of electrons in the bulk edge states, allowing us to extract the individual elements of the antidot scattering probability matrix described in Chapter 2, rather than just the trace of this matrix provided by the equilibrium conductance. Our device, shown in Fig. 4.1, is largely based on the design of the original spin-selective experiments of Kataoka et al. [19], with a few minor alterations as described below to facilitate its low-field operation. QPCs are added to each of the incoming and outgoing edges, behind which are ohmic contacts which allow us to determine the current or voltage of the modes allowed through each QPC. The device can be operated in a variety of modes, depending on whether the ohmic contacts are used to source or probe currents or voltages, but all of these configurations are easily analysed within the Landauer-Büttiker formalism presented in §2.1. Throughout this chapter, we refer to the spin-resolved LLs by their 'index' as counted from the edge of the sample. Thus modes (1,2) make up the LLL, (3,4) the next LL, etc., such that all odd (even) numbered modes consist of spin-↑ (spin-↓) electrons. In treating the SP model of antidot transport, we adopt the same labelling of LLL states in the $\nu_{\mathrm{AD}} = 2$ antidot, referring to the spin-preserving transmission and reflection resonances as, $1 \leftrightarrow 3/2 \leftrightarrow 4$ and $1 \leftrightarrow 1/2 \leftrightarrow 2$ respectively.

4.2.1 Design considerations

The spin-selective experiments of Kataoka et al. [19] proved that the double-frequency $\nu_{\mathrm{AD}} = 1$–2 oscillations observed at high B are fully spin-polarised, resulting from only "$2 \leftrightarrow 2$" tunnelling across the constrictions. This is in agreement with the self-consistent model in which the Coulomb blockade is lifted for spin-↓ tunnelling twice per AB cycle due to the capacitive interaction between spatially-separated rings of opposite spin [20]. For fields below $B \approx 3\,\mathrm{T}$, however, both inter-LL and spin-flip equilibration became much more pronounced, obscuring the interpretation of the selective injection/detection measurements. In order to extend the method to lower fields, we made two major alterations to the device. First, we used a wafer[1] with a significantly reduced carrier

[1] T792 — full specifications are in Appendix A. Measurements on T792 were performed in the dark, since the device became unstable after illumination. This is in contrast to most previous antidot experiments, in which strong AB oscillations were only observed after heavy illumination. Indeed, we tested several other wafers with similar basic parameters to T792 and found unsatisfactory results in the dark.

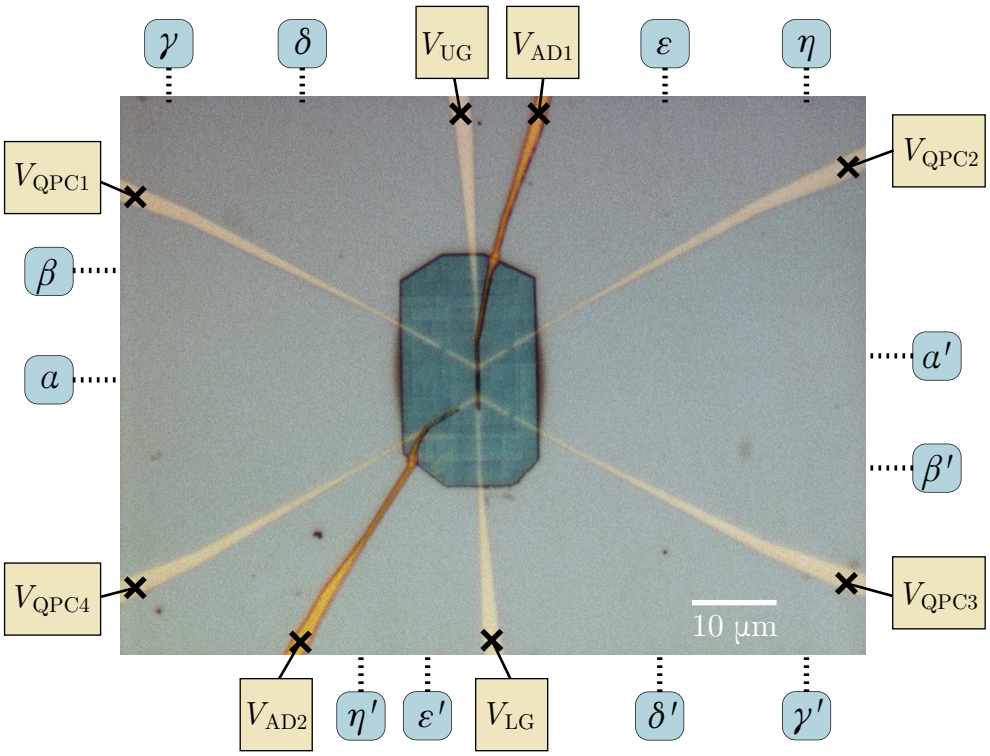

Figure 4.1: Optical microscope photograph of the device used for the spin-selective measurements in this chapter. Ohmic contacts to the 2DES are labelled by Greek letters. The first layer of metallic Schottky gates consists of the upper (UG), lower (LG), and four QPC gates, as well as isolated circular antidot gates (AD1 at the centre and AD2 in QPC4). The active region is covered by a layer of crosslinked polymer, through which metal bridging gates contact the antidots individually [83]. A larger view of the first layer alone is shown in the scanning electron micrograph of Fig. 4.5

density of $n_e = 1.1 \times 10^{11}$ cm^{-2}, compared to $n_e = 3 \times 10^{11}$ cm^{-2} in the experiments of Ref. [19]. With a reduced density, the filling factor in the bulk is lower for a given value of B, and the potential slope at the edges is shallower, causing the spacing between edge modes to be larger. The exchange effect is also stronger at lower densities [84], helping to reduce spin-flip scattering in edge transport as discussed above. Second, we redesigned the device used in Ref. [19] to eliminate the corners in the contours of the main edge between the QPCs and the central antidot, which are thought to contribute to inter-edge scattering [85, 86]. The edge contours at the Fermi energy were calculated using the `GatesCalc` program,[1] which computes the bare electrostatic potential due to the gates as the solution to Laplace's equation at the level of the 2DES. Examples of contours calculated through this method may be seen in Fig. 4.5 on page 81.

In addition to the modifications discussed above, we included a second antidot (AD2) into one of the QPCs, in the lower-left of the device as shown in Fig. 4.1. This serves a dual purpose: the two antidots in series reproduce the topology of the spin-filter proposed in Ref. [25], allowing us to explore the behaviour of such a device, and, by making AD2 lithographically smaller than the central antidot (AD1), we provide a method of exploring antidot size-effects in a single device. When necessary, we can still use AD2 as a simple QPC by applying a large negative bias to the gate QPC4, fully depleting one of the channels around the antidot. We can then use the AD2 gate to control the remaining QPC for injection/detection measurements of AD1. The antidot size plays an important role in determining the SP spacing between orbital states, which in the perturbative limit discussed in Chapter 1 is given by

$$\Delta E_{\mathrm{SP}} \simeq \left(\frac{\hbar}{eBR_{\mathrm{AD}}}\right) \left.\frac{dU}{dr}\right|_{R_{\mathrm{AD}}} . \tag{4.1}$$

Assuming that the slope of the potential at the Fermi level is relatively constant, this means that ΔE_{SP} is roughly inversely proportional to antidot size. We have also found that the antidot size has a significant effect on the inter-LL ($1 \leftrightarrow 3/2 \leftrightarrow 4$) coupling, with the transmission resonances disappearing at much lower B for smaller antidots. This is presumably related to either the reduced circumference over which this tunnelling may occur in a smaller antidot, or to the smoother deformation of the $\nu = 3{,}4$ edge contours, or both. In either case, it presents a conflicting goal in designing a spin-filter device

Unfortunately, it is still unclear what constitutes a 'good' wafer for antidot experiments, and it is often the case that a given wafer will only operate satisfactorily either in the dark or after illumination since the changes to the band structure produced by the rearrangement of donor charges is so severe.

[1] Written and maintained by Adam Thorn, available within the Semiconductor Physics Group at http://spz.sp.phy.cam.ac.uk/wiki/index.php/GatesCalc.

based on these transmission resonances, since a smaller antidot may provide a larger ΔE_{SP} and hence larger level selectivity, but may not operate at a large enough field to sustain non-equilibrium populations of edge modes. In fact, the $1\leftrightarrow3/2\leftrightarrow4$ transmission resonances we wish to enhance at the antidot are essentially the same inter-LL scattering events we want to avoid along the edges. With careful design and tuning, we have shown that this is possible in practice, but it is nonetheless a delicate balance to strike.

4.2.2 Calibration of edge equilibration

The non-equilibrium measurements we make in this chapter are easily analysed using the Landauer-Büttiker formalism presented in §2.1. In general, however, the transmission coefficients $T_{\alpha\beta}$ we measure result from a combination of scattering events at the antidot and inter-edge-mode scattering along the edges separating the injector and detector QPC from the antidot. In order to extract the contribution from antidot scattering alone, we must account for, or preferably eliminate, the edge scattering. To accomplish this, we first perform selective injection/detection measurements on the edges alone, by setting gate voltages appropriately to obtain the edge-mode topology shown schematically in Fig. 4.2. For example, to calibrate the scattering due to the full length of the top edge, we ground the voltages of the lower half of the device, including AD1, and use gates QPC1 and QPC2 to perform selective injection/detection. Or, by setting V_{BG} to a large negative value, it is possible to deplete the lower antidot constriction completely and use V_{AD1} to control the remaining QPC, in order to further isolate the scattering contributions from the injector and detector sides alone. Analogous settings allow for the calibration of the bottom edge.

Consider the experiment described in Fig. 4.2. After calibrating the injector and detector QPCs such that the gate voltages needed to produce integer filling factors f_{Inj} and f_{Det} are known for given settings of V_{CG} and B,[1] we set up the four-terminal measurement shown. The small AC excitation voltage V_0 applied to ohmic contact 2 in the injector leads to an initial population of the edge modes $\nu \leq f_{\mathrm{Inj}}$ to the chemical potential $\mu_{\mathrm{ex}} = -eV_0$, while the remaining $(\nu_{\mathrm{B}} - f_{\mathrm{Inj}})$ modes have $\mu = 0$, since they originated from ohmic 1, at ground potential. We denote the initial population by a

[1] The QPCs are calibrated with standard two- or four-terminal conductance measurements. Our device was sufficiently stable, and the integer plateaux were wide enough, that linear relationships between the QPC gate voltages needed for each filling factor and V_{CG}, B were sufficient for us to select the desired QPC filling factors accurately on demand throughout the experiment.

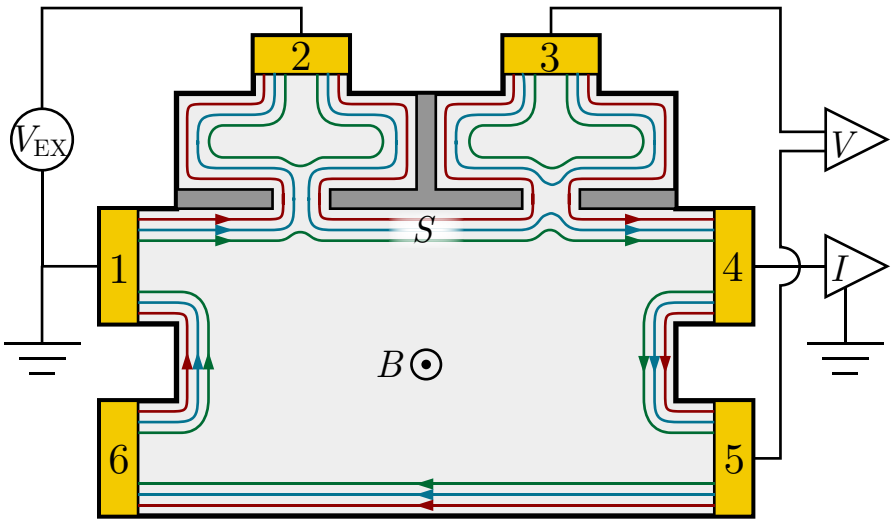

Figure 4.2: Schematic of the edge-mode network and experimental circuit for the calibration of scattering along the injector and detector edges. Contact 2 serves an the injector, and is subject to a small applied voltage $V_{\rm ex}$. The filling factor of the injector QPC determines the number of modes which are initially 'populated' with chemical potential $-eV_{\rm ex}$ along the main edge. After scattering amongst each other, a subset $\nu = 1$ to $f_{\rm Det}$ of modes are allowed into the detector. In a four-terminal measurement, we measure the current at contact 4 (the drain), and the potential difference between contacts 3 and 5.

vector $\mathbf{a}^{\rm in}$, where

$$a_i^{\rm in} = \begin{cases} 1 & \text{for } i \leq f_{\rm Inj}, \\ 0 & \text{otherwise.} \end{cases} \tag{4.2}$$

After propagating along the edge, the resulting population at the entrance to the detector is the vector $\mathbf{a}^{\rm out}$, where

$$a_i^{\rm out} = \sum_{i=1}^{\nu_{\rm B}} p_{ij} a_j^{\rm in} = \sum_{i=1}^{f_{\rm Inj}} p_{ij}, \tag{4.3}$$

in terms of the elements of the scattering probability matrix, p_{ij}. These are the probabilities $|t_{\alpha\beta,ij}|^2$ from the S-matrix of the full device, where α, β are the contacts in which the modes i, j terminate and originate, respectively. Note that since the initial phases of the modes are uncorrelated, the time-averaged quantities we measure do not reflect any of the phase information included in the S-matrix amplitudes $t_{\alpha\beta,ij}$.

The modes are then split at the detector QPC, with $\nu \leq f_{\mathrm{Det}}$ passing through to contact 3, and the remaining modes reflected to contact 4. Thus the transmission coefficient T_{32} for current passing from the injector to the detector is given by

$$T_{32} = \sum_{i=1}^{f_{\mathrm{Det}}} a_i^{\mathrm{out}} = \sum_{i=1}^{f_{\mathrm{Det}}} \sum_{j=1}^{f_{\mathrm{Inj}}} p_{ij}. \tag{4.4}$$

At this point, one could simply measure the current flowing out of contact 3 to extract T_{32} through the Landauer-Büttiker formula,

$$I_3 = \frac{e^2}{h} V_0 T_{32}, \qquad \text{for } V_3 = 0, \tag{4.5}$$

but this would be a two-terminal measurement, and so we would need to account for series resistance in the circuit to determine V_0. Instead, we make the four-terminal measurement shown in Fig. 4.2. For this configuration, the Landauer-Büttiker formalism gives the relations

$$I_4 = -I_2 = f_{\mathrm{Inj}} \frac{e^2}{h} V_0, \tag{4.6a}$$

$$V_3 = \frac{T_{32}}{f_{\mathrm{Det}}} V_0, \tag{4.6b}$$

$$V_5 = V_6 = 0, \tag{4.6c}$$

and hence the non-equilibrium conductance is given by

$$\begin{aligned} G_{\mathrm{Neq}} &= \frac{I_4}{V_3 - V_5} = \frac{e^2}{h} \left(\frac{f_{\mathrm{Inj}} f_{\mathrm{Det}}}{T_{32}} \right) \\ &= \frac{e^2}{h} f_{\mathrm{Inj}} f_{\mathrm{Det}} \left[\sum_{i=1}^{f_{\mathrm{Det}}} \sum_{j=1}^{f_{\mathrm{Inj}}} p_{ij} \right]^{-1}, \end{aligned} \tag{4.7}$$

independent of the excitation voltage V_0.

If the propagation along the edge is perfectly adiabatic, i.e. $p_{ij} = \delta_{ij}$, then Eq. (4.7) reduces to

$$G_{\mathrm{Neq}} = \frac{e^2}{h} \max(f_{\mathrm{Inj}}, f_{\mathrm{Det}}), \tag{4.8}$$

so we infer the presence of non-zero off-diagonal scattering probabilities when the measured value deviates from this result. Moreover, by making systematic measurements of $G_{\mathrm{Neq}}(f_{\mathrm{Inj}}, f_{\mathrm{Det}})$ for $f_{\mathrm{Inj}}, f_{\mathrm{Det}} = 1, 2, \ldots, N$, we can extract the individual scattering

probabilities p_{ij} for $i = 1, 2, \ldots, N$ by solving Eq. (4.7) to obtain[1]

$$p_{ij} = \frac{e^2}{h}\left[\frac{ij}{G_{\mathrm{Neq}}(i,j)} + \frac{(i-1)(j-1)}{G_{\mathrm{Neq}}(i-1,j-1)} - \frac{(i-1)j}{G_{\mathrm{Neq}}(i-1,j)} - \frac{i(j-1)}{G_{\mathrm{Neq}}(i,j-1)}\right]. \quad (4.9)$$

Scattering probabilities for propagation along the entire upper edge as a function of B and V_{UG} extracted through this method are shown in Fig. 4.3. Several important features are immediately apparent:

- Scattering between modes $\nu = 1$–4 and $\nu > 4$ is strongly suppressed in the range of B shown in Fig. 4.3. The elements for which $i, j = 5$ actually correspond to all states $\nu > 4$, measured by fully opening the injector and/or detector QPC. The bulk filling factor in this field range varies from $\nu_{\mathrm{B}} = 7$ to 6, but we conclude that the $\nu > 4$ modes remain largely decoupled from the two lowest LLs. This is expected for $\nu_{\mathrm{B}} \leq 6$, as the $n_{\mathrm{LL}} = 2$ LL moves into the bulk and begins to depopulate, but the degree of separation when $\nu_{\mathrm{B}} = 7$ is somewhat more surprising.

- Spin-flip scattering (e.g., p_{23}, p_{34}) is suppressed throughout the range of B considered. As discussed above, this is a prerequisite for spin-selective measurements.

- Inter-LL scattering between the lowest-two LLs is non-negligible (p_{13} and p_{24} nearly reach their maximum value of 0.5 for some settings of B and V_{UG}), but drops rapidly with increasing B in the region shown. As mentioned previously, in order to study antidot transmission resonances through non-equilibrium measurements we must find a regime in which the $1 \leftrightarrow 3/2 \leftrightarrow 4$ scattering is allowed at the antidot, but suppressed along the edge. For this device, this transition regime occurs for the range of B shown in Fig. 4.3.[2] Below $B \approx 1.1$ T, strong inter-LL scattering renders non-equilibrium measurements impossible, while for $B \gtrsim 1.25$ T, the antidot transmission resonances disappear. The patterns observed in p_{13} and p_{24} as a function of B and V_{UG} in Fig. 4.3 are similar but not identical, probably reflecting impurities which lie along the edge contour which have slightly different effects on each mode. By mapping the scattering through this method, we can identify settings for which both types of inter-LL scattering are strongly suppressed, even at the low-B end of the transition regime.

[1] In order to use Eq. (4.9) for $i, j = 1$, we define $G_{\mathrm{Neq}}(m, n) = 1$ for $m, n = 0$.

[2] As described in §4.2.3, these measurements were taken with the sample tilted at $\approx 60^\circ$ relative to the direction of B in order to enhance E_{Z}. This means that the perpendicular component $B_\perp$ is roughly one-half of the total field B used throughout this chapter.

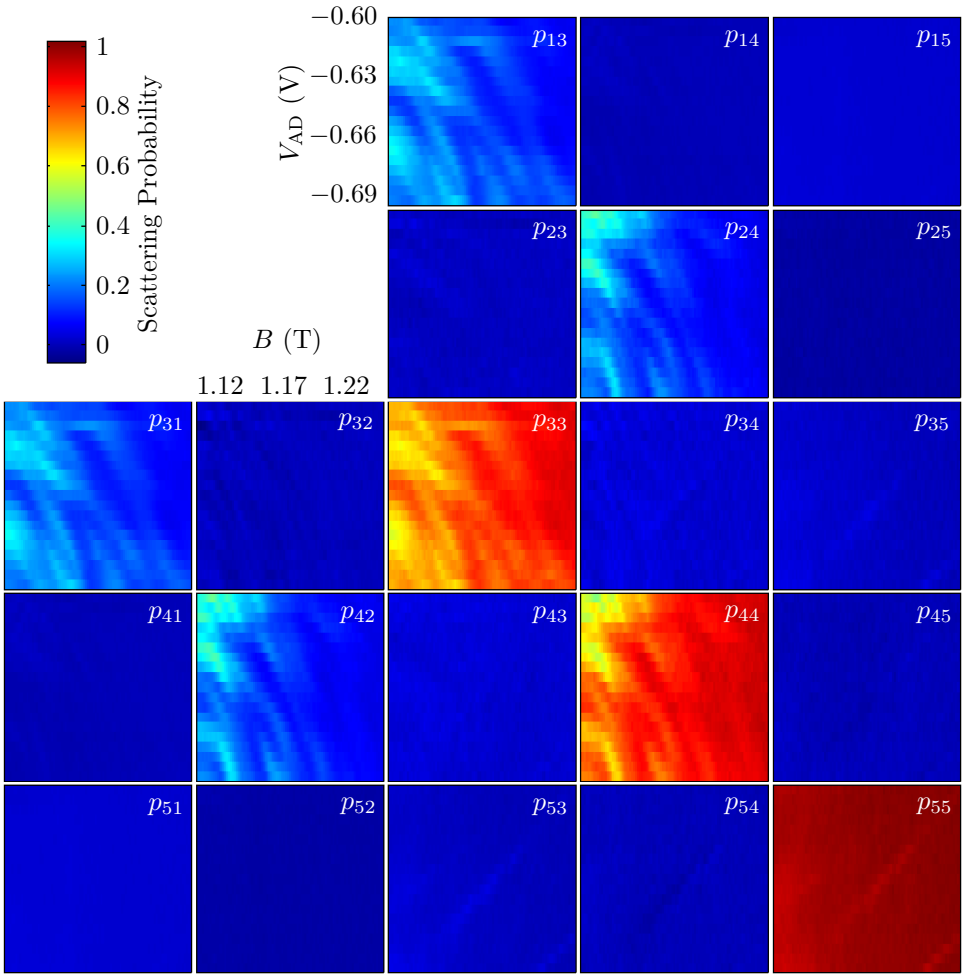

Figure 4.3: Scattering probabilities p_{ij} for propagation along the entire upper edge, from QPC1 to QPC2, as a function of B and V_{UG}. The elements $i, j = 5$ correspond to all bulk states $\nu > 4$. In the range of B considered, the bulk filling factor varies through $\nu_{\mathrm{B}} = 6$–7, but the 5^{th} column and row above demonstrate that these states have negligible coupling to states $\nu = 1$–4 throughout. Matrix elements for $i, j \leq 2$ were not computed in this case because QPC1 could not reach $f_{\mathrm{Inj}} = 1$ at these values of V_{UG}. The probability matrix is symmetric, so some data above is redundant, but it is included to assist visual perception of the patterns in scattering between modes.

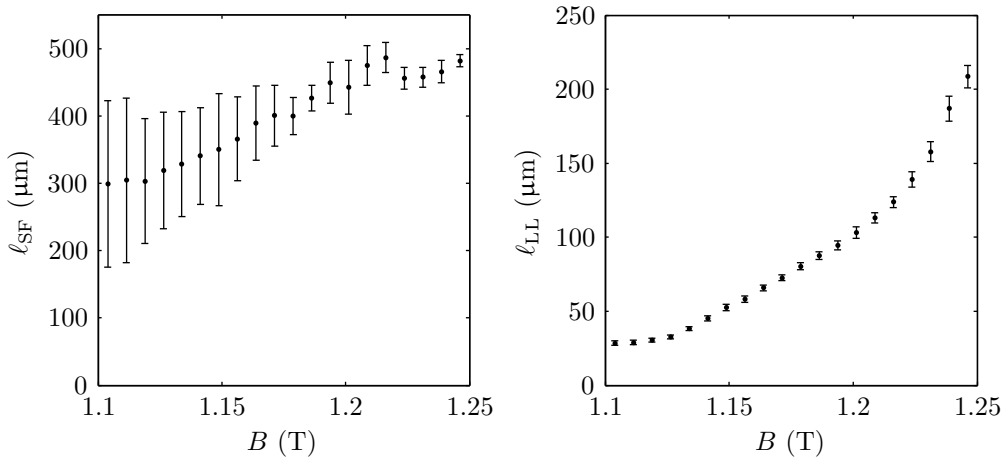

Figure 4.4: Equilibration lengths ℓ_{SF} and ℓ_{LL}, for spin-flip and inter-LL scattering, respectively, calculated from the scattering probabilities shown in Fig. 4.3 assuming no relaxation to $\nu > 4$. At lower B, this neglected scattering is of the same order as ℓ_{SF}, leading to the increased uncertainty in that measurement. In the case of inter-LL scattering, the uncertainty increases with B since ℓ_{LL} becomes larger than the path length $L = 10\,\mu\text{m}$.

For our purposes, it is enough to show experimentally that we can suppress both spin-flip and inter-LL scattering along the edge at low-B, but it is clear that much further investigation into the details of the edge-scattering is possible through this method. Similar studies have been performed before, [e.g., 82, 87–90], but to our knowledge none has considered the detailed structure of the scattering probabilities as shown in Fig. 4.3.

As an additional quantitative measure of edge-mode scattering, and for comparison with the previous studies cited above, we estimate the 'equilibration length' for both spin and inter-LL scattering, as shown in Fig. 4.4. These are computed through an extension of the procedure employed by Ref. [82]. We model the edge mode populations $\mathbf{a}(x)$ as a function of propagation distance through a set of coupled rate equations

$$\frac{d\mathbf{a}}{dx} = \mathrm{R}\mathbf{a}, \tag{4.10}$$

where the rate matrix R gives the scattering rates per unit length for the various transitions. Assuming no scattering to $\nu > 4$, a simple approximation[1] to these rates is given

[1] We have considered additional complications to this model, such as an account of the different scattering distances between pairs of opposite-spin modes. The algebra is more tedious, but leads broadly to the same result (within the error bars of Fig. 4.4).

by

$$\mathrm{R} = \begin{pmatrix} -(\ell_{\mathrm{LL}}^{-1} + 2\ell_{\mathrm{SF}}^{-1}) & \ell_{\mathrm{SF}}^{-1} & \ell_{\mathrm{LL}}^{-1} & \ell_{\mathrm{SF}}^{-1} \\ \ell_{\mathrm{SF}}^{-1} & -(\ell_{\mathrm{LL}}^{-1} + 2\ell_{\mathrm{SF}}^{-1}) & \ell_{\mathrm{SF}}^{-1} & \ell_{\mathrm{LL}}^{-1} \\ \ell_{\mathrm{LL}}^{-1} & \ell_{\mathrm{SF}}^{-1} & -(\ell_{\mathrm{LL}}^{-1} + 2\ell_{\mathrm{SF}}^{-1}) & \ell_{\mathrm{SF}}^{-1} \\ \ell_{\mathrm{SF}}^{-1} & \ell_{\mathrm{LL}}^{-1} & \ell_{\mathrm{SF}}^{-1} & -(\ell_{\mathrm{LL}}^{-1} + 2\ell_{\mathrm{SF}}^{-1}) \end{pmatrix}, \tag{4.11}$$

where ℓ_{LL}^{-1} and ℓ_{SF}^{-1} are the scattering rates between any pair of modes of the same or opposite spin, respectively. By solving Eq. (4.10) using this rate matrix, we can find expressions for ℓ_{SF} and ℓ_{LL} in terms of the occupations $\mathbf{a}^{\mathrm{out}}$ measured at $x = L$, where $L = 10$ μm is the path length between the QPCs. Several such relations may be obtained by considering different initial populations (through f_{Inj}) and subsets of the final mode occupations. For example,

$$\ell_{\mathrm{SF}}^{-1} = -\frac{1}{4L}\log(a_1^{\mathrm{out}} + a_3^{\mathrm{out}} - a_2^{\mathrm{out}} - a_4^{\mathrm{out}}), \qquad \text{for } f_{\mathrm{Inj}} = 3, \tag{4.12a}$$

$$\ell_{\mathrm{LL}}^{-1} = -\ell_{\mathrm{SF}}^{-1} - \frac{1}{2L}\log(a_1^{\mathrm{out}} + a_2^{\mathrm{out}} - a_3^{\mathrm{out}} - a_4^{\mathrm{out}}), \qquad \text{for } f_{\mathrm{Inj}} = 2. \tag{4.12b}$$

The equilibration lengths plotted in Fig. 4.4 are computed according to these relations, using the mean occupation vector $\bar{\mathbf{a}}^{\mathrm{out}}$, averaged over the range of V_{UG} considered. Changing V_{UG} corresponds to physically moving the edge contour relative to the background impurity potential, and so averaging in this way allows us to obtain the mean equilibration lengths for a given wafer as a function of B, using only a single pair of QPCs. Clearly, these results reflect our previous conclusions concerning the relative weakness of spin-flip scattering and the rapid change in inter-LL scattering as B increases. In particular, for $B \lesssim 1.15$ T, we see that the average equilibration length ℓ_{LL} is similar in magnitude to L, but we have shown that by carefully tuning gate voltages we can avoid scattering centres along the edge contour and so enhance the equilibration length significantly above the mean value.

4.2.3 Tuning the Zeeman energy: tilted field measurements

In this chapter we are interested in the antidot transmission resonances at filling factor $\nu_{\mathrm{AD}} = 2$. These have several practical advantages over the $\nu_{\mathrm{AD}} = 1$–2 reflection resonances which have been the focus of several previous studies [17, 19, 43], for example:

- For the purposes of studying spin- and charge-driven interactions in the $\nu = 2$ quantum Hall fluid, it is only on the $\nu_{\mathrm{AD}} = 2$ plateau that we can be reasonably

sure that the antidot is fully surrounded by a filled LL. Once reflection resonances start to occur, a theoretical description may need to account for the complicated energetics of a depopulating LL in the constrictions.

- From a more practical perspective, the tunnel couplings which govern reflection resonances depend on the width of the side constrictions, and so are strongly affected by changes in gate voltages. Sweeping the magnetic field has a much weaker effect on these tunnel couplings, and so has been the preferred technique in previous experiments, but as we showed in the previous section, changes in B strongly affect edge equilibration, which can obscure the interpretation of non-equilibrium measurements. We prefer to sweep instead the antidot gate voltage at a fixed magnetic field chosen to minimise edge scattering. The tunnel couplings between co-propagating edge modes, on the other hand, which control transmission resonances, depend only weakly (through the potential slope and background impurity potential) on the gate voltage.

- In addition to their strong dependence on gate voltages, the tunnel couplings for reflection resonances of different spins are strongly asymmetric. In fact, we show in the next section that the $\nu_{\mathrm{AD}} = 1$–2 resonances occur *only* through spin-$\downarrow$ ($2\leftrightarrow 2$) tunnelling, even in the low-B regime. Transmission resonances, on the other hand, are characterised by roughly equal tunnel couplings for spin-$\uparrow$ and spin-$\downarrow$ electrons, and so provide more obvious information about the spin selection rules for the antidot states themselves.

While these advantages motivate our decision to study transmission resonances, we have already mentioned in the previous section that such experiments require substantial amounts of fine tuning, in order to balance the enhanced edge equilibration at low B with the disappearance of the transmission resonances at higher fields. These two constraints leave a relatively narrow range of $B_\perp$ within which non-equilibrium measurements are possible for a given device,[1] which may not be ideal for particular applications. In the spin-filter device, for example, we require both of the SP excitation energies E_{Z} and $\Delta E_{\mathrm{SP}} - E_{\mathrm{Z}}$ (see §1.1.3) to be larger than the thermal broadening of the leads ($\approx 2kT$) in order to resolve individual states. At fixed B, we have some degree of control over ΔE_{SP} through the gate voltage, which changes the antidot size and hence ΔE_{SP} through Eq. (4.1). To gain independent control over E_{Z}, we can tilt the *direction* in which the magnetic field is applied, since both the tunnel couplings and ΔE_{SP} depend only on the

[1] For small antidots, such an overlap region may not even exist.

perpendicular component of the field, while E_Z depends on the full magnitude of B.

It would be ideal to have *in situ* control of the field direction, for example through the rotating sample holder used in Chapter 6, but unfortunately, technical difficulties with the rotating sample holder prevented its use for these experiments. We were, however, able to mount the device at a fixed orientation relative to the magnetic axis for a given cooldown. From initial measurements of our device in the standard perpendicular orientation, we determined that the desirable perpendicular field was around $B_\perp \approx 0.6\,\mathrm{T}$, and that the electron temperature[1] in the device was $T = 60$–$70\,\mathrm{mK}$ ($kT = 5$–$6\,\mu\mathrm{eV}$). The Zeeman energy at this field, in terms of the bare g-factor in GaAs, is only $E_Z \approx 15\,\mu\mathrm{eV}$, which is at the lower limit of the energy scales we can expect to resolve. Excitation spectra suggested that the SP energy was around $\Delta E_{SP} \approx 50$–$60\,\mu\mathrm{eV}$, and so we chose to raise the sample and remount it, tilted at an angle of $\approx 60°$ to the magnetic axis, to approximately double the Zeeman energy.

Our measurements suggest[2] that the g-factor is actually significantly enhanced (by a factor of ≈ 1.5) from the bare value of $g = -0.44$ in our device, so this seems to have been a slight over-rotation, resulting in a situation for the central antidot in which $E_Z \approx \Delta E_{SP}$. In a sense this was fortuitous, since it meant that we could observe state crossings as a function of B and V_{AD} within the parameter space available to us at this fixed angle. As we show later in this chapter, comparisons of the excitation spectra near these crossings with our theoretical models help to isolate the effects due to electron interactions and the underlying antidot energy spectrum from those due to other aspects of the experiment, such as applied bias, asymmetric tunnel barriers, and temperature.

4.3 Experimental results

Non-equilibrium measurements of the central antidot proceed analogously to the edge-scattering experiments described in §4.2.2. We use one QPC as an injector, to selectively populate a subset of source edge modes, and then use a second QPC as a detector, to individually measure the population of each mode in the drain. A typical measurement setup is shown in Fig. 4.5, although there are many variations. For example, by attaching the excitation voltage to a contact inside the injector as shown, we populate modes $\nu = 1$ to f_{Inj} of the source, but we can also populate the outer modes $\nu = f_{Inj} + 1$ to ν_B by reversing the connections to earth and V_{EX} on the left-hand side of the device. The

[1] The electron temperature is determined through an analysis of thermally-broadened peak lineshapes as a function of mixing-chamber temperature.

[2] This is especially clear in the measurements of Chapter 6, taken with a rotating sample holder.

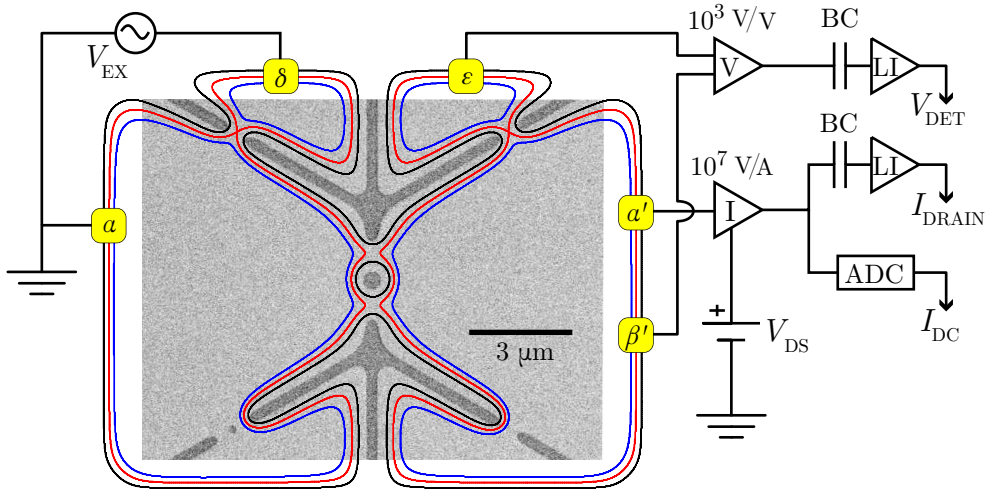

Figure 4.5: Scanning electron micrograph of the first metallic layer of a device similar to that used for the experiments in this chapter, with edge-modes and the non-equilibrium measurement circuit overlaid. The four-terminal non-equilibrium conductance G_{Neq} is measured using lock-in techniques, with an AC excitation voltage V_{EX} which has amplitude $eV_{\mathrm{EX}} \approx 3\,\mu\mathrm{eV} \lesssim kT$ and frequency $\approx 70\,\mathrm{Hz}$. The output of the current preamplifier is fed to both a lock-in amplifier (LI) and an analogue-to-digital converter (ADC), to measure the AC and DC components of the current, respectively. Blocking capacitors (BC) with a capacitance $C = 40\,\mu\mathrm{F}$ prevent DC components from overloading the LI amplifiers. A DC source-drain bias V_{SD}, applied to the drain through the current preamplifier, serves to cancel the input offset of the preamplifier for linear-response measurements, or to supply the source-drain bias for nonlinear transport experiments. Edge-mode contours were computed from the bare electrostatic potential of the gates using the `GatesCalc` program. The black contour represents both of the LLL edge modes ($\nu = 1, 2$), and the $\nu = 3$ and 4 modes are represented by red and blue contours, respectively.

second antidot in the constriction at the lower-left can also be operated as a detector QPC, allowing us to measure the populations of the reflected edge modes.

4.3.1 Spin-selective measurements in linear response

Selective detection measurements of the central antidot for the entire range of filling factor $\nu_{\mathrm{AD}} = 0$–2 are shown in Fig. 4.6. For such long sweeps, slow device drift on the scale of the fine resonance structure makes it impractical to simply subtract separate traces as described in §4.2.2 to extract the antidot scattering probabilities. Where necessary, we can still perform this subtraction for shorter, higher-resolution sweeps, or we can quantitatively extract scattering probabilities for resonances individually through peak-fitting procedures, but most of the important conclusions are readily observable by eye without any complicated analysis.

Since it is easier to interpret visually, the data presented in Fig. 4.6 are the result of two-terminal measurements, rather than the non-equilibrium four-terminal measurement shown in Fig. 4.5. The injector QPC is fully open, so all source modes are populated, and we separately measure the currents[1] flowing out of contacts ε in the detector and α' in the drain, which reflect the populations of the edge modes at the entrance to the detector QPC. When the detector is set at $f_{\mathrm{Det}} = 4$ (black curves in Fig. 4.6), all of the current appears in the detector as expected, since we have already shown that scattering to $\nu > 4$ modes is negligible. For $f_{\mathrm{Det}} < 4$, the signal is divided between G_{Det} and G_{Drain}, and we can determine which features of the trace are carried by individual modes by subtracting the curves 'by eye.' Two important features are immediately apparent:

- Perhaps the most striking detail in Fig. 4.6 is the nearly complete lack of structure in G_{Det} when $f_{\mathrm{Det}} = 1$ (middle panel, blue curve). This suggests that the $\nu = 1$ mode does not couple to the antidot at all,[2] except where the $\nu_{\mathrm{AD}} < 1$ oscillations begin around $V_{\mathrm{AD}} = -1.1\,\mathrm{V}$. This means that the $\nu_{\mathrm{AD}} = 2$ reflection resonances are due solely to spin-$\downarrow$ ($2\leftrightarrow 2$) tunnelling, with no contribution from the spin-$\uparrow$ ($\nu = 1$) state, in contradiction to the non-interacting Mace-Barnes model. This is essentially the same behaviour observed by Kataoka et al. [19] in the 'double-frequency' regime at much higher fields, which was interpreted as evidence for

[1] We plot two-terminal conductance $G = I/V_{\mathrm{EX}}$ instead of current since this is roughly independent of V_{EX} (in our case the series resistance of $\approx 300\,\Omega$ is almost negligible compared to the $\approx 10\,\mathrm{k}\Omega$ resistance of the device).

[2] To prove this statement, we must rule out any 'cancellation' due to scattering between other modes by checking the situation when $f_{\mathrm{Inj}} < 4$. In such experiments, the $f_{\mathrm{Det}} = 1$ trace is indeed featureless for all settings of f_{Inj}.

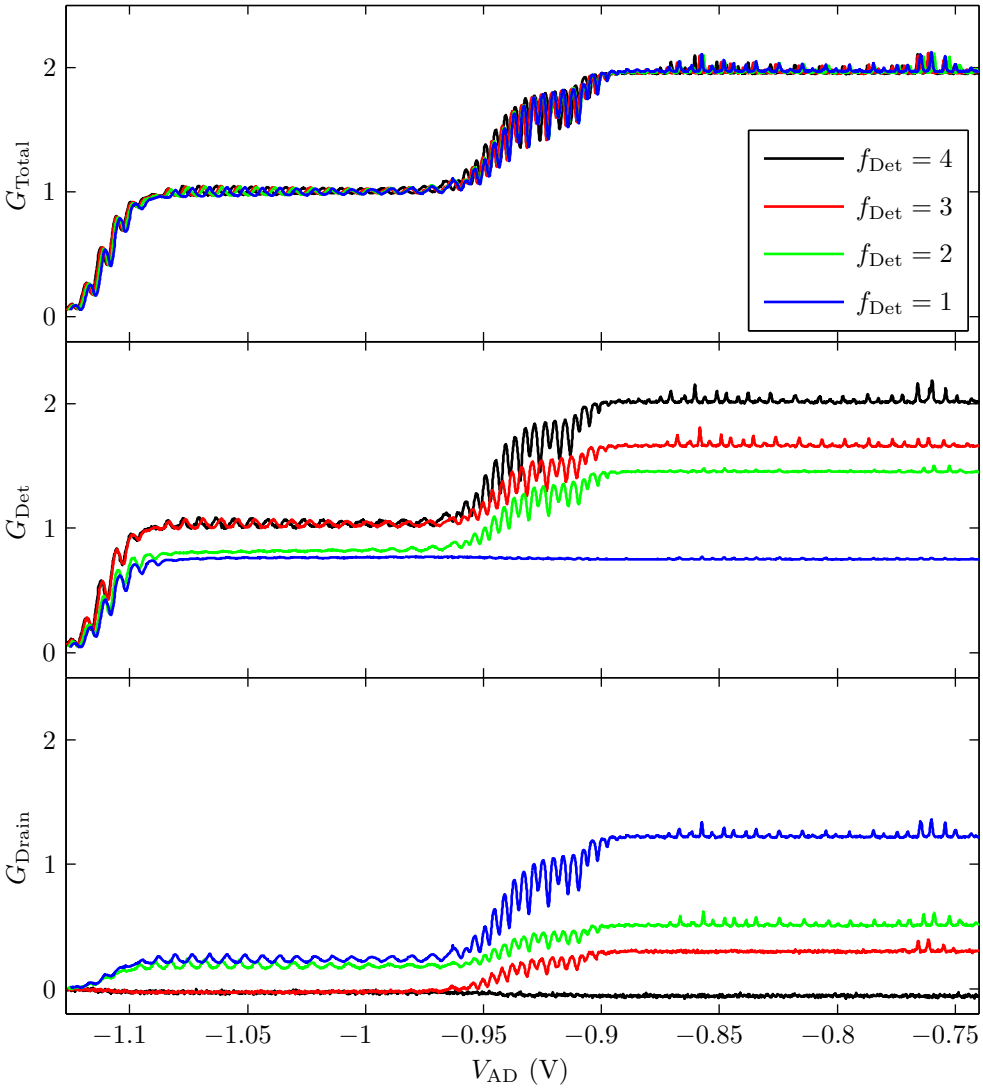

Figure 4.6: Selective detection measurements of the central antidot at $B_\perp = 0.6\,\mathrm{T}$, obtained by separately measuring the current flowing out of the detector (ohmic ε, middle panel) and drain (ohmic α', bottom panel) contacts, with $f_{\mathrm{Det}} = 1$–4 as labelled above, and the injector QPC fully open. The total conductance G_{Total} shown in the upper panel is the sum of the detector and drain measurements. Two-terminal conductances are given in units of e^2/h, with no corrections for series resistances in the circuit. These data were taken in a separate cooldown of the device than the rest of the measurements presented in this chapter.

compressible regions. Although the resonance spacings appear rather uniform in our experiments, we observe a clear odd-even modulation in amplitude apart from a few phase slips (e.g., around $V_{\mathrm{AD}} = -0.91\,\mathrm{V}$), and so we are clearly not in the double-frequency regime here.

- While the $\nu_{\mathrm{AD}} = 2$ reflection resonances appear only in spin-↓ channels (a signal appears in the $\nu = 4$ mode due to equilibration along the detector edge), the transmission resonances show nearly opposite behaviour. Consider for example the measurement of G_{Drain} at $f_{\mathrm{Det}} = 3$ (bottom panel, red curve), representing the population of the $\nu = 4$ state at the detector. Except for a few resonances near $V_{\mathrm{AD}} = -0.76\,\mathrm{V}$, the $\nu_{\mathrm{AD}} = 2$ plateau is nearly featureless. When f_{Inj} is reduced to 2 (green curve), however, the transmission resonances all appear in G_{Drain} with nearly their full amplitude. This implies that these conductance peaks are mostly the result of spin-↑ (1↔3) tunnelling, with 2↔4 only becoming significant within a small 'envelope' encompassing 4–5 resonances.[1] Again this is in direct contrast to the simple non-interacting model which predicts peaks of alternating polarisation, even though the resonances show clear odd-even modulation suggestive of the SP model. It is also inconsistent with a model based on compressible regions, which would predict tunnelling only through the outer spin-↓ state for transmission as well as reflection resonances.

Thus we find that the antidot resonances around $\nu_{\mathrm{AD}} = 2$ are spin-polarised, but not in the way predicted by the non-interacting model. Reflection resonances are fully spin-↓ (2↔2 tunnelling), and transmission resonances are dominated by spin-↑ (1↔3).

This unexpected result suggests that the spin of electrons involved in transport is determined by tunnel couplings to the leads, rather than by intrinsic selection rules of the antidot states. For reflection resonances this is not particularly surprising. The distance across the constriction for 2↔2 tunnelling is likely to be much greater than that for 1↔1 transport, especially since the long spin-equilibration length measured in §4.2.2 suggests that the $\nu = 1$ and 2 LLs are spatially separated. Our measurements suggest that the $\nu = 1$ state does not couple to the antidot at all in this regime, except for the reflection resonances at $\nu_{\mathrm{AD}} < 1$ where the $\nu = 2$ mode is fully excluded from the constrictions. We might hope to observe a stronger amplitude modulation of alternate reflection resonances if the antidot states were spin-selective, but when sweeping V_{AD} the 2↔2 coupling quickly becomes large enough to produce significant lifetime broadening,

[1] As seen in Fig. 4.7, detailed measurements show a small contribution from spin-↓ tunnelling to each peak, but the spin-↑ transmission is generally around an order of magnitude greater.

within the first few dips from the $\nu_{\mathrm{AD}} = 2$ plateau, from which point we would not expect to preserve the energy-selectivity required to probe individual antidot states.

The observed details of the transmission resonances, however, are harder to explain. Although the $\nu = 3$ mode is physically 'closer' to the antidot, we expect the $1\leftrightarrow3$ and $2\leftrightarrow4$ tunnel-couplings to be nearly identical based on the edge-mode topology. It is possible that details of the potential slope and edge-mode structure could lead to different tunnelling distances for these two processes, but we suspect instead that the most likely explanation for the dominance of $1\leftrightarrow3$ tunnelling is that an impurity on the drain side of the potential disrupts the $\nu = 4$ mode, decreasing the $2\leftrightarrow4$ coupling $\Gamma_{\mathrm{D}\downarrow}$ on that side. We have extensive experimental evidence for such nearby impurities, as described in §6.1 and believe that $\Gamma_{\mathrm{D}\downarrow} \ll \Gamma_{\mathrm{S}\downarrow}$ for several reasons explained later in this chapter. The odd-even amplitude modulation observed for the most part in Fig. 4.6 therefore suggests that the antidot states do have a spin 'character,' in the sense that alternate resonances are more or less transparent to the predominant spin-$\uparrow$ tunnelling, but the selectivity is clearly incomplete. These resonances do not suffer from significant lifetime broadening; in the region of magnetic field we study, their lineshape is well-matched by the Fermi-derivative function expected for thermally-broadened resonances, so we expect the transport to be energy-selective within the range of a few $kT \approx 10$–$15\ \mu\mathrm{eV}$. We concentrate on explaining the details of these transmission resonances for the remainder of this chapter.

The incomplete spin-selectivity we observe may be explained in two ways. Either the antidot spectrum is composed of 'pure' spin-states with an energy-spacing less than the thermal resolution of the leads, or the antidot states themselves are spin-hybridised as the result of the spin-orbit or hyperfine spin-mixing interactions. In either case we might expect that spin-$\uparrow$ would couple differently to alternate states, producing the amplitude modulation observed in Fig. 4.6, but there is a crucial observable difference between the two models. Spin is *conserved* during transport through nearly-degenerate pure-spin states, but this is not the case for hybridised states for which S_z is not a good quantum number; the spin of each electron passing through such a state precesses to an angle which depends on the length of time it remains there, and so the time-averaged output spin will be independent of the input spin. We can differentiate between these two mechanisms by using the injector QPC to populate only one of the $\nu = 3$ or 4 modes, as shown in Fig. 4.7.

The data in Fig. 4.7 were obtained through the non-equilibrium experimental setup shown in Fig. 4.5, with the detector set to $f_{\mathrm{Det}} = 3$ to separate the $\nu = 3$ and 4 edge modes. We plot both the two terminal conductance $G_{2\mathrm{T}\alpha'} = I_{\alpha'}/V_{\mathrm{EX}}$ (corresponding to

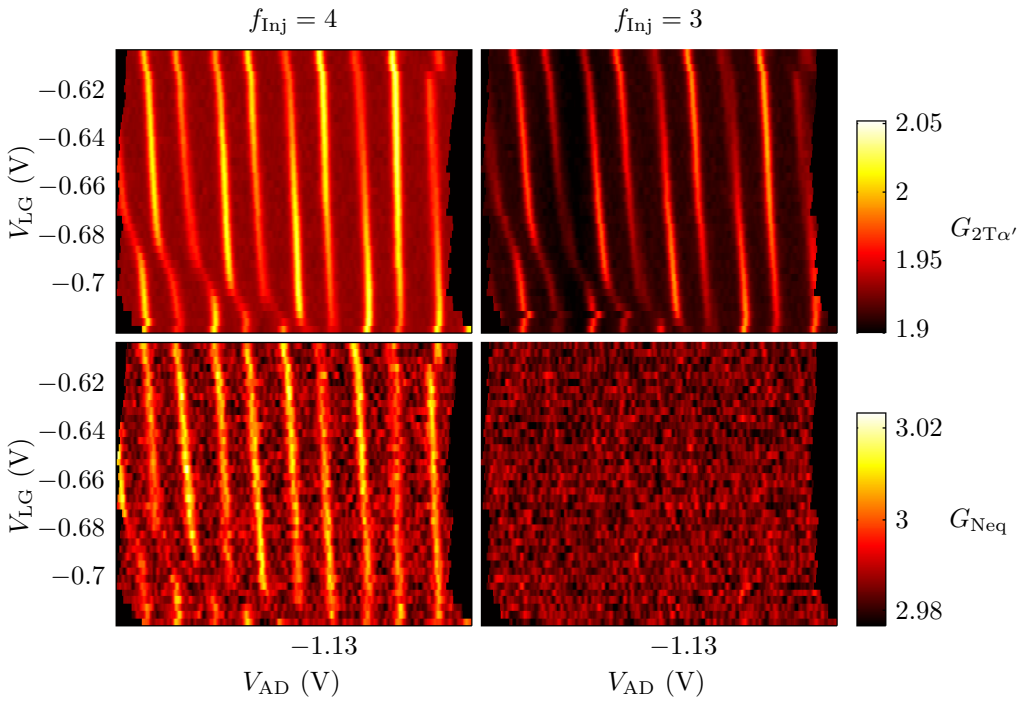

Figure 4.7: Non-equilibrium measurements of transmission resonances on the $\nu_{\mathrm{AD}} = 2$ plateau obtained by sweeping V_{AD} and stepping V_{LG}. The top and bottom rows respectively show the two-terminal antidot conductance $G_{2\mathrm{T}\alpha'} = I_{\alpha'}/V_{\mathrm{EX}}$ and the non-equilibrium conductance $G_{\mathrm{Neq}} = I_{\alpha'}/V_{\varepsilon\beta'}$ in units of e^2/h, with $f_{\mathrm{Det}} = 3$ throughout and $f_{\mathrm{Inj}} = 4$ and 3 in the left and right columns, respectively. The disruption to the resonances in the bottom-left corner is the result of a nearby impurity, as described in §6.1. Sweeps are individually shifted horizontally to correct for device drift and to clarify the resonance pattern.

G_{Tot} in Fig. 4.6) and the non-equilibrium conductance $G_{\mathrm{Neq}} = I_{\alpha'}/V_{\varepsilon\beta'}$. Through the Landauer-Büttiker formalism, we may write G_{Neq} in the form

$$G_{\mathrm{Neq}} = f_{\mathrm{Det}} \frac{e^2}{h} \left[1 + \frac{\sum_{i=f_{\mathrm{Det}}+1}^{\nu_{\mathrm{B}}} a_i^{\mathrm{Det}}}{\sum_{i=1}^{f_{\mathrm{Det}}} a_i^{\mathrm{Det}}} \right], \tag{4.13}$$

where the vector $\mathbf{a}^{\mathrm{Det}}$ gives the populations of the edge modes at the entrance to the detector. For $f_{\mathrm{Det}} = 3$, the second term in brackets above is dominated by variations of

the numerator, so we can approximate

$$G_{\mathrm{Neq}} \simeq \frac{3e^2}{h}\left[1+\frac{1}{A}a_4^{\mathrm{Det}}\right], \tag{4.14}$$

where $A \simeq a_1^{\mathrm{Det}} + a_2^{\mathrm{Det}} \approx 2$ is a constant depending only on the edge-equilibration.[1] Features observed in G_{Neq} therefore reflect changes in the population of the $\nu = 4$ mode at the detector.

When $f_{\mathrm{Inj}} = 4$, such that all source modes are populated (left column of Fig. 4.7), we see a strong signal in $G_{2\mathrm{T}\alpha'}$, and a much weaker corresponding signal in G_{Neq}, implying that electrons passing through the antidot may enter either the spin-↑ ($\nu = 3$) or the spin-↓ ($\nu = 4$) mode of the drain, although they are much more likely to take the spin-↑ channel due to the asymmetric tunnel couplings. We also observe an odd-even pattern of amplitudes for these resonances, and, interestingly, the pattern systematically reverses as a function of V_{LG}. With a closer look, it is also clear that the 'brighter' resonances in $G_{2\mathrm{T}\alpha'}$, which is dominated by spin-↑, are correspondingly 'dimmer' in the spin-↓ signal of G_{Neq}, again suggesting that the antidot states do have a 'preferred' spin, even though the selection is incomplete.

By setting $f_{\mathrm{Inj}} = 3$ (right column of Fig. 4.7), we no longer populate the $\nu = 4$ source channel, and a different picture emerges. We still observe a strong signal in $G_{2\mathrm{T}\alpha'}$, but now G_{Neq} is essentially featureless.[2] Taken together, these measurements imply that electron spin is *conserved* in passing from the source to the drain, since by removing the source of spin-↓ electrons, we measure only the spin-↑ signal in the drain. This suggests an interpretation of the results based on pure, nearly-degenerate spin-states, rather than a hybridised-spin model. To be absolutely sure of this interpretation, we must check also the *reflected* current when $f_{\mathrm{Inj}} = 3$, since highly asymmetric couplings $\Gamma_4^{\mathrm{S}} \gg \Gamma_4^{\mathrm{D}}$ will result in the majority of any 'spin-flip' current appearing in the $\nu = 4$ mode on the source side of the device. This is accomplished by using one constriction of the smaller antidot in QPC4 as a second detector. We measure the current flowing out of contact ε', with the filling factor of QPC4 also set to three, but we want the contribution from the $\nu = 4$ mode which is reflected by this constriction and arrives in

[1] Equilibration along the top edge is independent of both V_{AD} and V_{LG}.

[2] The resonances in $G_{2\mathrm{T}\alpha'}$ appear to darken in Fig. 4.7 but this mainly reflects the decreased background resulting from a small amount of equilibration along the injector edge. This equilibration also explains the extremely faint resonance signal remaining in G_{Neq}.

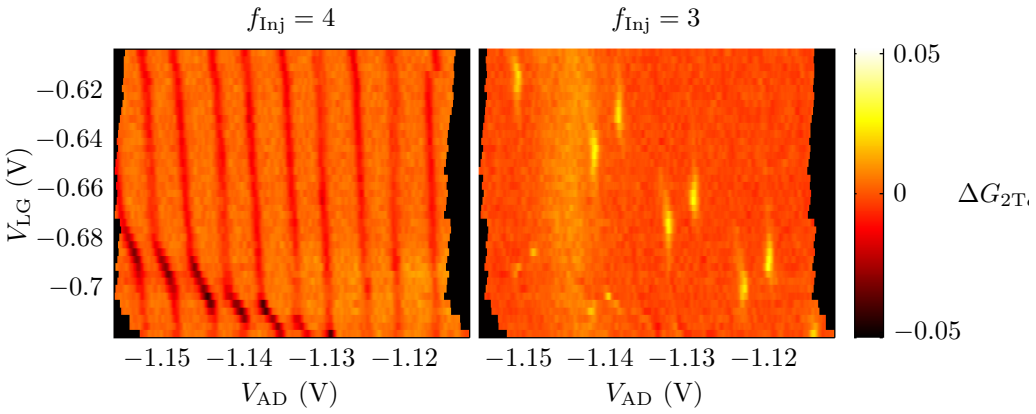

Figure 4.8: Non-equilibrium measurements of the *reflected* population of the $\nu = 4$ state, taken together with the data of Fig. 4.7, for $f_{\mathrm{Inj}} = 4$ (left panel) and 3 (right panel). Since the background level is strongly affected by changing edge-equilibration as a function of V_{LG}, we plot the variation $\Delta G_{2\mathrm{T}\alpha}$ obtained by subtracting the mean of each horizontal sweep, in order to clarify the antidot resonance structure.

the grounded contact α'. By current conservation, this is given by

$$G_{2\mathrm{T}\alpha} = f_{\mathrm{Inj}} \frac{e^2}{h} - G_{2\mathrm{T}\alpha'} - G_{2\mathrm{T}\varepsilon'}, \tag{4.15}$$

up to a constant offset due to series resistance. These measurements are shown in Fig. 4.8. When $f_{\mathrm{Inj}} = 4$, we observe weak dips in $G_{2\mathrm{T}\alpha}$ corresponding to the transmitted spin-$\downarrow$ current detected in G_{Neq}. When $f_{\mathrm{Inj}} = 3$ the resonance pattern mostly disappears, and we are left with a clear pattern of bright 'spots,' representing spin-flip processes in which a spin-$\uparrow$ electron enters the antidot from the $\nu = 3$ source state and then returns to the source $\nu = 4$ state as spin-$\downarrow$. With closer inspection, we see that the locations of these spin-flip events correspond to the places in which the bright-dark pattern of resonance pairs reverses in Fig. 4.7, and further analysis shows that they also correspond to the 'closest approach' in V_{AD} of each pair of resonances. This behaviour is highly suggestive of crossings between the energy levels of opposite-spin states. There is faint evidence for spin-flip features matching those of Fig. 4.8 in the transmitted G_{Neq} data shown in the lower-right panel of Fig. 4.7, but they are clearly much weaker than those seen in the reflected current. This observation implies that $\Gamma_{\mathrm{D}\downarrow} \ll \Gamma_{\mathrm{S}\downarrow}$, which we believe to be the result of a nearby impurity which disrupts the $\nu = 4$ edge mode near the antidot.

4.3.2 Discussion of linear response data

From the linear-response measurements presented in the previous section, we obtain a picture of antidot transport with the following important characteristics:

- The antidot resonances we observe are not spin-selective. Amplitude modulations suggest that states have a 'preferred' spin, but since the modulation is rarely larger than a factor of ≈ 2, it is clear that the electrons of the 'un-preferred' spin may pass through the antidot easily.[1] The spin polarisation we observe in the transmitted current is driven instead by the antidot-lead couplings, which are much stronger for spin-$\uparrow$ tunnelling than for spin-$\downarrow$.

- Generally, spin is conserved during transport.[2] Note that this does not preclude Kondo-like *cotunnelling* events in which an electron on the antidot of one spin is replaced by an electron of the opposite spin. These processes would not be detected as spin-flips in the time-averaged quantities we measure, since such an event must eventually be followed by the reverse tunnelling process in order for the antidot to maintain an equilibrium spin state.

- With careful tuning of external fields, we can find specific regimes in which spin is not conserved for individual electrons on the antidot. These locations appear to correspond to 'crossings' of opposite-spin states of the antidot addition spectrum.

These features may be broadly described in terms of three important energy scales. The first is the thermal energy $E_{\mathrm{Therm}} \approx 2kT$, which defines the energy window of allowed tunnelling events about E_{F}. The others, which we discuss below, are the energy separation of antidot states with differing (pure) spin, and the energy scale for hybridisation of opposite-spin states, which we attribute to the spin-orbit interaction based on an analysis of the anticrossings observed in Fig. 4.8.

4.3.2.1 Spin-conserved transport

Considering first the 'usual' case in which spin is conserved during transport, such that the total antidot spin-projection S_z is a good quantum number, sequential transport is

[1] If the tunnel couplings were equal for both spins, a factor of two modulation in spin-selectivity would result in observed polarisations of only $\approx 30\%$.

[2] The data shown in Figs. 4.7 and 4.8 were chosen to highlight the observed pattern of spin-flip events. Throughout the entire range of parameters we studied, such events are even more rare than they appear in Fig. 4.8.

governed by the chemical potentials $\mu_\sigma(N, S_z)$, given by

$$\mu_\uparrow(N, S_z) = U(N+1, S_z + \tfrac{1}{2}) - U(N, S_z) \tag{4.16a}$$
$$\mu_\downarrow(N, S_z) = U(N+1, S_z - \tfrac{1}{2}) - U(N, S_z), \tag{4.16b}$$

in terms of the configuration energy $U(N, S_z)$ of an antidot with N particles[1] and total spin S_z. At a resonance condition between configurations with N and $N+1$ particles, transport of both spin-↑ and spin-↓ electrons will be energetically allowed if one or both of the following conditions hold:

$$\left|\mu_\uparrow(N, S_{z0}) - \mu_\downarrow(N, S_{z0})\right| \lesssim E_{\text{Therm}} \tag{4.17a}$$
$$\text{or} \quad \left|\mu_\uparrow(N, S'_{z0} - \tfrac{1}{2}) - \mu_\downarrow(N, S'_{z0} + \tfrac{1}{2})\right| \lesssim E_{\text{Therm}}, \tag{4.17b}$$

where S_{z0} and S'_{z0} are the ground-state spins of the antidot states with N and $N+1$ particles, respectively. These are equivalent to the conditions

$$\mu^{\pm}_{\text{SF}}(N, S_{z0}) \lesssim E_{\text{Therm}} \quad \text{or} \quad \mu^{\pm}_{\text{SF}}(N+1, S'_{z0}) \lesssim E_{\text{Therm}}, \tag{4.18}$$

written in terms of the 'spin-flip' chemical potentials defined by

$$\mu^{\pm}_{\text{SF}}(N, S_z) = U(N, S_z \pm 1) - U(N, S_z). \tag{4.19}$$

Thus we identify μ_{SF}, together with $E_{\text{Therm}} \approx 2kT$ as the relevant energy scale for spin-selective tunnelling. The observed lack of spin-selectivity in our experiments implies that Eq. (4.18) must hold for each $N \leftrightarrow N+1$ transition. Within the non-interacting theory described in §1.1.3, this corresponds to a near-degeneracy between pairs of states in the opposite-spin 'ladders' of the SP spectrum. In particular, within the SP model we find

$$\mu^{\pm}_{\text{SF}}(N, S_z) = (1 \pm 2S_z)\Delta E_{\text{SP}} - E_{\text{Z}}, \tag{4.20}$$

and Eq. (4.18) will be satisfied whenever $E_{\text{Z}} - n\Delta E_{\text{SP}} \lesssim E_{\text{Therm}}$ for any nonnegative integer n.

[1] For an antidot, N corresponds either to the number of electrons within some 'cutoff' orbital, beyond which all states are filled, or the number of 'holes' in the otherwise-occupied LLs, as described in §1.3.1.

4.3.2.2 Spin-flip transport

Next, we consider the regime in which spin is *not* conserved, as at the locations of the bright 'spots' on the right-hand panel of Fig. 4.8. Spin relaxation may occur either through hyperfine coupling between electrons and GaAs nuclei, or through the phonon-mediated spin-orbit interaction. A useful overview of these interactions in the context of quantum dots is provided in the review of Hanson et al. [5]. These two mechanisms are characterised by very different time- and energy-scales, which we can use to decouple their contributions to our experimental observations.

We can describe the hyperfine interaction in terms of an effective magnetic field B_{HF}, known as the Overhauser field, which accounts for the randomly-oriented ensemble of nuclear spins interacting with a given electron [91]. The component of this field perpendicular to the externally applied $\mathbf{B}$ will lead to mixing between antidot states with spin projection S_z and $S_z + 1$, but due to energy-conservation requirements, this mixing is only strong when these states satisfy $\mu_{\mathrm{SF}}^{\pm} \lesssim \varepsilon_{\mathrm{HF}}$, where $\varepsilon_{\mathrm{HF}} = g\mu_{\mathrm{B}}B_{\mathrm{HF}}$ is the energy scale for the hyperfine interaction. The magnitude of the Overhauser field resulting from statistical variations of N nuclei[1] is given by $B_{\mathrm{N,max}}/\sqrt{N}$, where $B_{\mathrm{N,max}} = 5.3\,\mathrm{T}$ is the field that would be produced by the full polarisation of all GaAs nuclei. The dominant hyperfine contribution is a contact interaction proportional to the overlap between the electron and nuclear spatial probability densities, so we can estimate N from the spatial size of the electron wave function and the nuclear density of the GaAs crystal, $n_{\mathrm{GaAs}} = 44\,\mathrm{nm}^{-3}$. For typical antidot wave functions with radius $r_{\mathrm{AD}} \approx 400\,\mathrm{nm}$ and width $\ell_{\mathrm{B}} \approx 30\,\mathrm{nm}$ at $B_{\perp} = 0.6\,\mathrm{T}$, we have $(2\pi r_{\mathrm{AD}}\ell_{\mathrm{B}})n_{\mathrm{GaAs}} \approx 3 \times 10^6\,\mathrm{nm}^{-1}$, and with the quantum well thickness in the z-direction of $\approx 10\,\mathrm{nm}$, we estimate that each electron in the antidot couples to $N \approx 10^7$–10^8 nuclei, and therefore sees an Overhauser field with rms magnitude $B_{\mathrm{HF}} \approx 1\,\mathrm{mT}$. This corresponds to an extremely small coupling energy of $\varepsilon_{\mathrm{HF}} \approx 25\,\mathrm{neV}$, and so spin-flips can only occur through the hyperfine mechanism when antidot spin-configuration energies are very nearly degenerate. When such coupling occurs, electron spins will precess about the Overhauser field with a rate $\varepsilon_{\mathrm{HF}}/h \approx 10\,\mathrm{MHz}$, which is comparable to the rate at which electrons pass through the antidot, estimated from typical transport currents of $\approx 1\,\mathrm{pA} = e(6\,\mathrm{MHz})$, so we could expect hyperfine coupling to produce spin-flips in our experiments. Besides the spin-precession frequency, hyperfine effects are characterised by a very long time-scale,

[1] The scale for nuclear magnetic moments is set by the nuclear magneton, $\mu_{\mathrm{N}} = \hbar|e|/2m_p = 3.2\,\mathrm{neV/T}$, which is much smaller than the Bohr magneton for electrons, $\mu_{\mathrm{B}} = \hbar|e|/2m_e = 60\,\mu\mathrm{eV/T}$, and so the nuclear Zeeman energy $E_{\mathrm{Z,N}} = g\mu_{\mathrm{N}}B$ always satisfies $E_{\mathrm{Z,N}} \ll kT$ for experimentally accessible temperatures and fields.

measured in minutes to hours, associated with the relaxation of nuclear spins which have been 'pumped' through hyperfine interactions with electrons, and with the complicated feedback loops which may result from such pumping. This long time-scale often serves as an experimental signature of the hyperfine effect, but we did not observe any effects of this nature in our experiments.

Spin-orbit coupling, on the other hand, results from electric fields in the semiconductor material due to both the band offset at the GaAs-AlGaAs heterojunction (the Rashba contribution) and the bulk inversion asymmetry of the GaAs crystal (the Dresselhaus contribution). The strength of the interaction, $\varepsilon_{\mathrm{SOI}}$, depends both on the magnitude of these electric fields and on the electron momentum vector[1] $\mathbf{k}$, so the spin-orbit interaction is sensitive to the electron density $n_e = k_{\mathrm{F}}^2/2\pi$. The spin-orbit strength is therefore highly sample-dependent[2] and precise measurements of its value are not trivial. For two-dimensional ballistic motion, Miller et al. [92] used a model of weak (anti)localisation measurements to separately extract the different spin-orbit contributions in a GaAs heterostructure as a function of electron density. At the lowest density they considered, $n_e = 1.4 \times 10^{11}$ cm^{-2}, they found roughly similar magnitudes for the Rashba and linear Dresselhaus coupling strengths, of $\varepsilon_{\mathrm{SOI}} \approx 20\,\mu$eV. We would expect this value to be slightly lower in our device, which has $n_e = 1.1 \times 10^{11}$ cm^{-2}, but even so it is clear that the spin-orbit interaction is a much stronger effect in two-dimensional systems than the hyperfine coupling discussed above.

Based on this estimate, we might actually expect spin-orbit coupling to dominate over the energy scales $\mu_{\mathrm{SF}}^{\pm}$ and kT we have been discussing so far, in contrast to our observation of spin-conservation in most cases. In zero dimensions, however, several of the mechanisms which dominate spin-relaxation in two dimensions are suppressed [93], and so the effect on antidot states may actually be significantly weaker. The main effect of spin-orbit coupling in zero-dimensions is a reorganisation of the SP levels into admixtures of states with different spin and orbital quantum numbers m and s. As for the familiar spin-orbit coupling in atomic systems, mixing occurs predominantly between zero-dimensional states with the same value of $j = m + s$ [94], and this suggests an interesting difference between antidots and quantum dots. In contrast to quantum dots, LLL antidot states with the same j do not cross as B is increased. As can be

[1] Note, however, that the Rashba and linear-in-k Dresselhaus terms (the Dresselhaus contribution also has a cubic term, although this is usually suppressed relative to the linear terms by confinement in the z-direction) produce spin-rotations over a *length* ℓ_{SOI} which is k-independent, since the increased spin-precession rate at higher k is compensated for by the larger linear velocity. This description is useful for ballistic electron motion in two dimensions, but less so for edge states or zero-dimensional systems.

[2] The Rashba contribution, in particular, depends on details of the heterostructure which influence the electric field perpendicular to the 2DES.

seen in Fig. 1.5 on page 10, when E_Z is increased relative to ΔE_{SP}, the first crossings between SP states occur between the $|m, s\rangle$ states $|m, \frac{1}{2}\rangle$ and $|m-1, -\frac{1}{2}\rangle$, which have $\Delta j = 2$. Subsequent crossings have even larger Δj. These selection rules are only strict for a system with perfect circular symmetry, which of course our real device does not have, but this may still help explain the relative weakness of spin-orbit coupling which we observe.

To obtain a quantitative measure of the spin-mixing in our device for comparison with the energy scales ε_{HF} and ε_{SOI}, we can measure the evolution of the resonance peak positions through a region in which spin-flips occur. The data in Fig. 4.9 is obtained from the positions of the peaks in Fig. 4.8, for the resonances which mix around $(V_{AD}, V_{LG}) = (-1.13\,\text{V}, -0.67\,\text{V})$. The peak positions are converted to energy using the 'lever-arm' scaling discussed in §2.3, which is obtained from non-linear transport measurements. Their energy-separation shows a clear anticrossing, which is well-matched by the standard hyperbolic function

$$\Delta E(V) = E_C + \varepsilon\sqrt{1 + \left(\frac{V - V_0}{\beta}\right)}, \tag{4.21}$$

where ε is the spin-mixing strength, E_C is the charging energy in the constant-interaction model, and V_0, β are additional free parameters in the fit. We expect that the effect of making V_{LG} more negative is to decrease ΔE_{SP} by flattening the slope of the antidot potential in the lower constriction, through the 'geometric' effect discussed in Chapter 3. Similar fits to the other crossings in Fig. 4.8 give consistent results, although the fits are less constrained due to the limited range of data available. The measured value of $\varepsilon = 3.5 \pm 2.2\,\mu\text{eV}$ (with errors at 95% confidence) is clearly inconsistent with the much smaller hyperfine energy ε_{HF}, implying that the spin-mixing we observe is due to the spin-orbit interaction. Furthermore, since the spin-orbit coupling is large enough to keep states separated by at least $\varepsilon_{SOI} \gg \varepsilon_{HF}$, the hyperfine effect is unlikely to couple spins at all in our device.[1] The measured value of ε_{SOI} is also consistent with our requirement that

$$\varepsilon_{SOI} < \mu_{SF}^{\pm} \lesssim E_{Therm} \tag{4.22}$$

in the regions where spin is conserved, since $E_{Therm} \approx 10$–$15\,\mu\text{eV}$. As discussed above, we find that Eq. (4.22) holds for the majority of the parameter space we explored, while

[1] Typical lead-antidot tunnel couplings in our device are $\Gamma \approx 500\,\text{MHz}$, corresponding to lifetime-broadening energies of $\hbar\Gamma \approx 0.5\,\mu\text{eV}$, which therefore also satisfy $\hbar\Gamma \ll \varepsilon_{SOI}$.

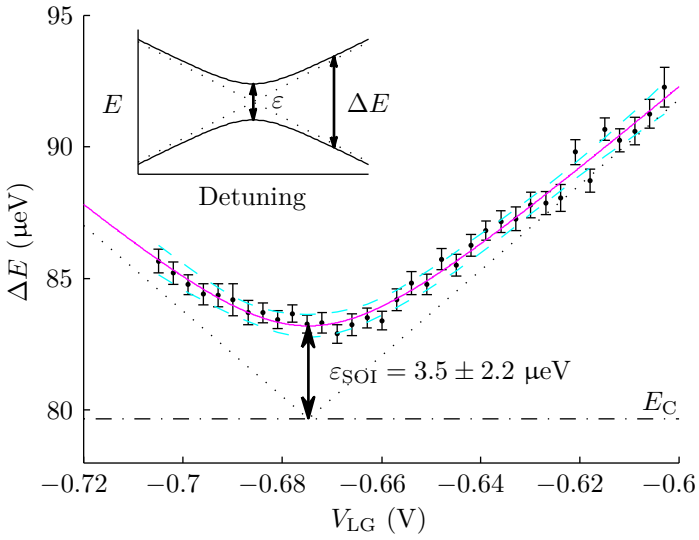

Figure 4.9: Energy separation of a pair of transmission resonances from Fig. 4.7, with best-fit function (magenta curve) and 95% confidence intervals (dashed cyan curve) of the anticrossing form given by Eq. (4.21). As shown, the spin-orbit coupling parameter $\varepsilon_{\mathrm{SOI}}$ is the difference between the constant charging energy E_{C} (with best-fit value given by the horizontal dot-dashed line) and the closest approach of the two states. The best-fit value of $\varepsilon_{\mathrm{SOI}}$ and errors at 95% confidence are given. Separations in V_{AD} are converted to energy using the 'lever-arm' scaling $\alpha_{\mathrm{G}} = 0.022\,\mathrm{eV/V}$ measured from Fig. 4.10 on page 96. The uncertainty in this scaling is much less than those of the fit parameters. Shown in the inset is the general form of anticrossing states, ignoring E_{C}, defined by an anticrossing energy ε at zero detuning, and asymptotic unperturbed states at large detuning (dotted lines), to show the relationship between the energy eigenvalues and their separation ΔE.

the condition

$$\mu_{\mathrm{SF}}^{\pm} < \varepsilon_{\mathrm{SOI}} < E_{\mathrm{Therm}} \tag{4.23}$$

holds at the positions of crossings between antidot states of opposite spin.

This concludes our discussion of spin-mixing. In Chapter 5 we will concentrate on the regime in which spin is conserved, in an effort to explain why $\mu_{\mathrm{SF}}^{\pm} \lesssim E_{\mathrm{Therm}}$ in all our measurements. Although it is beyond the scope of this work, it would certainly be interesting to further investigate the spin-orbit effect in antidots. In particular, it is highly likely that spin-orbit coupling renormalises the effective g-factor for antidot states, which could explain the somewhat enhanced value which we observe in our measurements.

4.3.3 Non-linear measurements: excitation spectra

While the spin-selective linear-response measurements discussed in the previous section provide crucial new information about spin selection rules for antidot transport resonances, they do not give us a direct measure of the antidot energetics. To convert experimental adjustments of the external fields V_{AD} or B into changes in the antidot chemical potential, we need the capacitive couplings,[1] or 'lever-arm' scalings, which can be obtained from the slope of the ground-state resonance positions as a function of drain-source bias V_{DS}, as described in §2.3. This conversion factor then enables us to measure changes in the energy separation between resonances, as in Fig. 4.9, and to estimate the electron temperature in our device, by fitting the resonance line-shapes to a thermally broadened Fermi-function derivative, Eq. (2.98) on page 55. In addition to the lever-arm scalings, non-linear I-V measurements of $\nu_{\mathrm{AD}} = 2$ transmission resonances show much additional structure, which we can use to reconstruct the *excitation spectrum* of the antidot. These serve as an important set of complementary measurements to our spin-selective experiments at zero bias, since we have already seen that the energy-spacing of antidot states plays a crucial role in determining the spin-selectivity of transport. Any model we propose to explain the spin-selective measurements must also reproduce the observed excitations, and vice versa.[2]

An example of such non-linear conductance measurements is shown in Fig. 4.10. We clearly observe the Coulomb blockade diamond pattern of the ground-state lines familiar to studies of single quantum dots, as well as additional structure in the transport regions outside the diamonds. The additional lines parallel to the Coulomb diamonds correspond to excitation energies, measured though their separation in V_{DS}, in the range $E_{\mathrm{ex}} \approx 15$–$50\,\mu\mathrm{eV}$. It is important to note that we would not observe distinct lines for states separated by less than $\approx 15\,\mu\mathrm{eV}$, since these would not be resolved by the thermally broadened peaks. Still, the clear presence of 'gaps' of up to $\approx 50\,\mu\mathrm{eV}$ implies either an antidot energy spectrum with these spacings, or that strict selection rules prohibit transport through states at intermediate energies.

In addition to the excited state lines, we observe two additional important features in Fig. 4.10:

[1] Since the magnetic field changes the size of antidot states, it changes the antidot 'effective charge' as described in §1.2.3 and so can be treated in the same way as a capacitively-coupled surface gate.

[2] While it would certainly be desirable to employ the two techniques together, i.e. to use the selective injection/detection technique to measure the spin-selectivity of excited states, in practice we find that selective edge-mode population is only effective for chemical potential differences of $\lesssim 30\,\mu\mathrm{eV}$, and so we generally perform non-linear measurements with the injector and detector gates fully open so that all incident modes are equilibrated.

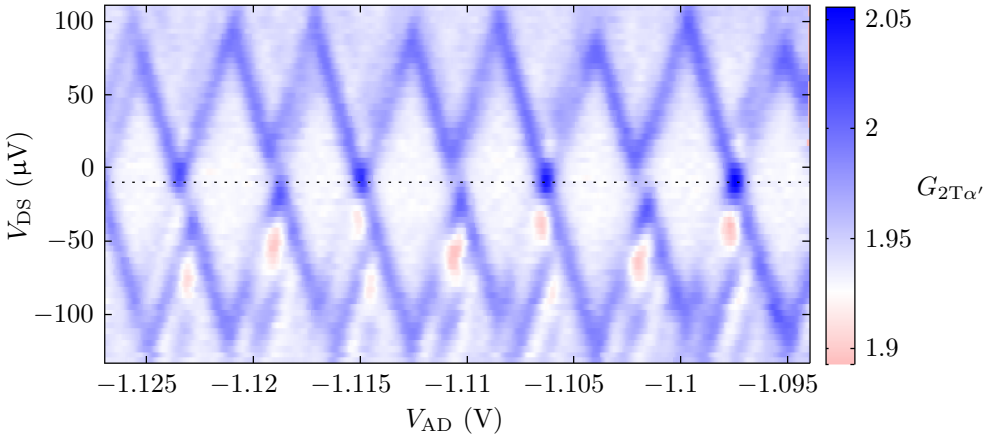

Figure 4.10: Two-terminal differential conductance of antidot transmission peaks on the $\nu_{AD} = 2$ plateau, in units of e^2/h. DC bias is applied to the drain contact α', and the injector is fully open. Colours are scaled such that white corresponds to the $2e^2/h$ conductance plateau, which is shifted from the ideal value by series resistances in the circuit. Individual sweeps are shifted horizontally using interleaved calibration sweeps at zero bias to account for device drift during the run. External fields B, V_{UG}, V_{LG} are set to similar values as for the measurements shown in Figs. 4.7 and 4.8. The horizontal dotted line corresponds to the zero of the current preamplifier, as determined from simultaneous measurements of the DC component of the transport current. Measurements are taken at $B = 1.21$ T.

- The regions which appear red, predominantly at negative V_{DS}, correspond to the occurrence of negative differential conductance (NDC), in which the transmitted current actually drops as the bias is increased.[1] As is well-known in the quantum dot literature [e.g., 95, 96] the observation of NDC implies the presence of a 'slow' state which becomes accessible with increasing DC bias, and which competes with the remaining transport channels in such a way as to reduce the average rate at which electrons pass through the system. Such slow states are usually associated with some form of 'spin blockade' [97], in which selection rules and/or spin-selective barriers affect the rates associated with different transitions.

- Furthermore, we notice that many of the ground state lines with positive slope,

[1] In the case of a $\nu_{AD} = 2$ antidot, the conductance always remains positive due to the background conductance of the LLL edge modes which propagate freely through the constrictions. By checking in turn the conductance of the constrictions alone and by employing the selective detection technique at low bias, we can show that the dips in conductance below $2e^2/h$ are due to a reduction in the transmitted current through the antidot rather than an effect in the constrictions.

which track the chemical potential of the drain, appear to be 'broken' around $V_{\mathrm{DS}} = 0$. We are not aware of any previous observations of this behaviour in the quantum dot literature, suggesting that it reflects a unique property of the system we are probing. We often observe features like this near regions where spin-mixing occurs, as in Fig. 4.8, although they do not coincide precisely with the locations of state crossings. When we zoom in on a few of these 'broken' lines and compare them to corresponding spin-resolved measurements at zero bias, we see that the line-shape of the spin-↑ zero-bias conductance peak is strongly asymmetric, requiring a model with two separate peaks for a good fit, as shown in Fig. 4.11. In between the two spin-↑ peaks we find a smaller single peak in the spin-↓ channel.

We explain these features below in terms of a spin-dependent asymmetry in the tunnel barriers which, combined with suitable DC bias, results in a dynamic 'pumping' of the antidot spin-configuration.

We begin by showing how dynamic spin-pumping can result in dislocations in the Coulomb-blockade boundaries near zero bias. From the non-equilibrium measurements in §4.3.1 we have already seen that the spin-↓ tunnel couplings are highly asymmetric, with $\Gamma_{\mathrm{D}\downarrow} \ll \Gamma_{\mathrm{S}\downarrow}$. An analysis of the amplitudes of the resonances in Figs. 4.7 and 4.8 suggests that $\Gamma_{\mathrm{S}\downarrow} \simeq \Gamma_{\mathrm{S}\uparrow} \simeq \Gamma_{\mathrm{D}\uparrow} \approx 500\,\mathrm{MHz}$, and that $\Gamma_{\mathrm{D}\downarrow}$ is roughly an order of magnitude lower. As shown in Fig. 4.12, this asymmetry in combination with a DC drain-source bias affects the dynamic equilibrium of the antidot (N, S_z) states, and can change the maximally-occupied state. When V_{DS} is positive (negative), the suppressed rate for spin-↓ electrons leaving (entering) the antidot enhances the occupation probabilities of states with lower (higher) S_z. If the spin-flip energies $\mu^{\pm}_{\mathrm{SF}}$ are small for both the N and $N+1$ ground-state configurations, then a small bias may be sufficient to change the maximally-occupied S_z configurations by ± 1, causing a shift in the resonance position which reflects the new chemical potential. These conditions may be met when the ground-state transition involves the blocked spin-↓ transport channel, and we instead observe nearby spin-↑ resonances as the borders of the Coulomb-blockade region. The specific configuration shown in Fig. 4.12 is only an example; the same essential features can occur in several ways. In most cases, the spin-configuration is efficiently pumped only in one of the four 'branches,' since the bias must supply both the asymmetry to pump S_z and the energy to maintain the excited-state population at the position of the new resonance. The resonances shown as blurred lines in Fig. 4.12 are a simplified approximation, since the position of the actual resonance peak depends on the overlapping

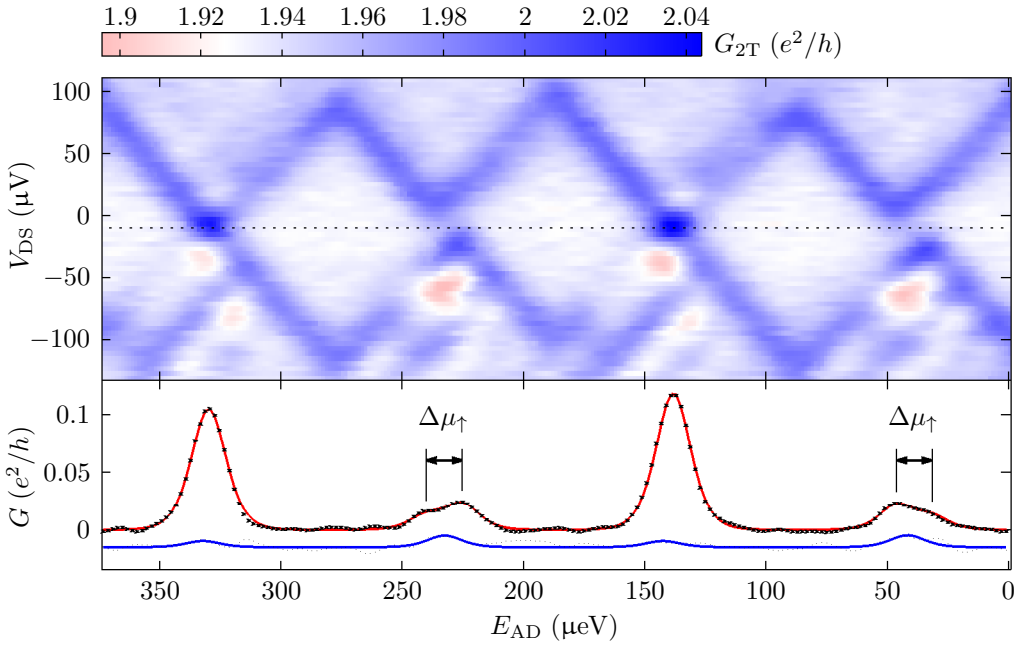

Figure 4.11: Upper panel — Close-up view of non-linear conductance measurements from Fig. 4.10 between $V_{AD} = -1.117\,V$ and $-1.1\,V$, with V_{AD} scaled to E_{AD} using the lever-arm factor $\alpha_G = 2.2 \times 10^4$ μeV/V. Lower panel — Spin-resolved conductance at zero bias (along the dotted horizontal line in the upper panel) with best-fit curves to the separate contributions $G_\uparrow$ (red curve) and $G_\downarrow$ (blue curve). The fitting function consists of thermally-broadened peaks (Fermi-function derivatives) with a common width parameter corresponding to the electron temperature, with best-fit value $T_{elec} = 54.9 \pm 0.5\,mK$. Counting from the left, the second and fourth resonances in $G_\uparrow$ clearly require two peaks for a good fit; their best-fit positions are marked above by vertical lines, and their separation is the energy scale $\Delta\mu_\uparrow \approx 15$ μeV as described in the text. The data and fit of $G_\downarrow$ is vertically offset for clarity.

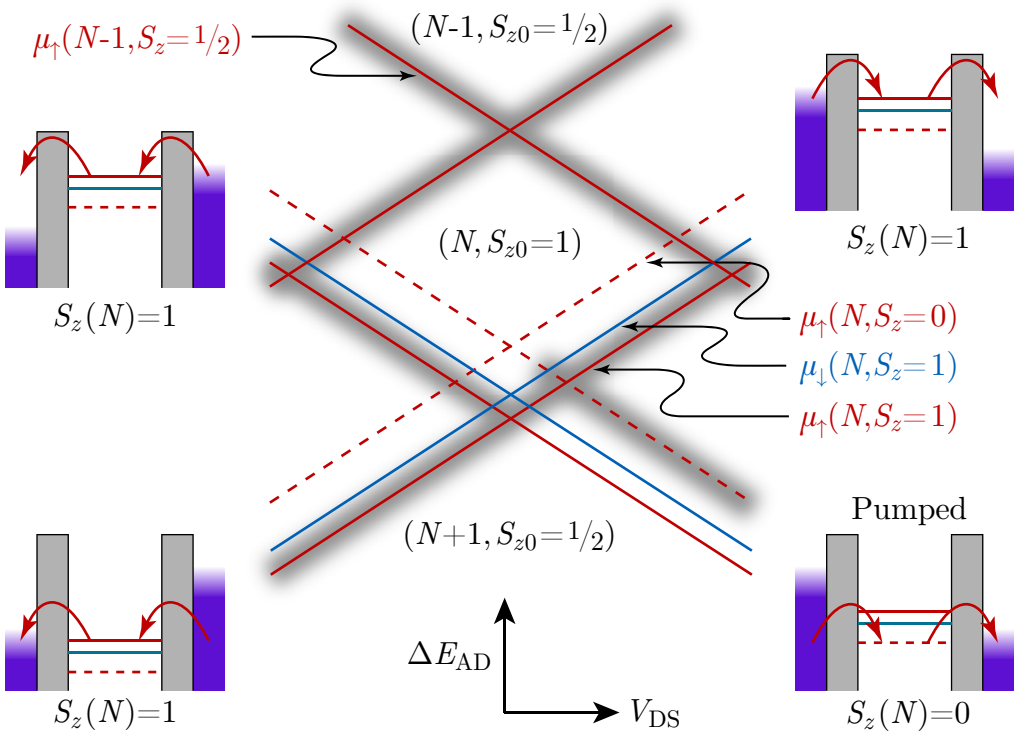

Figure 4.12: Schematic of the dynamic spin-pumping mechanism which results in 'broken' ground-state lines near $V_{\mathrm{DS}} = 0$. The locations where the antidot chemical potentials align with either the source or drain chemical potential are shown as a function of V_{DS} and the capacitive energy ΔE_{AD} added by the antidot gate voltage. The ground-state spin-$\downarrow$ transition $(N, 1) \leftrightarrow (N+1, 1/2)$, shown in blue, is suppressed by a very large tunnel barrier for spin-$\downarrow$ between the antidot and the drain, so transport occurs instead through the two neighbouring spin-$\uparrow$ transitions, shown in red. For each 'branch,' tunneling diagrams show, from left to right, the configuration of the source, antidot, and drain chemical potentials. The blurred lines show the resulting positions of the observed Coulomb-blockade boundaries. In this case, dynamic pumping of the branch in the lower-right results in the appearance of a broken line around zero bias. The upper-right branch is not strongly pumped because the source cannot maintain an occupation in $(N, 0)$ when it is aligned with $\mu_\uparrow(N, 0)$, as it can when the drain is aligned with $\mu_\uparrow(N, 0)$. The adjacent ground-state resonance $(N-1, 1/2) \leftrightarrow (N, 1))$ involves spin-$\uparrow$, and therefore behaves normally as a single resonance split by drain-source bias.

contributions from several transitions, and these contributions change as a function of bias within each branch. But even with these complications, the appearance of a dislocation in the line tracking the drain chemical potential is maintained, and occasionally the instability is such that both spin-↑ transitions can be thermally-activated at zero bias, resulting in an asymmetric or double peak as observed in Fig. 4.11. We will see in Chapter 5 how this behaviour may be reproduced in a sequential tunneling model which incorporates asymmetric tunnel couplings.

With this interpretation of the features observed in our non-linear transport data, we can identify the energy-separation of the double-peaks in Fig. 4.11 as the difference between two spin-↑ chemical potentials. This represents an important additional energy scale which we must reproduce with a model of the system:

$$\begin{aligned}\Delta\mu_{\uparrow}(N,S_z) &= \mu_{\uparrow}(N,S_z+1)-\mu_{\uparrow}(N,S_z),\\ &= \mu^{+}_{\mathrm{SF}}(N{+}1,S_z+\tfrac{1}{2})-\mu^{+}_{\mathrm{SF}}(N,S_z).\end{aligned} \tag{4.24}$$

Within the SP model it is easy to show that $\Delta\mu_{\uparrow} = \Delta E_{\mathrm{SP}}$. The observed value of $\Delta\mu_{\uparrow} \approx 15\ \mu\mathrm{eV}$, however, is too small to produce the excitation spectrum we observe, which requires $\Delta E_{\mathrm{SP}} \approx 30$–$50\ \mu\mathrm{eV}$. We discuss the implications of this inconsistency in Chapter 5.

A similar consideration of the transport channels which become available at different locations in the $(V_{\mathrm{DS}}, V_{\mathrm{AD}})$ plane explains the observation of NDC in the non-linear transport data. Taking the configuration depicted in Fig. 4.12 as an example, we note that the chemical potential $\mu_{\downarrow}(N, S_z = 0)$ enters the transport window at $V_{\mathrm{DS}} > 0$ just to the right of the $\mu_{\uparrow}(N, S_z = 1)$ line. This results in a *decrease* in transmitted current, since spin-↓ electrons will enter the dot through $(N, 0) \rightarrow (N+1, -1/2)$ but then become trapped by the large exit barrier. Analogously, the chemical potential $\mu_{\downarrow}(N, S_z = 2)$ becomes available to the left of $\mu_{\uparrow}(N, S_z = 0)$ line at negative V_{DS}, leading to NDC through a similar effect. Most likely, the NDC is mainly observed at $V_{\mathrm{DS}} < 0$ in the experimental data because the source-drain asymmetry changes at positive bias, probably due to a bias-induced charging event of the nearby impurity.

4.3.4 Confirmation from a second antidot

As described in §4.2.2, spin-selective measurements of transmission resonances are limited to a relatively narrow range of B by the conflicting requirements that 1↔3 and 2↔4 coupling should be suppressed along the edge but present at the antidot. Furthermore, the observation of state-crossings and spin-flip transport as described in §4.3.2.2 sug-

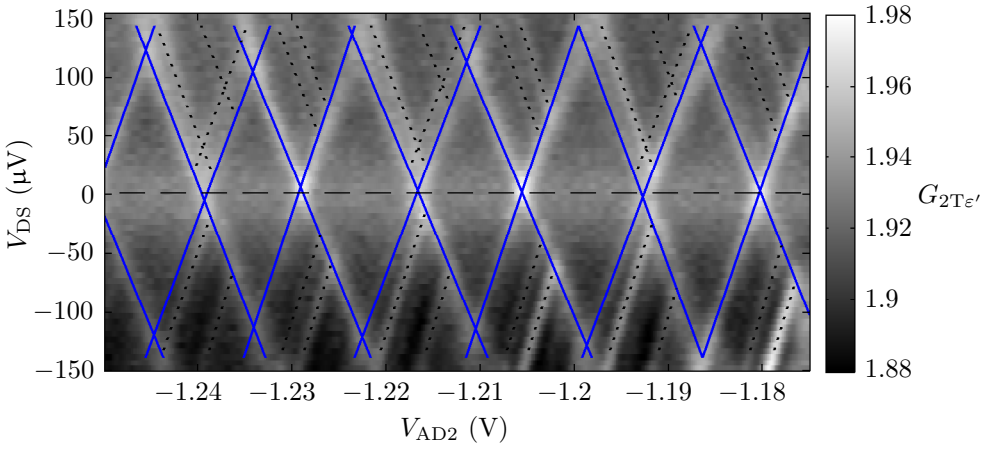

Figure 4.13: Non-linear transport measurements of the second antidot on our device, with bias applied to the drain contact ε'. Ground-state and excited-state transitions are marked as solid blue and dotted black lines, respectively. Measurements are taken at $B = 0.75$ T.

gests that we are close to a degeneracy point in the antidot configuration energy $U(S_z)$. Based on the tilted-field measurements of Chapter 6, taken later from the same device, we believe this to be the first set of LLL state-crossings, i.e. $S_{z0} = 0 \rightarrow S_{z0} = 1$ for even-N occupation numbers. In the SP model, this transition occurs when $\Delta E_{\mathrm{SP}} = E_{\mathrm{Z}}$, and although we have already shown that several details of the non-linear measurements seem inconsistent with a non-interacting model, we might wonder whether the behaviour we observe (in particular, that $\mu^{\pm}_{\mathrm{SF}} \lesssim E_{\mathrm{Therm}}$) is simply the result of a coincidental degeneracy between the SP energy scales.

From Eq. (4.1) we see that $\Delta E_{\mathrm{SP}} \sim (BR_{\mathrm{AD}})^{-1}$, so we can change the SP energy spacing through either B or V_{AD}, which controls the antidot size. For measurements of the central antidot, we were able to vary both B and R_{AD} by $\approx 20\%$, but this is probably not enough to ensure that ΔE_{SP} is changed by more than $E_{\mathrm{therm}} \approx 15$ μeV. The second antidot on our device, however, is lithographically much smaller, with a diameter of 200 nm compared to 300 nm for AD1. The excitation spectrum we observe, shown in Fig. 4.13, contains a very regular pattern of excitation energies, with alternating values of ≈ 20 μeV and ≈ 40 μeV. These data seem fully consistent with the SP model, within which we identify the excitations as E_{Z} and $\Delta E_{\mathrm{SP}} - E_{\mathrm{Z}}$, respectively, such that $E_{\mathrm{Z}} = 20$ μeV, $\Delta E_{\mathrm{SP}} = 60$ μeV, and $E_{\mathrm{C}} \approx 100$ μeV. This agrees with the expected value for the Zeeman energy at $B = 0.75$ T of $|g|\mu_{\mathrm{B}}B = 19$ μeV.

With both $E_{\mathrm{Z}}, \Delta E_{\mathrm{SP}} > E_{\mathrm{Therm}}$, we would expect to observe nearly complete spin-

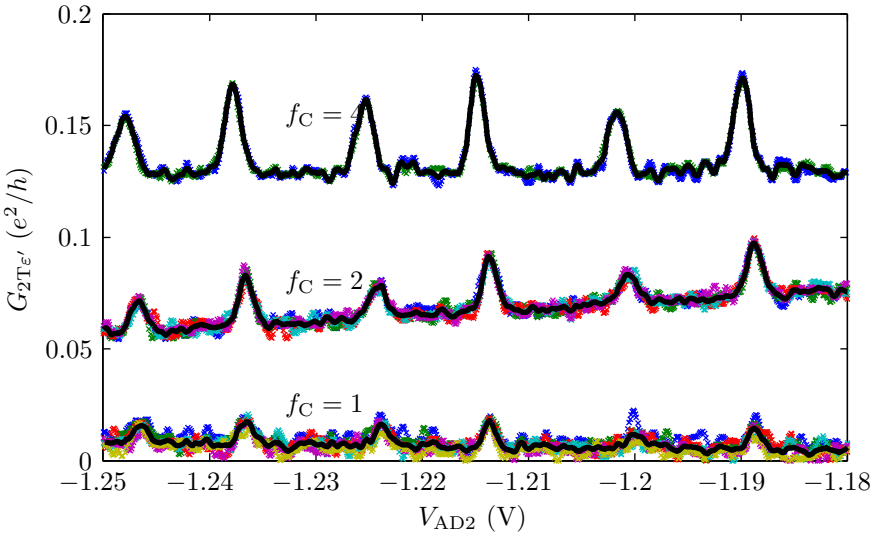

Figure 4.14: Two-terminal conductance measured from contact ε' as a function of the filling factor of the central constriction f_C. With V_{UG} set to a large negative voltage such that the upper antidot constriction is pinched off, the lower constriction functions as a standard injector QPC to selectively populate modes with the excitation signal applied to contact α'. At the low field used for these measurements ($B = 0.75$ T), equilibration between edge-modes 1↔3 and 2↔4 is significant, but spin-scattering is still suppressed, so setting $f_C = 1$ results in a population of only spin-↑ modes $1, 3, 5, \ldots$ at the antidot. Solid black lines represent the average of several sweeps at each f_C setting as shown, and each set of traces has an arbitrary vertical offset for clarity.

polarised transport based on the SP model, but that is not what we observe. While we do not have enough QPCs to perform full injection/detection measurements of AD2, we can use one channel of AD1 as an injector to partially populate the edge-modes incident on AD2. Due to its smaller size, we were forced to use much lower fields of $B \approx 0.6$–0.8 T in order to observe transmission resonances. At these fields significant equilibration occurs between edge modes of the same spin, but calibration measurements similar to those presented in §4.2.2 show that spin-scattering is still suppressed below $\approx$ 5–10%, so by setting central QPC to $f_C = 1$, we populate only the spin-↑ modes. Measurements of a few $\nu_{AD} = 2$ transmission resonances corresponding to the data in Fig. 4.13 are shown in Fig. 4.14, for injector filling factors $f_C = 1$ (spin-↑ partially populated), 2 (both spins partially populated) and 4 (both spins fully populated). It is difficult to know exactly what are the populations incident on AD2 in order to interpret the amplitude variations in Fig. 4.14, but the important result is that, at $f_C = 1$ when only one spin is

injected, all resonances remain with roughly similar amplitudes. Thus the transmitted current is not spin-polarised, even though the observed SP energy scales seem to imply $\mu_{\mathrm{SF}}^{\pm} > E_{\mathrm{Therm}}$. This is strong evidence that additional physics is playing an important role 'behind the scenes' in our system, somehow softening the spin-excitation energy μ_{SF} while preserving SP-like excitation energies. In Chapter 5 we describe a model of electron-electron interactions with exactly these properties and compare simulated data incorporating this model with our measurements.

4.4 Conclusions

In this chapter we have demonstrated the power of the non-equilibrium selective injection/detection technique to extract the individual transmission coefficients of a mesoscopic device in the quantum Hall regime. By using this technique to measure the spins of electrons transmitted through LLL antidot states, we have discovered that, contrary to expectation, the individual resonances are not spin-polarised. Generally we find that spin is conserved during transport, although we can detect certain regimes in which this is not the case, which coincide with (anti)crossings between antidot energy levels. We attribute the non-conservation of electron spin to the spin-orbit effect, which mixes opposite spin states that pass within a characteristic energy $\varepsilon_{\mathrm{SOI}} \approx 3\ \mu\mathrm{eV}$ of each other. In the measurements in which spin is conserved, the observed lack of spin-polarisation still requires that the spin-flip excitation energy of the antidot remain small, $\mu_{\mathrm{SF}}^{\pm} \lesssim E_{\mathrm{Therm}} \approx 15\ \mu\mathrm{eV}$, but we observe clear excitation energies in non-linear transport experiments which do not satisfy this condition. Measurements of a second, much smaller antidot on the same device prove that the lack of spin-selectivity is not a coincidence of SP energy scales, but rather a more general feature of antidots in this low-B regime, which requires an explanation including physics beyond the non-interacting model. In Chapter 5 we explain these results by modeling the antidot as a maximum density droplet of holes, as described in §1.3.1, and explore the implications of our measurements for the physics of interacting electrons.

Chapter 5

Spin-Resolved Transport: Modeling and Discussion

In this chapter we discuss the implications of the experimental results presented in Chapter 4. We propose a model to explain these results in terms of an interacting theory of antidot ground states within the Hartree-Fock framework. In order to test this proposal, we develop a computational model of spin-resolved sequential transport through an antidot, for an arbitrary antidot energy-spectrum and set of selection rules, including spin- and energy-dependent tunnel barriers. We find excellent agreement between our experimental observations and these transport calculations when the antidot ground-state is modeled as an interacting maximum density droplet (MDD) of holes in the lowest Landau level (LLL). We consider the limitations of the Hartree-Fock model, particularly with regards to excitation spectra of the MDD, and propose an effective theory for the antidot edge excitations which agrees with our experiments and encompasses most of the relevant physics.

5.1 Maximum density droplets

A brief introduction to the theory of MDDs within a Hartree-Fock approach is presented in §1.3 of this thesis. The concept of an MDD forms an integral part of our understanding of interactions in quantum Hall fluids, and is particularly relevant for the theoretical description of quantum dots at high magnetic fields. The review by Reimann and Manninen [98] provides a useful discussion of both experimental and theoretical efforts to understand the electronic structure of quantum dots, in which the MDD phase is covered in some detail. The description of an antidot in terms of an MDD of 'holes' within the

LLL has been developed in previous theoretical works [44, 45], but these have mainly focused on effects observed at higher magnetic fields than those considered here.

5.1.1 The exchange effect

We begin with a few simple arguments based on dimensional analysis to introduce the basic physics considered in this chapter. Recall that the major experimental results which we seek to explain are the following: the antidot excitation spectrum shows clear evidence of excitation energies $E_{\rm ex} \gg kT$, consistent with the SP picture of orbital states, but transport at zero bias is not spin-selective. Since spin is conserved during transport, the total antidot spin S_z must be a good quantum number, but the spin-excitation energy $\mu^{\pm}_{\rm SF}$ defined in Eq. (4.19) on page 90 must be smaller than that predicted by the SP model, to satisfy $\mu^{\pm}_{\rm SF} \lesssim E_{\rm Therm}$ at every resonance.

Within the SP model described in §1.1.3 for a $\nu_{\rm AD} = 2$ antidot, the LLL energy spectrum consists of two 'ladders' of orbital states with approximately uniform spacing $\Delta E_{\rm SP}$, and with opposite spin. The spacing between the ladders is the Zeeman energy, $E_{\rm Z}$. When $\Delta E_{\rm SP} > E_{\rm Z}$ as we typically expect, the ground-state total spin alternates between $S_z = 0$ for even values of the occupation number N, and $S_z = \frac{1}{2}$ for odd N, and the lowest-energy excitations for these configurations are $\Delta E_{\rm SP} - E_{\rm Z}$ and $E_{\rm Z}$, respectively. Consider the form of the spin-configuration energy $U(S_z)$ for fixed N within this model. Starting for example from $S_z = 0$ with even N, we obtain the lowest-energy configurations at higher S_z by promoting successive electrons from the upper ladder of spin-$\downarrow$ electrons into the lowest available state of the lower spin-$\uparrow$ ladder. Each time we do this, we gain the Zeeman energy by moving between ladders, but have to pay orbital energy costs of $\Delta E_{\rm SP}$, $3\Delta E_{\rm SP}$, $5\Delta E_{\rm SP}, \ldots$, to reach the next available state. Thus the configuration energy is given by

$$\begin{aligned} U(S_z) &= \sum_{i=1}^{S_z} \Big[(2i-1)\Delta E_{\rm SP} - E_{\rm Z} \Big] \\ &= \Delta E_{\rm SP} S_z^2 - E_{\rm Z} S_z. \end{aligned} \tag{5.1}$$

It is easy to show that $U(S_z)$ takes this basic form for all available values of S_z, and for both odd and even N. Up to an irrelevant constant, Eq. (5.1) is equivalent to

$$U(S_z) = \Delta E_{\rm SP}(S_z - S_z^*)^2, \tag{5.2}$$

where the minimum $S_z^* = E_{\rm Z}/2\Delta E_{\rm SP}$ is between 0 and $\frac{1}{2}$ when $\Delta E_{\rm SP} > E_{\rm Z}$. In general,

the spin-flip energy is therefore of order $\mu_{\rm SF}^{\pm} \simeq U(S_z^* \pm 1) - U(S_z^*) = \Delta E_{\rm SP}$, and it takes a special coincidence (e.g., $\Delta E_{\rm SP} \approx E_{\rm Z}$) to have $\mu_{\rm SF}^{\pm} \approx kT \ll \Delta E_{\rm SP}$.

When we include interactions within Hartree-Fock theory, as described in §1.3.1, the configuration energy of each Slater orbital contains both a positive contribution from the 'direct' Coulomb term, which describes the usual repulsive effect of the Coulomb interaction, and also a negative contribution from the 'exchange' term, which favours parallel alignment of spins. Assuming that the antidot potential is strong enough to compensate for the direct term and preserve the MDD as the ground state, the predominant new contribution to $U(S_z)$ arises from the exchange term, which we can approximate in terms of the 'overlap' between SP states at the spin-polarised edge. The scale of the exchange interaction is the Coulomb energy scale

$$J \approx \frac{e^2}{4\pi\epsilon\epsilon_0 \ell_{\rm B}}, \tag{5.3}$$

and if we approximate the SP states as annuli with width $\ell_{\rm B}$ and radius $\ell_{\rm B}\sqrt{2m}$, for orbital quantum numbers $m \gg 1$, the width of the spin-polarised edge is $w = 2S_z\Delta r$, where the separation of successive orbital states is $\Delta r \approx \ell_{\rm B}^2/R_{\rm AD}$. For small values of S_z, such that $w \ll \ell_{\rm B}$, the exchange effects therefore reduce the configuration energy by an amount $\approx Jw/\ell_{\rm B}$ for each of the $2S_z$ electrons in the spin-polarised edge. Thus the total contribution to $U(S_z)$ is of order (dropping factors of two which are not significant within this approximation)

$$\Delta E_{\rm exchange} \approx -J\frac{\Delta r}{\ell_{\rm B}} S_z^2 = -KS_z^2, \tag{5.4}$$

where

$$K \approx \frac{e^2}{4\pi\epsilon\epsilon_0 R_{\rm AD}} \tag{5.5}$$

is the energy scale of the exchange interaction. As S_z increases and the width of the spin-polarised region increases such that $w \gtrsim \ell_{\rm B}$, the exchange contribution begins to saturate and Eq. (5.4) ceases to be a good approximation. We can account for this by adding higher-order terms to the spin functional, and since the Coulomb energy is independent of the spin *direction*, the next available term is a quartic:

$$\Delta E_{\rm exchange} \approx -KS_z^2 + \beta S_z^4, \tag{5.6}$$

where $\beta \ll K$. Non-parabolicity of the confinement potential may also contribute to the magnitude of the higher-order terms, but this must also be an even functional of S_z.

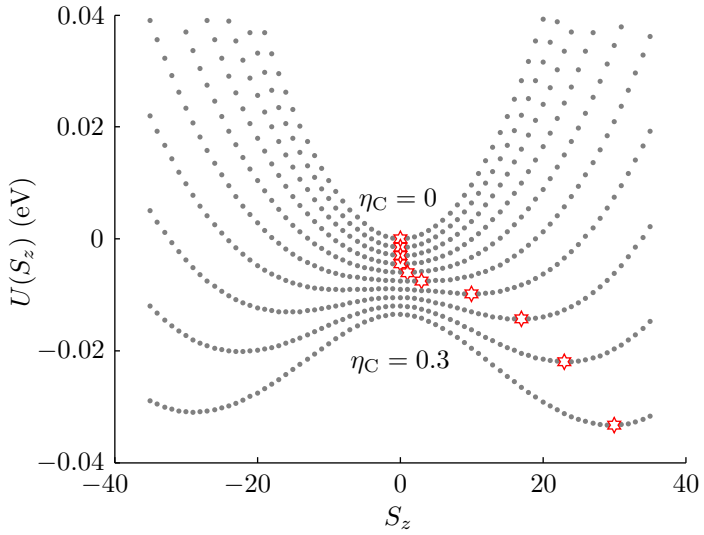

Figure 5.1: Configuration energy $U(S_z)$ for MDDs as the Coulomb interaction is 'turned on,' via uniform steps of the interaction strength η_C. A red star denotes the ground state S_{z0} configuration for each calculation. Calculations for different η_C are offset vertically for clarity. Parameters used in this calculation: $B_\perp = 0.65\,\mathrm{T}$, $\Delta E_{SP} = 100\,\mu\mathrm{eV}$, $E_Z = 40\,\mu\mathrm{eV}$, $R_{AD} = 400\,\mathrm{nm}$ ($N = 130$ holes).

Putting all this together, we obtain a spin functional of the form

$$U(S_z) = -E_Z S_z + (\Delta E_{SP} - K)S_z^2 + \beta S_z^4 + \cdots , \tag{5.7}$$

which we can approximate as a quadratic about the minimum S_z^* as in Eq. (5.2),

$$U(S_z) \approx \alpha(S_z - S_z^*)^2. \tag{5.8}$$

Several examples of the configuration energy $U(S_z)$ are shown in Fig. 5.1, calculated for antidot MDD states using Eq. (1.89) on page 26. These demonstrate the evolution from a non-interacting configuration ($\Delta E_{SP} \gg K$) to a strongly-interacting one ($K \gg \Delta E_{SP}$) as the Coulomb interaction strength η_C is increased. For most of this parameter range, the spin-flip scale $\mu_{SF} \approx \alpha$ is dominated by the quadratic term of Eq. (5.7), such that $\alpha \approx \Delta E_{SP}$ when $K \ll \Delta E_{SP}$ and $\alpha \approx 2K$ when $K \gg \Delta E_{SP}$. But in the crossover regime where $K \approx \Delta E_{SP}$, the curvature near $S_z = 0$ is dominated by the quartic term, such that $\alpha \approx \beta$ is systematically suppressed. Since the small parameter $\beta \ll \Delta E_{SP}$ is likely to satisfy $\beta \lesssim kT$, this is a regime in which we would not expect to observe spin-selectivity

in transport. For $R_{\mathrm{AD}} = 400\,\mathrm{nm}$ as determined from the Aharonov-Bohm period in our device, Eq. (5.5) yields $K \approx 300\,\mu\mathrm{eV}$. This is larger than the orbital energy spacing $\Delta E_{\mathrm{SP}} \approx 50$–$100\,\mu\mathrm{eV}$ we observe in transport measurements, but is a similar order of magnitude. We also expect that Eq. (5.5) significantly over-estimates the strength of exchange, since in Eq. (5.3) we did not account for the extent of the wave function either around the antidot or perpendicular to the 2DES, or for screening by other parts of the device. These factors are roughly included through the multiplicative parameter η_{C} which we vary to control the strength of the Coulomb interactions.

While the spin-excitation energy may be significantly suppressed by exchange, especially when $\Delta E_{\mathrm{SP}} \approx K$, a key feature of this model is that the orbital excitation energy is *preserved*. Fundamentally, this is because the orbital excitations represent modulations of the electron density at the edge of the MDD, in which total spin is conserved. The exchange interaction only affects energy-differences between states with different spin, and so it leaves these density-excitations unaltered. This is demonstrated in Fig. 5.2, in which we plot the lowest-energy edge-excitations as well as the spin-flip chemical potential μ_{SF} as functions of the Coulomb interaction strength. We will discuss the MDD excitation spectrum in more detail in §5.1.3, but the two edge-excitations shown in Fig. 5.2 may be simply interpreted as the singlet (ΔE_S) and T_0 triplet (ΔE_{T_0}) components of the possible excitations involving the outermost spin-↑ and spin-↓ particles of the MDD. The remaining $T_\pm$ triplet states belong to other S_z subspaces, so these correspond to the spin-flip potentials $\mu_{\mathrm{SF}}^{\pm}$. Exchange interactions affect the energy of the S_z-conserving triplet state along with the spin-flip states, but not the singlet state. The 'crossover' region $K \approx \Delta E_{\mathrm{SP}}$ occurs at $\eta_{\mathrm{C}} \approx 0.15$, coinciding with the first few spin-flips of the even-N ground state.

This exchange-driven *spin-charge separation* is the essence of our explanation for the observations described in Chapter 4. In the following sections we will discuss further details of the MDD configuration, and explain the model we use to incorporate other aspects of the experiment, such as the spin-pumping effect discussed in §4.3.3 due to asymmetric and spin-dependent tunnel barriers. This transport model enables us to make detailed comparisons between theoretical predictions and our experimental results.

5.1.2 Stability of the MDD

As discussed in §1.3.3, the MDD is the stable ground state configuration only if the confinement potential[1] is strong enough to overcome the repulsive action of the Coulomb

[1] N.B. For an antidot this refers to the 'confinement' of holes, since the antidot potential is repulsive for electrons.

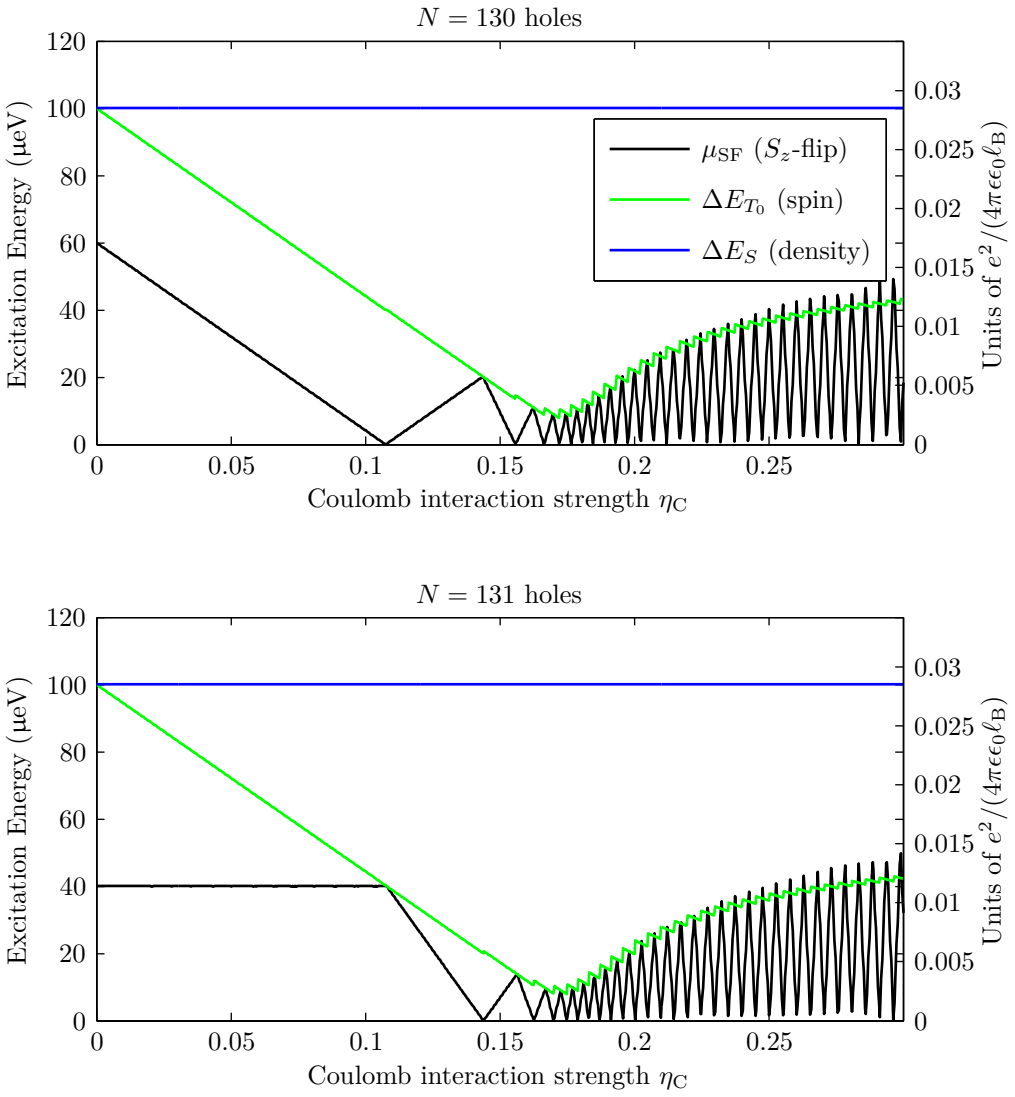

Figure 5.2: MDD edge excitation energies as a function of the Coulomb interaction strength η_C, for both even (top) and odd (bottom) occupation numbers. As labeled in the legend, we plot the spin-flip energy $\mu_{SF} = \min(\mu^+_{SF}, \mu^-_{SF})$, and the lowest-energy S_z-preserving excitations for the outermost holes of the MDD, corresponding to spin (triplet, ΔE_{T_0}) and density (singlet, ΔE_S) excitations. The Coulomb interaction suppresses the spin excitation energies (both μ_{SF} and ΔE_{T_0}), eventually leading to a series of S_z-flips of the ground state, but leaves the density excitation ΔE_S unchanged. Parameters used in this calculation: $B_\perp = 0.65$ T, $\Delta E_{SP} = 100$ μeV, $E_Z = 40$ μeV, $R_{AD} = 400$ nm.

force. For a given set of parameters, it is therefore important to check the stability of the MDD, using Eq. (1.92) on page 28. A phase diagram showing the locations of ground-state spin-flips and the instability point for a parabolic potential is given in Fig. 5.3. In order to compare the model with our experimental data, we are interested in the region around the first few transitions in the ground-state spin S_{z0} away from the spin-unpolarised state. These spin-flips correspond to the 'kinks' in μ_{SF} which appear in Fig. 5.2. In particular, in order to model the spin-pumping behaviour observed in the non-linear transport measurements presented in §4.3.3, we require the regime in which $S_{z0} = \frac{1}{2}$ for odd-N configurations, but $S_{z0} = 1$ for even-N configurations, which is shaded in grey in Fig. 5.3. These calculations show that the MDD is the stable ground state throughout the low-S_z parameter range in which we are interested, and remains so up to a significant value of the ground-state polarisation.

The choice of potential has only a very small effect on the dynamics of the edge, especially for energy scales at which we can approximate the radial gradient as locally linear, but it can affect the stability of the MDD phase. For a parabolic potential, the MDD first becomes unstable at the *centre* of the dot, as shown in Fig. 1.8 on page 29, since the central holes have the largest contribution from the Coulomb interaction. If we consider instead a more realistic 'bell-shaped' potential, with the gradient at R_{AD} set appropriately to match ΔE_{SP} at the edge, the added depth of the confining potential at the centre counteracts this effect and causes the MDD phase to be stable for an even greater range of parameter space. If the bell shape becomes so narrow that the gradient at the edge is rapidly flattening with increasing R, the opposite is true: the MDD first becomes unstable at the *edge*, since the confinement for the outer spin drops rapidly with increasing S_z. We expect that the most realistic situation for typical device parameters is a bell-shaped potential with characteristic 'width' similar to R_{AD}. Such a potential is nearly the ideal with regards to exploring MDD physics, since this is the shape for which the MDD phase is at its most stable.

5.1.3 Excitation spectra

For circularly-symmetric potentials, the z-projection of the total orbital angular momentum (AM), given by $M = \sum_i L_{zi}$, where L_{zi} is the orbital quantum number of the i^{th} particle, is a good quantum number of the multi-particle antidot state. Given a fixed number of holes N_{h} and the spin-projection S_z, the minimum value which M may take

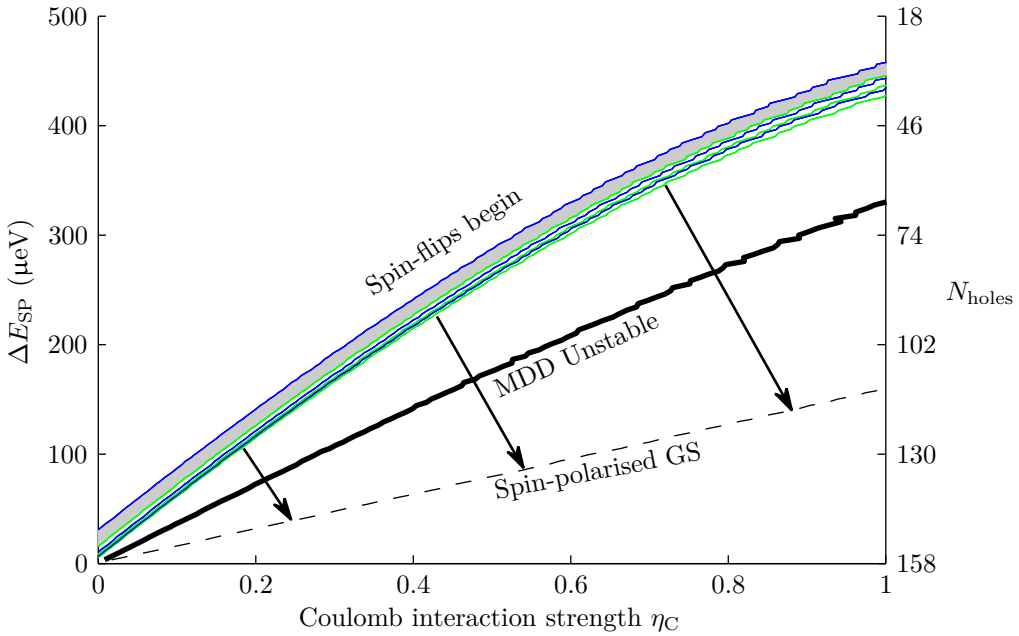

Figure 5.3: Phase diagram of the MDD ground state for a parabolic antidot as a function of the Coulomb interaction strength η_{C} and ΔE_{SP}. The first few transitions of S_z are shown for both odd-N (green) and even-N (blue) configurations, and arrows note the direction of increasing S_z. Below the dashed black curve, the ground-state MDD is fully spin polarised. The grey shaded region between the first two spin flips denotes the regime in which both $S_{z0} = \frac{1}{2}$ for odd-N, and $S_{z0} = 1$ for even-N configurations, as required for the spin-pumping mechanism described in §4.3.3. The thick black curve marks the boundary of the MDD phase, below which MDDs are unstable. For a parabolic potential, the number of holes within the fixed radius $R_{\mathrm{AD}} = 400\,\mathrm{nm}$ varies as a function of ΔE_{SP} as marked on the right-hand axes, since the length scale $\ell = \ell_{\mathrm{B}}/\sqrt{b}$ depends on the confinement, in terms of the confinement parameter b defined by Eq. (1.28) on page 9. Other parameters used in this calculation: $B_{\perp} = 0.65\,\mathrm{T}$, $E_{\mathrm{Z}} = 30\,\mu\mathrm{eV}$.

due to Fermi exclusion is

$$\begin{aligned} \min(M) &= \tfrac{1}{4}N_{\rm h}(N_{\rm h}-2)+S_z^2 \\ &= \tfrac{1}{2}N_{\uparrow}^{\rm h}(N_{\uparrow}^{\rm h}-1)+\tfrac{1}{2}N_{\downarrow}^{\rm h}(N_{\downarrow}^{\rm h}-1). \end{aligned} \tag{5.9}$$

The MDD is the single Slater orbital with this minimum value of M, and is therefore an eigenstate of the interacting Hamiltonian. If the MDD is stable, then it will be the sole ground state configuration, $|\mathrm{MDD}\rangle = |N_{\rm h}, S_z\rangle_0$. We can therefore sort the *excitations* of this MDD ground state by the number of additional AM quanta, $\Delta M = M - \min(M) = 1, 2, \ldots$, required to form each state. We write these states in the form $|N, S_z, \Delta M, p\rangle$, where $p = 1, 2, \ldots, d$ labels the states within each subspace of definite AM, and the dimension d of each subspace is the number of ways of distributing ΔM quanta of AM amongst the particles in the MDD, accounting for Fermi exclusion.

We can obtain excited-state Slater orbitals with definite ΔM by promoting individual particles of the MDD to obtain such states, but these 'fermionic' configurations, defined by occupation numbers $(\mathbf{n}_{\uparrow}^{\rm h}, \mathbf{n}_{\downarrow}^{\rm h})$, are not eigenstates of the Hamiltonian in general. This is because the individual AM quantum numbers L_{zi} of the SP states are not conserved by the interaction term in the Hamiltonian, which produces nonzero matrix elements between pairs of Slater orbitals which differ by exactly two occupation numbers [46]. It is possible, however, to determine the eigenspectrum by constructing the full set fermionic basis states for a given value of ΔM and then diagonalising the resulting matrix Hamiltonian. The excitations plotted in Fig. 5.2 are examples of this procedure for the $\Delta M = 1$ subspace, whose eigenspace consists of a 'spin' and a 'density' excitation. In the fermionic basis, the excitations consist of an individually-excited spin-$\uparrow$ or spin-$\downarrow$ particle, which have roughly similar energies. After diagonalising the 2×2 matrix constructed from these states, we find that the eigenstates are a spatially-symmetric 'triplet' excitation with a small energy gap, corresponding to a change in S^2, and a spatially-antisymmetric 'singlet' excitation corresponding to a modulation of the electron density along the edge, with a much larger energy gap. Excitation energies for larger values of ΔM are shown in Fig. 5.4, with the corresponding sets of fermionic excitations provided for comparison. For each ΔM subspace, the largest excitation corresponds to a singlet transition which is essentially a pure density modulation similar to the 'bosonic' modes of a Tomonaga-Luttinger liquid for spinless electrons [52]. The calculations in Fig. 5.4 correspond to the 'crossover' region of Fig. 5.2 at $\eta_{\rm C} = 0.17$, and we find in this regime that the singlet mode is well-separated from the remaining transition energies for all ΔM. The lower-energy modes consist of combinations of spin and density excitations.

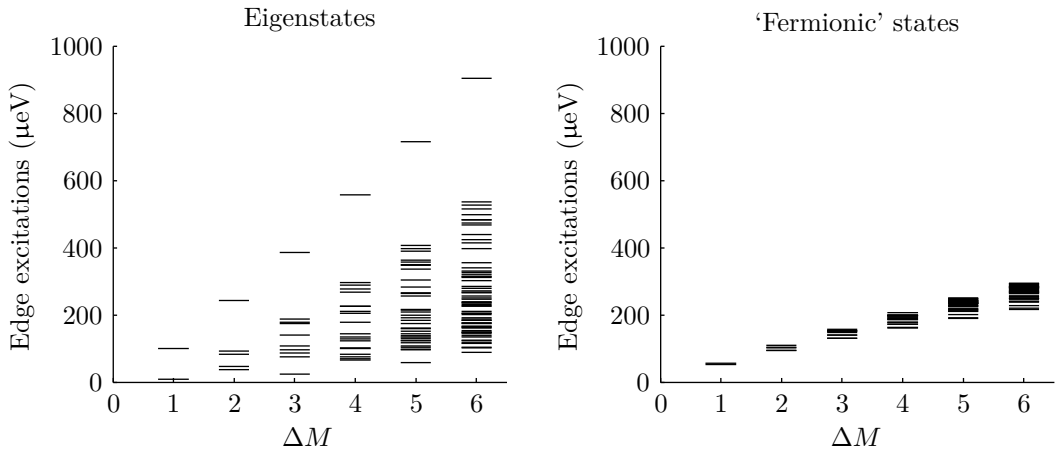

Figure 5.4: Comparison of edge excitation energies obtained by diagonalising the interacting Hamiltonian within subspaces of definite AM (left), and the corresponding excitations within the 'fermionic' picture obtained by promoting individual particles to higher orbitals (right). The subspaces are labeled by ΔM, the number of AM quanta added to the MDD state. Within each AM subspace, the 'fermionic' excitation energies are simply the diagonal terms of the Hamiltonian matrix. Parameters used in this calculation: $B_\perp = 0.65$ T, $\Delta E_{\mathrm{SP}} = 100$ μeV, $E_{\mathrm{Z}} = 40$ μeV, $R_{\mathrm{AD}} = 400$ nm, $\eta_{\mathrm{C}} = 0.17$.

5.2 Model of non-linear transport

To directly compare the predictions of the MDD model with our experimental results, we need a flexible method to compute the antidot conductance, preferably in both the linear and non-linear regimes. The easiest method by far is to construct and solve a rate-equation matrix for the steady-state occupation probabilities of the antidot, within the sequential-transport framework presented in §2.3. With this method, the physics of the antidot enters the calculation in the form of

1. A set of eigenstates and associated energy spectrum, and
2. A set of matrix elements for transitions between states. In the simplest case these are simply a set of boolean 'selection rules.'

The remaining parts of the calculation, incorporating the tunnel barriers (possibly spin- and/or energy-dependent) and bias (possibly mode-dependent through the non-equilibrium population of edge modes), form a 'shell' within which we can explore essentially arbitrary models of the antidot physics. Limitations of the model stem mainly from the perturbative approximation to the tunneling rates, which is strictly valid only in

the 'weak coupling' regime where all the tunnel couplings $\Gamma_{r\sigma}$ satisfy $h\Gamma_{r\sigma} \ll kT$. The amplitude of the transmission resonances in our experiments imply typical couplings of order $\Gamma \approx 500\,\mathrm{MHz}$–$1\,\mathrm{GHz}$, with corresponding lifetime broadening $h\Gamma \approx 2$–$4\,\mu\mathrm{eV}$. With an electron temperature around $T_{\mathrm{elec}} \approx 50\,\mathrm{mK}$, we have $kT \approx 5\,\mu\mathrm{eV}$ and so we are close to the edge of the model's range of validity. We still find very close agreement between the features observed in the experiment and the predictions of our model, but it is important to bear in mind that the sequential transport model does not include lifetime broadening due to quantum fluctuations, or higher order 'cotunneling' processes which may be present in the experiment. Further documentation on the model discussed in this section, along with the programs themselves, implemented in the MATLAB® programming language, are available in the open repository *DSpace@Cambridge*.[1]

For a given model of the antidot spectrum, only a subset of configurations participate in transport due to energy considerations, but in general it can be a difficult problem to determine which states to keep, especially for systems of many particles which have a very large number of possible configurations. Given a set of values for the external fields (gate voltages, magnetic field, and drain-source bias), we can determine the ground-state configuration, but if the energy spacing between states is small, or if V_{DS} is large, the steady-state solution will contain significant populations of many exited states as well. Our solution to this problem is to start with a relatively small subset of states, chosen to be the ground-state configuration plus all of the excited states which are 'accessible' through a single tunneling event, i.e., the states with energy ε_i such that the chemical potential

$$\mu_i = \varepsilon_i - \varepsilon_{\mathrm{GS}} \tag{5.10}$$

is within the 'energy window' defined by the chemical potentials of the leads:

$$\left[\min(\mu_{\mathrm{S}}, \mu_{\mathrm{D}}) - E_{\mathrm{Therm}},\, \max(\mu_{\mathrm{S}}, \mu_{\mathrm{D}}) + E_{\mathrm{Therm}}\right], \tag{5.11}$$

where $E_{\mathrm{Therm}} \approx 4kT$. If we find that many of these excited states have significant occupation probabilities, we can add to this set all of the states which are 'connected' to the significant excited states through the same rule, in terms of the chemical potentials for transitions from each excited state. By continuing to expand the set of states in this way, we will eventually reach a situation in which all of the newly-added states have sufficiently low occupation probability for convergence of the transport current to a desired tolerance. For both conceptual and computational purposes, it is useful to think of the

[1] *DSpace@Cambridge* is the institutional repository of the University of Cambridge, available at http://www.dspace.cam.ac.uk/.

system in terms of an abstract graph, in which the set of configurations correspond to nodes and the selection rules define the connections, or 'edges.' The procedure described above always results in a graph which is *fully-connected*, meaning that it is possible to move between any two nodes of the graph given enough transitions. It is important to maintain this property throughout any manipulations of the model, to avoid a situation in which the population can become artificially 'trapped' in a disconnected portion of the graph.

To make comparisons with our spin-selective measurements, we need a method of organising the antidot configurations which allows us to keep track of the *spin* of each electron which tunnels into or out of the antidot. Below we outline the procedure we use to accomplish this, using the fermionic configurations defined by occupation vectors $(\mathbf{n}_\uparrow, \mathbf{n}_\downarrow)$ as an example.[1] To begin, we consider only transitions between ground-state configurations with different occupation numbers N at zero bias, with chemical potentials $\mu_0(N)$. Given a set of capacitances as described in §2.3, the condition $\mu_0(N) = 0$ defines the value of the gate voltage V_G at which charge degeneracy occurs for the $N \leftrightarrow N+1$ transition at zero bias. In between these resonance positions, the condition $\mu(N-1) = -\mu(N)$ defines an 'inflection point' within each Coulomb blockade region. On one side of the inflection point we need only consider configurations with occupation numbers $(N-1, N)$, while on the other we consider only $(N, N+1)$ states. In the plane of $(V_\mathrm{G}, V_\mathrm{DS})$ these become inflection lines which pass vertically through the centre of each Coulomb diamond, and divide the calculation region by the occupation numbers involved. This means that we cannot fully model the transport at high bias above the crossings of adjacent ground state lines, since we would then need to consider more than two sets of occupation states of the antidot.

Next, we divide the configurations within each region (defined by occupation numbers N, $N+1$) by their total spin projection S_z. Suppose the ground-state spin for the N-particle state is S_{z0} and for the $N+1$ particle state is $S_{z0} - \frac{1}{2}$. Given these values, we

[1] For the purposes of this discussion we consider electron occupation numbers since this is the standard picture for quantum dot transport, but these are simply related to the hole occupation numbers by $\mathbf{n}^\mathrm{h}_\sigma = \mathbf{1} - \mathbf{n}^\mathrm{e}_\sigma$.

begin by constructing the vector of configurations:

$$\{|\Psi_{\mathrm{AD}}\rangle\} = \begin{pmatrix} \{|N{+}1, S_{z0}{-}\frac{3}{2}\rangle\} \\ \{|N, S_{z0}{-}1\rangle\} \\ \{|N{+}1, S_{z0}{-}\frac{1}{2}\rangle\} \\ \{|N, S_{z0}\rangle\} \\ \{|N{+}1, S_{z0}{+}\frac{1}{2}\rangle\} \\ \{|N, S_{z0}{-}1\rangle\} \end{pmatrix}, \tag{5.12}$$

where each $\{|N, S_z\rangle\}$ corresponds to a vector of individual states $|N, S_z, q_\uparrow, q_\downarrow\rangle$, where q_σ labels the configuration of the spin-σ particles. In the presence of interactions these states are not true eigenstates of the Hamiltonian, but they provide a qualitative approximation to the excitation gaps in most cases. In §5.3.3 later in this chapter we consider an effective model to better capture the physics of the edge excitations. For any model, the number of excited states to include is determined through a consideration of the chemical potentials for transitions to or from the ground states with spin $S_z \pm \frac{1}{2}$ as described above. With this arrangement for the configurations, the selection rules take the block-matrix form

$$\begin{pmatrix} 0 & W^{+\downarrow}_{S_{z0}-1} & & & \cdots & 0 \\ W^{-\downarrow}_{S_{z0}-\frac{3}{2}} & 0 & W^{-\uparrow}_{S_{z0}-\frac{1}{2}} & & & \vdots \\ & W^{+\uparrow}_{S_{z0}-1} & 0 & W^{+\downarrow}_{S_{z0}} & & \\ & & W^{-\downarrow}_{S_{z0}-\frac{1}{2}} & 0 & W^{-\uparrow}_{S_{z0}+\frac{1}{2}} & \\ \vdots & & & W^{+\uparrow}_{S_{z0}} & 0 & W^{+\downarrow}_{S_{z0}+1} \\ 0 & \cdots & & & W^{-\downarrow}_{S_{z0}+\frac{1}{2}} & 0 \end{pmatrix}, \tag{5.13}$$

where, assuming the vectors of states $\{|N, S_z\rangle\}$ are listed as subsequent groups of spin-$\uparrow$ states (labeled by $q_\uparrow$) for each spin-$\downarrow$ state (labeled by $q_\downarrow$), the sub-matrices $W^{\pm\sigma}_{S_z}$ are given by

$$W^{\pm\uparrow}_{S_z} = \mathbf{1}_\downarrow \otimes M^{\pm\uparrow}_{S_z}, \tag{5.14a}$$

$$W^{\pm\downarrow}_{S_z} = M^{\pm\downarrow}_{S_z} \otimes \mathbf{1}_\uparrow. \tag{5.14b}$$

The matrices $M^{\pm\sigma}_{S_z}$ contain the selection rules for transitions in the spin-σ configuration individually, and are easily worked out by comparing the occupation vectors $\mathbf{n}_\sigma$ of the initial and final states. For example, $M^{+\uparrow}_{ij} = 1$ whenever the $q_\uparrow = i$ state of the $N{+}1$

configurations results from adding a single spin-↑ particle to the $q_\uparrow = j$ state of the N configurations, which we can write as

$$M_{ij}^{+\uparrow} = \begin{cases} 1 & \text{if} \quad \mathbf{n}_\uparrow(i) \cdot [\mathbf{1} - \mathbf{n}_\uparrow(j)] = 1, \\ 0 & \text{otherwise.} \end{cases} \tag{5.15}$$

Similar relations determine the selection rules for other types of processes.

The rate matrix has a similar form to Eq. (5.13), where the nonzero selection rules are replaced by the transition rates

$$R_{ij}^{\pm\sigma} = \sum_{r=\mathrm{S,D}} \Gamma_\sigma^r(\mu_{ij}) W_{ij}^{\pm\sigma} f_r^\pm(\mu_{ij}), \tag{5.16}$$

where $f_r^+ = f_r$ is the Fermi function of lead r, and $f_r^- = 1 - f_r$. As described in §2.3, we then add diagonal elements to the rate matrix to impose a net balance of rates in equilibrium, and an extra row of ones to enforce normalisation, constructing the master equation in the form of Eq. (2.82) on page 53. The solution to this equation gives the steady state occupation probability of each state $|N, S_z, q_\uparrow, q_\downarrow\rangle$, which we then use to compute the current flowing through the system. The current is most easily computed using Eq. (2.83), by isolating the transition rate involving only a single lead, e.g. for the source,

$$S_{ij}^{\pm\sigma} = \Gamma_\sigma^{\mathrm{S}}(\mu_{ij}) W_{ij}^{\pm\sigma} f_{\mathrm{S}}^\pm(\mu_{ij}). \tag{5.17}$$

Including signs to account for the direction of current flow, we can then write

$$I = e \sum_{ij} T_{ij} P_j, \tag{5.18}$$

where P_j are the equilibrium occupation probabilities and

$$T = \begin{pmatrix} 0 & S_{S_{z0}-1}^{+\downarrow} & & & \cdots & 0 \\ -S_{S_{z0}-\frac{3}{2}}^{-\downarrow} & 0 & -S_{S_{z0}-\frac{1}{2}}^{-\uparrow} & & & \vdots \\ & S_{S_{z0}-1}^{+\uparrow} & 0 & S_{S_{z0}}^{+\downarrow} & & \\ & & -S_{S_{z0}-\frac{1}{2}}^{-\downarrow} & 0 & -S_{S_{z0}+\frac{1}{2}}^{-\uparrow} & \\ \vdots & & & S_{S_{z0}}^{+\uparrow} & 0 & S_{S_{z0}+1}^{+\downarrow} \\ 0 & \cdots & & & -S_{S_{z0}+\frac{1}{2}}^{-\downarrow} & 0 \end{pmatrix}. \tag{5.19}$$

This procedure is easily generalised to account for additional effects. For example, we

can include spin-conserving relaxation of excited states within each set $\{|N, S_z\rangle\}$ by adding block matrices describing these processes to the main diagonal of Eq. (5.13). Spin non-conserving relaxation due to spin-orbit coupling or the hyperfine interaction could also be included by adding terms to the next off-diagonal blocks (connecting states $\{|N, S_z\rangle\}$ with $\{|N, S_z \pm 1\rangle\}$). Note, however, that this model only obtains the steady-state ($t \to \infty$) configuration, so we are not able to investigate coherent effects due to spin-precession with this procedure.

In calculations, we iterate this procedure until we reach convergence, adding additional S_z-configurations and excited states until the occupation probability of the 'outermost' states falls below a given threshold. We can see at this point how it is easily possible to produce very large matrices, since the total number of configurations is given roughly by

$$\begin{aligned}\text{dim} = (\#\ \text{spin-}\uparrow\ \text{states per}\ S_z) \times (\#\ \text{spin-}\downarrow\ \text{states per}\ S_z) \\ \times (\#\ S_z\ \text{configurations}).\end{aligned} \quad (5.20)$$

Luckily, the rate matrix is also very sparse, which makes solving the rate equations numerically tractable in most cases. In some important cases, however, the problem becomes so large that solving the master equation is computationally prohibitive. Unfortunately, this is often the case around the 'crossover' region discussed in §5.1, since we need to consider a large number of S_z configurations when the S_z-excitation energy is small, and this is exactly the regime we wish to investigate. The computation-limiting step is almost always the Gaussian elimination procedure used to solve the master equation, which scales badly with the dimension of the rate matrix. Even though we take advantage of parallel-computing resources provided by *CamGrid*,[1] we run into insurmountable memory limitations with matrices above a given size.

To solve this problem, we have developed a number of routines which attempt to shrink the system in an intelligent way, keeping only the states which contribute to transport for a given set of external parameters, since this is often a small subset of the total number of possible states determined from energy considerations. These routines are inspired by the picture of the rate matrix as an abstract graph, and rely on several computationally-efficient algorithms from the field of graph theory (see the book by Bollabas [99] for a good introduction). After solving the master equation for an initial subset of states as described above, we determine the 'important' states by threshold-

[1] *CamGrid* is a distributed computing resource coordinated by the Cambridge eScience Centre. More information is available at http://www.escience.cam.ac.uk/projects/camgrid/.

ing the probability vector. We then use several graph algorithms, particularly Dijkstra's shortest-path algorithm [100], to determine the minimal connected graph which incorporates the important nodes, and then 'expand' these nodes into additional excited states as needed to achieve convergence. The level of approximation involved in this procedure may be carefully controlled, for instance by changing the threshold used to determine which states are retained, or the number of new states which are added in each iteration. Our tests have shown, for several important cases where the full matrices become impractically large, that we can use these methods to speed up the calculation by more than an order of magnitude with a loss of accuracy in the computed current much less than one percent. These routines were used in several of the calculations presented in this chapter, and they have been of critical importance in enabling a practical investigation of many of the features we discuss.

5.3 Comparisons with experimental results

At this point we are ready to use the transport calculations described in the previous section together with the MDD model of §5.1 to compare the predictions of our theory with the experimental results of Chapter 4. Below we show how the MDD model successfully reproduces both the observed spin-resolved conductance in linear response and the energy scales observed in the non-linear transport experiments, while non-interacting models fail to do so. We also investigate the 'spin-pumping' mechanism in more detail and consider an effective theory to describe the edge-excitations of the MDD.

5.3.1 Non-linear transport

We begin with a consideration of the non-linear transport experiments discussed in §4.3.3. The important features of these experiments, including the associated spin-resolved measurements at zero bias, are summarised by Fig. 4.11, which we use in this section as a reference for comparison of theoretical results. Recall that the observations are characterised by three important energy scales inherent to the antidot physics:

- The spin-flip excitation energy $\mu^{\pm}_{\mathrm{SF}} = U(S_z \pm 1) - U(S_z)$, which must always satisfy $\mu^{\pm}_{\mathrm{SF}} \lesssim E_{\mathrm{Therm}} \approx 10\ \mu\mathrm{eV}$ such that transport is not spin-selective.
- The orbital excitation energy E_{ex} inferred from the extra lines in non-linear transport measurements. The separations of these lines imply that $E_{\mathrm{ex}} \approx 50$–$60\ \mu\mathrm{eV}$.

- The spin-pumping energy scale $\Delta\mu_\uparrow = \mu_\uparrow(N, S_z{+}1) - \mu_\uparrow(N, S_z)$, which determines the size of the 'break' in ground-state lines due to dynamic pumping of S_z caused by the combination of DC bias and asymmetric spin-dependent tunnel barriers. This is observed to be midway between μ_{SF} and E_{ex}, with characteristic spacings around $\Delta\mu_\uparrow \approx 20$–$30\ \mu\mathrm{eV}$.

Within the SP model, these are given by (see Eqs. (1.31), (4.20), and the discussion on page 100 for more details)

$$\mu_{\mathrm{SF}}^{\pm} = (1 \pm 2S_z)\Delta E_{\mathrm{SP}} - E_{\mathrm{Z}}, \tag{5.21a}$$

$$E_{\mathrm{ex}} = \pm s E_{\mathrm{Z}} + j\Delta E_{\mathrm{SP}}, \tag{5.21b}$$

$$\Delta\mu_\uparrow = \Delta E_{\mathrm{SP}}, \tag{5.21c}$$

in terms of the SP energy scales ΔE_{SP} and E_{Z}. It is relatively easy to see that these relations are inconsistent with the values observed in the experiment, but we provide a few specific examples of calculations for further illumination.

In Fig. 5.5 we show transport calculations within the non-interacting model for two different choices of ΔE_{SP}, with $E_{\mathrm{Z}} = 30\ \mu\mathrm{eV}$ as expected at $B = 1.2\ \mathrm{T}$. The other parameters in the simulation, such as the capacitances between the antidot states and external voltages and the strength and asymmetry of tunnel barriers, are chosen based on the slopes and amplitudes of the lines observed in Fig. 4.11 as described in §2.3. In the first calculation (left panels) we choose $\Delta E_{\mathrm{SP}} = 60\ \mu\mathrm{eV}$ in order to match the observed excitation spectrum. This is mostly successful (the negative differential conductance (NDC) is more pronounced then in the experiment but this is affected by our particular choice of tunnel barriers), but the simulation clearly fails to reproduce the spin-resolved conductance at zero bias. As expected when $\mu_{\mathrm{SF}} \approx 30\ \mu\mathrm{eV} > E_{\mathrm{Therm}}$, the model predicts spin-selective resonances with alternate polarisation for successive peaks, contrary to our observations. If we instead choose $\Delta E_{\mathrm{SP}} = 30\ \mu\mathrm{eV}$ (right panels) to match the observed value of $\Delta\mu_\uparrow$, then we observe 'breaks' in the ground-state line tracking the drain chemical potential, as predicted by the spin-pumping model (see Fig. 4.12 on page 99). The spin-flip energy μ_{SF} is also much reduced, and so the spin-resolved conductance is consistent with experiments. The excitation spectrum, however, is clearly inconsistent with our measurements, with lines spaced much too closely together and no clear NDC.

We therefore proceed to add interactions to the model, including the Hartree-Fock contribution to the configuration energy of each state, which we compute for the Slater-

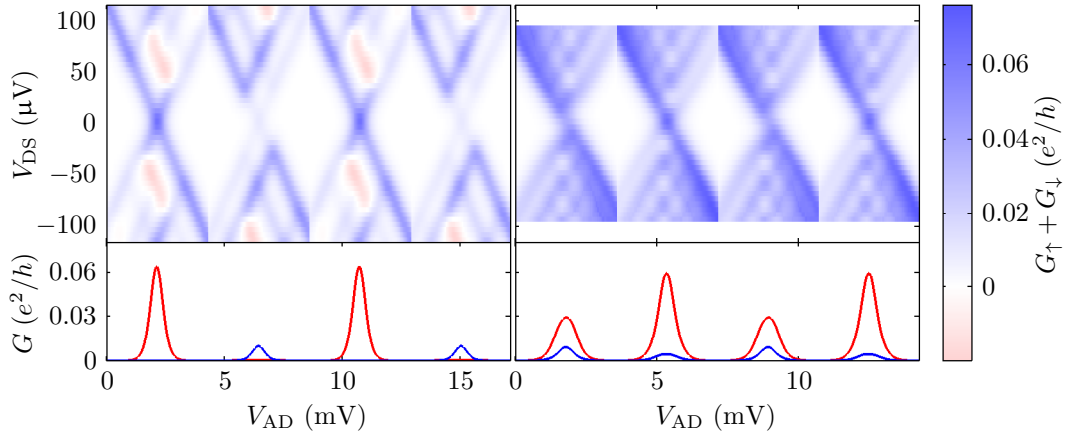

Figure 5.5: Transport calculations for the single-particle model, for comparison with the data in Fig. 4.11 on page 98. Total conductance $G_\uparrow + G_\downarrow$ is plotted in the upper panels, with the zero-bias spin-resolved conductance shown in the lower panels, where red (blue) curves represent $G_\uparrow$ ($G_\downarrow$). Left — If we choose $\Delta E_{SP} = 60$ μeV to match the excitations in Fig. 4.11, the zero-bias conductance is spin-polarised in contradiction to the experiment. Right — If we set $\Delta E_{SP} = 20$ μeV instead to match μ_{SF}, we reproduce the splitting of the 'broken' ground-state lines, but the excitations observed in the transport window are clearly much more closely-spaced than in the experimental data, and we observe no NDC. Parameters used in this calculation: $E_Z = 30$ μeV, $R_{AD} = 400$ nm, $T = 55$ mK, $\Gamma_{S\uparrow} = \Gamma_{D\uparrow} = \Gamma_{S\downarrow} = 600$ MHz, $\Gamma_{D\downarrow} = 50$ MHz.

determinant wave function corresponding to the *empty* (hole) orbitals of the fermionic state $|N, S_z, q_\uparrow, q_\downarrow\rangle$. To fix the strength of the Coulomb interactions, controlled by η_C, we use excitation energy diagrams like Fig. 5.2 and phase diagrams like Fig. 5.3. Given a value for the orbital excitation scale, which is set by the constant ΔE_{SP} for a parabolic potential,[1] we choose η_C appropriately to reach a point in the crossover region where S_z-flips just start to occur. Some fine tuning is often required to reproduce specific features like the spin pumping and NDC observed in the experiment, but this is to be expected since these effects rely on a delicate balance between different excitation scales of the antidot and strengths of the various tunnel-couplings, and we have tuned the experimental system quite substantially in order to observe them in the first place.

An example of the calculated transport including interactions is shown in Fig. 5.6. Most of the parameters are the same as in Fig. 5.5, although we have chosen the tunnel

[1] N.B. We are only probing the physics of the *edge*, so assuming the potential varies slowly on the scale of ℓ_B, the details of the potential are not important. The potential shape is mainly important for the stability of the MDD phase, as discussed in §5.1.2.

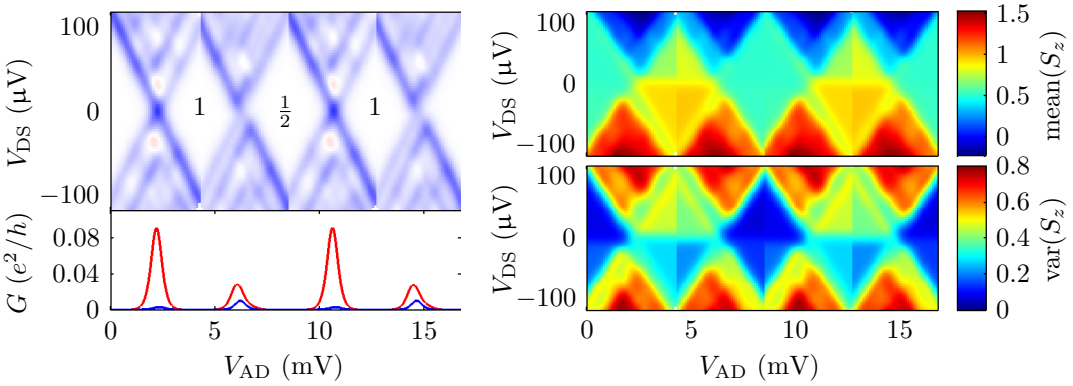

Figure 5.6: Transport calculations for the antidot MDD model. Top left — Total non-linear conductance $G_\uparrow + G_\downarrow$, with colour scale as in Fig. 4.11. Numbers printed in each Coulomb diamond show the ground-state spin configuration. Bottom left — Zero-bias spin-resolved conductances $G_\uparrow$ (red curve) and $G_\downarrow$ (blue curve). Right panels — Mean spin configuration (top) showing bias-induced pumping, and the standard deviation (bottom), corresponding to the non-linear transport calculations in the top left. Parameters used in this calculation: $\Delta E_{\mathrm{SP}} = 70\,\mu\mathrm{eV}$, $E_{\mathrm{Z}} = 40\,\mu\mathrm{eV}$, $R_{\mathrm{AD}} = 400\,\mathrm{nm}$, $T = 55\,\mathrm{mK}$, $\Gamma_{\mathrm{S}\uparrow} = \Gamma_{\mathrm{D}\uparrow} = 900\,\mathrm{MHz}$, $\Gamma_{\mathrm{S}\downarrow} = 300\,\mathrm{MHz}$, $\Gamma_{\mathrm{D}\downarrow} = 60\,\mathrm{MHz}$, $\eta_{\mathrm{C}} = 0.08$.

barriers more carefully to reproduce the peak amplitudes in Fig. 4.11. Qualitatively, this model does an excellent job of reproducing our observations. The excitations have the correct scale, and the exchange interactions reduce μ_{SF} sufficiently to break the spin-selectivity at zero bias. Moreover, the interactions suppress $\Delta\mu_\uparrow$ as well, such that the breaks in ground-state lines have the right magnitude. Upon close inspection, it is also apparent that the spin-↑ conductance peaks corresponding to these 'frustrated' resonances are widened and asymmetric in qualitative agreement with the experiment.

5.3.2 Spin pumping

Within our transport model, we can gain further insight into the spin-pumping mechanism which causes the breaks in ground-state lines near zero bias. In particular, we can compute both the average spin configuration and the standard deviation from the occupation probabilities:

$$\mathrm{mean}(S_z) = \sum_i P_i S_z(i), \tag{5.22}$$

$$\mathrm{stdev}(S_z) = \left[\sum_i P_i \Big(S_z(i)\Big)^2 - \Big(\mathrm{mean}(S_z)\Big)^2\right]^{1/2}, \tag{5.23}$$

as shown in the right-hand panels of Fig. 5.6. Plots of the average spin show the pumping directly; in this case a positive (negative) bias drives the system to a lower (higher) spin than in equilibrium due to the asymmetric tunnel barriers. The standard deviation gives a measure of the level of 'frustration' at a given configuration, and increases in regions where the pumping mechanism competes with energy considerations to determine the steady-state occupations. Note that the vertical discontinuities visible within the Coulomb blockade diamonds correspond to the points at which we switch between a consideration of N–1 $\leftrightarrow$ N to N $\leftrightarrow$ N+1 transitions. The available pumping mechanisms change across these boundaries, affecting the standard deviation of S_z in particular. This does not affect the reliability of the transport results, however, mainly reflecting the fact that the steady-state occupations are not particularly well-defined in the Coulomb-blockaded regions, since no current is flowing to provide equilibration.

At this point we briefly consider another experiment which demonstrates the spin-pumping mechanism. In standard non-linear transport the pumping is provided by the combination of the bias and spin-dependent tunnel barriers which are more strongly asymmetric for one spin than the other. A similar effect occurs if we supply a spin-dependent *bias*, using the selective-injection technique. The quantum Hall edge modes cannot withstand a large non-equilibrium bias without suffering significant equilibration, but we have determined through injection/detection measurements with the quantum point contacts on our device that the $\nu = 3$ and $\nu = 4$ modes can maintain differences in chemical potentials of up to $\approx$ 30–40 μeV. Since this is greater than the scale we expect for the spin-flip potentials $\mu_{\mathrm{SF}}^{\pm}$, spin-pumping experiments using this technique are feasible.

To apply a non-equilibrium bias without driving large currents through the constrictions on either side of the antidot, we apply a DC potential to the *bulk modes* via contact α on the source side of the device, including the spin-↓ mode $\nu = 4$. This is accomplished by setting the injector constriction to $f_{\mathrm{Inj}} = 3$, and connecting the injector ohmic contact δ to DC ground, such that the modes ν = 1–3 reach the antidot with $\mu_{\mathrm{S}\uparrow} = 0$, while modes $\nu \geq 4$ have the chemical potential $\mu_{\mathrm{S}\downarrow} - eV_{\mathrm{S}}$. To measure the effect of this non-equilibrium potential on the transport, we apply a small AC excitation to modes ν = 1–3 through the injector.[1] Since the $\nu = 4$ mode does not feel the excitation, the antidot transmission resonances we measure are due to spin-↑ transport only. With this experiment we are therefore probing the effect on $G_{\uparrow}$ of a change in the chemical potential $\mu_{\mathrm{S}\downarrow}$, while the remaining $\mu_{\mathrm{S}\uparrow} = \mu_{\mathrm{D}\uparrow} = \mu_{\mathrm{D}\downarrow} = 0$.

[1] It is also possible to apply the excitation to modes $\nu \geq 4$ with the DC bias, but this gives a much weaker signal since the tunnel barriers are much higher for spin-↓ transport than for spin-↑.

The results of this experiment are depicted in the top-left panel of Fig. 5.7. The bias induces clear transitions at specific values of V_S for each resonance, providing direct measurements of the antidot spin-flip potentials $\mu_{SF}^{\pm}$. Note that, aside from the stepwise dislocations, the resonance positions are independent of V_S. This implies that the capacitive coupling between the antidot states and the external voltage V_S is very small. This is to be expected since the $\nu \geq 4$ states are separated from the antidot by the $\nu = 3$ mode, and provides further evidence that the difference in chemical potentials $\mu_{S\uparrow}$ and $\mu_{S\downarrow}$ is maintained at the position of the antidot.

The remaining panels in Fig. 5.7 describe a simulation of the experiment using our transport model. Clear discontinuities are observed in the resonances with spacings corresponding to $\Delta\mu_{\uparrow}(N, S_z)$, as the steady-state occupation of the dot changes due to the non-equilibrium bias. This behaviour is reproduced by the transport model, calculated for the same set of system parameters as in Fig. 5.6, but with the bias applied only to the spin-$\downarrow$ electrons in the source lead. In this case, a positive (negative) bias corresponds to a reduced (increased) chemical potential for spin-$\downarrow$ in the source, and so a net flow of spin-$\downarrow$ electrons out of (into) the dot, thereby increasing (reducing) the steady-state S_z. The maximally-occupied spin is likely to flip once the bias reaches the appropriate spin-flip potential $\mu_{SF}^{\pm}$, but the resonance will only shift when *both* the N and N+1 configurations undergo a spin-flip. It is thus a complicated procedure to extract particular energy scales from experiments like this, but the potential to do so clearly exists, and for this purpose the simulations prove an invaluable tool for comparisons.

5.3.3 An effective model for excitations

As discussed in §5.1.3, the excited states which appear in our transport calculation are not eigenstates of the Hamiltonian when interactions are included. They do seem to have approximately the right energies, judging by the good qualitative agreement between the calculations in Fig. 5.6 and the experimental data in Fig. 4.11, but it would be better to have a justification for using them, or preferably to isolate the important characteristics which make the predictions of the model consistent with our experiments. We can compute the actual eigenspectrum by diagonalising the Hamiltonian for each set of fermionic orbitals at a given level of excitation, ΔM, but the selection rules for tunneling then become much more complicated. Furthermore, effects beyond Hartree-Fock mean-field theory are likely to be important for a full description of the excited states. Electron *correlation*, in particular, which is ignored in the Slater-orbital picture we use here, has been shown to modify the excitation of quantum-dot MDDs significantly

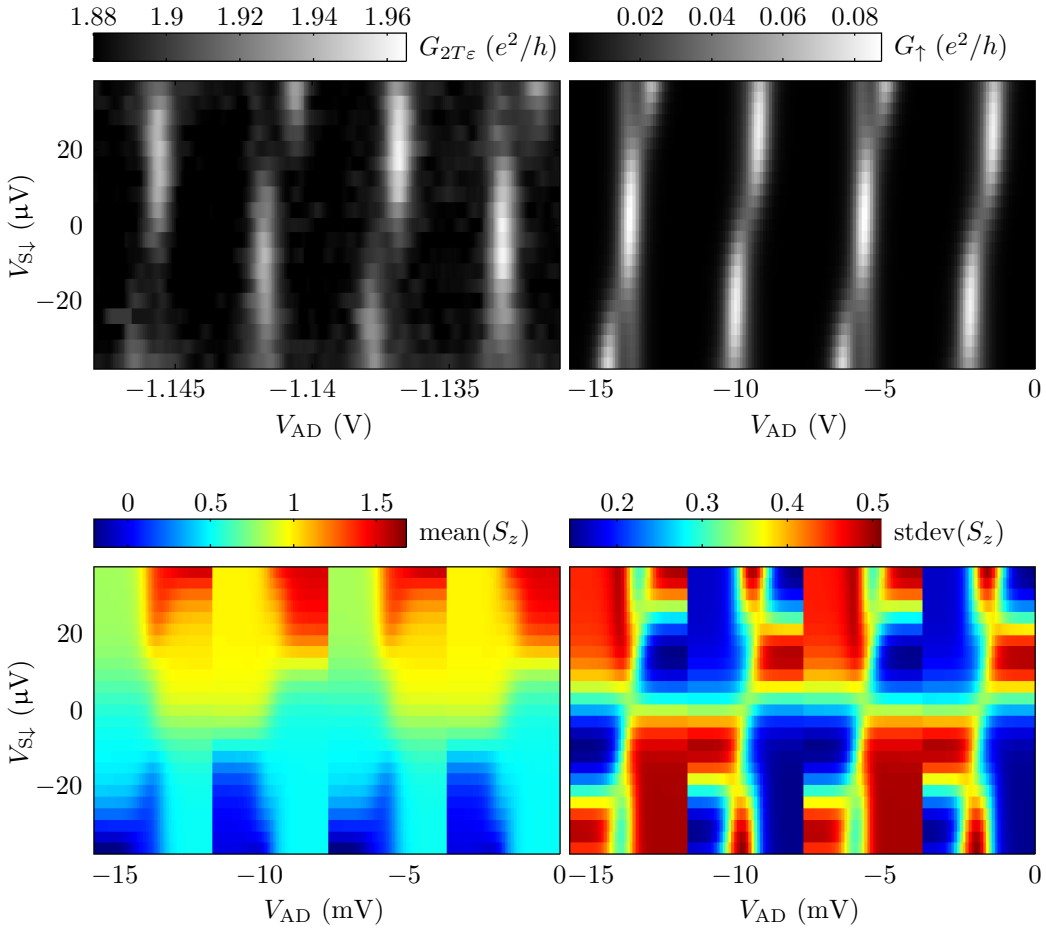

Figure 5.7: Top left — Experimental data showing two-terminal differential conductance at the detector (contact ε) with $f_{\mathrm{Det}} = f_{\mathrm{Inj}} = 3$, when DC bias is applied only to the modes $\nu \geq 4$ through contact α, and AC bias is applied to modes $\nu \leq 3$ through contact δ in the injector. Top right — Spin-↑ conductance computed in our model of this measurement, with DC bias applied to spin-↓ only, and AC bias applied to spin-↑ at the source. Bottom panels — Steady state values of the average (left) and standard deviation (right) of S_z within the calculation, showing the effects of spin pumping. The discontinuities in the Coulomb blockade regions result from the different pumping mechanisms available given the occupation numbers $(N, N{+}1)$ we consider in each region. These will be smoothed out in the real system. Parameters used in this calculation: $\Delta E_{\mathrm{SP}} = 50\,\mu\mathrm{eV}$, $E_{\mathrm{Z}} = 30\,\mu\mathrm{eV}$, $R_{\mathrm{AD}} = 400\,\mathrm{nm}$, $T = 55\,\mathrm{mK}$, $\Gamma_{\mathrm{S}\uparrow} = \Gamma_{\mathrm{D}\uparrow} = 900\,\mathrm{MHz}$, $\Gamma_{\mathrm{S}\downarrow} = 300\,\mathrm{MHz}$, $\Gamma_{\mathrm{D}\downarrow} = 60\,\mathrm{MHz}$, $\eta_{\mathrm{C}} = 0.05$.

[101]. But rather than introducing further complications to a model which already seems to work, we would prefer instead to simplify it, in order to distill the essential ingredients which are necessary to reproduce our results. In this section we therefore consider an 'effective' model for the excitation spectrum of the edge and a set of simple selection rules based on Luttinger Liquid theory, which are consistent with our experiments and succinctly describe the important physics of the system.

We have already seen that the $\Delta M = 1$ subspace consists of a pair of excitations which we identify respectively with a 'spin' and 'density' mode of the MDD edge. If we consider these to be the fundamental modes of excitation for the edge, then we can write a general antidot state in the form $|N, S_z, n_\mathrm{L}, n_\mathrm{S}\rangle$, where n_L and n_S are the number of excitations in the orbital (density) and spin modes, respectively. The energy of such a state is then simply

$$\hat{H}|N, S_z, n_\mathrm{L}, n_\mathrm{S}\rangle = \big(U_\mathrm{MDD}(N, S_z) + n_\mathrm{L}\varepsilon_L + n_\mathrm{S}\varepsilon_S\big)|N, S_z, n_\mathrm{L}, n_\mathrm{S}\rangle, \tag{5.24}$$

where ε_L and ε_S are the orbital- and spin-excitation energies associated with these edge modes, and U_MDD is the configuration of the unexcited MDD. Due to the spin-charge separation introduced by exchange, we expect that ε_S is significantly lower than ε_L. With a glance back to the eigenspectra in Fig. 5.4, we observe that this model will qualitatively reproduce the Hartree-Fock excitations, capturing the separation of scales between the high-energy singlet modes and the low-energy pure spin modes, and with combinations of the two filling the region in between.

The selection rules for transport are equally important to the dynamics of the system. For orbital excitations, we have no particular reason to limit possible transitions, and so we allow

$$\Delta n_\mathrm{S} = 0, \pm 1, \pm 2, \ldots, \qquad \text{such that } n_\mathrm{S}^\mathrm{final} \geq 0. \tag{5.25}$$

The changes in spin, however, must be supplied by the spin-$\frac{1}{2}$ electrons passing to and from the antidot. With the definition $n_\mathrm{S} = S - S_z$, where S is the total spin, we therefore allow $\Delta S = \pm\frac{1}{2}$ for each event, while ΔS_z is determined by the spin-projection ($\uparrow$ or $\downarrow$) of the electron involved. Since $\Delta n_\mathrm{S} = \Delta S - \Delta S_z$, this means that

$$\Delta n_\mathrm{S} \in \begin{cases} \{0, -1\}, & \text{if } \Delta S_z = +\frac{1}{2}, \\ \{0, +1\}, & \text{if } \Delta S_z = -\frac{1}{2}, \end{cases} \tag{5.26}$$

where again we require that $n_\mathrm{S}^\mathrm{final} \geq 0$.

By replacing the fermionic chemical potentials and selection rules described in §5.2

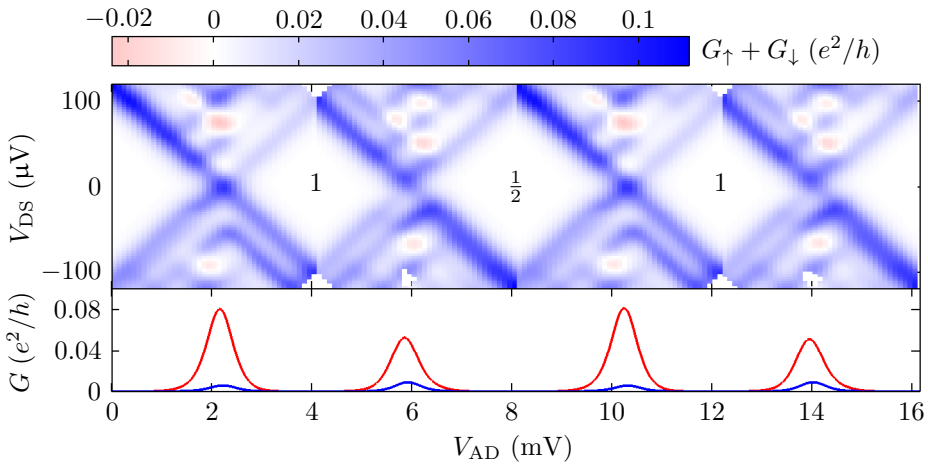

Figure 5.8: Transport calculations for the effective model of edge excitations, with $\varepsilon_L = 100\,\mu\mathrm{eV}$ and $\varepsilon_S = 27\,\mu\mathrm{eV}$. Total differential conductance $G_\uparrow + G_\downarrow$ is shown in the top panel, and spin-resolved conductances $G_\uparrow$ (red curve) and $G_\downarrow$ (blue curve) at zero bias are shown in the lower panel. Numbers printed in each Coulomb diamond show the ground-state spin configuration. The parameters used in this calculation are similar to those in Fig. 5.2: $\Delta E_{\mathrm{SP}} = 100\,\mu\mathrm{eV}$, $E_{\mathrm{Z}} = 30\,\mu\mathrm{eV}$, $R_{\mathrm{AD}} = 400\,\mathrm{nm}$, $T = 55\,\mathrm{mK}$, $\Gamma_{\mathrm{S}\uparrow} = \Gamma_{\mathrm{D}\uparrow} = 900\,\mathrm{MHz}$, $\Gamma_{\mathrm{S}\downarrow} = 300\,\mathrm{MHz}$, $\Gamma_{\mathrm{D}\downarrow} = 60\,\mathrm{MHz}$, $\eta_{\mathrm{C}} = 0.14$.

with those of this effective theory, we can use our transport model to simulate non-linear measurements and explore the observable consequences of the theory. An example of the calculated non-linear transport for an antidot described by the effective model is shown in Fig. 5.8. With a very small amount of tuning, we again find very close agreement with the experiment. We therefore conclude that this approximate model of edge excitations captures the all the qualitatively important aspects of the antidot physics. Notice that the excited state lines with energies $\approx 30\,\mu\mathrm{eV}$ observed in the simulation correspond to *spin* excitations. This choice of energy scales is required to reproduce the observed combination of excitation lines and negative differential conductance observed in the measurements, which results from a combination of spin-dependent tunnel barriers and the strict selection rules which apply to spin transitions.

5.4 Conclusions

Combining the various results of the modeling described in the previous sections, we arrive at the following conclusions regarding the role of interactions in our measurements:

- We have shown that the energy scales observed in our experiments are inconsistent with the SP model. In particular, the excitation energies visible in non-linear transport require a relatively large value for ΔE_{SP}, which does not agree with either the consistently small value of μ_{SF} or the small observed splitting, $\Delta\mu_{\uparrow}$, of transport lines due to spin pumping.

- The interacting MDD model correctly captures the *spin-charge separation* of the excitations at the antidot edge, in which both μ_{SF} and $\Delta\mu_{\uparrow}$ are softened by exchange while orbital excitation energies are preserved. By combining the MDD antidot model with the dynamic effects of bias and asymmetric tunnel barriers, we can qualitatively reproduce the experimental measurements of spin-resolved transport at zero bias, standard non-linear transport, and non-equilibrium bias measurements. Calculations of the steady-state spin populations within our model provide further insight into the interplay between the antidot energetics and the spin pumping induced by asymmetric tunnel barriers and/or bias.

- Using an effective model for the edge excitation-spectrum, we have shown that the particular details of the eigenspectrum are not crucial for qualitative comparisons, and that our observations are consistent with the spectrum of spin and density modes predicted by Hartree-Fock theory for the antidot eigenstates. Strict spin selection-rules appear to be a requirement, however, in order to explain the combination of excitation lines and negative differential conductance we measure.

We have also presented the details of a method for modeling spin-resolved transport through a zero-dimensional system such as a quantum dot or antidot. It provides the flexibility to directly compare the predictions of arbitrary physical models of the dot/antidot with experimental results, incorporating the real-world importance of spin- and energy-dependent tunnel couplings. Considering all the subtle and interesting effects we have discovered in the low-B regime, we believe this combination of experimental and theoretical techniques presents great potential to explore spin-related effects in more complicated regimes, such as at the breakdown of the MDD phase at higher B or for an antidot at $\nu_{\mathrm{AD}} = 1$, where the existence of Skyrmions or other non-trivial ground states is an intriguing possibility.

Chapter 6

Tilted-Field Measurements

In this chapter we present several additional measurements of the device studied in Chapters 4 and 5. They are taken in the same low-field regime of the central antidot, at filling factor $\nu_{\mathrm{AD}} = 2$, and with essentially the same experimental setup, but with the addition of a sample holder offering in situ control of the inclination angle of the device. This allows us to independently control the perpendicular component of the magnetic field, $B_{\perp}$, which determines the orbital properties of the electrons in the two dimensional electron system (2DES), from the total magnitude of the field, B_{Tot}, which to a good approximation affects spin properties only. For the $\nu_{\mathrm{AD}} = 2$ lowest Landau level (LLL) antidot states, this means that we can vary the Zeeman energy, E_{Z}, separately from the single-particle orbital energy spacing, ΔE_{SP}. This extra degree of freedom offers valuable additional information about the antidot eigenspectrum, providing further confirmation of the model of low-B antidot physics we develop in Chapter 5 in terms of maximum density droplets (MDDs) in the LLL. Here we describe the calibration and operation of the rotating sample holder and the results of preliminary measurements. Unfortunately a long series of technical delays meant that the rotator was only functional for our final measurement run, but we were still able to explore its capabilities with 'proof of principle' experiments, and to gain some additional insight into the physics of our antidot in the process.

Also in this chapter, we present experimental evidence for 'molecular antidot states' formed in the presence of unintentional impurities close to the antidot. We investigated the effects of these impurities in some detail in the course of our experiments, mainly in an effort to isolate their contributions to our measurements, in order to be confident that they did not influence our conclusions about the physics of the main antidot. Many of our measurements of impurity effects are interesting in their own right, however, and

here we provide some examples of fully controllable, coherent coupling between the main antidot in our device and a small impurity in one of the side channels.

6.1 A coherently-coupled 'antidot molecule'

Molecular antidot states have been experimentally detected in a few previous investigations. Gould et al. [102] designed and fabricated a double antidot for the purposes of exploring such a system, and their measurements provided a few surprises with regards to the frequency of Aharonov-Bohm oscillations. These were interpreted through a model of charging-dominated resonance conditions in which the molecular 'spectator modes' only provide a transport path, without significantly affecting the resonance structure. While measuring an antidot in the fractional quantum Hall regime, Maasilta and Goldman [103] noticed 'phase slips' and strange resonance shapes, which they attributed to coherent quasiparticle tunneling between their intentional antidot and a nearby impurity. Such phase slips have occasionally been observed in antidot Aharonov-Bohm oscillations in the integer quantum Hall regime and it has long been suspected that they result from the background disorder potential, but as far as we are aware no one has previously investigated the anomalous resonances as a function of a second parameter. In our measurements we usually prefer to sweep the antidot voltage, V_{AD}, rather than B, since the magnetic field strongly affects equilibration between edge modes, which can obscure the interpretation of the non-equilibrium measurements described in Chapter 4. Changing V_{AD} necessarily affects the size of the antidot depletion region, making it more likely to encounter features of the 2DES background potential, and it could be for this reason that we noticed more impurity effects in our experiments than most previous studies. Additionally, our device was fabricated on a wafer with lower electron density ($n_e = 1.1\,\mathrm{cm}^{-2}$) than in most antidot experiments. Since disorder tends to be more significant for lower densities due to the reduced screening ability of the 2DES, it is possible that we are more likely to find strong impurities near the antidots in our devices.

In our $\nu_{\mathrm{AD}} = 2$ transmission resonances, we initially noticed a few strangely-shaped resonances in sweeps of V_{AD} or B, which were often accompanied by abnormal spacings with neighboring conductance peaks. Usually the strange line shapes were asymmetric peaks, but occasionally we observed overlapping but clearly-resolved double peaks. Eventually we measured the antidot transmission in the plane of V_{AD} and B, and found that the strange resonances correspond to locations where states seem to 'disappear' from the antidot spectrum as B is increased, as shown in Fig. 6.1. Broadly, this behaviour seems to make sense, since the increasing magnetic field causes the width of both the

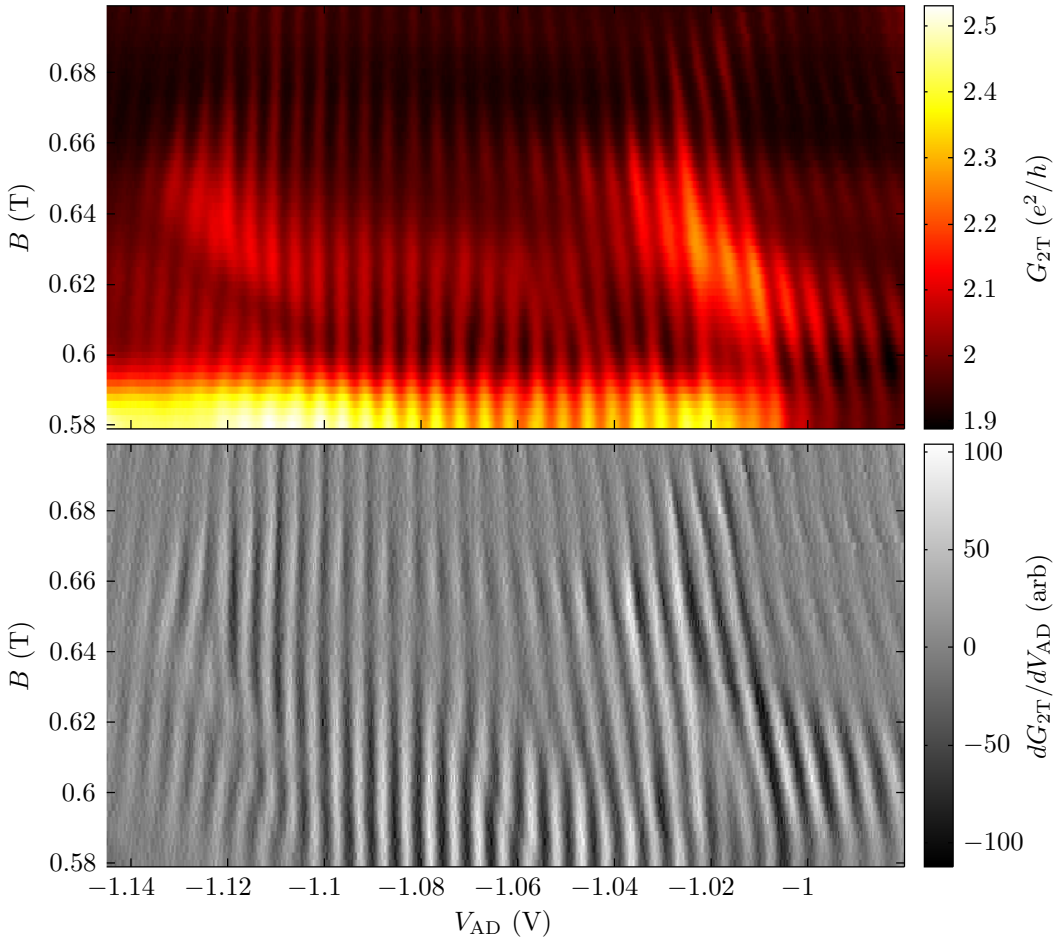

Figure 6.1: Top — Two-terminal antidot conductance as a function of V_{AD} (swept) and B (stepped), in the vicinity of anomalous resonances due to antidot-impurity coupling. Horizontal offsets have been applied to individual sweeps to 'straighten' the resonance pattern and remove an overall slope in the (V_{AD}, B) plane, to make it easier to track resonance positions by eye. Bottom — Derivative of the data in the top panel with respect to V_{AD}, in which the evolution of resonance positions is clearer. These data were taken at zero tilt angle, so $B = B_{\perp}$.

impurity and antidot states, given approximately by the magnetic length $\ell_B = \sqrt{\hbar/eB}$, to shrink, thereby reducing the spatial overlap of the wave functions. Thus an impurity state which was incorporated into the antidot as a molecular wave function at low B should eventually decouple as the field is increased. We know from basic quantum mechanics that a molecule resulting from the coupling of two different spatial states should consist of two molecular wave functions with different eigenenergies; in the simplest case these are the symmetric and antisymmetric combinations of the original states. Our transport measurements only probe the states which are connected to the antidot, so we should see both resonances of the molecular state, but will only observe one for the antidot state when the impurity has fully decoupled.

Despite this qualitative agreement with our expectations, there are confusing features of the measurements in Fig. 6.1. First, it is surprising that the impurity resonances disappear from the antidot spectrum within such a small range of B, especially given the relatively weak $1/\sqrt{B}$ dependence of the wave function width on magnetic field. Also, we are surprised that the impurity only seems to affect a single antidot resonance, with the others simply shifting their positions slightly to account for the added or subtracted state. The B-dependence of both charging and antidot single-particle energies depends inversely on antidot area, as described in §1.2.3. We expect the impurity to be much smaller than the lithographically-defined antidot with $R_{AD} \approx 400$ nm, and therefore for its eigenenergies to have a much stronger dependence on magnetic field.[1] We would also expect a weaker capacitive coupling between the impurity energies and V_{AD} than for the main antidot states. Keeping in mind that our linear response conductance measurements probe resonances only when they are at the Fermi level, we would therefore expect the impurity states to show a vastly different trajectory in the (V_{AD}, B) plane, and to pass through several normal resonances while the two wave functions are weakly coupled. The difference between our expectations as outlined above and the observations remains unexplained at this time.

While the effects of changing magnetic fields on the antidot-impurity coupling are somewhat confusing, measurements at constant B are more easily explained. Both the impurity and antidot states have small capacitive couplings to other gates on the device in addition to the antidot gate. In some cases, this provides a means of *locating* the impurity on the device, at least approximately. Shown in Fig. 6.2 are two more 'resonance maps,' with two terminal conductance measured as a function of V_{AD}, with

[1] For example, if the impurity background results from the electrostatic perturbations produced by nearby ionised donors, we expect the potential to vary on the scale of the spacer layer, which in this case is 60 nm. Therefore, if the impurity has $R_{Imp} \approx 100$ nm, the $1/R^2$ dependence of dU/dB means that energies of the impurity states should vary 10–20 times faster with B than those of the large antidot.

stepped voltages applied in turn to the nearby side gates V_{UG} and V_{LG} (see Fig. 4.1 on page 70 for a device photo and gate labels). As a function of V_{UG} (upper panel), the resonances shift with a uniform negative slope, whose magnitude is determined by the ratio of the antidot states' capacitive couplings to the antidot gate and upper gate, respectively. When V_{LG} is varied, on the other hand, as shown in the lower panel, we observe a series of shifts in the resonances, along a line with much flatter slope in the $(V_{\mathrm{AD}}, V_{\mathrm{LG}})$ plane. Following lines from bottom to top in the lower panel of Fig. 6.2, these shifts evolve from 'dislocations' of the resonance position toward more *positive* V_{AD} on the right-hand side of the plot to smooth 'deformations' towards more *negative* V_{AD} on the left-hand side, which steadily get weaker. This means that at some point a state is added to the antidot spectrum (i.e., if we pick a 'connected' resonance on the far left and another on the far right and count the number of lines between them, we find one more along the top edge of the plot than along the bottom).

We identify the anomalous line in Fig. 6.2 with an impurity in or near the lower channel, which has a much larger capacitive coupling to V_{LG} than the normal antidot states and a correspondingly shallower slope. As we follow it from bottom right to top left in the figure, the antidot potential is increasing (as V_{AD} becomes more negative) to account for the decreasing potential from V_{LG}, in order to keep the impurity state at the Fermi level. The antidot is getting larger along this line, and so the antidot-impurity coupling increases. At the bottom right, the two wave functions are mostly uncoupled, but the antidot states shift in response to the discrete charging of the nearby impurity, which is occupied by an electron above the impurity line and unoccupied below. As the antidot becomes larger and the coupling increases, we start to see clear anticrossings between the states. In this regime, the right-to-left shifts are produced by two anticrossings in quick succession, as each antidot state evolves continuously into an 'impurity-like' state following the trajectory of the impurity line, and then into the neighbouring antidot state. All of these transitions are measured at the Fermi level, as the changing gate voltages cause the antidot energy spectrum to 'slide past' the impurity state.

The mode-selective injection/detection technique presented in Chapter 4 provides a nice method to probe the changing 'character' of states in this region. In the top panel of Fig. 6.3 we show transmission resonances in the anticrossing regime similar to those in Fig. 6.2, while in the bottom panel we show simultaneous measurements of the *reflected* signal in edge modes 1 and 2. This is obtained by using one constriction of the bottom-left antidot (the other is pinched off) as a detector with filling factor $f_{\mathrm{Det2}} = 2$ and measuring the current flowing into contact ε'. Wherever the resonances

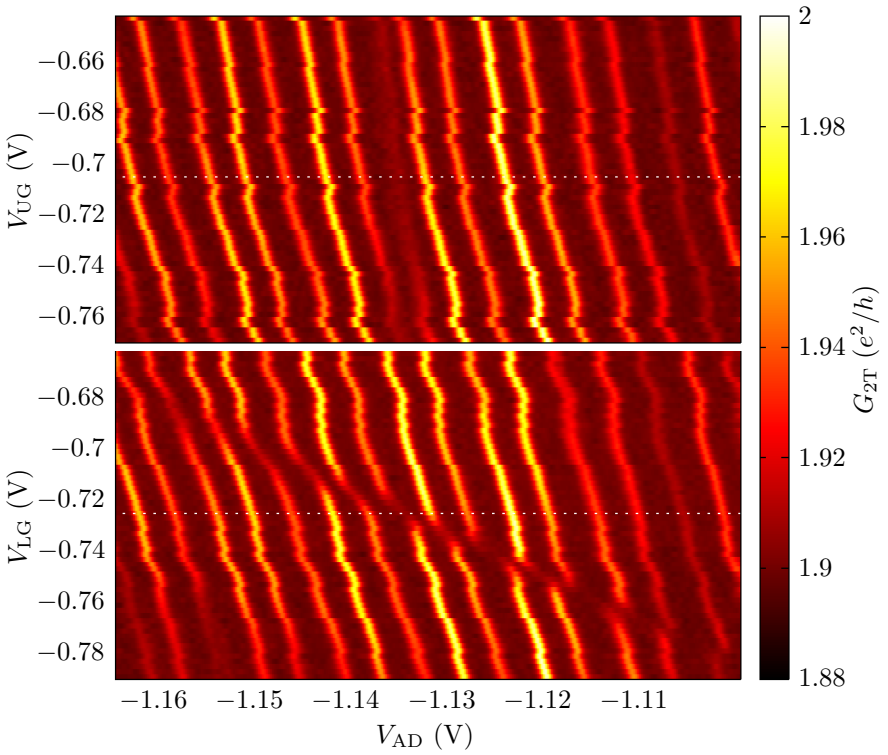

Figure 6.2: Two terminal antidot conductance as a function of V_{AD} (swept) and stepped side-gate voltages V_{UG} (top) and V_{LG} (bottom). Dotted white lines show the 'intersection' of these two datasets, marking the fixed value of each side gate voltage which is used for the opposite set of measurements.

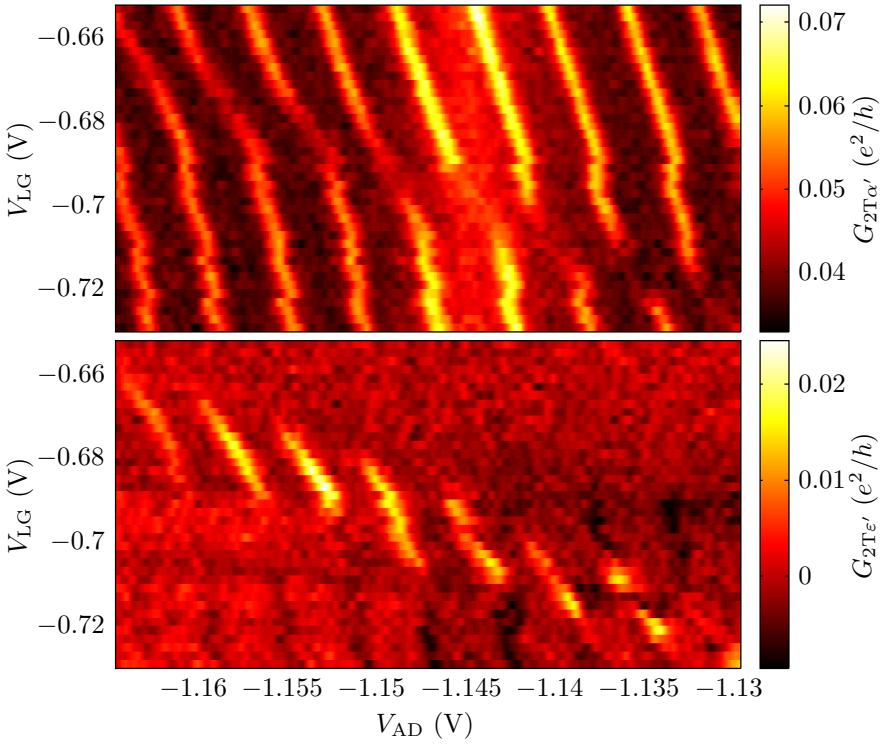

Figure 6.3: Two terminal conductances reflecting the currents *transmitted* to the drain contact α' (top) and *reflected* to the lower-left detector contact ε' (bottom), as a function of V_{AD} and V_{LG}, with $f_{\mathrm{Det2}} = 2$. Since equilibration between edge modes between the antidot and the detector varies strongly as a function of V_{LG}, obscuring the resonance structure, the mean value of each horizontal sweep has been subtracted in the lower panel.

become more 'impurity-like,' we observe a strong signal in this reflected current, while the transmitted signal becomes weaker. The faint negative signal in the reflected current (dark lines corresponding to antidot resonance positions) result from significant V_{LG}-dependent equilibration between the edge modes traveling from the antidot to the detector. Thus we conclude that the impurity state provides a 'link' between the antidot states and the normally unperturbed LLL edge modes flowing through the lower constriction, redirecting current from the drain to the bottom-left detector.

From the measurements in Figs. 6.2 and 6.3, it seems that the impurity states do not demonstrate any particular 'preference' for coupling to individual antidot states. This observation provides further evidence for the lack of spin-selectivity in the antidot resonances, the impurity resonances, or in both. Since the single-particle spacing satisfies $\Delta E_{\mathrm{SP}} \sim 1/R$, we expect a larger orbital energy spacing for the impurity than for the antidot, and so these may very likely be spin-selective. But if the antidot resonances actually result from transmission through several states including both spins, we would expect to see the effects of antidot-impurity coupling on every resonance line, as observed in the experiment. Of course it is possible that something more complicated is taking place to form the many-body antidot-impurity molecular states, but without spin-selective antidot states as a reference it is difficult to extract further information from the measurements.

This concludes our discussion of molecular antidot states, for the purposes of understanding the observable effects of antidot-impurity coupling in our device, but there is still scope for much further investigation. In particular, the details of the 'appearance' of molecular states in the resonance spectrum as B is reduced remains to be understood. We spent some effort in 'tracking' individual impurity resonances like those in Figs. 6.2 and 6.3 through the parameter space of $(B, V_{\mathrm{AD}}, V_{\mathrm{LG}})$, and our measurements seem to suggest that the splittings observed in Fig. 6.1 are actually unrelated to this 'channel impurity.' With careful analysis, small dislocations running through the resonance map of Fig. 6.1 may be observed to coincide with the expected locations of impurity states from measurements like Fig. 6.2 (for example, such a feature is visible in Fig. 6.1 starting from the bottom around $V_{\mathrm{AD}} \approx -1.06\,\mathrm{V}$ and running towards the top left). It is therefore possible that these features represent an entirely different phenomenon, although at this point it seems most likely that they reflect interactions between the antidot and an impurity somewhere else in the device.

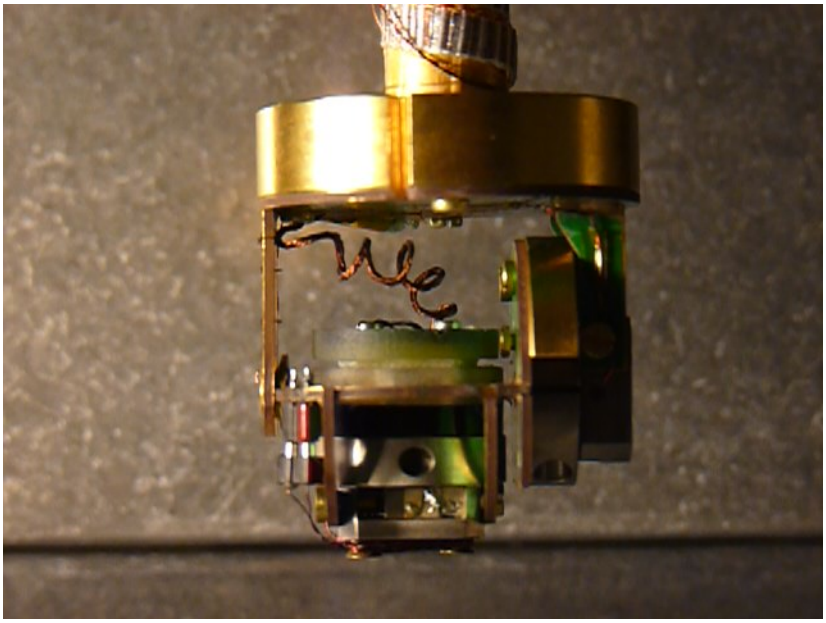

Figure 6.4: Photograph of the rotating sample holder used for the measurements described in this chapter. The sample, mounted in a standard LCC package, sits on a stage sandwiched between two PCB layers (horizontal in the photograph). The twenty pads on the bottom of the package are pressed against a set of pogo pins mounted in the stage, which make electrical contact to the bundle of copper wire seen in the picture, which connects to a loom of twisted pair wiring in the fridge at the mixing chamber plate. The sample holder is shown mounted on the end of a gold-plated copper tailpiece, in the orientation used for measurements. Two attocube® piezoelectric rotators provide in situ positioning: one on the right side of the photograph controls the inclination angle, and a second mounted directly below the sample controls the azimuthal rotation. In our measurements, only the inclination rotator was functioning.

6.2 Operation of an in situ rotation unit

A photograph of our rotating sample holder is shown in Fig. 6.4. It was designed and assembled by *Cambridge Magnetic Refrigeration*, but after several years of delays in fixing flaws with the original product, we eventually completed the intricate wiring and final assembly ourselves. In its final form, it provides dual-axis in situ angular positioning through a pair of attocube® ANR50 piezoelectric rotation units. These operate on a 'slip-stick' mechanism, in which the piezoelectric components ('piezos') are driven by a sawtooth-shaped voltage pulse. Within the riser of each pulse, the piezos expand or shrink to move the mechanism, but then snap back to their original position with the sudden return to ground potential, applying a force which overwhelms the

static friction between the axle and the piezo, leaving the stage at a new orientation. Although they are very fragile to mechanical stress and must be handled with care, the piezos perform efficiently even at base temperature of a dilution refrigerator and in high magnetic fields. In practice, the necessarily large driving voltages lead to enormous pickup in the experimental circuit, and the resulting currents produce significant heating of the fridge, so we cannot take measurements while sweeping the angle; instead we must step to a desired orientation and wait for the system to settle before taking data. In our experiments, we only used the inclination rotator, to adjust $B_\perp$ relative to B_{Tot} (the other rotator was defective), and we achieved suitable low-temperature operation with a sawtooth wave with amplitude 60–70 V (the maximum supplied by the pulse generator is 70 V) and frequency 50 Hz.

The angular response to the motor is not uniform or symmetric, however (i.e., N steps in one direction followed by N steps in the opposite direction generally does not return the stage to its original orientation), so we require a separate sensor to determine the orientation inside the fridge. Since the sample is already mounted at the centre of a solenoid magnet, it is convenient to use Hall effect sensors for this purpose. These give the component of B perpendicular to the sensor through a measurement of the Hall voltage V_{H} due to the the (classical) Hall effect,

$$R_{\mathrm{H}} = \frac{V_{\mathrm{H}}}{I} = \frac{B_\perp}{ned}, \tag{6.1}$$

where n is the three-dimensional electron density and d is the thickness of the sensor. A Hall sensor is mounted in the lid of the sample holder which holds the chip package in place, with an orientation perpendicular to that of the sample. It would have been ideal to mount two such Hall sensors on the sample holder to gain dual-axis measurement capability, but unfortunately we are limited to one due to wiring constraints of the sample holder design. In our case, however, we can use the device itself as a second sensor, since near zero magnetic field the quantum Hall effect is weak and R_{H} is approximately linear in B. By mounting the sensor perpendicular to the sample, we retain the ability to measure both rotation angles in most cases.

Calibration of the Hall sensor to measure the inclination angle in this orientation is relatively straightforward. In terms of the inclination angle, θ, the Hall resistances R_{S} and R_{D} of the sample and device, respectively, are given by

$$R_{\mathrm{D}} = A_{\mathrm{D}} B \cos(\theta) \qquad \text{near } B_\perp = 0 \tag{6.2a}$$

$$R_{\mathrm{S}} = A_{\mathrm{S}} B \sin(\theta - \delta), \tag{6.2b}$$

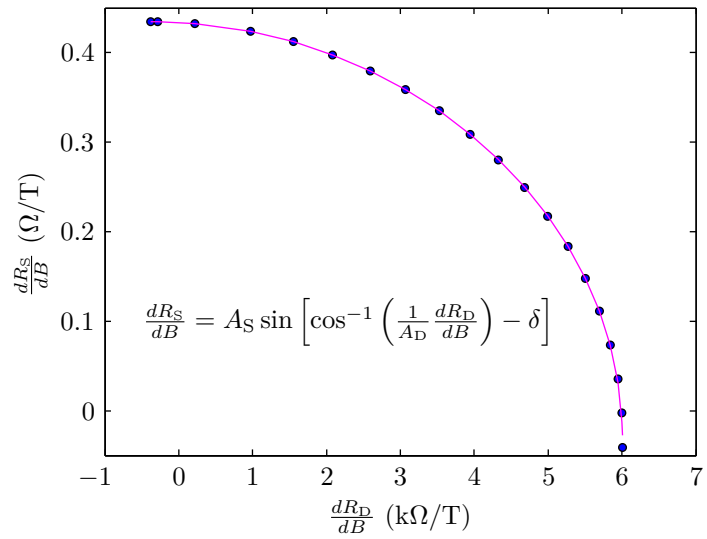

Figure 6.5: Hall-resistance measurements (blue circles) of the the device and probe-mounted Hall sensor, with the best-fit function (magenta curve) of the form printed inside the axes. The parameters (A_S, A_H, δ) define the calibration function for the Hall sensor, Eq. (6.4), giving the inclination angle of the device in terms of R_S/B. The best-fit values are $A_S = 0.435\,\Omega/\mathrm{T}$, $A_D = 6.005\,\mathrm{k}\Omega/\mathrm{T}$, and $\delta = 3.6°$.

in terms of constants A_S and A_D, and a possible misalignment angle between the device and the sensor, δ. Taking the derivative with respect to B and eliminating θ from these equations, we obtain the relation

$$\frac{dR_S}{dB} = A_S \sin\left[\cos^{-1}\left(\frac{dR_D}{dB}\frac{1}{A_D}\right) - \delta\right], \tag{6.3}$$

which we can use to determine the constant parameters A_S, A_D, and δ. We step the rotator through the full 90° range, stopping occasionally to take simultaneous measurements of the slopes of R_H for both the sensor and the device.[1] An example of these calibration measurements, with a best-fit function in the form of Eq. (6.3), is given in Fig. 6.5. With the calibration parameters determined from such a fit, we can then determine θ during our experiment through a measure of R_S, with the relation

$$\theta = \sin^{-1}\left(\frac{R_S}{A_S B}\right) + \delta. \tag{6.4}$$

[1]Note that in order to obtain an accurate value of R_H it is preferable to measure the diagonal resistance at both positive and negative field. The true Hall resistance is then given by $[R(B) - R(-B)]/2$, independent of longitudinal effects.

Near $\theta \approx 90°$, Eq. (6.4) becomes sensitive to small changes in R_S, and in this regime it is preferable to use low-field measurements of the device, for which

$$\theta = \cos^{-1}\left(\frac{R_D}{A_D B}\right) \tag{6.5}$$

is better constrained.

6.3 Independent control of the Zeeman energy

There are several potentially interesting applications of tilted-field measurements, but the most obvious involve the control of the Zeeman energy, $E_Z = g\mu_B B_{Tot}$, independently of $B_\perp$, to separate the effects of spin from the orbital wave functions. In order to accomplish this, we step θ and B_{Tot} together such that $B_\perp = B\cos(\theta)$ remains constant. We can measure the effects of changing E_Z through standard linear-response conductance measurements, since the evolution of resonance positions reflects changes in the ground-state chemical potentials of the antidot.

In Fig. 6.6 we show two examples of this measurement, in which sweeps of V_{AD} across the $\nu_{AD} = 2$ transmission resonances are taken at a series of angles chosen to produce uniform steps in B_{Tot}, with $B_\perp$ fixed. For most inclination angles, a measurement of the Hall sensor resistance is sufficient to determine θ accurately enough for these experiments, but when $\theta \geq 80°$ the uncertainty in Eq. (6.4) becomes unacceptably large, and we must use a measurement of the device to determine the angle, and hence the appropriate value of B_{Tot} to use at each step. This can be the device Hall resistance near $B_\perp \approx 0$ T as explained in the previous section or another $B_\perp$-dependent feature. In the measurements shown in Fig. 6.6, we use the position of a riser in between quantum Hall plateaux to determine θ without sweeping the field all the way to zero between each V_{AD} trace. Even so, small errors in the measurement of θ for each sweep combined with device drift tend to obscure the resonance pattern, and so we have used a series of peak-fitting routines to 'line up' the resonances in Fig. 6.6.

Several features are immediately apparent in these measurements. The pattern of (anti)crossing resonances is unmistakable; especially in the upper panel of Fig. 6.6, taken at a lower value of $B_\perp$, sets of right- and left-moving states can be followed clearly through the pattern. This is obviously consistent with the behaviour we expect from the 'ladder-states' of the single-particle model (see §1.1 for details), in which a steady increase of E_Z causes spin-↑ and spin-↓ states to cross, as the ground-state spin-projection of the occupied states, S_z, increases. In transport measurements the resonances do not

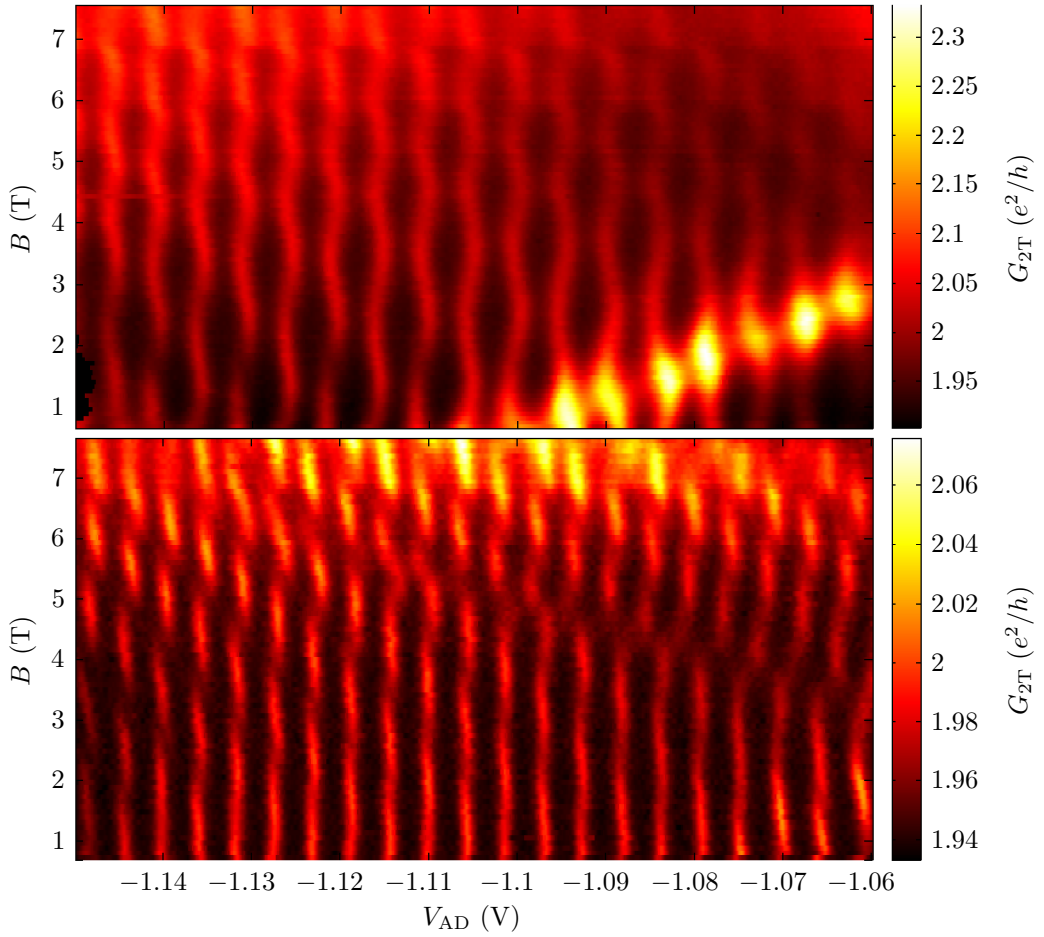

Figure 6.6: Antidot transmission resonances as a function of V_{AD} and B_{Tot}, with $B_{\perp}$ fixed at 0.62 T and 0.72 T in the top and bottom panels, respectively, obtained by stepping the tilt angle and sweeping V_{AD}. Small horizontal offsets are applied to individual sweeps to correct for slight mis-calibrations of the tilt angle.

actually cross each other because the are separated by the charging energy required to add additional electrons to the antidot. We also notice, particularly in the lower panel at higher $B_\perp$, that states moving left have larger amplitude than those moving right. The left-moving states are traveling *down* the antidot energy spectrum as E_Z increases, so they correspond to spin-↑ eigenstates, and the difference in amplitude simply reflects the spin-asymmetric tunnel barriers we discovered in the measurements of Chapter 4. As S_z increases with E_Z, the physical 'gap' between the inner spin-↑ and outer spin-↓ edges should increase, which we might expect to enhance the spin-↓ tunneling instead, but we should bear in mind that a similar spatial separation occurs for the $\nu = 3$ and 4 edge modes, and that the combined effect could be different than we might naïvely expect. We can also not fail to notice the 'envelope' of large-amplitude resonances which passes through the upper panel with much shallower slope than the resonances themselves. This corresponds to one of the impurity states discussed in §6.1, which we can infer from the positive slope to be spin-↓. The shallow slope results from the smaller capacitive coupling between the impurity state and V_{AD} compared to the main antidot states. A slightly more subtle feature occurs in the lower panel above $B \approx 3$ T, in which a new left-moving state seems to 'appear' in the spectrum, causing the nearby resonances to shift and rearrange around it. This is presumably a spin-↑ impurity state, which gets incorporated into the antidot as a molecular state as the size of the antidot increases (towards more negative V_{AD}). Finally, we observe that both the amplitude and width of resonances increases with B_{Tot}. This probably reflects the changes in tunnel barriers which occurs as both the source and drain edge modes and the antidot edges rearrange spatially with changing E_Z.

While the structure we observe in measurements like Fig. 6.6 seems consistent with the single-particle model excluding interactions, we note that it is also completely consistent with the interacting MDD theory described in Chapter 5. As described in §5.1, in the MDD theory the Zeeman energy simply serves to break the degeneracy in the configuration energy functional $U(S_z)$, determining the ground-state spin S_{z0}, while the combination of ΔE_{SP} and exchange energies determine the shape of the minimum, and in particular the energy scale for spin-excitations. Thus changing E_Z in the MDD model simply results in successive changes in S_{z0}, and with changes in the ground-state chemical potentials which mimic those of the single-particle model. In future experiments, it would be interesting to investigate the changes in the excitation spectrum which result from adjustments of E_Z, through detailed non-linear transport spectroscopy measurements. In our device, such measurements were not particularly enlightening, mainly

because of a large electron temperature which obscured most of the excitation lines.[1]

Besides an investigation of excitations as a function of E_Z, it would clearly also be interesting to apply the spin-selective measurement technique to these experiments. In particular, one could perform measurements of spin-flip events which likely occur due to spin-orbit coupling near the (anti)crossings of opposite-spin states, to see if the strength of the coupling depends on the pair of orbital states involved.

For now, we present only this first glimpse of the range of experiments possible with a rotating sample holder. We hope that further experiments will follow up on some of the unanswered questions posed above regarding the spin structure of antidots, and that future researchers will use the rotator with other devices to add an extra degree of freedom to their experiments.

[1]The rotating sample holder is slightly too large to fit in the standard heat-shield of our dilution refrigerator. We tried to use a slightly larger one, but the tolerances are so small that we could not avoid it touching the 4 K inner vacuum can and generating a large heat load on the dilution unit. Running without the heat shield, we measured electron temperatures of ≈ 150 mK, increased by a factor of three over our previous run, which made it impossible to resolve the excitations we hoped to observe.

Conclusions and Suggestions for Further Work

In this work we have studied the physics of the lowest Landau level ($\nu_{\mathrm{AD}} = 2$) eigenstates of a quantum antidot in the low magnetic field regime, through a series of experiments and theoretical models. We carefully consider the non-interacting single-particle model which has been used to understand low-field antidot measurements in the past, in an effort to understand the emergence of effects at higher fields which appear to require an interacting physical description. We conclude that, while most *orbital* effects appear to be consistent with non-interacting physics, the *spin* structure of the low-field antidot is not. Through extensive measurements of *spin-resolved transport*, which exploit the properties of edge modes in the quantum Hall regime, we discover a spectrum of antidot excitations which demonstrates *spin-charge separation* between the energy scales for spin and density excitations of the antidot edge. We interpret these results in terms of a model of the $\nu_{\mathrm{AD}} = 2$ antidot as a maximum density droplet (MDD) of 'holes' in the lowest Landau level, and analyse its expected excitations within Hartree-Fock mean-field theory. Using a transport model we have developed to simulate experimental data for a wide range of theoretical antidot models, we find excellent agreement between our observations and the predictions of the MDD picture. Thus our experiments are of general importance to the wider community interested in MDDs as they relate to quantum Hall physics and quantum dots at high magnetic fields. In several important ways, our antidot experiments are more versatile and powerful than previous experimental investigations of MDD configurations in quantum dots, and we believe there is much potential remaining for the techniques presented in this work to address further important questions about the MDD phase and any other many-particle states which may become important in different regimes.

In the course of nearly any Ph.D. research, unanticipated side avenues appear, many of which warrant significant further investigation. Occasionally these side avenues even

develop into the central thrust of the work, which is exactly what happened in this case. We designed the spin-selective experiment, not sure if the edge modes would actually be spin-selective at such low fields but fully expecting the antidot states to be. Instead we quickly found the opposite, and thus ensued a long endeavour to answer the question: why? In the process, we noticed several other intriguing effects, some of which we investigated and some not. A few of these extra measurements were presented in Chapter 6, including a few preliminary experiments with the rotating sample holder which we had expected to form an integral part of most of our experiments, before it was broken and remained unusable and out of our hands for three years. Thus many potentially interesting experiments remain, a few of which we briefly discuss below. The 'field' of antidot research is very small, but we have shown with this work that the potential impact of antidot experiments is somewhat wider than commonly assumed, being of particular importance to the much larger group interested in quantum dot physics. We therefore hope that some of these projects may soon come to fruition.

First, the obvious extensions of our central results concerning spin-resolved transport experiments are to carry out similar experiments in other regimes of the antidot. In particular it would be interesting to investigate the breakdown of the MDD at higher fields, since the transition between the MDD and a 'lower density droplet' has been the subject of much theoretical work. Such measurements would also shed further light on the structure of the high-field antidot configurations responsible for 'double-frequency' Aharonov-Bohm resonances, which have provoked debate within the community in the past and are still not fully understood. Also of interest would be measurements at filling factor $\nu_{\mathrm{AD}} = 1$, since the potential exists to detect nontrivial ground states with 'canted' spin order (e.g., Skyrmions) which have been proposed theoretically.

Furthermore, we believe that potential may still exist for the 'spin-filter' application employing an antidot with spin-selective resonances, despite our experiments showing the contrary. Our analysis of the energy scales implied by our measurements and comparisons with the interacting model suggest that our device was very near the 'crossover' regime in which the antidot ground state first starts to develop a spin-polarisation. We therefore believe that it should be possible to engineer a new device which moves far enough towards the non-interacting model to behave in the way required for the spin-filter application. Mainly this requires a larger orbital energy scale ΔE_{SP}, which could be obtained through a variety of means, for example by reducing the antidot size, increasing the electron density (since this may cause the potential slope at the Fermi energy to be steeper), or by directly increasing the potential slope induced by the antidot gate by depositing it in an etched region closer to the 2DES. We have actually already fabri-

cated some devices with a few of these modifications, so these experiments could begin immediately.

Although we did not focus on it due to our preoccupation with finding descriptions for the 'usual' observations of spin-conserved transport, we have included in this work the first observations of spin-nonconservation due to spin-orbit coupling in an antidot. Since antidot states have such a uniform spectrum and are so easily controlled, there is certainly potential to investigate these spin-orbit effects further and possibly to develop useful applications. One more ambitious idea would be to use the coherent spin-evolution provided 'for free' by the spin-orbit coupling to manipulate spins controllably in electronic devices based on quantum Hall topology. This would require the temporal control of electrons tunneling to and from the antidot, to reproducibly achieve a desired spin rotation. Potential for this control possibly exists in the form of a 'pump,' such as the one proposed [24] for the purposes of measuring the charge of fractional quantum Hall quasiparticles. Electrons could be controllably added to the antidot by pulsing one of the side gates with a suitable bias applied to the edge modes to make it likely for an electron to tunnel on but not off from the antidot. After a desired waiting time for rotation, the other side gate could be pulsed to remove the electron, and its spin measured through selective detection at a quantum point contact. This experiment requires pulse times to be much faster than the rotation time scale of the spins on the antidot. Based on our estimate for the spin-orbit coupling strength of $\varepsilon_{\mathrm{SOI}} \approx 3\,\mu\mathrm{eV}$, we require pumping frequencies faster than $\varepsilon_{\mathrm{SOI}}/h \approx 1\,\mathrm{GHz}$ which is near the limit of current experimental capabilities, but it may be possible to tune the coupling strength to a lower value, either by varying the Rashba coefficient through a top or bottom gate, or by finding pairs of antidot states with intrinsically weaker coupling.

As discussed in §6.1, while several aspects of the 'molecular antidot' measurements seem to have straightforward explanations, some of the observations remain to be understood. The details of the states which 'appear' in the antidot resonance spectrum as the magnetic field is reduced do not seem to agree with our expectations. This could simply be a result of a mis-estimation of the relevant sizes and field-dependence of the impurity states, and some additional modeling could help to clear up the discrepancy. The Green's function calculations used in Chapter 3 would be particularly amenable to this task, since it would be straightforward to create a simulated potential for an antidot molecule and investigate what effects may be expected due to non-interacting physics only.

Finally, it would clearly be desirable to extend the tilted-field experiments we presented in Chapter 6 along the lines discussed at the end of §6.3. In particular, we dis-

covered tantalising evidence of strange new behaviour in a few non-linear spectroscopy experiments at large tilt angle (where E_Z is significantly enhanced over its usual value) taken at the very end of our measurement run. The features are faint due to weak coupling and the elevated electron temperature, but the Coulomb-blockade pattern seems to be severely distorted, with splittings of lines appearing at many values of DC bias and no clear 'zero' at which lines merge onto single peaks. It is almost as if the Coulomb blockade is completely broken in this regime, although we have no idea why this should be. Further measurements of the evolution of these spectra as E_Z is increased would hopefully help to answer some of these questions. Of course there is always the chance that more measurements will rather pose more questions than they manage to answer, but such is the fun of exploring quantum devices with the lens provided by a new experimental technique.

Appendix A

Wafer Properties

The device studied in Chapters 4–6 was fabricated on the wafer T792, grown by Ian Farrer of the molecular beam epitaxy team in the Semiconductor Physics group. It is essentially a standard Si-doped GaAs/AlGaAs high-electron-mobility transistor, with a slightly larger spacer than usual between the two-dimensional electron gas (2DEG) and the doping layer to further enhance mobility. Its important properties are included in the table below. The values marked (light) show the result of heavy illumination with a red light-emitting diode. We tried illuminating our device but found that the gates became ineffective or unstable, so all the experiments presented in this thesis were performed in the dark.

T7972 properties	
Electron density (dark)	1.1×10^{11} cm^{-2}
Electron density (light)	1.8×10^{11} cm^{-2}
Mobility (dark)	2.56×10^{6} cm/(V $\cdot$ s)
Mobility (light)	3.51×10^{6} cm/(V $\cdot$ s)
Spacer thickness	60 nm
Total depth of 2DEG	276.7 nm

Appendix B

Derivation of Tunneling Rates

The expression

$$W^p_{s'\chi'\to s\chi} \simeq \frac{2\pi}{\hbar}\left|\langle\chi s|H_{\rm tun}|\chi' s'\rangle\right|^2 \delta(E_s - E_{s'} + E_\chi - E_{\chi'} + p\mu_r), \tag{B.1}$$

is derived directly from Fermi's golden rule for tunneling between an isolated state on the quantum dot $|\ell\sigma\rangle$ and one of a continuum of states $|k\sigma\rangle$ in the non-interacting reservoir r. In §2.3.2 we require an expression for the total rate for the dot transition, given by the trace over all states in the reservoirs,

$$\gamma^p_{s'\to s} = \sum_{\substack{\chi\chi' \\ N(\chi')=N(\chi)+p}} W^p_{s'\chi'\to s\chi}\rho^{\rm eq}_{\rm res}(\chi'), \tag{B.2}$$

which we proceed to derive in this appendix.

The density of states $\rho^{\rm eq}_{\rm res}$ of a reservoir with chemical potential μ is given by the grand canonical distribution

$$\rho^{\rm eq}_{\rm res}(\chi) = \frac{e^{-\beta(E_\chi - \mu\hat{n}(\chi))}}{\mathcal{Z}_{\rm F}(\mu, V_r, T)} = \frac{e^{-\beta\sum_\alpha(\varepsilon_\alpha-\mu)n_\alpha}}{\prod_{\alpha'}(1+e^{-\beta(\varepsilon_{\alpha'}-\mu)})}, \tag{B.3}$$

where $\beta = 1/kT$ and $\mathcal{Z}_{\rm F}$ is the partition function for fermions. The reservoir configuration χ is represented by a set of occupation numbers n_α for the single-particle states $|k\sigma\rangle$ in the reservoirs, which we sometimes label by a single index α for notational simplicity.

For tunneling to and from a given lead, the matrix elements in Eq. (B.1) are given by

$$\left|\langle \chi s|H_{\rm tun}|\chi' s'\rangle\right|^2 = \sum_{k\ell\sigma}\sum_{k'\ell'\sigma'}\Big[T_{k\ell\sigma}T^*_{k'\ell'\sigma'}\langle\chi|a^\dagger_{k\sigma}|\chi'\rangle\langle s|a_{\ell\sigma}|s'\rangle\langle\chi'|a_{k'\sigma'}|\chi\rangle\langle s'|a^\dagger_{\ell'\sigma'}|s\rangle + T^*_{k\ell\sigma}T_{k'\ell'\sigma'}\langle\chi|a_{k\sigma}|\chi'\rangle\langle s|a^\dagger_{\ell\sigma}|s'\rangle\langle\chi'|a^\dagger_{k'\sigma'}|\chi\rangle\langle s'|a_{\ell'\sigma'}|s\rangle\Big]. \quad \text{(B.4)}$$

The first term above represents tunneling of an electron from the dot to the reservoir ($p=-1$), while the second term represents the opposite process ($p=+1$), so only one term contributes to Eq. (B.1) given a choice of p.

To evaluate Eq. (B.2), we first perform the sum over χ. For the first term of Eq. (B.4) this yields

$$\sum_{\chi}\langle\chi|a^\dagger_{k\sigma}|\chi'\rangle\langle\chi'|a_{k'\sigma'}|\chi\rangle = \delta_{0,n'_{k\sigma}}\delta_{kk'}\delta_{\sigma\sigma'}, \quad \text{(B.5)}$$

and so, performing also the sums over k' and σ', we obtain

$$\gamma^-_{s'\to s} = \frac{2\pi}{\hbar}\sum_{\chi'}\sum_{k\sigma}\rho^{\rm eq}_{\rm res}(\chi')\delta_{0,n'_{k\sigma}}\sum_{\ell\ell'}T_{k\ell\sigma}T^*_{k\ell'\sigma}\langle s|a_{\ell\sigma}|s'\rangle\langle s'|a^\dagger_{\ell'\sigma}|s\rangle\delta(E_s-E_{s'}+\varepsilon_{k\sigma}), \quad \text{(B.6)}$$

where we have used the relation

$$E_{\chi'}-E_\chi = p(\varepsilon_{k\sigma}+\mu), \quad \text{(B.7)}$$

to simplify the energy-conserving δ-function. We can now perform the sum over χ', equivalent to a sum over all possible configurations $\{n'_\alpha\}$, with the result

$$\begin{aligned}\sum_{\chi'}\rho^{\rm eq}_{\rm res}(\chi')\delta_{0,n'_{k\sigma}} &= \sum_{\{n'_\alpha\}}\frac{e^{-\beta\sum_\alpha(\varepsilon_\alpha-\mu)n'_\alpha}}{\prod_{\alpha'}\left(1+e^{-\beta(\varepsilon_{\alpha'}-\mu)}\right)}\delta_{0,n'_{k\sigma}}\\ &= \frac{\prod_\alpha\left(1+e^{-\beta(\varepsilon_\alpha-\mu)}(1-\delta_{\alpha,k\sigma})\right)}{\prod_{\alpha'}\left(1+e^{-\beta(\varepsilon_{\alpha'}-\mu)}\right)}\\ &= \frac{1}{1+e^{-\beta(\varepsilon_{k\sigma}-\mu)}} = 1-f_\mu(\varepsilon_{k\sigma}).\end{aligned} \quad \text{(B.8)}$$

Energy conservation requires

$$\varepsilon_{k\sigma} = p(E_s-E_{s'}), \quad \text{(B.9)}$$

and so by combining Eqs. (B.6) and (B.8) we obtain the desired result for the transition

rate as a result of tunneling from the dot to reservoir r,

$$\gamma^{-}_{r,s'\to s} = \sum_{\ell\ell'\sigma} \Gamma^{r}_{\ell\ell'\sigma}(E_{s'} - E_s)\langle s|a_{\ell\sigma}|s'\rangle\langle s'|a^{\dagger}_{\ell'\sigma}|s\rangle\Big[1 - f_r(E_{s'} - E_s)\Big], \tag{B.10}$$

in terms of the spectral function $\Gamma^{r}_{\ell\ell'\sigma}(E)$ defined by Eq. (2.78) on page 52.

For the second term in Eq. (B.4), a similar analysis of the sums over χ, k', and σ' yields

$$\gamma^{+}_{s'\to s} = \frac{2\pi}{\hbar}\sum_{\chi'}\sum_{k\sigma}\rho^{\mathrm{eq}}_{\mathrm{res}}(\chi')\delta_{1,n'_{k\sigma}}\sum_{\ell\ell'}T^{*}_{k\ell\sigma}T_{k\ell'\sigma}\langle s|a^{\dagger}_{\ell\sigma}|s'\rangle\langle s'|a_{\ell'\sigma}|s\rangle\delta(E_s - E_{s'} - \varepsilon_{k\sigma}), \tag{B.11}$$

and we obtain

$$\begin{aligned}\sum_{\chi'}\rho^{\mathrm{eq}}_{\mathrm{res}}(\chi')\delta_{1,n'_{k\sigma}} &= \frac{\prod_{\alpha}\left((1-\delta_{\alpha,k\sigma}) + e^{-\beta(\varepsilon_\alpha-\mu)}\right)}{\prod_{\alpha'}\left(1 + e^{-\beta(\varepsilon_{\alpha'}-\mu)}\right)} \\ &= \frac{e^{-\beta(\varepsilon_\alpha-\mu)}}{1+e^{-\beta(\varepsilon_{k\sigma}-\mu)}} = f_\mu(\varepsilon_{k\sigma}).\end{aligned} \tag{B.12}$$

for the sum over χ'. Therefore, the transition rate for an electron tunneling into the dot from reservoir r is given by

$$\gamma^{+}_{r,s'\to s} = \sum_{\ell\ell'\sigma}\Gamma^{r}_{\ell\ell'\sigma}(E_s - E_{s'})\langle s|a^{\dagger}_{\ell\sigma}|s'\rangle\langle s'|a_{\ell'\sigma}|s\rangle f_r(E_s - E_{s'}). \tag{B.13}$$

References

[1] C. J. B. Ford, S. Washburn, M. Büttiker, C. M. Knoedler, and J. M. Hong, Phys. Rev. Lett. **62**, 2724 (1989). xii

[2] L. W. Molenkamp, A. A. M. Staring, C. W. J. Beenakker, R. Eppenga, C. E. Timmering, J. G. Williamson, C. J. P. M. Harmans, and C. T. Foxon, Phys. Rev. B **41**, 1274 (1990).

[3] J. Spector, H. L. Stormer, K. W. Baldwin, L. N. Pfeiffer, and K. W. West, Appl. Phys. Lett. **56**, 967 (1990). xii

[4] N. W. Ashcroft and N. D. Mermin, *Solid State Physics*, New York: Holt, Rinehart and Winston, 1976. xii, 20

[5] R. Hanson, L. P. Kouwenhoven, J. R. Petta, S. Tarucha, and L. M. K. Vandersypen, Rev. Mod. Phys. **79**, 1217 (2007). xiii, 91

[6] H. A. Fertig, L. Brey, R. Côté, and A. H. MacDonald, Phys. Rev. B **50**, 11018 (1994). xiii

[7] D.-H. Lee and C. L. Kane, Phys. Rev. Lett. **64**, 1313 (1990).

[8] S. L. Sondhi, A. Karlhede, S. A. Kivelson, and E. H. Rezayi, Phys. Rev. B **47**, 16419 (1993). xiii

[9] R. C. Ashoori, H. L. Stormer, J. S. Weiner, L. N. Pfeiffer, K. W. Baldwin, and K. W. West, Phys. Rev. Lett. **71**, 613 (1993). xiii

[10] P. Hawrylak, C. Gould, A. Sachrajda, Y. Feng, and Z. Wasilewski, Phys. Rev. B **59**, 2801 (1999).

[11] T. H. Oosterkamp, J. W. Janssen, L. P. Kouwenhoven, D. G. Austing, T. Honda, and S. Tarucha, Phys. Rev. Lett. **82**, 2931 (1999). xiii

[12] F. E. Camino, W. Zhou, and V. J. Goldman, Phys. Rev. B **76**, 155305 (2007). xiii

[13] Y. Ji, Y. Chung, D. Sprinzak, M. Heiblum, D. Mahalu, and H. Shtrikman, Nature **422**, 415 (2003). xiii

[14] I. Neder, M. Heiblum, Y. Levinson, D. Mahalu, and V. Umansky, Phys. Rev. Lett. **96**, 016804 (2006). xiii

[15] Y. Zhang, D. T. McClure, E. M. Levenson-Falk, C. M. Marcus, L. N. Pfeiffer, and K. W. West, Phys. Rev. B **79**, 241304 (2009). xiii

[16] D. R. Mace, C. H. W. Barnes, G. Faini, D. Mailly, M. Y. Simmons, C. J. B. Ford, and M. Pepper, Phys. Rev. B **52**, R8672 (1995). xiv, 20, 67

[17] C. J. B. Ford, P. J. Simpson, I. Zailer, D. R. Mace, M. Yosefin, M. Pepper, D. A. Ritchie, J. E. F. Frost, M. P. Grimshaw, and G. A. C. Jones, Phys. Rev. B **49**, 17456 (1994). xiv, 20, 56, 66, 78

[18] M. Kataoka, C. J. B. Ford, G. Faini, D. Mailly, M. Y. Simmons, and D. A. Ritchie, Phys. Rev. B **62**, R4817 (2000). 45, 56, 57, 66

[19] M. Kataoka, C. J. B. Ford, M. Y. Simmons, and D. A. Ritchie, Phys. Rev. B **68**, 153305 (2003). 20, 68, 69, 71, 78, 82

[20] H.-S. Sim, M. Kataoka, H. Yi, N. Y. Hwang, M.-S. Choi, and S.-R. E. Yang, Phys. Rev. Lett. **91**, 266801 (2003). xiv, 20, 45, 56, 58, 66, 69

[21] D. B. Chklovskii, B. I. Shklovskii, and L. I. Glazman, Phys. Rev. B **46**, 4026 (1992). xiv, 57, 66

[22] H.-S. Sim, M. Kataoka, and C. Ford, Physics Reports **456**, 127 (2008). xiv, 20, 37, 66

[23] C. P. Michael, Antidot resonances at the border of the non-interacting and self-consistent models, Master of philosophy, University of Cambridge, 2004. xiv, xvi, 56, 67

[24] S. H. Simon, Phys. Rev. B **61**, R16327 (2000). xiv, 146

[25] I. V. Zozoulenko and M. Evaldsson, Appl. Phys. Lett. **85**, 3136 (2004). xiv, 68, 71

[26] L. D. Landau and E. M. Lifshitz, *Quantum Mechanics*, Oxford: Butterworth-Heinemann, 1997. 3

[27] Z. F. Ezawa, *Quantum Hall Effects: Field Theoretic Approach and Related Topics*, World Scientific, 2000. 4

[28] C. Darwin, Proc. Cambridge Philos. Soc. **27**, 86 (1930). 5

[29] V. Fock, Z. Phys. **47**, 446 (1928). 5

[30] K. v. Klitzing, G. Dorda, and M. Pepper, Phys. Rev. Lett. **45**, 494 (1980). 7, 31

[31] M. Büttiker, Phys. Rev. B **38**, 9375 (1988). 7, 31, 34

[32] W. Ehrenberg and R. E. Siday, Proc. Phys. Soc. B **62**, 8 (1949). 16

[33] Y. Aharonov and D. Bohm, Phys. Rev. **115**, 485 (1959). 16

[34] M. V. Berry, Proc. R. Soc. Lond. A **392**, 45 (1984). 16

[35] T. T. Wu and C. N. Yang, Phys. Rev. D **12**, 3845 (1975). 16

[36] A. van Oudenaarden, M. H. Devoret, Y. V. Nazarov, and J. E. Mooij, Nature **391**, 768 (1998). 16

[37] N. Osakabe, T. Matsuda, T. Kawasaki, J. Endo, A. Tonomura, S. Yano, and H. Yamada, Phys. Rev. A **34**, 815 (1986). 16

[38] G. Timp, A. M. Chang, J. E. Cunningham, T. Y. Chang, P. Mankiewich, R. Behringer, and R. E. Howard, Phys. Rev. Lett. **58**, 2814 (1987). 16

[39] C. G. Smith, M. Pepper, R. Newbury, H. Ahmed, D. G. Hasko, D. C. Peacock, J. E. F. Frost, D. A. Ritchie, G. A. C. Jones, and G. Hill, J. Phys.: Condens. Matter **1**, 6763 (1989). 18

[40] V. J. Goldman, J. Liu, and A. Zaslavsky, Phys. Rev. B **77**, 115328 (2008). 18

[41] M. Kataoka, C. J. B. Ford, G. Faini, D. Mailly, M. Y. Simmons, D. R. Mace, C.-T. Liang, and D. A. Ritchie, Phys. Rev. Lett. **83**, 160 (1999). 19

[42] A. S. Sachrajda, Y. Feng, R. P. Taylor, G. Kirczenow, L. Henning, J. Wang, P. Zawadzki, and P. T. Coleridge, Phys. Rev. B **50**, 10856 (1994). 20

[43] M. Kataoka, C. J. B. Ford, M. Y. Simmons, and D. A. Ritchie, Phys. Rev. Lett. **89**, 226803 (2002). 20, 66, 78

[44] H. S. Sim, N. Y. Hwang, M. Kataoka, H. Yi, M. S. Choi, and S. R. Eric Yang, Physica E **22**, 554 (2004). 20, 59, 105

[45] N. Y. Hwang, S.-R. E. Yang, H.-S. Sim, and H. Yi, Phys. Rev. B **70**, 085322 (2004). 20, 59, 105

[46] H. A. Bethe and R. W. Jackiw, *Intermediate Quantum Mechanics*, Menlo Park, California: Benjamin Cummings, 3rd edition, 1986. 21, 22, 23, 112

[47] C. C. J. Roothaan, Rev. Mod. Phys. **23**, 69 (1951). 23

[48] G. G. Hall, Proc. R. Soc. Lond. A **205**, 541 (1951). 23

[49] V. Melik-Alaverdian, N. E. Bonesteel, and G. Ortiz, Phys. Rev. B **60**, R8501 (1999). 24

[50] G. Murthy and R. Shankar, Phys. Rev. B **65**, 245309 (2002). 24

[51] W. Bishara and C. Nayak, Phys. Rev. B **80**, 121302 (2009). 24

[52] M. Stone, H. W. Wyld, and R. L. Schult, Phys. Rev. B **45**, 14156 (1992). 24, 27, 112

[53] E. V. Tsiper, J. Math. Phys. **43**, 1664 (2002). 24

[54] J. M. Luttinger, J. Math. Phys. **4**, 1154 (1963). 27

[55] S. Tomonaga, Prog. Theor. Phys. **5**, 544 (1950). 27

[56] S. P. Shukla, M. Shayegan, S. R. Parihar, S. A. Lyon, N. R. Cooper, and A. A. Kiselev, Phys. Rev. B **61**, 4469 (2000). 28

[57] M. Büttiker, Phys. Rev. Lett. **57**, 1761 (1986). 31

[58] R. Landauer, IBM J. Res. Dev. **1**, 233 (1957). 31

[59] R. Landauer, Philosophical Magazine **21**, 863 (1970). 31

[60] A. D. Stone and A. Szafer, IBM J. Res. Dev. **32**, 384 (1988). 31

[61] H. U. Baranger and A. D. Stone, Phys. Rev. B **40**, 8169 (1989). 32, 37, 40, 42, 44

[62] S. Ihnatsenka and I. V. Zozoulenko, Phys. Rev. B **74**, 201303 (2006). 37, 45, 59

[63] D. J. Griffiths, *Introduction to Quantum Mechanics*, Prentice Hall, 1995. 37

[64] E. N. Economou, *Green's Functions in Quantum Physics*, volume 7, Springer Berlin Heidelberg, third edition edition, 2006. 37

[65] A. MacKinnon, Z. Phys. B **59**, 385 (1985). 44, 63

[66] D. V. Averin and K. K. Likharev, J. Low Temp. Phys. **62**, 345 (1986). 46

[67] D. V. Averin, A. N. Korotkov, and K. K. Likharev, Phys. Rev. B **44**, 6199 (1991). 46

[68] C. W. J. Beenakker, Phys. Rev. B **44**, 1646 (1991). 55

[69] Y. Meir, N. S. Wingreen, and P. A. Lee, Phys. Rev. Lett. **66**, 3048 (1991). 46

[70] L. P. Kouwenhoven, G. Schön, and L. L. Sohn, *Mesoscopic Electron Transport*, chapter Introduction to Mesoscopic Electron Transport, pages 1–44., Kluwer, Dordrecht, 1997. 46

[71] M. Kataoka, C. J. B. Ford, G. Faini, D. Mailly, M. Y. Simmons, and D. A. Ritchie, Physica E **12**, 782 (2002). 56

[72] M. Kataoka, C. J. B. Ford, M. Y. Simmons, and D. A. Ritchie, Physica E **22**, 558 (2004). 56, 66

[73] C. Michael, M. Kataoka, C. Ford, G. Faini, D. Mailly, M. Simmons, and D. Ritchie, Physica E **34**, 195 (2006). 56, 59, 61, 67

[74] I. Karakurt, V. J. Goldman, J. Liu, and A. Zaslavsky, Phys. Rev. Lett. **87**, 146801 (2001). 57, 59, 66

[75] M. Kataoka and C. J. B. Ford, Phys. Rev. Lett. **92**, 199703 (2004). 59

[76] V. J. Goldman, Phys. Rev. Lett. **92**, 199704 (2004). 57, 66

[77] L. P. Kouwenhoven, T. H. Oosterkamp, M. W. Danoesastro, M. Eto, D. G. Austing, T. Honda, and S. Tarucha, Science **278**, 1788 (1997). 59

[78] P. L. McEuen, E. B. Foxman, U. Meirav, M. A. Kastner, Y. Meir, N. S. Wingreen, and S. J. Wind, Phys. Rev. Lett. **66**, 1926 (1991). 59

[79] J. H. Davies, I. A. Larkin, and E. V. Sukhorukov, J. Appl. Phys. **77**, 4504 (1995). 61, 63

[80] B. Rosenow and B. I. Halperin, Phys. Rev. Lett. **98**, 106801 (2007). 66

[81] B. J. van Wees, E. M. M. Willems, C. J. P. M. Harmans, C. W. J. Beenakker, H. van Houten, J. G. Williamson, C. T. Foxon, and J. J. Harris, Phys. Rev. Lett. **62**, 1181 (1989). 68

[82] G. Müller, D. Weiss, A. V. Khaetskii, K. von Klitzing, S. Koch, H. Nickel, W. Schlapp, and R. Lösch, Phys. Rev. B **45**, 3932 (1992). 68, 69, 77

[83] C. J. B. Ford, T. J. Thornton, R. Newbury, M. Pepper, H. Ahmed, D. C. Peacock, D. A. Ritchie, J. E. F. Frost, and G. A. C. Jones, Appl. Phys. Lett. **54**, 21 (1989). 70

[84] A. P. Smith, A. H. MacDonald, and G. Gumbs, Phys. Rev. B **45**, 8829 (1992). 71

[85] O. Olendski and L. Mikhailovska, Phys. Rev. B **72**, 235314 (2005). 71

[86] J. J. Palacios and C. Tejedor, Phys. Rev. B **45**, 9059 (1992). 71

[87] B. W. Alphenaar, P. L. McEuen, R. G. Wheeler, and R. N. Sacks, Phys. Rev. Lett. **64**, 677 (1990). 77

[88] S. Komiyama, H. Hirai, M. Ohsawa, Y. Matsuda, S. Sasa, and T. Fujii, Phys. Rev. B **45**, 11085 (1992).

[89] H. Hirai, S. Komiyama, S. Fukatsu, T. Osada, Y. Shiraki, and H. Toyoshima, Phys. Rev. B **52**, 11159 (1995).

[90] A. Würtz, R. Wildfeuer, A. Lorke, E. V. Deviatov, and V. T. Dolgopolov, Phys. Rev. B **65**, 075303 (2002). 77

[91] I. A. Merkulov, A. L. Efros, and M. Rosen, Phys. Rev. B **65**, 205309 (2002). 91

[92] J. B. Miller, D. M. Zumbühl, C. M. Marcus, Y. B. Lyanda-Geller, D. Goldhaber-Gordon, K. Campman, and A. C. Gossard, Phys. Rev. Lett. **90**, 076807 (2003). 92

[93] A. V. Khaetskii and Y. V. Nazarov, Phys. Rev. B **61**, 12639 (2000). 92

[94] P. Pietiläinen and T. Chakraborty, Phys. Rev. B **73**, 155315 (2006). 92

[95] A. T. Johnson, L. P. Kouwenhoven, W. de Jong, N. C. van der Vaart, C. J. P. M. Harmans, and C. T. Foxon, Phys. Rev. Lett. **69**, 1592 (1992). 96

[96] J. Weis, R. J. Haug, K. v. Klitzing, and K. Ploog, Phys. Rev. Lett. **71**, 4019 (1993). 96

[97] D. Weinmann, W. Häusler, and B. Kramer, Phys. Rev. Lett. **74**, 984 (1995). 96

[98] S. M. Reimann and M. Manninen, Rev. Mod. Phys. **74**, 1283 (2002). 104

[99] B. Bollabas, *Random Graphs*, Academic Press, London, 1985. 118

[100] E. W. Dijkstra, Numerische Mathematik **1**, 269 (1959). 119

[101] M. Korkusiński, P. Hawrylak, M. Ciorga, M. Pioro-Ladrière, and A. S. Sachrajda, Phys. Rev. Lett. **93**, 206806 (2004). 126

[102] C. Gould, A. S. Sachrajda, M. W. C. Dharma-wardana, Y. Feng, and P. T. Coleridge, Phys. Rev. Lett. **77**, 5272 (1996). 130

[103] I. J. Maasilta and V. J. Goldman, Phys. Rev. Lett. **84**, 1776 (2000). 130